



Universitetet
i Stavanger

FACULTY OF SCIENCE AND TECHNOLOGY

MASTER'S THESIS

Study program/specialization:

Petroleum Engineering / Drilling and Well
Technology

Spring semester, 2021

Open

Author:

Harald Halvorsen

Program coordinator:

Supervisor: Mesfin Belayneh

Working title of Master's thesis:

Drill-in fluids and hydraulic fracturing characterization of lost circulation material

Credits (ECTS): 30

Keywords:

- Drill-in fluids
- Viscoelasticity
- CaCO₃
- Nanoparticle
- Hydraulic performance simulations
- Self-healing seal effect
- Hydraulic fracturing

Number of pages: 177

+ supplemental material/other: 7

Stavanger, 15.06.2021

Abstract

Conventional water-based and oil-based drilling fluids use barite as weight control material. However, the main concern with barite particles is that it damages the near wellbore formation permeability and hence reduces reservoir productivity. Therefore, reservoir drill-in fluids are applied to drill-in the reservoir section to reduce formation damage. Drill-in fluids are formulated with high density brines along with polymers, and CaCO₃ particles as lost circulation material (LCM).

In this thesis, Sodium formate and Potassium formate-based drill-in fluids were designed and characterized at the UIS lab. Moreover, Cesium/Potassium-based drill-in fluids were formulated and characterized its properties along with its hydraulic fracturing performance. Some of the main results are summarized as follows:

- ✓ At different micron sized CaCO₃ particle concentrations, the sodium and potassium fluids performed thermal stable rheology properties until 80°C.
- ✓ CaCO₃ nanoparticles improve the particle stability and thermal stability in potassium and sodium formate fluid systems formulated with micron sized CaCO₃.
- ✓ The cesium/potassium base mud exhibited a self-healing seal effect after the well was fractured.
- ✓ Addition of 2wt% micron sized quartz LCM particles in the cesium/potassium base mud, increased the fracturing and re-fracturing pressure by 6.5% and 5.4% respectively.

Acknowledgment

First, I wish to thank my supervisor Mesfin Belayneh for his exceptional guidance and motivational support throughout the whole thesis period. Your willingness to take your time and share your remarkable knowledge has been of great help.

I also would like to thank the lab engineers at UIS, Sivert B. Drangeid and Kim A.N. Vorland for always taking their time to support me with the technical challenges regarding the hydraulic fracturing and rheometer equipment's.

In addition, I wish to thank Professor Bernt S. Aadnøy for sharing his unique knowledge.

Table of contents

HEADING	i
Abstract.....	ii
Acknowledgment.....	iii
Table of contents.....	iv
List of Figures.....	ix
List of Tables.....	xv
List of Symbols	xviii
List of Abbreviations.....	xxi
1 Introduction.....	1
1.1 Background.....	1
1.2 Problem definition	3
1.3 Objective.....	4
1.4 Research program	4
2 Literature study.....	6
2.1 Case studies on formate brines	6
2.1.1 Formate brines	6
2.1.2 Cs formate experience at Kvitebjørn field, Norway.....	7
2.1.3 Na/K and K formate experience at Ghawar field, Saudi Arabia	9
2.1.4 Cs formate experience at Eagle Ford and Tuscaloosa field, USA	10
2.1.5 Cs/K formate experience at Martin Linge field, Norway.....	12
2.1.5.1 Martin Linge fluid design.....	12
2.1.5.2 Martin Linge fluid properties	13
2.2 Case studies on Stress Cage Theory	14
2.2.1 Stress Cage Theory.....	15
2.2.2 Extended leak-off test experience at Arkoma basin, USA.....	16
2.2.3 Lab experience of LCM material effect on wellbore strength, Canada	18
3 Theory	20
3.1 Rheology.....	20
3.1.1 Plastic viscosity	20
3.1.2 Yield point.....	20
3.1.3 Gel strength	21
3.1.4 Shear stress.....	21
3.1.5 Shear rate.....	21
3.2 Rheological models	22

3.2.1	Newtonian fluid	22
3.2.2	Non-Newtonian fluid.....	23
3.2.2.1	Bingham plastic model	24
3.2.2.2	Power-law model.....	26
3.2.2.3	Herschel-Bulkley model.....	27
3.2.2.4	Unified model.....	29
3.2.2.5	Robertson-Stiff model	30
3.3	Viscoelasticity.....	31
3.3.1	Oscillatory tests	32
3.3.2	Approaches to measure viscoelastic performance.....	36
3.3.2.1	Temperature sweep	36
3.3.2.2	Amplitude sweep.....	38
3.4	Well program	40
3.4.1	Equivalent circulating density	40
3.4.2	Pump pressure	40
3.5	Well fracture models.....	43
3.5.1	Non-Penetrating fracture model	43
3.5.2	Penetrating fracture model	44
3.6	Lost circulation material	45
3.7	Particle size of bridging materials	46
3.8	Fracture propagation process	48
4	Experimental work.....	49
4.1	Materials and methods	49
4.1.1	Materials.....	49
4.1.1.1	Sodium formate.....	49
4.1.1.2	Potassium formate.....	49
4.1.1.3	Cesium formate	50
4.1.1.4	Starch	50
4.1.1.5	Xanthan gum	50
4.1.1.6	CaCO ₃	50
4.1.1.7	Quartz.....	51
4.2	Characterization methods	52
4.2.1	Haver EML 200 digital shaker and sieve procedure	52
4.2.2	API static filter press and filtrate procedure.....	53
4.2.3	OFITE Model 800 viscometer and rheology measurement procedure	54
4.2.4	Anton Paar MCR 302 Rheometer and viscoelastic test procedure	56
4.2.5	Sonics vibra-cell and ultrasonic test procedure	57

4.2.6	Enerpac hydraulic fracturing setup and fracking procedure	58
4.3	Laboratory drilling fluid formulation	60
4.3.1	Na-formate drilling fluid formulation	60
4.3.1.1	Na-formate mixing method and time	60
4.3.1.2	Test design 1: Effect of CaCO ₃ particle size in Na-formate drill-in fluid.....	62
4.3.1.3	Test design 2: Effect of CaCO ₃ particle concentration in Na-formate drill-in fluid	63
4.3.1.4	Test design 3: Effect of polymer concentration in Na-formate drill-in fluid ...	64
4.3.1.5	Test design 4: Comparison between CaCO ₃ type 1 and CaCO ₃ type 2 in Na-formate drill-in fluid	64
4.3.2	K-formate drilling fluid formulation	65
4.3.2.1	Test design 5: Effect of CaCO ₃ particle concentration in K-formate drill-in fluid	65
4.3.3	Nano-based Na and K-formate drilling fluid formulation.....	66
4.3.3.1	Nano-based K-formate mixing method and time	66
4.3.3.2	Test design 6: Effect of CaCO ₃ NP's in K-formate drill-in fluid.....	67
4.3.3.3	Test design 7: Effect of CaCO ₃ NP's in Na-formate drill-in fluid	68
4.3.4	Na/K-formate drilling fluid formulation	68
4.3.4.1	Na/K ratios mixing method and time	68
4.3.4.2	Test design 8: Effect of Na/K ratios	69
4.3.5	Cs/K-formate drilling fluid formulation.....	70
4.3.5.1	Cs/K mixing method and time.....	70
4.3.5.2	Test design 9: Characterization of modified Cs/K drill-in fluid	71
4.3.5.3	Test design 10: Hydraulic fracturing of Cs/K drill-in fluid.....	72
5	Results and discussion.....	74
5.1	Test design 1: Effect of CaCO ₃ particle size in Na-formate drill-in fluid.....	74
5.1.1	Effect of CaCO ₃ particle size on polymer mix and filtration properties	74
5.1.2	Effect of CaCO ₃ particle size on rheological properties	75
5.1.3	Effect of CaCO ₃ particle size on viscoelastic properties.....	78
5.1.3.1	Effect of CaCO ₃ particle size on amplitude sweep	78
5.2	Test design 2: Effect of CaCO ₃ particle concentration in Na-formate drill-in fluid .	79
5.2.1	Effect of CaCO ₃ particle concentration on filtration properties	79
5.2.2	Effect of CaCO ₃ particle concentration on rheological properties.....	80
5.2.3	Effect of CaCO ₃ particle concentration on viscoelastic properties	83
5.2.3.1	Effect of CaCO ₃ particle concentration on temperature sweep.....	83
5.2.3.2	Effect of CaCO ₃ particle concentration on amplitude sweep.....	84
5.3	Test design 3: Effect of polymer concentration in Na-formate drill-in fluid	86
5.3.1	Effect of polymer concentration on filtration properties	86

5.3.2	Effect of polymer concentration on rheological properties	87
5.3.3	Effect of polymer concentration on viscoelastic properties	89
5.3.3.1	Effect of CaCO ₃ polymer concentration on temperature sweep	89
5.3.3.2	Effect of CaCO ₃ polymer concentration on amplitude sweep	90
5.4	Test design 4: Comparison between CaCO ₃ type 1 and CaCO ₃ type 2 in Na-formate drill-in fluids.....	91
5.4.1	Effect of CaCO ₃ particle type on filtration properties.....	91
5.4.2	Effect of CaCO ₃ particle type on rheological properties.....	91
5.4.3	Effect of CaCO ₃ particle type on viscoelastic properties	94
5.4.3.1	Effect of CaCO ₃ particle type on temperature sweep.....	94
5.4.3.2	Effect of CaCO ₃ particle type on amplitude sweep.....	95
5.5	Test design 5: Effect of CaCO ₃ particle concentration in K-formate drill-in fluid ..	95
5.5.1	Effect of CaCO ₃ particle concentration on filtration properties.....	95
5.5.2	Effect of CaCO ₃ particle concentration on rheological properties.....	96
5.5.3	Effect of CaCO ₃ particle concentration on viscoelastic properties	99
5.5.3.1	Effect of CaCO ₃ particle concentration on temperature sweep.....	99
5.5.3.2	Effect of CaCO ₃ particle concentration on amplitude sweep.....	100
5.6	Test design 6: Effect of CaCO ₃ NP's in K-formate drill-in fluid	101
5.6.1	Effect of CaCO ₃ NP's on filtration properties.....	101
5.6.2	Effect of CaCO ₃ NP's on rheological properties.....	102
5.6.3	Effect of CaCO ₃ NP's on viscoelastic properties	105
5.6.3.1	Effect of CaCO ₃ NP's on temperature sweep	105
5.6.3.2	Effect of CaCO ₃ NP's on amplitude sweep.....	106
5.6.4	Effect of CaCO ₃ NP's on particle stability.....	106
5.7	Test design 7: Effect of CaCO ₃ NP's in Na-formate drill-in fluid	107
5.7.1	Effect of CaCO ₃ NP's on filtration properties.....	107
5.7.2	Effect of CaCO ₃ NP's on rheological properties.....	108
5.7.3	Effect of CaCO ₃ NP's on viscoelastic properties	110
5.7.3.1	Effect of CaCO ₃ NP's on temperature sweep	110
5.7.3.2	Effect of CaCO ₃ NP's on amplitude sweep.....	111
5.7.4	Effect of CaCO ₃ NP's on particle stability.....	112
5.8	Test design 8: Effect of Na/K ratios	113
5.8.1	Effect of Na/K ratios on filtration properties	113
5.8.2	Effect of Na/K ratios on rheological properties	114
5.8.3	Effect of Na/K ratios on viscoelastic properties.....	116
5.8.3.1	Effect of Na/K ratios on temperature sweep	116
5.8.3.2	Effect of Na/K ratios on amplitude sweep	117
5.9	Test design 9: Characterization of modified Cs/K drill-in fluid.....	118

5.9.1	Effect of Cs/K on pH and density properties	118
5.9.2	Effect of polymer mix on filtration and rheological properties.....	118
5.9.3	Effect of Cs/K ageing on rheological properties	122
5.9.4	Effect of modified Cs/K on viscoelastic and rheological properties	123
5.9.4.1	Effect of modified Cs/K on temperature sweep	123
5.9.4.2	Effect of modified high viscous Cs/K on temperature	124
5.9.4.3	Effect of modified less viscous Cs/K on temperature	125
5.9.4.4	Effect of modified Cs/K leftover mud on temperature.....	126
5.9.4.5	Viscosity comparison between modified Cs/K fluids on lower shear rates ...	126
5.9.4.6	Flow comparison between modified Cs/K fluids at higher temperatures	127
5.9.4.7	Flow comparison between modified Cs/K fluids at ambient conditions.....	128
5.9.5	Particle stability in Cs/K drill-in fluid.....	129
5.10	Test design 10: Hydraulic fracturing characterization on Cs/K drill-in fluid	130
5.10.1	Cs/K drill-in fluid for fracking on rheological properties	130
5.10.2	Cs/K drill-in fluid for hydraulic fracturing on viscoelastic properties	132
5.10.3	Particle stability on Cs/K design mud	134
5.10.4	Effect of Cs/K design mud on density and rheological properties	135
5.10.5	Hydraulic fracturing of Cs/K drill-in fluids	137
5.10.5.1	Test 1: Core 1	137
5.10.5.2	Test 2: Core 2	138
5.10.5.3	Average fracture breakdown pressures	140
5.10.5.4	Deviation between Cs/K design mud and Cs/K base mud.....	140
6	Simulation work	142
6.1	Nano-based potassium system.....	142
6.1.1	ECD thermal stability analysis	142
6.1.2	Pump pressure thermal stability analysis	144
6.2	Nano-based sodium system	145
6.2.1	ECD thermal stability analysis	146
6.2.2	Pump pressure thermal stability analysis	147
7	Conclusion.....	149
8	References	152
APPENDICES	156

List of Figures

Figure 1.1: The periodic table of elements [10].	2
Figure 1.2: Illustrative sketch of the problem definition [11]. Whether LCM in Cs/K drill-in fluids enhances wellbore strength or not?	3
Figure 1.3: Summary of the research activities performed in this thesis.	5
Figure 2.1: Formate brines used in drill-in and completion fluids [14].	7
Figure 2.2: Location map of the Kvitebjørn field (red/light red area in red square) in North Sea [16].	8
Figure 2.3: Location map of Ghawar field (green area in green circle) onshore Saudi Arabia [18].	9
Figure 2.4: Location map of Eagle Ford and TMS shale fields (green area at location map) onshore USA [21].	11
Figure 2.5: Location of the Martin Linge field [15].	12
Figure 2.6: Stress cage theory for wellbore strengthening effect [22].	16
Figure 2.7: Location map of the Arkoma basin [23].	16
Figure 2.8: Extended leak-off test at Arkoma basin [22].	18
Figure 2.9: Optimal blends compared with unblended fluids and WBM control sample [9].	19
Figure 3.1: Left: Shear stress profile. Right: Shear rate profile [27].	22
Figure 3.2: Linear relationship of shear stress-shear rate of a Newtonian fluid [29].	23
Figure 3.3: Shear stress-shear rate relationship of a classic drilling mud and Newtonian fluid [29].	24
Figure 3.4: Shear stress-shear rate relationship of the Bingham plastic model [29].	25
Figure 3.5: Shear stress-shear rate relationship of the power-law model [29].	27
Figure 3.6: Shear stress-shear rate relationship of the Herschel-Bulkley model [29].	29
Figure 3.7: Example of log-log plot to determine A and B parameters for R-S model. In this example $A = 1.313$ and $B = 0.6186$ [36].	31
Figure 3.8: An overview of the ranges of material behavior [40].	31
Figure 3.9: Illustration of oscillatory shear test from the two-plate model [39].	32
Figure 3.10: Mathematical described oscillatory test for the two-plate model [39].	33
Figure 3.11: graphical representation of shear stress and shear strain against time [39].	34
Figure 3.12. Temperature sweep of a viscous fluid sample [39].	37
Figure 3.13: Temperature sweep of a gel formation [39].	38
Figure 3.14: Strain amplitude sweep of a sample showing elastic and/or gel behavior in the LVE range [39].	39

Figure 3.15: Stress amplitude sweep showing yield stress, yield-zone, and flow point of a sample [39].	39
Figure 3.16: Illustrative sketch of the dynamic frictional pressure losses in the hydraulic system [43].	41
Figure 3.17: Non-penetrating fracture model [11].	43
Figure 3.18: Penetrating fracture model [11].	45
Figure 3.19: Fracture pressure vs. Moh's scale [47].	46
Figure 3.20: Incorrect sized CaCO ₃ in drill-in fluid [49].	47
Figure 3.21: Correct sized CaCO ₃ in drill-in fluid [49].	47
Figure 3.22: Illustration of the fracture propagation process [47].	48
Figure 4.1: Particle size distribution for CaCO ₃ type 1 and CaCO ₃ type 2 (mass% and cumulative PSD).	51
Figure 4.2: Haver EML 200 digital shaker for sieving the CaCO ₃ particles.	53
Figure 4.3: API static filter press with measuring cylinder.	54
Figure 4.4: OFITE model 800 viscometer with heating cup.	55
Figure 4.5: Anton Paar MCR 302 rheometer.	57
Figure 4.6: Sonics vibra-cell.	58
Figure 4.7: Enerpac hydraulic fracturing experimental setup.	60
Figure 5.1: API Filtrate loss for <63, 71-90 and 0-<355 microns with in-situ vs. in-situ + ex-situ polymer treatment.	75
Figure 5.2: Shear stress on rpm for <63, 71-90 and 0-<355-micron sized CaCO ₃ at 20°C.	76
Figure 5.3: Shear stress on rpm for <63, 71-90 and 0-<355-micron sized CaCO ₃ at 50°C.	76
Figure 5.4: Shear stress on rpm for <63, 71-90 and 0-<355-micron sized CaCO ₃ at 80°C.	77
Figure 5.5: API filtrate loss for the 25g, 45g and 65g CaCO ₃ particle concentration in Na-formate fluid.	80
Figure 5.6: Shear stress on rpm for 25g, 45g and 65g CaCO ₃ particle concentration at 20°C.	81
Figure 5.7: Shear stress on rpm for 25g, 45g and 65g CaCO ₃ particle concentration at 50°C.	81
Figure 5.8: Shear stress on rpm for 25g, 45g and 65g CaCO ₃ particle concentration at 80°C.	82
Figure 5.9: Temperature sweeps for 25g, 45g and 65g CaCO ₃ particle concentrations.	84
Figure 5.10: Strain amplitude sweep for 25g, 45g and 65g CaCO ₃ particle concentrations.	85
Figure 5.11: API filtrate loss for the 1.19g XG and 1.39g XG polymer concentrations.	86
Figure 5.12: Shear stress on rpm for the 1.19g XG and 1.39g XG polymer concentrations at 20°C.	87

Figure 5.13: Shear stress on rpm for the 1.19g XG and 1.39g XG polymer concentrations at 50°C.....	88
Figure 5.14: Shear stress on rpm for the 1.19g XG and 1.39g XG polymer concentrations at 80°C.....	88
Figure 5.15: Temperature sweeps for the 1.19g XG and 1.39g XG polymer concentrations..	90
Figure 5.16: API filtrate loss for the 25g CaCO ₃ type 1 and 25g CaCO ₃ type 2.	91
Figure 5.17: Shear stress on rpm for the CaCO ₃ type 1 and CaCO ₃ type 2 at 20°C.	92
Figure 5.18: Shear stress on rpm for the CaCO ₃ type 1 and CaCO ₃ type 2 at 50°C.	92
Figure 5.19: Shear stress on rpm for the CaCO ₃ type 1 and CaCO ₃ type 2 at 80°C.	93
Figure 5.20: Temperature sweeps for the CaCO ₃ type 1 and CaCO ₃ type 2.....	94
Figure 5.21: API filtrate loss for the 25g, 45g and 65g CaCO ₃ particle concentrations.	96
Figure 5.22: Shear stress on rpm for 25g, 45g and 65g CaCO ₃ particle concentration at 20°C.	97
Figure 5.23: Shear stress on rpm for 25g, 45g and 65g CaCO ₃ particle concentration at 50°C.	97
Figure 5.24: Shear stress on rpm for the 25g, 45g and 65g CaCO ₃ particle concentrations at 80°C.....	98
Figure 5.25: Temperature sweeps for the 25g, 45g and 65g CaCO ₃ particle concentrations.	100
Figure 5.26: Strain amplitude sweeps for 25g, 45g and 65g CaCO ₃ particle concentrations.	100
Figure 5.27: API filtrate loss for the reference fluid with 1wt%, 2.05wt% and 3wt% CaCO ₃ NP fluid systems.....	102
Figure 5.28: Shear stress on rpm for the reference fluid with 1wt%, 2.05wt% and 3wt% CaCO ₃ NP's at 20°C.....	102
Figure 5.29: Shear stress on rpm for the reference fluid with 1wt%, 2.05wt% and 3wt% CaCO ₃ NP's at 50°C.....	103
Figure 5.30: Shear stress on rpm for reference fluid with 1wt%, 2.05wt% and 3wt% CaCO ₃ NP's at 80°C.....	104
Figure 5.31: Temperature sweeps for the reference fluid with 1wt%, 2.05wt% and 3wt% CaCO ₃ NP's.....	105
Figure 5.32: Particle stability for cooked K-formate reference fluid with 1wt%, 2.05wt% and 3wt% CaCO ₃ NP's.	107
Figure 5.33: API filtrate loss for the reference fluid with 1wt%, 2wt% and 3wt% CaCO ₃ NP fluid systems.....	108

Figure 5.34: Shear stress on rpm for the reference fluid with 1wt%, 2wt% and 3wt% CaCO ₃ NP's at 20°C.....	108
Figure 5.35: Shear stress on rpm for the reference fluid with 1wt%, 2wt% and 3wt% CaCO ₃ NP's at 50°C.....	109
Figure 5.36: Shear stress on rpm for the reference fluid with 1wt%, 2wt% and 3wt% CaCO ₃ NP's at 80°C.....	109
Figure 5.37: Temperature sweeps for the reference fluid with 1wt%, 2wt% and 3wt% CaCO ₃ NP's.....	111
Figure 5.38: Particle stability for the cooked Na-formate reference fluid with 1wt%, 2wt% and 3wt% CaCO ₃ NP's.	112
Figure 5.39: API filtrate loss for the Na/K 50/50, 60/40 and 70/30 fluid systems.....	113
Figure 5.40: Shear stress on rpm for the Na/K 50/50, 60/40 and 70/30 ratios at 20°C.....	114
Figure 5.41: Shear stress on rpm for the Na/K 50/50, 60/40 and 70/30 ratios at 50°C.....	114
Figure 5.42: Shear stress on rpm for the Na/K 50/50, 60/40 and 70/30 ratios at 80°C.....	115
Figure 5.43: Temperature sweeps for the Na/K 50/50, 60/40 and 70/30 ratios.	117
Figure 5.44: Strain amplitude sweeps for the Na/K 50/50, 60/40 and 70/30 ratios.	117
Figure 5.45: Left: High viscous Cs/K before extra mix. Right: High viscous Cs/K after 15 min extra mix.....	119
Figure 5.46: API filtrate loss test performed before and after extra polymer mix for the high viscous and less viscous Cs/K fluids.....	119
Figure 5.47: Shear stress on rpm for the high viscous Cs/K fluid system at 20°C.	120
Figure 5.48: Shear stress on rpm for the less viscous Cs/K fluid system at 20°C.	121
Figure 5.49: Shear stress on rpm for the high viscous Cs/K tested right away and after 3 days of ageing at 20°C.....	122
Figure 5.50: Temperature sweeps for the unmodified Sinomine, high viscous modified Cs/K, and less viscous modified Cs/K fluids.	124
Figure 5.51: Shear stress on shear rate for the high viscous modified Cs/K fluid at 50°C and 80°C.....	125
Figure 5.52: Shear stress on shear rate for the less viscous modified Cs/K fluid at 50°C and 80°C.....	125
Figure 5.53: Shear stress on shear rate for the Cs/K 50/50 ratio at 50°C and 80°C.....	126
Figure 5.54: Viscosity comparison between the high viscous Cs/K, less viscous Cs/K and 50/50 Cs/K ratio for lower shear rates at 50°C and 80°C.	127

Figure 5.55: Flow comparison between high viscous Cs/K, less viscous Cs/K and 50/50 Cs/K ratio at 50°C and 80°C. 127

Figure 5.56: Shear stress on rpm for the high viscous Cs/K, less viscous Cs/K and 50/50 Cs/K ratio at 20°C. 128

Figure 5.57: Particle stability for the 100% less viscous Cs/K in a 1-hour time frame. 129

Figure 5.58: Particle stability for the 2/3 less viscous Cs/K + 1/3 high viscous Cs/K in a 1-hour time frame..... 130

Figure 5.59: Shear stress on rpm for the light viscous Cs/K for fracturing, original 100% less viscous Cs/K and Cs/K 50/50 ratio at 20°C. 131

Figure 5.60: Temperature sweeps for the light viscous Cs/K for fracking and original 100% less viscous Cs/K at 20°C..... 132

Figure 5.61: Shear stress on shear rate for the light viscous Cs/K fracking mud, 100% less viscous Cs/K and Cs/K 50/50 ratio at 50°C and 80°C. 133

Figure 5.62: Viscosity on shear rate for the light viscous Cs/K fracking mud, original 100% less viscous Cs/K and Cs/K 50/50 ratio at 50°C and 80°C. 134

Figure 5.63: Particle stability for the design mud in a 1-hour time frame. 135

Figure 5.64: Shear stress on rpm for the Cs/K base mud and Cs/K design mud at 20°C. 136

Figure 5.65: Fracture breakdown pressures for the Cs/K base mud and Cs/K design mud at core 1. 137

Figure 5.66: 10 min re-fracturing pressure for the Cs/K base mud and Cs/K design mud at core 2. 139

Figure 5.67: Fracture breakdown pressures for the Cs/K base mud and Cs/K design mud at core 2. 139

Figure 5.68: Average fracture breakdown pressures between the Cs/K base mud and Cs/K design mud. 140

Figure 5.69: % change in average fracture pressure between the Cs/K design mud and Cs/K base mud..... 141

Figure 6.1: Thermal stability analysis on ECD for the K-formate reference fluid and 1wt% CaCO₃ NP..... 143

Figure 6.2: Thermal stability analysis on ECD for the K-formate reference fluid and 1wt% CaCO₃ NP..... 143

Figure 6.3: Thermal stability analysis on pump pressure for the K-formate reference fluid and 1wt% CaCO₃ NP. 144

Figure 6.4: Thermal stability analysis on pump pressure for the K-formate reference fluid and 1wt% CaCO₃ NP 145

Figure 6.5: Thermal stability analysis on ECD for the Na-formate reference fluid and 1wt% CaCO₃ NP..... 146

Figure 6.6: Thermal stability analysis on ECD for the Na-formate reference fluid and 1 wt% CaCO₃ NP..... 146

Figure 6.7: Thermal stability analysis on pump pressure for the Na-formate reference fluid and 1wt% CaCO₃ NP. 147

Figure 6.8: Thermal stability analysis on pump pressure for the Na-formate reference fluid and 1wt% CaCO₃ NP. 148

List of Tables

Table 2.1: Cs/K formate drill-in fluid composition at the Martin Linge field [12].	13
Table 2.2: Cs/K formate drill-in fluid properties at the Martin Linge field [12].	14
Table 3.1: Parameters to state a materials viscoelastic behavior [39].	36
Table 3.2: Summary of parameters for the Unified hydraulics model [38].	42
Table 4.1: Na-formate fluid system with mixing steps, mixed chemicals, mixing method and time.	61
Table 4.2: Composition for the Na-formate test design 1 with <63, 71-90 and 0-<355 microns CaCO ₃ particle sizes.	63
Table 4.3: Composition for Na-formate test design 2 with increased CaCO ₃ particle concentration.	63
Table 4.4: Composition for Na-formate test design 3 with increased polymer concentration.	64
Table 4.5: Composition for Na-formate test design 4 with CaCO ₃ type 1 and CaCO ₃ type 2 comparison.	65
Table 4.6: Composition for K-formate test design 5 with increased CaCO ₃ particle concentration.	65
Table 4.7: Nano-based K-formate fluid system with mixing steps, mixed chemicals, mixing method and time.	66
Table 4.8: Composition for nano-based K-formate in test design 6.	67
Table 4.9: Composition for the nano-based Na-formate systems in test design 7.	68
Table 4.10: sodium/potassium fluid system with mixing steps, mixed chemicals, mixing method and time.	69
Table 4.11: Composition for the Na/K ratios in test design 8.	70
Table 4.12: Cs/K-formate fluid system with mixing steps, mixed chemicals, mixing method and time.	70
Table 4.13: Mud composition for the high viscous Cs/K and less viscous Cs/K drill in fluids.	72
Table 4.14: Mud composition for the Cs/K base mud and Cs/K design mud for hydraulic fracturing.	73
Table 5.1: Rheological parameters for the <63, 71-90 and 0-<355-micron sized CaCO ₃ at 20, 50 and 80°C.	78
Table 5.2: Important parameters obtained from the amplitude sweeps for <63, 71-90 and 0-<355-micron sized CaCO ₃ .	79

Table 5.3: Rheological parameters for the 25g, 45g and 65g CaCO ₃ particle concentrations at 20, 50 and 80°C.	83
Table 5.4: Important parameters obtained from the amplitude sweeps for 25g, 45g and 65g CaCO ₃ particle concentrations.	85
Table 5.5: Rheological parameters for the 1.19g XG and 1.39g XG polymer concentrations at 20, 50 and 80°C.	89
Table 5.6: Important parameters obtained from the amplitude sweeps for the 1.19g XG and 1.39g XG polymer concentrations.	90
Table 5.7: Rheological parameters for the CaCO ₃ type 1 and CaCO ₃ type 2 at 20, 50 and 80°C.	94
Table 5.8: Important parameters obtained from the amplitude sweeps for the CaCO ₃ type 1 and CaCO ₃ type 2.	95
Table 5.9: Rheological parameters for the 25g, 45g and 65g CaCO ₃ particle concentrations at 20, 50 and 80°C.	99
Table 5.10: Important parameters obtained from the amplitude sweeps for the 25g, 45g and 65g CaCO ₃ particle concentrations.	101
Table 5.11: Rheological parameters for the reference fluid with 1wt%, 2.05wt% and 3wt% NP's at 20, 50 and 80°C.	104
Table 5.12: Important parameters obtained from the strain amplitude sweeps for the reference fluid, 1wt%, 2.05wt% and 3wt% CaCO ₃ NP's.	106
Table 5.13: Rheological parameters for the reference fluid with 1wt%, 2wt% and 3wt% NP's at 20, 50 and 80°C.	110
Table 5.14: Important parameters obtained from the strain amplitude sweeps for the reference fluid with 1wt%, 2wt% and 3wt% CaCO ₃ NP's.	112
Table 5.15: Rheological parameters for the Na/K 50/50, 60/40 and 70/30 ratios at 20, 50 and 80°C.	116
Table 5.16: Important parameters obtained from the strain amplitude sweeps for the Na/K 50/50, 60/40 and 70/30 ratios.	118
Table 5.17: pH and density for the high viscous Cs/K and less viscous Cs/K fluid systems.	118
Table 5.18: Rheological parameters for the high viscous and less viscous Cs/K before and after extra polymer mix.	121
Table 5.19: Rheological parameters for the high viscous Cs/K tested right away and after 3 days static ageing.	123

Table 5.20: Rheological parameters for the high viscous Cs/K, less viscous Cs/K and Cs/K 50/50 ratio at 20°C. 128

Table 5.21: Rheological parameters for the Cs/K 50/50 ratio, Cs/K for fracturing and 100% less viscous Cs/K at 20°C..... 131

Table 5.22: Density for the base mud, design mud and high viscous Cs/K fluid systems..... 135

Table 5.23: Rheological parameters for the Cs/K base mud and Cs/K design mud. 136

Table 6.1: Summarize of the viscometer data applied for K-formate hydraulic performance simulations..... 142

Table 6.2: Summarize of the viscometer data applied for Na-formate hydraulic performance simulations..... 145

List of Symbols

A	Consistency index in Roberston-Stiff model [dimensionless]
A_s	Surface area exposed to shear [m^2]
B	Flow index for Robertson-Stiff model [dimensionless]
C	Correction factor for Robertson-Stiff model [s^{-1}]
D	Pipe diameter [m]
f	Frequency [Hz]
F	Applied Force [N]
g	Gravitational acceleration [m/s^2]
G'	Storage modulus [Pa]
G''	Loss modulus [Pa]
k	Consistency index [$lbf^n/100sqft$]
L	Length [m]
n	Flow index [dimensionless]
N_{Re}	Reynolds number [dimensionless]
P_o	Formation pore pressure [specific gravity]
P_{pump}	Pump pressure [psi]
P_{wf}	Well fracture pressure [specific gravity]
q	Flow rate [m^3/s]
r	Radius [m]
R_x	Viscometer dial reading at x RPM [$^\circ$]
t	Time [s]
T	Temperature [$^\circ$]
v	Velocity [m/s]

γ_A	Shear strain amplitude [dimensionless]
$\dot{\gamma}$	Shear rate [s^{-1}]
δ	Phase shift angle [degrees]
$\Delta P_{\text{annulus,drillcollar}}$	Dynamic frictional pressure loss in the annular spacing between the wellbore and the drill collar [psi]
$\Delta P_{\text{annulus,drillpipe}}$	Dynamic frictional pressure loss in the annular spacing between the wellbore and the drill pipe [psi]
ΔP_{bit}	Dynamic frictional pressure loss in drill bit nozzles [psi]
$\Delta P_{\text{drillcollar}}$	Dynamic frictional pressure loss in drill collar [psi]
ΔP_{pipe}	Dynamic frictional pressure loss in the drill pipe [psi]
$\Delta P_{\text{surface}}$	Dynamic frictional pressure loss in the surface flowlines [psi]
ΔP_{total}	Total dynamic frictional pressure loss [psi]
η	Shear-viscosity [cP]
μ	Viscosity [cP]
μ_a	Apparent viscosity [cP]
μ_p	Plastic viscosity [cP]
π	Pi [constant]
ρ	Density [specific gravity]
σ_h	Minimum horizontal in-situ stress [specific gravity]
σ_H	Maximum horizontal in-situ stress [specific gravity]
σ_t	Tangential (Hoop) in-situ stress [specific gravity]
τ	Shear stress [Pa]
τ_A	Shear stress amplitude [Pa]
τ_B	Shear stress for Bingham plastic model [Pa]
τ_f	Flow stress [Pa]

τ_{HB}	Shear stress for Herschel-Bulkley model [Pa]
τ_{PL}	Shear stress for Power Law model [Pa]
τ_{R-S}	Shear stress for Robertson-Stiff model [Pa]
τ_{UN}	Shear stress for Unified model [Pa]
τ_y	Yield stress [lbf/100sqft]
τ_{yL}	Lower yield stress [lbf/100sqft]
ω	Angular frequency [rad/s]

List of Abbreviations

API	American Petroleum Institute
AV	Apparent viscosity
BOPD	Barrels of oil per day
CaCO ₃	Calcium carbonate
CMC	Cellulose gum
Cs	Cesium
DIF	Drill-in fluid
ECD	Equivalent circulating density
EOR	Enhanced oil recovery
HPHT	High pressure high temperature
K	Potassium
KCL	Potassium chloride
LCM	Lost circulation material
LVE	Linear viscoelastic range
LSYS	Lower shear rate yield stress
MMSCFD	Million standard cubic feet per day
MW	Mud weight
Na	Sodium
NCS	Norwegian Continental Shelf
NP	Nanoparticle
OBM	Oil-based drilling fluids
PCF	Pounds per cubic feet
PSD	Particle size distribution
PV	Plastic viscosity
ROP	Rate of penetration
TMS	Tuscaloosa marine shale
TVD	True vertical depth
UIS	University of Stavanger
UK	United Kingdom
U.S.	United States of America
WBM	Water-based drilling fluids
WSM	Wellbore strength material

XG	Xanthan gum
YP	Yield point
YS	Bingham yield stress
RPM	Revolutions per minute
R-S	Robertson-Stiff model

1 Introduction

This section presents the background, problem definition, objective, and research program the thesis work is based on.

1.1 Background

Drilling fluids is a crucial part of the drilling process for oil and gas wells. The drilling fluids have several functions like carrying cuttings to the surface, lubricate and cool the drill string and bit to control well pressure. The consequence of a wrongly designed fluids among others result in lost circulation (i.e., due to wellbore fracturing), kick influx, well collapse, formation damage and shale swelling can be mentioned. As a result, the non-productive time will increase, which indirectly increases undesired expenses for the industry. Therefore, it is important to drill the well with a correct mud composition to prevent these challenges [1].

Oil-based drilling fluids (OBM) and water-based drilling fluids (WBM) are the commonly used muds for drilling oil and gas wells. The advantages with OBM's over the WBM's is that it has lower coefficient of friction and it inhibit shale swelling since the barite particles are oil-wetted [2]. However, the barite particles in OBM are applied as weight material and damages the zone mechanically around the near-wellbore wall in the reservoir section. When the skin factor in this zone is increased, the permeability is reduced hence the hydrocarbon productivity of the reservoir will decrease. Other disadvantages with OBM's are barite sagging since it has negative impact on the environment.

Therefore, drill-in fluids (DIF's) is a fluid exclusively designed for drilling the reservoir section. In contrast to barite particles as weighting material in OBM's, a drill-in fluid consists of a high-density brine as the weighting component to increase the mud weight. DIFs are designed to minimize formation damage because the composition consists of fine calcium carbonate (CaCO_3) particles as lost circulation material (LCM). These particles will plug the pores in the near-wellbore wall and act as a bridging material, compared to barite particles the formation skin reduces considerably. The CaCO_3 particles are thereafter removed easily by acid treatment before production start.

The use of nanoparticles (NPs) in tech firms has an increasingly impact in the technological industry for the last decades. From data engineering like nanochips in an Apple iPhone, to controlled medical nano-objects that can go into blood cells of a human to for example dissolve clogged blood vessels for heart patients. In the petroleum industry, NPs had interesting results when added to a drilling fluid composition. The interesting thing about NPs that independent of its size it can have an impact on the drilling fluid characteristics like rheological parameters [3, 4, 5], filtrate loss and mud cake thickness [3, 6], drilling fluid lubricity [7], improved thermal and electrical conductivity [8], and increase the wellbore strength [9].

The periodic table gives information about the element’s ionization energy, atomic radius, and ability to form chemical bonds. From the periodic table in figure 1.1, sodium (Na), potassium (K) and cesium (Cs) are placed in column 1A as alkali metals. All these elements have positive electrons in its outer shell. Cesium has a larger atomic radius, hence higher atomic weight than potassium and sodium. However, the elements ionization energy and electronegativity are opposite; Na has a higher ability to bond with other elements than K and Cs respectively [10].

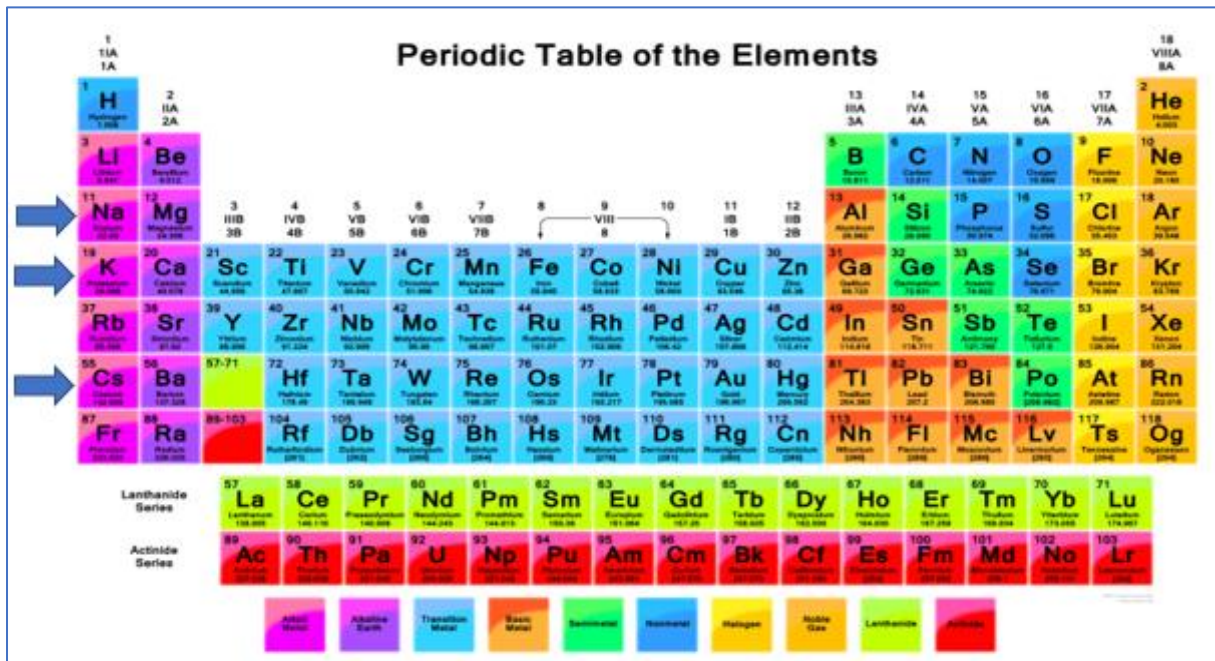


Figure 1.1: The periodic table of elements [10].

Up to the knowledge of the thesis author, hydraulic fracturing experiments conducted with Cs/K formate based drill-in fluid has not been documented in the literature. Therefore, this will be investigated in this thesis work.

1.2 Problem definition

Over the years, University of Stavanger have run several hydraulic fracturing experiments on WBM's and OBM's. From figure 1.2, hydraulic fracturing experiment is performed for water-based drilling fluid, and presents the penetrating and non-penetrating case for this fluid respectively [11]. The non-penetrating case presents a higher wellbore strength compared to the penetrating case.

The problem definition is to investigate whether LCM enhances wellbore strength or not in cesium/potassium reservoir drill-in fluid. Additionally, the atomic weights of sodium and potassium-formate fluids have been designed to compare the group 1A alkali metals ionization performance in drill-in fluids. The problems to be addressed in this thesis are:

- Effect of LCM on wellbore strength in Cs/K formate drill-in fluid.
- CaCO_3 LCM's performance in Na and K-formate drill-in fluids.
- CaCO_3 Nanoparticle performance in Na and K-formate drill-in fluids.

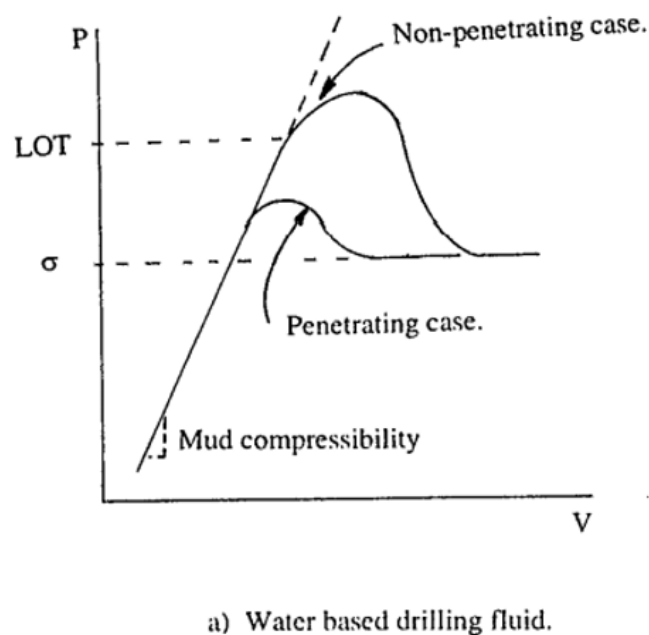


Figure 1.2: Illustrative sketch of the problem definition [11]. Whether LCM in Cs/K drill-in fluids enhances wellbore strength or not?

1.3 Objective

The objective of the thesis is to describe and answer the problem definition in section 1.2. The work scope comprises of experimental and simulation studies. The main activities are:

- Review and present field case studies on the performance of formate fluids in drilling.
- Synthesize Na - and K-formate drill-in fluids and characterize its behavior.
- Investigate CaCO₃ nanoparticle impact in Na - and K-formate based fluids.
- Perform hydraulic simulation studies on Na - and K-based CaCO₃ nanoparticle fluids.
- Cs/K-formate drill-in fluids synthesis and fluid properties characterization.
- Use the Cs/K drill-in fluid to run hydraulic fracturing and investigate the effect of quartz LCM on wellbore strength.

1.4 Research program

The research program used in this thesis is presented in figure 1.3. The research consists of three main parts: Literature study, experimental work, and simulation work.

In the first part, case studies on formate brines as drill-in fluids are based on field experienced mud and lab design from paper. The relevant base article for the thesis is the drilling fluid applied in the North Sea at the Martin Linge field [12]. Relevant theories for analysis of drilling fluid properties are reviewed. Description of the drilling fluid additives added to the experimental mud design are included in the literature study part of the thesis, even though it is presented in the experimental work section.

In the second part, experimental lab work at UIS on drill-in fluids has been performed. The fluids are hence characterized based on API filtrate loss, rheological and viscoelastic properties. Moreover, the impact of nanoparticle on the fluid behaviors will be investigated. The experimental part of the thesis is completed by hydraulic fracturing characterization of the modified Cs/K drill-in fluid along with the effect of lost circulation materials on wellbore strength.

The third part deals with simulation work on ECD and pump pressure to study fluid behavior in the considered experimental well.

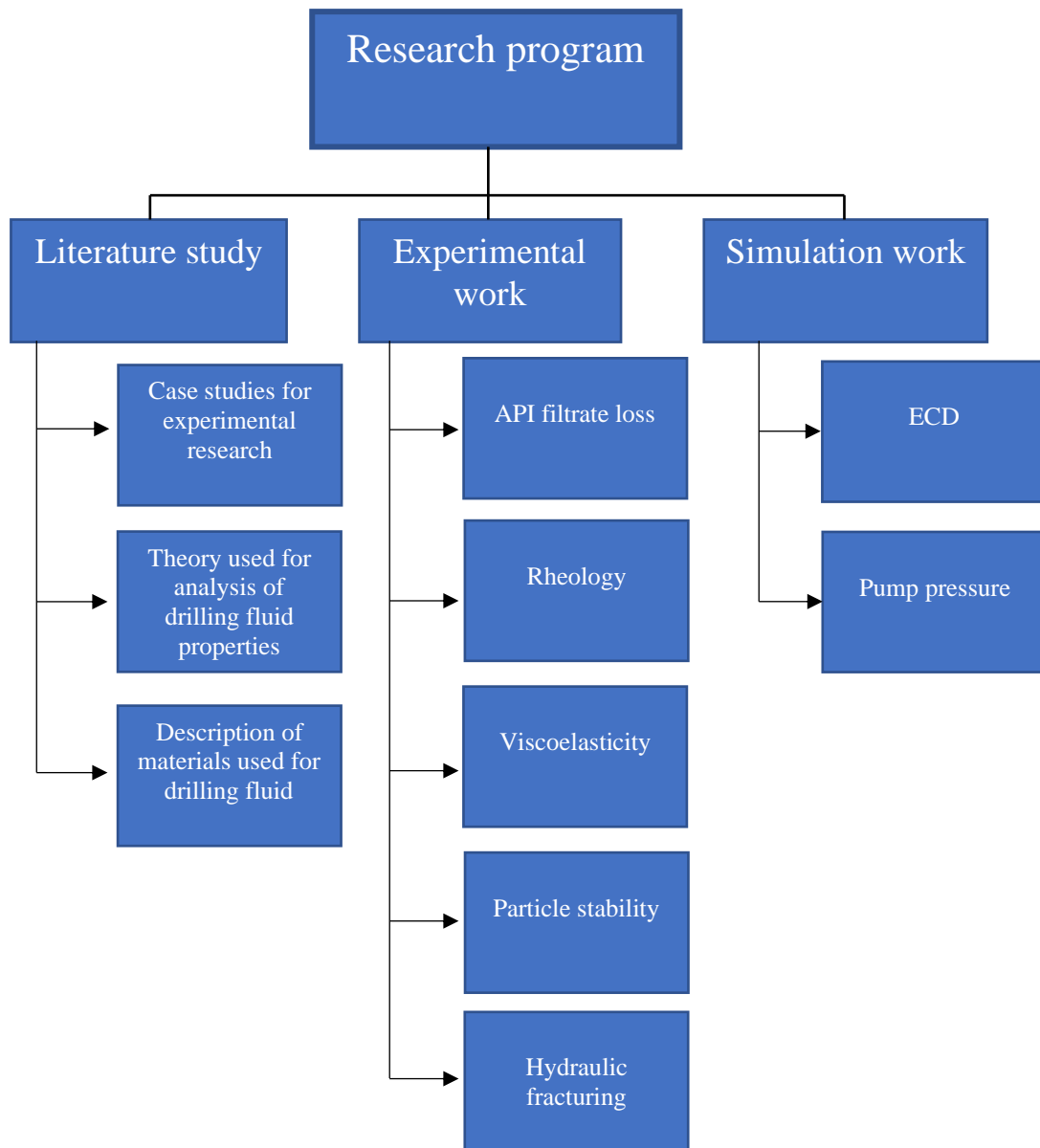


Figure 1.3: Summary of the research activities performed in this thesis.

2 Literature study

This section presents case studies on formate drill-in fluids and experiences on hydraulic fracturing experiments. Subsection 2.1.5 is the essential case study in this thesis from the Martin Linge field at the Norwegian continental shelf [12]. Table 2.1 presents the mud composition which is the starting point for all the laboratory designed drill-in fluids in this thesis.

2.1 Case studies on formate brines

For a general understanding of the challenges and success of brine solutions in drill-in fluids, there will be presented five case studies in chapter 2.1 and an introduction to formate brines in drill-in fluids. These case studies are experience based on well operations around the world. The case studies will summarize the following information:

- The type of formate brine used in the drill-in fluid.
- The field they applied.
- The condition of the reservoir.
- The challenges they had
- The success they had

2.1.1 Formate brines

In the petroleum industry there are three types of formate-based fluids that is most applied. These are sodium formate, potassium formate and cesium formate [13]. All of these are different types of brine. Another type of drilling fluid related to brine is calcium bromide. However, this type of brine is rarely applied in well operations. A reason for this could be to its high density and low solubility in water. The chemical formula, solubility in water and density of typical formate brines is presented in figure 2.1 [14].

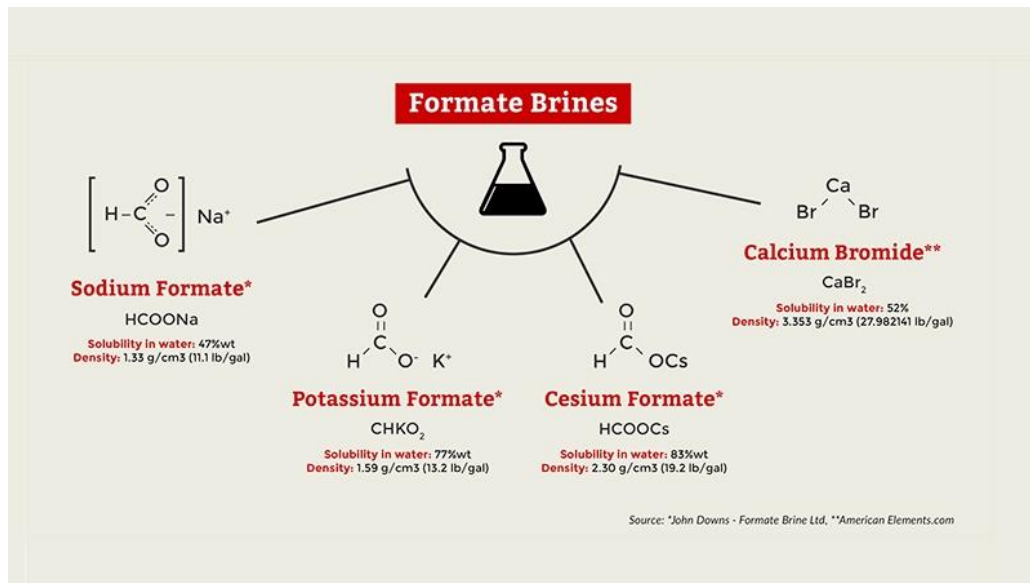


Figure 2.1: Formate brines used in drill-in and completion fluids [14].

Since the commercial use of formate-based drill-in fluids in 1993, these have been applied in 100s of HPHT wells. The advantages of formate brines in contrast to a conventional HPHT drilling fluid, is that it reduces formation damage (skin) when drilling in the reservoir section. At high temperatures it maintains the material properties, reduces hydraulic flow resistance, low likelihood for differential sticking, good lubrication for the whole drill string, low corrosion-rates and little risk of environmental pollution (biodegradable) [13]. Formate-based drill-in fluids are normally applied in [13]:

- ✓ Deep slim hole drilling
- ✓ Shale drilling
- ✓ Reservoir drilling
- ✓ Drilling in salt and gas hydrate formations

2.1.2 Cs formate experience at Kvitebjørn field, Norway

From 2004 until 2006, Equinor performed drilling and completion of highly dense and deviated wells at HPHT conditions at the Kvitebjørn field in the North Sea. The Kvitebjørn field is located approximately 150 km northwest of Bergen. See figure 2.2 for field location [15].

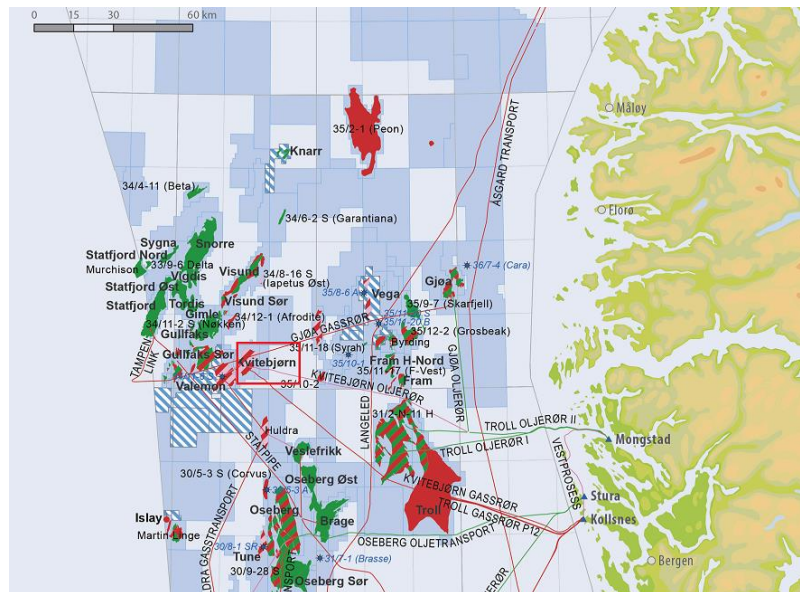


Figure 2.2: Location map of the Kvitebjørn field (red/light red area in red square) in North Sea [16].

The challenge was to drill through large sections of shale layers into the reservoir with 11,700 psi pressure and 311°F reservoir temperature. An extended-reach exploration well to Valemon field was also drilled with inclinations up to 69°. The objective was to drill into the reservoir section with lowest well control issues and obtain maximum productivity at the Kvitebjørn field. For this purpose, cesium formate was chosen for drilling and completion. Cesium formate was used for both drilling of the original well path and the extended-reach exploration well. Seven HPHT wells were drilled successfully using cesium formate; 2 wells completed with perforated liner/cement and 5 wells with sand screen completion [17]. The application of a cesium formate-based fluid showed clear performance benefits on the following issues [17]:

- ✓ Low ECD
- ✓ Moderate-to-high ROP
- ✓ Excellent wellbore stability while logging
- ✓ Good hole cleaning
- ✓ High reservoir productivity with low skin
- ✓ Effective and problem free completions
- ✓ Zero well control incidents in all 15 HPHT drilling operations
- ✓ Zero well control incidents in all 20 HPHT completion operations

2.1.3 Na/K and K formate experience at Ghawar field, Saudi Arabia

From 2004 through 2008, Saudi Aramco drilled 44 gas wells at HPHT conditions at the Ghawar field in Saudi Arabia. The Ghawar field is known as the world's largest hydrocarbon field and is located approximately 200 km east of Riyadh. See figure 2.3 for field location [18].



Figure 2.3: Location map of Ghawar field (green area in green circle) onshore Saudi Arabia [18].

Potassium and sodium/potassium-based drill-in fluids were chosen to drill the reservoir section at the Ghawar field. These reservoir-drill in fluids were used in pre-Khuff, Jauf and Unayzah sandstone reservoir with temperature up to 323°F. The fluids were applied in Saudi Aramco's Khuff carbonate reservoir, with single and dual lateral drilling of horizontal wells [19]. Sodium/potassium formate-based fluids were primarily used to [19]:

- ✓ Reduce formation damage (skin factor) in reservoir.
- ✓ Prevent stuck pipe situations.
- ✓ Better drill bit performance
- ✓ Lower pump pressure
- ✓ Solids content and temperature stability at HPHT conditions
- ✓ Na/K formate fluids good for re-use.

In the well JFYN-A, 1,214 feet of 5-7/8" hole, were cut across reservoir using a re-used 92 pounds per cubic foot potassium-based fluid. Hence a potassium brine-based drill-in fluid were chosen for this well. This interpretation resulted in a flowrate increase to 45 mmscfd with 358

bopd oil on a 44/64” choke [19]. The application of potassium formate-based drill-in fluid showed [19]:

- ✓ Increased production rate more than expected by operator

Later they performed laboratory core gas tests from well Khuff-C, which showed 91% return permeability after flowing K formate fluid through the cores. Compared to 40% return permeability by flowing through the cores with a KCL polymer drilling fluid [19]. Both formate-based fluids contained CaCO_3 as lost circulation material. LCM particles were tested at fine, medium, and coarse particle sizes to drill in extreme overbalanced well conditions at Khuff-C. As an example, an 81 pcf Na formate drill-in fluid were used to drill and complete the 3675 feet horizontal section at Khuff-B re-entry sidetrack well. This well operation showed [19]:

- ✓ Increased production rate without enzyme or acid treatment
- ✓ Recycling of formate drill-in fluids reduced overall mud costs.

2.1.4 Cs formate experience at Eagle Ford and Tuscaloosa field, USA

In 2020, a major case study from University of Oklahoma were performed on two of the largest shale basins at the U.S. mainland; Eagle Ford shale basin in the southwestern region of Texas and Tuscaloosa marine shale (TMS) in the states of Louisiana and Mississippi. More than 70% of drilling challenges occur in shale formations, and approximately 90% of these challenges are related to wellbore instability issues. The study from Oklahoma consisted of a HPHT drilling simulation of a KCL drilling fluid, conventional WBM and cesium formate drilling fluid as well as a clay swelling formation study [20]. In this case study, the experience related to Cs formate brine will be highlighted. See figure 2.4 for field location of Eagle Ford and Tuscaloosa [21].



Figure 2.4: Location map of Eagle Ford and TMS shale fields (green area at location map) onshore USA [21].

The Tuscaloosa marine shale consists mainly of shale with interbedded siltstone layers. However, there are areas at TMS that are sandstone dominated. From a core sample of TMS, it was discovered that 51% of the mineralogy consist of clay. The Eagle Ford shale are classified mainly by 15% quartz, 55% calcite and 20% clay of the total mineral components [20].

The cesium formate based drill-in fluid were tested on torque and friction factor, drilling performance, ROP and clay swelling index. Clay-swelling are a very common drilling issue in clay-dominated shale formations like Eagle Ford and Tuscaloosa. The clay swelling index was exclusive for this study and was calculated by the change in mixture volume (clay + water) over a certain period and presented as a percentage of swelled clay. The clay swelling index has a linearly characteristic as the clay adsorbs water. More water in the mixture equals less clay [20].

The cesium formate-based drilling fluid were tested in comparison with 1 weight% and 2 weight% KCL mud and a conventional WBM. These tests were performed on Eagle Ford and Tuscaloosa shale formations. The results for cesium formate-based drilling fluid are as follows [20]:

- ✓ Lowest clay swelling index.
- ✓ Very low torque and friction factor.
- ✓ Higher drilling performance than conventional WBM.
- ✓ Highest ROP

For the final drill-in fluid formulation; concentrated cesium/potassium formate blend, HT modified starch and CaCO₃ LCM/ bridging material for fluid loss control. Xanthan gum polymer were added as a component to the total mud composition to provide required fluid viscosity. Both medium (24 micron) and fine (11 micron) CaCO₃ particle sizes were chosen from the D₅₀ particle size distribution. The formulated drill-in fluid composition at the Martin Linge is presented in table 2.1 [12].

Component	Quantity [kg/m³]	Quantity [lb/bbl]
Cesium formate (2.20 SG)	1617	566
Potassium formate (1.57 SG)	336	117.5
Purified xanthan gum	1.57	0.55
High-temperature modified starch	15.7	5.5
pH buffer: K₂CO₃ / KHCO₃	11.4-14.3	4-5
Calcium carbonate – medium (D₅₀ = 24 μm)	50	17.5
Calcium carbonate – fine (D₅₀ = 11 μm)	50	17.5

Table 2.1: Cs/K formate drill-in fluid composition at the Martin Linge field [12].

2.1.5.2 Martin Linge fluid properties

The filter loss control and rheology from the drill-in fluid formulation in table 2.1, were measured before and after fluid in cell hot-rolled in oven (ageing) at HPHT conditions. The HPHT rheology was first measured at the Intertek facility in Houston, Texas with a Fann 77 rheometer. Initially, the rheology was measured at the same conditions using a Fann 35 viscometer. These two observations showed that the test results correlated well between the performed rheometer and viscometer measurements [12].

At Martin Linge, the HPHT fluid loss control was the primary target by the operator. The first specification from the operator was <10 ml filtrate loss of total collected volume. The formation water and filtrate showed good compatibility at Martin Linge. From this approval and with the ambition to fully exploit the benefits of reducing polymer and solid content concentrations, the HPHT fluid loss control specification alternated to <15 ml by the operator [12].

Table 2.2 presents the Cs/K drill-in fluid properties at Martin Linge. The viscometer responses before ageing show that the plastic viscosity and yield point are at 28 centipoise and 21

lbf/100sqft respectively. The fluids rheology is thermal stable compared before and after ageing, as the rheological properties does not change a lot [12].

AGEING CONDITIONS	Before aging	16 hours dynamic at 140°C (284°F) and 200 psi		48 hours dynamic at 140°C (284°F) and 200 psi		72 hours static at 140°C (284°F) and 200 psi	
Fann 35 rheology at 49°C (120°F)							
600 RPM	77	81		81		76	
300 RPM	49	52		51		48	
200 RPM	38	41		40		38	
100 RPM	24	27		26		25	
6 RPM	5	6		5		5	
3 RPM	3	4		3		3	
GELS 10" (lbs/100 ft ²)	4	4		4		3	
GELS 10' (lbs/100 ft ²)	8	6		4		4	
PV (cP)	28	29		30		28	
YP (lbs/100 ft ²)	21	23		21		20	
HPHT filter medium		50 µm ceramic disc	120 µm ceramic disc	50 µm ceramic disc	50 µm ceramic disc	50 µm ceramic disc	120 µm ceramic disc
Temperature (°C)		140	140	140	140	140	140
Δ pressure (psi)		500	500	500	500	500	500
API (Actual x 2) (mL)		19.0	18.0	19.6	15.2	17.4	12.8
Total vol. collected (mL)		9.5	9.0	9.8	7.6	8.7	6.4
Spurt loss (mL)		4.2	5.5	4.2	5.8	3.2	3.4
Filter cake thickness (mm)		1	1	1	1	1	1
pH (1:10 dilution)		10.16		10.07		10.04	

Table 2.2: Cs/K formate drill-in fluid properties at the Martin Linge field [12].

2.2 Case studies on Stress Cage Theory

This subsection contains stress cage theory in a case study form. The three case studies will cover field experience on how stress cage theory has successfully described industrial wellbore strength scenarios. These case studies will summarize the following information:

- The method implemented to increase wellbore strength.
- The field they applied.
- The condition of the reservoir.
- The challenges they had
- The success they had

2.2.1 Stress Cage Theory

When bridging materials plugs at the fracture opening, the hoop stress around the wellbore circumference increases, hence the wellbore is strengthened. This is referred to as “stress cage theory” and is illustrated in figure 2.6 [22].

Mud loss to formation is a frequent problem during drilling. A drilling fluids mud weight are designed to effectively control and maintain wellbore stability. The mud losses to the formation occur when the mud weight exceeds the fracture resistance. A major challenge occurs during drilling of depleted reservoirs were the pore pressure drops, as the formation hydrocarbon rocks are less wetted, hence the interbedded shale rock formations maintain its pore pressure. Therefore, the mud weight required to geomechanically support shale formations exceeds the fracture gradient for sand and siltstone formations. It is more profitable to strengthen the wellbore around depleted zones to get access to the difficult reserves [22]. There are several benefits with wellbore strengthening around weak zones [22]:

- ✓ Connection between wellbore and depleted zones.
- ✓ Decreased loss of circulation in deep-water drilling.
- ✓ No mud loss when running casing or cementing.
- ✓ Enhanced well control.
- ✓ No casing strings.
- ✓ Option to expandable casing.

The challenges can be solved by designing a drilling fluid consisting of LCM and/or wellbore strength material for effective wellbore strengthening in drilling operations. For example, CaCO_3 or graphite [22]. These fluids will create a mud cake consisting of bridging particles to seal the existing fracture near the fracture opening. Provided that the bridge is low-permeable with good pressure isolation, this will provide stress cage effect at the wellbore wall [22].

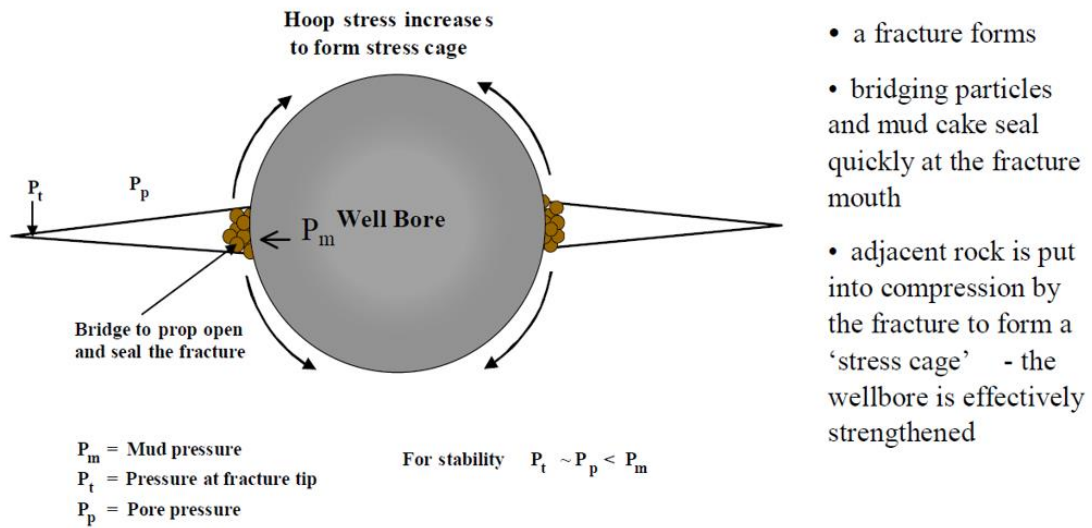


Figure 2.6: Stress cage theory for wellbore strengthening effect [22].

2.2.2 Extended leak-off test experience at Arkoma basin, USA

The Arkoma basin is located onshore in the state of Oklahoma and Arkansas. The basin consists of a typical shale formation and a vertical HPHT well was drilled to see if a designer mud could increase wellbore strength in shale. The reserves are primarily dry gas. However, areas in the western Arkoma basin consists of gas condensate [22, 23]. The location map of Arkoma is presented in figure 2.7 [23].



Figure 2.7: Location map of the Arkoma basin [23].

The challenge with shale formations are low-permeable rocks. The bridge at the fracture opening therefore needs to be impermeable to prevent pressure build-up in the fracture, therefore low fluid loss mud needs to be circulated in the wellbore [22].

After cleaning the well, an extended leak-off test was performed using a solids-free base mud with density 9.0 pounds per gallon and high HPHT fluid loss. From figure 2.8, the pressure curves are presented for the extended leak-off test. By circulating the base mud (without LCM), the formation fractured at approximately 1200 psi. At maximum (formation fracture pressure) the mud pumps stopped to prevent fracture growth. After stopping well circulation the base mud pressure was constant at 800 psi. This is the fracture propagation pressure measured at fracture tip. The base muds pressure curve also followed the earlier performed casing integrity test which indicated no fluid loss at casing shoe. The same test was repeated (curve not shown) and simply reached the same stabilized pressure at approximately 800 psi (fracture re-opened). Then the base mud was substituted with the design mud (with LCM) [22]. The design mud contained the following properties [22]:

- ✓ Ultra-low HPHT fluid loss
- ✓ Bridging solids range 10-800 micronized diameter.
- ✓ CaCO₃ /graphite blend

This created a sealed fracture and from figure 2.8 showed an increased fracture pressure to approximately 2000 psi before seal breaks. As a result, an improvement with over 850 psi pressure increase, equivalent to 5.4 pounds per gallon mud weight. The designer mud were then circulated a second time (curve not shown) but failed to re-seal the fracture and eventually the pressure stabilized at 800 psi like the base mud [22]. From this field experience the following was concluded [22]:

- ✓ The designer mud is a preventative treatment (fracture too large for particles to bridge under second circulation)
- ✓ Loss of circulation situations are time dependent (not reliable to wait for a propped fracture which then form a stress cage)

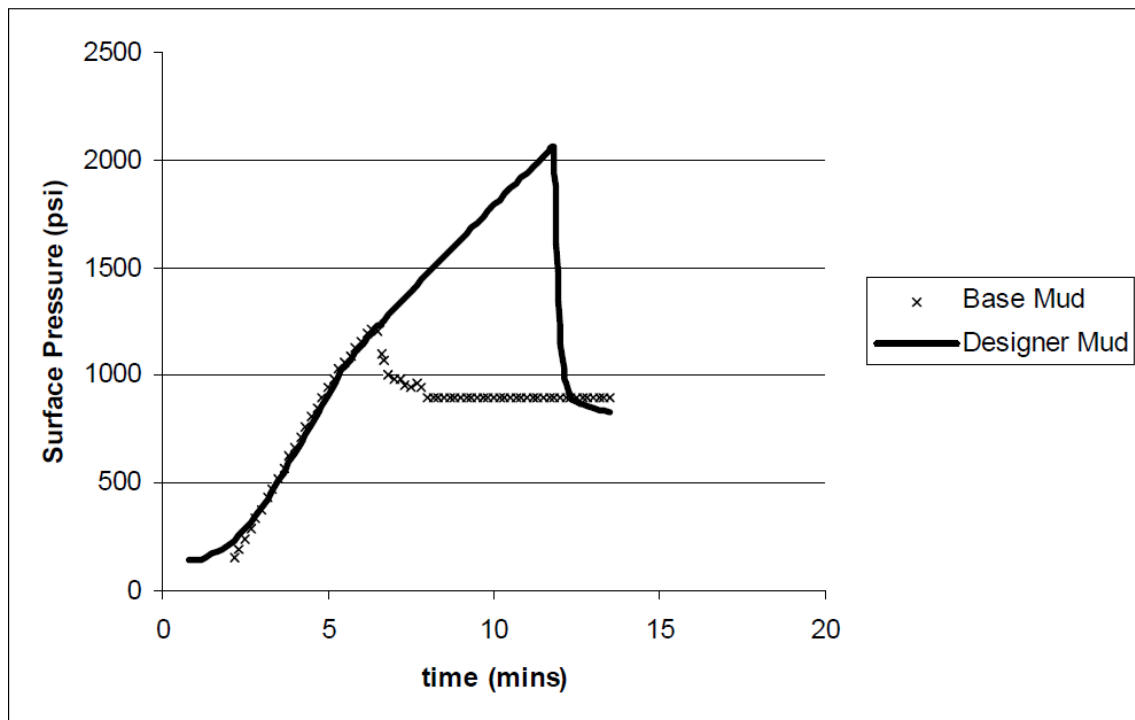


Figure 2.8: Extended leak-off test at Arkoma basin [22].

2.2.3 Lab experience of LCM material effect on wellbore strength, Canada

At the University of Calgary in Canada, an LCM drilling fluid blend were mixed for WBM and OBM diesel oil fluid to effectively enhance wellbore strengthening for both permeable and impermeable formations [9]. Hydraulic fracturing experiments were performed with an optimal drilling fluid combination of nano and micron sized LCM materials (graphite + CaCO₃). The nanoparticles were in-house prepared calcium carbonate and iron (III) hydroxide and added separately to each fluid (NP1 blend and NP2 blend). The purpose of the different blends was to prop open and seal the fractures from test experiments to enhance stress cage. The blend with highest increase in fracture pressure and lowest deviation from rheological properties were selected as drilling fluid [9].

The optimal WBM blend of Iron (III) hydroxide + graphite was selected as drilling fluid and showed a fracture pressure increase by 1668 psi which equals 70% over the unblended WBM with moderate impact on fluid rheology. The OBM optimal blend of calcium carbonate + graphite showed a fracture pressure increase by 568 psi which equals 36% over the unblended OBM (diesel oil invert emulsion) [9]. This blend also resulted in moderate impact on fluid rheology. Figure 2.9 represents the optimal blends for WBM and OBM (diesel oil). This is referred to as blend 3 (NP1-iron based + graphite) for WBM and blend 8 (NP2- calcium based

+ graphite) for OBM. Blend 9 (NP1-iron based + CaCO_3) and blend 10 (NP2-calcium based + CaCO_3) are also presented in figure 2.9 with WBM control sample [9]:

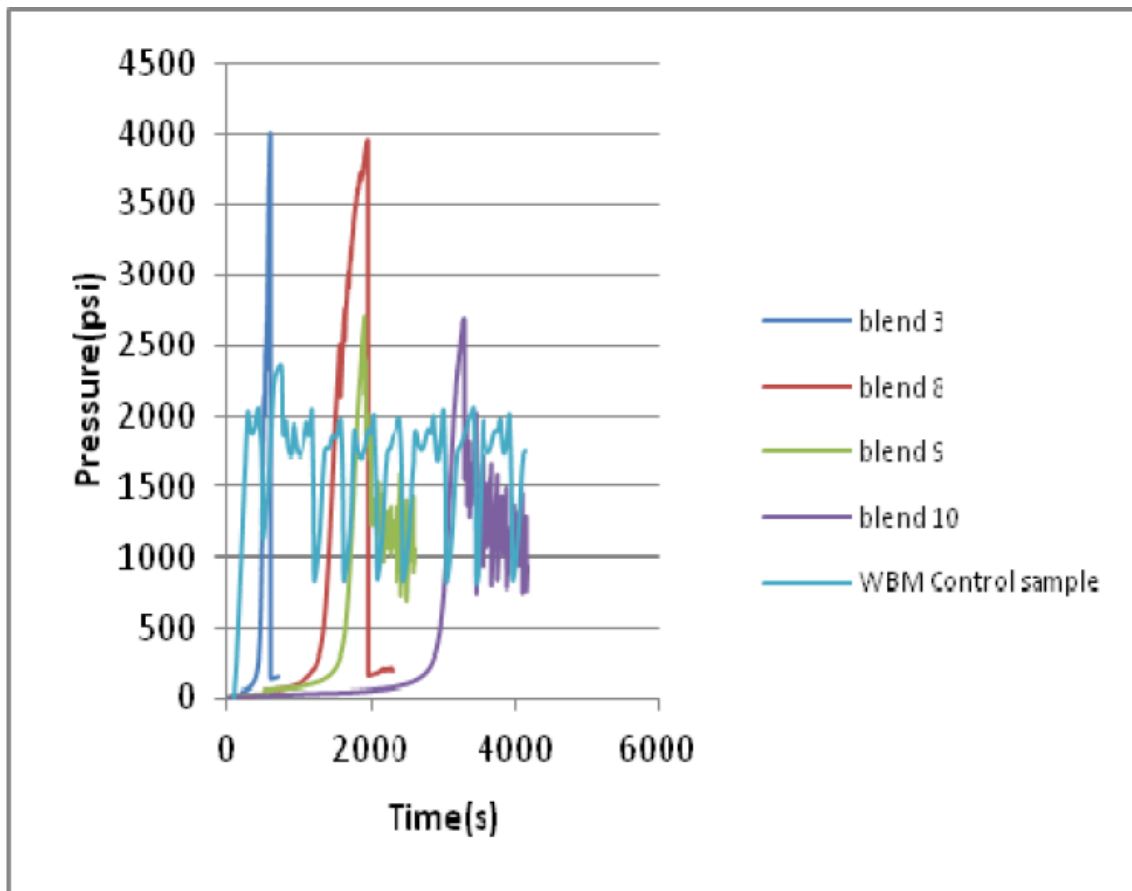


Figure 2.9: Optimal blends compared with unblended fluids and WBM control sample [9].

The wellbore strengthening effect depends on the blended fluids 10 min gel strength and plastic viscosity results. In both concrete and sandstone showed absolute fracture sealing while running 2nd cycle (re-opening fracture) which showed excellent prop and seal from the blend. The results showed a 25% increase in fracture pressure over the unblended fluids in the impermeable concrete core. This makes the LCM blends applicable for wellbore strengthening in shale formations and could be interesting for field application [9].

3 Theory

This theory section describes and elaborates the fundamental knowledge that the experimental work is based on.

3.1 Rheology

Rheology is defined as the theory of deformation and flow of matter [24]. For a drilling fluid, its primarily a study of flow behavior in pipes and other relevant flow medium. It focuses mainly on the flow characteristic and the relationship between flow rate and flow pressure. There are three fundamentally relationships to determine the flow regime of a drilling fluid [1]:

- Laminar flow; low velocity. The flow is orderly.
- Transient flow; intermediate state between laminar and turbulent flow.
- Turbulent flow; high velocity. The flow is disorderly.

The above flow regimes are defined as Reynolds number (N_{Re}). To maintain a well-functioning drilling fluid depends on certain rheological parameters like plastic viscosity, yield point, gel strength and shear stress-shear rate relationship. All the mentioned fluid properties determine the wellbore hydraulics [1].

3.1.1 Plastic viscosity

Viscosity is the resistance of a fluid to flow (μ). Plastic viscosity (PV) is the mechanical friction resistance that occurs in the drilling fluid. This resistance originates from particles and velocities in the different fluid layers. PV gives information about the fluids solid content, size and distribution but are also affected by the liquid viscosity. PV are denoted as centipoise (cP) [25].

3.1.2 Yield point

The yield point (YP) is the necessary force per area to be applied for a fluid to flow. The yield point is also a good measurement for how good the solids are suspended in the liquid phase. The electrochemical forces from particle-to-particle interaction in the drilling fluid defines the yield point value. YP are normally denoted as lbf/100sqft [25].

3.1.3 Gel strength

There are clear similarities between yield point and gel strength. Gel strength is defined as the stiffness of the fluid during static fluid condition. Stiffness is a thixotropic ability. During tripping there are no fluid circulation in the well, hence stiffness properties are important to prevent solid particles dropping to the bottom. Gel strength is denoted as lbf/100sqft [25].

3.1.4 Shear stress

Shear stress is defined as the force to sustain the movement of a fluid flowing through an area [26]. From figure 3.1 the sketch to the left illustrates shear stress applied to an upper layer of a body. The blue area is any fluid. The fluid layer in the middle of the two adjacent layers flows faster in the middle centerline than close to the wall of layers. The increase in viscosity is then caused by friction between the layers [25]. Shear stress is defined in equation 3.1 [26].

$$\tau = \frac{F}{A_s} \quad (3.1)$$

Where:

- τ = Shear stress [Pa]
- F = Applied force [N]
- A_s = Surface area exposed to shear [m²]

3.1.5 Shear rate

Shear rate is defined as the rate of change of velocity when one layer of fluid passes over an adjacent layer divided by the distance between them [26]. From figure 3.1 the sketch to the right illustrates applied shear rate to a body. The blue area is any fluid. The upper layer is moving with a constant velocity over a certain fluid. The radius of the velocity profile is defined as the distance from centerline to tubing wall. Shear rate is presented in equation 3.2 [27].

$$\dot{\gamma} = \frac{v}{r} \quad (3.2)$$

Where:

- $\dot{\gamma}$ = Shear rate [sec⁻¹]
- v = Velocity [m/s]
- r = Distance from tubing wall [m]

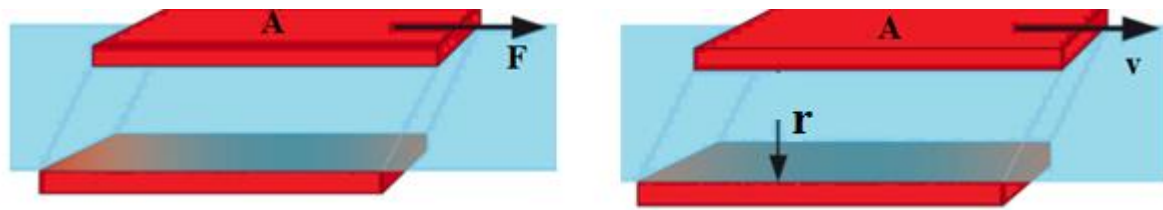


Figure 3.1: Left: Shear stress profile. Right: Shear rate profile [27].

3.2 Rheological models

From a lab viscometer a drilling fluids shear stress is measured at different shear rates. To describe the drilling fluids rheological properties a model is implemented to try to fit the experimental data from the lab with model parameters. This minimizes errors of parameters being calculated like yield stress, consistency index, flow index and is crucial for a safe drilling operation. Several models have been developed to try to describe experimental fluid data as accurately as possible. However, none of them are universal enough to precisely describe the drilling fluid behavior [28]. A fluid distinguishes between two characteristics: Newtonian and Non-Newtonian fluids.

3.2.1 Newtonian fluid

A Newtonian fluid is precisely proportional between shear stress and shear rate in laminar flow. From a mathematical perspective, it is a straight line starting from the origin and increases linearly. Pressure and temperature affect the fluids viscosity. Viscosity is defined by shear stress divided by shear rate. The apparent viscosity is the slope at the stress-strain curve for a Newtonian fluid behavior, ergo has a single viscosity value for every shear rate. Fluids that can be characterized as a Newtonian are typically water, light oil, and salt solutions because the particles are no larger than fluid molecules. This can be seen from equation 3.3 [29, 30].

$$\tau = \mu \dot{\gamma} \quad (3.3)$$

Where:

- τ = Shear stress [Pa]
- μ = Viscosity [cP]
- $\dot{\gamma}$ = Shear rate [sec^{-1}]

From figure 3.2 the linear relationship of a Newtonian fluid is illustrated as a function of shear stress and shear rate. It is also referred to as the consistency curve from a drilling perspective [29].

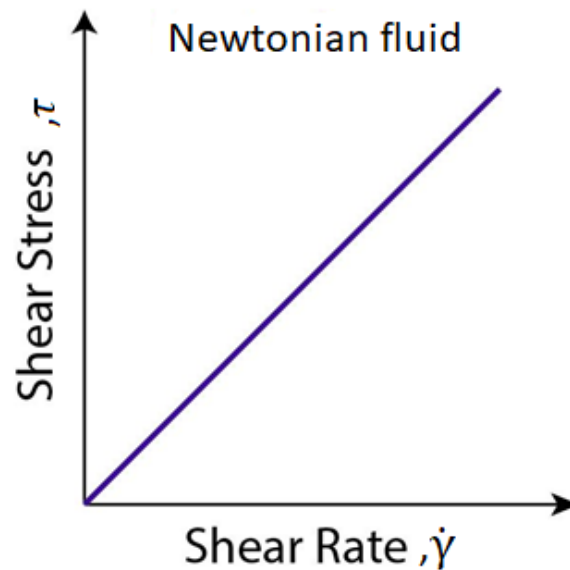


Figure 3.2: Linear relationship of shear stress-shear rate of a Newtonian fluid [29].

3.2.2 Non-Newtonian fluid

Drilling fluids are often characterized as Non-Newtonian fluid. The considerable difference between a Newtonian and Non-Newtonian fluid is the chemical reaction between fine particle suspension in the drilling mud [29]. This provokes pressure and temperature changes between suspended solid particles and thus viscosity changes. From a mathematical perspective, Non-Newtonian fluid presents a non-linear curve with no applied yield stress. This fluid has shear rate dependent viscosity and needs stress forces to evoke fluid movement [29, 30].

From figure 3.3 presents no fixed value for drilling mud viscosity, and yield stress is applied. The viscosity also decreases with increasing shear rate in contrast with the Newtonian fluid where the viscosity is fixed at all shear rates [29].

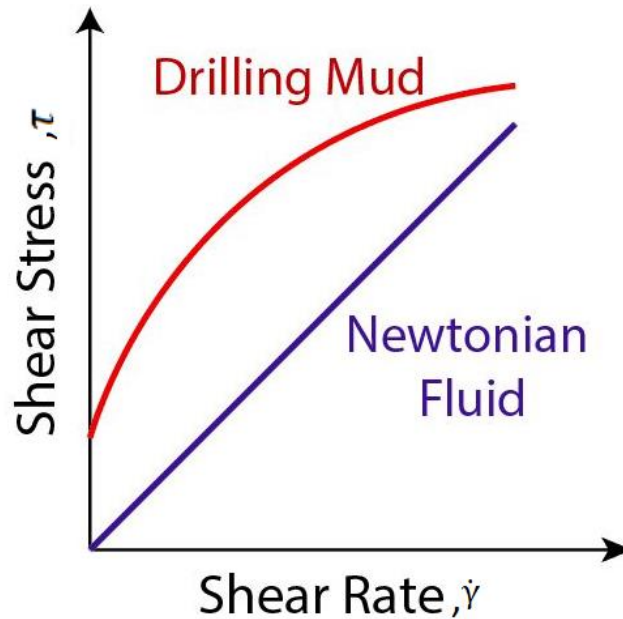


Figure 3.3: Shear stress-shear rate relationship of a classic drilling mud and Newtonian fluid [29].

3.2.2.1 Bingham plastic model

The most frequently used rheology models to determine drilling fluids is the Bingham plastic model [29]. A drilling fluid that approximately suits the Bingham plastic model is clay muds which have high solid content. This matches well with Bingham theory that there needs some applied stress to initiate flow, and at high stress values the viscosity is fixed with increased shear rates. The model is described by the two parameters Bingham yield stress (YS) and plastic viscosity (PV) [1]. The Bingham plastic model is presented in equation 3.4 [31].

$$\tau_B = \tau_y + \mu_p \cdot \dot{\gamma} \quad (3.4)$$

Where:

- τ_B = Shear stress for Bingham plastic model [$\frac{\text{lbf}}{100\text{ft}^2}$]
- τ_y = Yield stress [$\frac{\text{lbf}}{100\text{ft}^2}$]
- μ_p = Plastic viscosity [cP]
- $\dot{\gamma}$ = Shear rate [sec^{-1}]

The shear rate values are constant from the viscometer. To determine the two parameters: plastic viscosity and Bingham yield stress, equation 3.5 and 3.6 should be used [32, 33, 34]. The apparent viscosity (AV) is an important rheological parameter to enhance hole cleaning

efficiency in drilling operations. The oil industry applies the apparent viscosity in the Bingham plastic rheological model and is presented in equation 3.7 [35].

$$\mu_p = R_{600} - R_{300} \quad (3.5)$$

$$\tau_y = R_{300} - \mu_p = 2 \cdot R_{300} - R_{600} \quad (3.6)$$

$$\mu_a = \frac{R_{600}}{2} \quad (3.7)$$

Where:

- R_{600} = Viscometer dial reading at 600 RPM, [°]
- R_{300} = Viscometer dial reading at 300 RPM, [°]
- μ_a = Apparent viscosity [cP]

From figure 3.4 the Bingham plastic model is illustrated. It shows a clear yield point where the shear rate equals zero and the slope of the curve is fixed and defined as the fluids plastic viscosity [29].

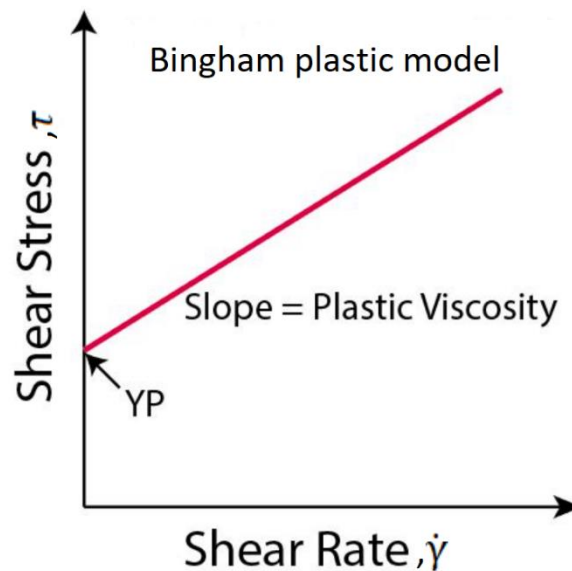


Figure 3.4: Shear stress-shear rate relationship of the Bingham plastic model [29].

3.2.2.2 Power-law model

The power-law rheological model describes the flow of shear thinning fluids. In WBM's where high-density brines are used as weighting material with polymer materials, and no or little solid particles, it possesses shear thinning properties. Hence the power-law model may be applied to characterize this flow behavior [1]. The power-law model is presented in equation 3.8 [29, 1].

$$\tau_{PL} = k \dot{\gamma}^n \quad (3.8)$$

Where:

- τ_{PL} = Shear stress for Power-law model [$\frac{\text{lbf}}{100\text{ft}^2}$]
- $\dot{\gamma}$ = Shear rate [sec^{-1}]
- n = Flow index [dimensionless]
- k = Consistency index [$\frac{\text{lbf}^n}{100\text{ft}^2}$]

The parameter n represents the degree of deviation from a Newtonian fluid. It is a different measure of shear thinning fluid as the rate of change of viscosity changes with the shear rates [1]. The change in parameter n represents the following flow characteristics [1]:

- $n < 1$, the fluid acts shear thinning. The apparent viscosity decreases with increasing shear rate.
- $n = 1$, the fluid acts Newtonian. The apparent viscosity is independent of shear rate.
- $n > 1$, the fluid acts shear thickening. The apparent viscosity increases with increasing shear rate.

The shear rate values are constant from the viscometer. To determine the two parameters: flow index and consistency index, equation 3.9 and 3.10 should be used. In addition, these equation also determines the rheological n and k parameters for the unified model in section 3.2.2.4. These parameters are well-suited to determine thermal stability effects on drilling fluids [32, 33, 34].

$$n = 3.32 \log \left(\frac{R_{600}}{R_{300}} \right) \quad (3.9)$$

$$k = \frac{R_{300}}{511^n} = \frac{R_{600}}{1022^n} \quad (3.10)$$

Where:

- R_{600} = Viscometer dial reading at 600 RPM [°]
- R_{300} = Viscometer dial reading at 300 RPM [°]

From figure 3.5 the power-law model is illustrated. It has no yield point with an exponential change with increasing shear rates. In figure 3.5 the apparent viscosity decreases with increasing shear rates. This indicates a similar flow characteristic to drilling fluids [1, 29, 30].

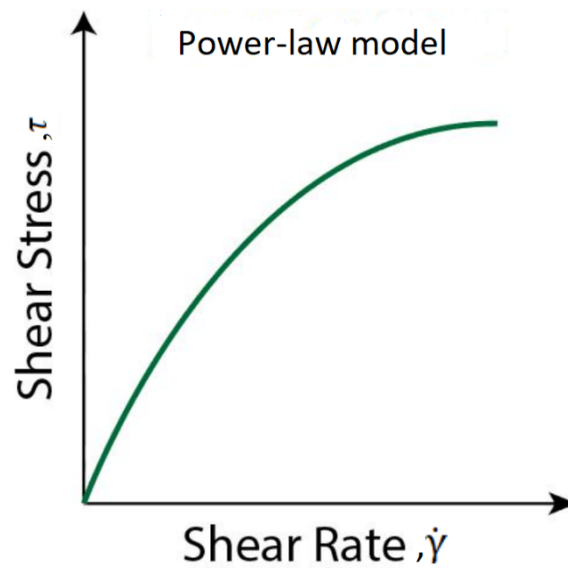


Figure 3.5: Shear stress-shear rate relationship of the power-law model [29].

3.2.2.3 Herschel-Bulkley model

This model is a yielded power-law model. The Herschel-bulkley model is typical for clay muds as the fluid's consistency curve intersects the shear stress-axis at a value greater than zero. This indicates that a gel strength structure is established [29, 1]. The model is represented by three rheological parameters and is presented in equation 3.11 [29].

$$\tau_{HB} = \tau_y + k \dot{\gamma}^n \quad (3.11)$$

Where:

- τ_{HB} = Shear stress for Herschel-Bulkley model [$\frac{\text{lb f}}{100\text{ft}^2}$]

- τ_y = Yield stress [$\frac{\text{lbf}}{100\text{ft}^2}$]
- $\dot{\gamma}$ = Shear rate [sec^{-1}]
- n = Flow index [dimensionless]
- k = Consistency index [$\frac{\text{lbf}^n}{100\text{ft}^2}$]

The shear rate values are constant from the viscometer. The two parameters consistency index and flow index are estimated from curve fitting between measured data and model. This can be performed in Microsoft Excel by plotting the difference between shear stress and yield stress (equation 3.12) on shear rate and from this plot a trendline. The equation of the trendline gives values for consistency index and flow index which are further applied in equation 3.11. The yield stress is estimated from equation 3.12 [36].

$$\tau_y = \frac{\tau^{*2} - \tau_{\min} \cdot \tau_{\max}}{2\tau^* - \tau_{\min} - \tau_{\max}} \quad (3.12)$$

The max and min shear stress values are readings at 600 RPM and 3 RPM from the viscometer. The parameter τ^* is determined by interpolation from the corresponding shear rate presented in equation 3.13 [36].

$$\dot{\gamma}^* = \sqrt{\dot{\gamma}_{\min} \dot{\gamma}_{\max}} = \sqrt{5.11 \cdot 1021.38} \approx 72.25 \text{ s}^{-1} \quad (3.13)$$

The Herschel-bulkley model can describe all Non-Newtonian fluids as well as Newtonian fluids. This makes the model flexible in describing different fluid behavior. There are mainly six classes related to this model [30].

- $\tau_y = 0$ and $n < 1$, the fluid acts shear thinning (pseudoplastic).
- $\tau_y = 0$ and $n = 1$, the fluid acts Newtonian.
- $\tau_y = 0$ and $n > 1$, the fluid acts shear thickening (dilatant).
- $\tau_y > 0$ and $n < 1$, the fluid acts shear thinning with yield stress.
- $\tau_y > 0$ and $n = 1$, the fluid acts Bingham plastic.
- $\tau_y > 0$ and $n > 1$, the fluid acts shear thickening with yield stress.

From figure 3.6 the Herschel-Bulkley model is illustrated. It has a clear yield point and a pseudoplastic behavior. The yield stress can be estimated both from the 3 RPM reading and then calculating n and k from the 600 and 300 RPM, or by mathematical curve fitting between measured data and model [29, 36].

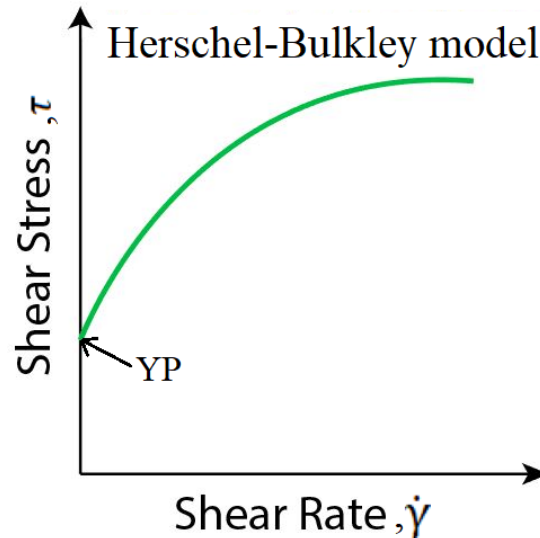


Figure 3.6: Shear stress-shear rate relationship of the Herschel-Bulkley model [29].

3.2.2.4 Unified model

This model is likewise the Herschel-Bulkley model a yielded power-law model. The unified model is simplified to be more applicable to mud engineering in the field in contrast to the more advanced Herschel-Bulkley model. The main contrast between the models is that the unified model estimates the yield stress by using the two lowest shear stress values at reading 3 and 6 RPM [36, 37]. The rheological flow and consistency index are estimated from equation 3.9 and 3.10 respectively from the power law model. The unified model is presented in equation 3.14 [37].

$$\tau_{UN} = \tau_{yL} + k \dot{\gamma}^n \quad (3.14)$$

Where:

- τ_{UN} = Shear stress for unified model [$\frac{\text{lbf}}{100\text{ft}^2}$]
- τ_{yL} = Lower yield stress [$\frac{\text{lbf}}{100\text{ft}^2}$]
- $\dot{\gamma}$ = Shear rate [sec^{-1}]
- n = Flow index [dimensionless]

- $k = \text{Consistency index } \left[\frac{\text{lbft}^n}{100\text{ft}^2} \right]$

The lower shear rate yield stress (LSYS) parameter is estimated from equation 3.15 [37].

$$\tau_{yL} = (2R_3 - R_6) \cdot 1.066 \quad (3.15)$$

3.2.2.5 Robertson-Stiff model

The Robertson-stiff model (R-S) is a general approach to describe rheological behavior of cement slurries and drilling fluids. The model parameters for R-S are defined as A, B and C, where A and B are like the flow index and consistency index of a power-law fluid, and the parameter C is a correction factor to the shear rate. The term $(\dot{\gamma} + C)$ is treated as the effective shear rate [36]. It is rarely used in the drilling industry due to its complexity in determining the parameters A, B and C [36]. The R-S model is presented in equation 3.16 [38].

$$\tau_{R-S} = A(\dot{\gamma} + C)^B \quad (3.16)$$

The yield stress of the R-S model is estimated in equation 3.17 [36].

$$\tau_y = AC^B \quad (3.17)$$

Where the parameter C is determined from equation 3.18 [36].

$$C = \frac{\dot{\gamma}_{\min} \dot{\gamma}_{\max} - \dot{\gamma}^{*2}}{2\dot{\gamma}^* - \dot{\gamma}_{\min} - \dot{\gamma}_{\max}} \quad (3.18)$$

The variable $\dot{\gamma}^*$ is the shear rate value corresponding to the shear stress geometric mean τ^* . It is determined after interpolation to the corresponding geometric mean shear stress. The geometric mean shear stress is calculated from equation 3.19 [36].

$$\tau^* = \sqrt{\tau_{\min} \tau_{\max}} \quad (3.19)$$

Equation 3.20 plots a straight line of log-log coordinates of shear stress on effective shear rates. An example of equation 3.20 plotted is presented in figure 3.7 as a logarithmic form of equation

3.20. The parameters A and B are determined by presenting the equation of the trendline. This method is performed by linear regression technique [36].

$$\log(\tau) = \log(A) + B \log(\dot{\gamma} + C) \quad (3.20)$$

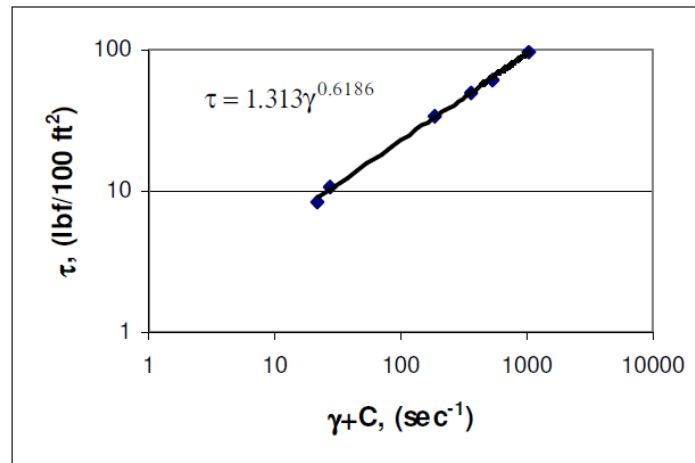


Figure 3.7: Example of log-log plot to determine A and B parameters for R-S model. In this example $A = 1.313$ and $B = 0.6186$ [36].

3.3 Viscoelasticity

A viscoelastic fluid show both elastic and viscous behavior simultaneously under application of shear. All kind of materials with shear behavior acts in a range between two extremes: flow of an ideally viscous liquid and deformation of ideally elastic solids. The purely elastic region is based on Hooke’s law while an ideally viscous liquid behaves accordingly to the law of a Newtonian fluid. The range in between is called the viscoelastic region. As illustrative examples an ideally viscous liquid acts like water, a viscoelastic liquid like hair shampoo, a viscoelastic solid like cream and rigid steel balls as an ideally elastic solid [39, 27]. The ranges of typical material behavior are presented in figure 3.8 [40].



Figure 3.8: An overview of the ranges of material behavior [40].

In drilling fluids, viscoelastic properties are important to determine the gel structure. The gel is important to keep the solid particles from settling, ergo improve cuttings transport and solid suspension in the liquid both under circulation and no circulation conditions. In most drilling operations' viscosity acts as the dominant factor. However, under large deformations the gel shows viscoelastic response. Another important factor is the gels' ability to prevent fluid invasion from wellbore annulus into the reservoir and therefore lost circulation issues. Accordingly, viscoelasticity is a desired property in drilling operations even though application of viscoelastic data in the field are not extensively used [41].

3.3.1 Oscillatory tests

Oscillatory tests are applied to determine a materials viscoelastic property. The basic principle is normally described by the two-plate model; a certain amount of material is put in between a stationary plate and an upper moveable plate with oscillating motion performance. Physically it will look more like a back-and-forth movement of the moveable plate onto the material. For the upper movable plate, a drive wheel produces the oscillating motion with a pushing rod connected to the upper plate at one end, and at the other end its fixed to the upper plate [39]. From figure 3.9 is an illustration of the two-plate model [39].

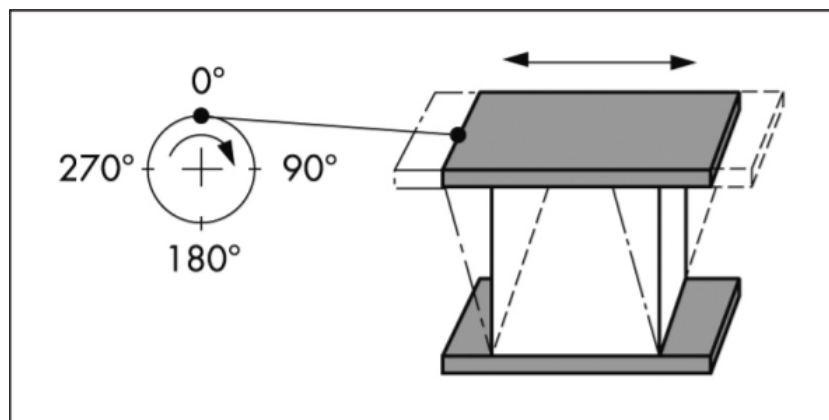


Figure 3.9: Illustration of oscillatory shear test from the two-plate model [39].

There is a height between the two plates defined as the shear gap (h). The shear force ($\pm F$) creates the back-and-forth motion on the upper plate cross-section area from the wheel drive rotation. This motion creates shearing of the material. Under shearing conditions, the material is deflected with deflection path ($\pm s$) and deflection angle ($\pm \phi$). Two shear conditions must be met to obtain accurate rheological parameter estimation [39]:

1. No wall-slip condition and the material show adhesion effects on both plates.
2. The material is homogeneous over the whole shear gap (no plastic deformation).

From figure 3.10 the oscillatory shear test is described mathematically for the two-plate model illustrated in figure 3.9 [39].

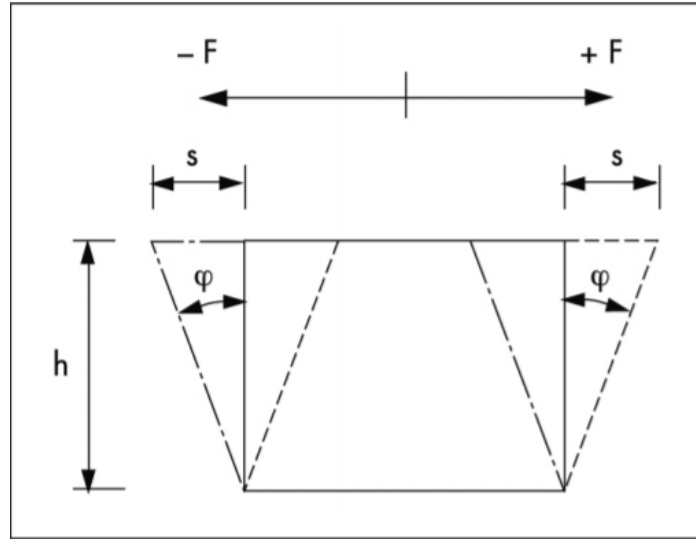


Figure 3.10: Mathematical described oscillatory test for the two-plate model [39].

For viscoelastic behaviour on oscillatory test **the shear stress and shear strain** are time-dependent sinusoidal functions. The shear strain is fixed for both pre-set and measuring results and defined by equation 3.21 [39].

$$\gamma(t) = \gamma_A \sin(\omega t) \quad (3.21)$$

The shear stress is at pre-set conditions defined by equation 3.22. However, the result from measurements is affected by a phase shift angle. This effect is presented in equation 3.23 [39].

$$\tau(t) = \tau_A \sin(\omega t) \quad (3.22)$$

$$\tau(t) = \tau_A \sin(\omega t + \delta) \quad (3.23)$$

Where:

- γ_A = Shear strain amplitude [dimensionless]
- τ_A = Shear stress amplitude [Pa]

- t = Time [s]
- ω = Angular frequency [rad/s]
- δ = Phase shift angle [degrees]

By expanding and collecting terms from equation 3.21, 3.22 and 3.23, the shear stress can be expressed in terms of shear strain. The final combination is presented in equation 3.26 and are plotted as the shear stress function in figure 3.11 [39].

$$\tau(t) = \tau_A [\sin(\omega t) \cos \delta + \cos(\omega t) \sin \delta] \quad (3.24)$$

$$\tau(t) = \gamma_A \left[\left(\frac{\tau_A}{\gamma_A} \cos \delta \right) \sin \omega t + \left(\frac{\tau_A}{\gamma_A} \sin \delta \right) \cos \omega t \right] \quad (3.25)$$

$$\tau(t) = \gamma_A [G' \sin \omega t + G'' \cos \omega t] \quad (3.26)$$

From figure 3.11 is a graphical representation of the sinusoidal functions of resulting shear stress and preset shear strain against time. The shear stress is also defined by a sinusoidal function, although in figure 3.11 it is affected by the phase shift angle and therefore shear stress do not equal zero as time equals zero ($\tau(t = 0) \neq 0$). The phase angle (δ) from equation 3.27 is also presented in the figure denoted as “phase lag” for the time-dependent shear stress, and the amplitude γ_A are shown for the plotted shear strain [39].

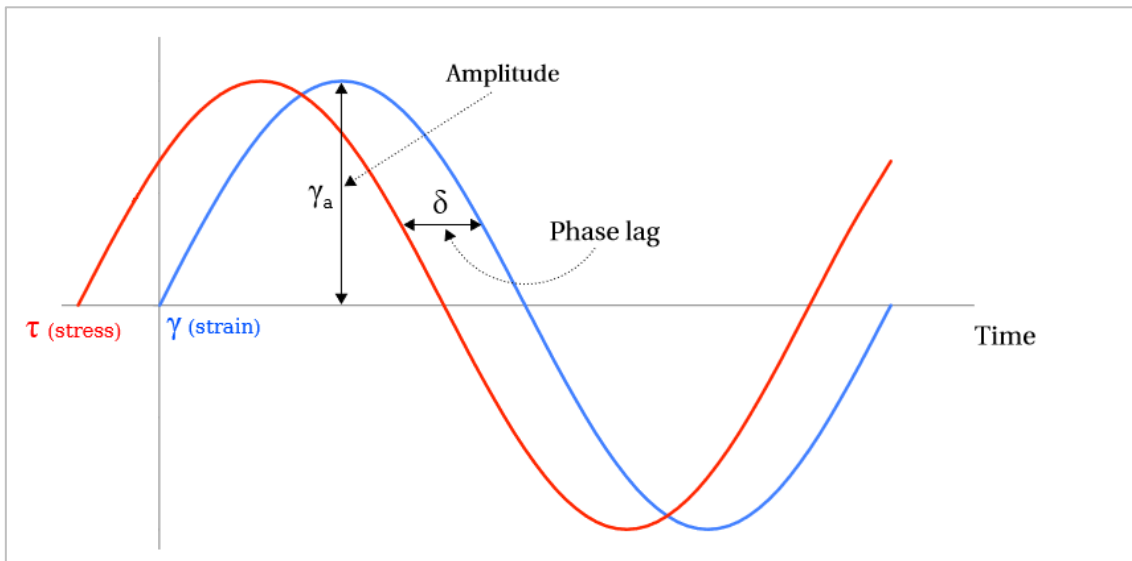


Figure 3.11: graphical representation of shear stress and shear strain against time [39].

The phase shift angle occurs in between the sinusoidal functions for shear stress and shear strain. In other words, it acts between the pre-set and measured resulting curve for the oscillatory test. This angle is also referred to as the loss angle and is a factor in stating a materials behavior. As a rule of thumb, the loss angle always behaves between 0 and 90 degrees and is defined in equation 3.27 [39].

$$0^{\circ} \leq \delta \leq 90^{\circ} \quad (3.27)$$

The energy stored for a material is called **storage modulus (G')**. This modulus represents the elastic behavior of the material. It is a measure of the deformation energy stored by a sample when shear is applied. Materials that indicate completely storage of applied energy shows reversible deformation behavior. These materials are finally unshaped still after applied load cycle [39]. The storage modulus is defined in equation 3.28 [39].

$$G' = \frac{\tau_A}{\gamma_A} \cos \delta \quad (3.28)$$

The loss modulus (G'') is a measure of the deformation energy used up during a shear process of a material. The loss modulus represents the viscous behavior of material. After applied deformation the sample is lost. The energy is spent in the material structure changing process. There is relative motion between molecules and particles with frictional forces interacting together to create viscous heat. This process consumes energy from the material (lost energy). This material shows irreversible deformation behavior after load and finally changed shape [39]. The loss modulus is defined in equation 3.29 [39].

$$G'' = \frac{\tau_A}{\gamma_A} \sin \delta \quad (3.29)$$

The damping or loss factor are defined in equation 3.30. It is the quotient of the loss modulus over the storage modulus of a material (ratio of the viscous and elastic portion). From equation 3.26 the limits for the loss angle are presented. However, for the damping factor the limits therefore behave in the range between zero and infinity [39].

$$\tan \delta = \frac{G''}{G'} \quad (3.30)$$

Table 3.1 represents parameters to state a materials viscoelastic behavior based on phase angle and viscous moduli. Under ideally viscous conditions the phase angle = 90° and the storage modulus decrease towards zero. For a purely elastic deformation the phase angle = 0° and hence the loss modulus decreases towards zero. Phase angle values in-between purely viscous flow and elastic deformation identifies the viscoelastic range, where the 50/50 ratio between viscous and elastic proportions states the material point of intersection ($G' = G''$) and the phase angle = 45° [39]. Table 3.1 also includes damping factor ranges on material behavior [39].

Ideally viscous flow behavior	Behavior of a viscoelastic liquid	Viscoelastic behavior showing 50/50 ratio of the viscous and elastic proportions	Behavior of a viscoelastic gel or solid	Ideally elastic deformation behavior
$\delta = 90^\circ$	$90^\circ > \delta > 45^\circ$	$\delta = 45^\circ$	$45^\circ > \delta > 0^\circ$	$\delta = 0^\circ$
$\tan \delta \rightarrow \infty$	$\tan \delta > 1$	$\tan \delta = 1$	$\tan \delta < 1$	$\tan \delta \rightarrow 0$
$G' \rightarrow 0$	$G'' > G'$	$G' = G''$	$G' > G''$	$G'' \rightarrow 0$

Table 3.1: Parameters to state a materials viscoelastic behavior [39].

3.3.2 Approaches to measure viscoelastic performance

There are mainly four oscillatory test methods to measure viscoelastic behavior. The test methods are presented as followed [39].

- Amplitude sweep
- Frequency sweep
- Temperature sweep
- Time sweep

The theory behind each oscillatory test method applied in this thesis will be presented in the following subsections.

3.3.2.1 Temperature sweep

Temperature sweep is an oscillatory test where amplitude and frequency are held constant while temperature is increased linearly between two pre-set temperatures. The constant angular frequency is pre-set to $\omega = 10 \left(\frac{\text{rad}}{\text{s}}\right)$. Since $\omega = 2\pi f$, the frequency value corresponds approximately to 1.6 Hz [39].

The sweep test occurs under rotational steady state conditions (pre-set constant shear rate). Hence, measured shear viscosity (η) is presented on a linear plot. Shear viscosity is defined as shear stress divided by shear rate and presented in equation 3.31 [39].

$$\eta = \frac{\tau}{\dot{\gamma}} \quad (3.31)$$

In contrast to equation 3.3, the viscosity from the sweep test is measured at one shear rate and temperature-dependent shear stress, while equation 3.3 calculates viscosity dependent on all shear rates with corresponding shear stresses. Shear stress (τ) and shear viscosity (η) are proportional following the relationship from equation 3.31, and similarly the shear rate ($\dot{\gamma}$) and shear viscosity (η) are inverse proportional from the same relationship [39].

Figure 3.12 presents a temperature sweep test for a viscous fluid sample at a constant shear rate. The shear viscosity decreases by increase in temperature [39].

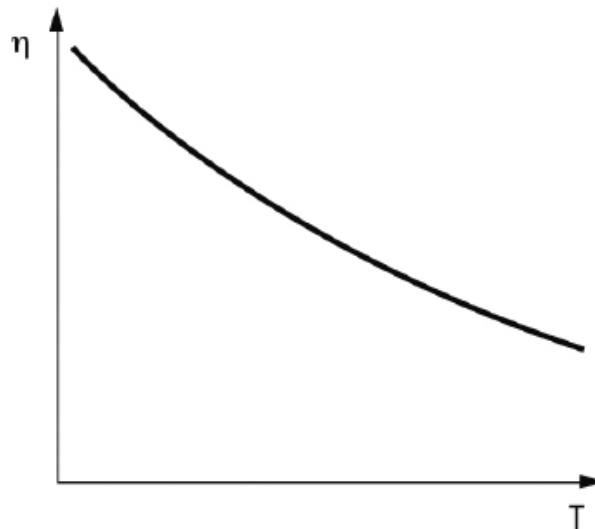


Figure 3.12. Temperature sweep of a viscous fluid sample [39].

Figure 3.13 presents a temperature sweep test for a gel formation sample. For this figure, the shear viscosity decreases to a minima where it starts to increase exponentially with temperature increase [39].

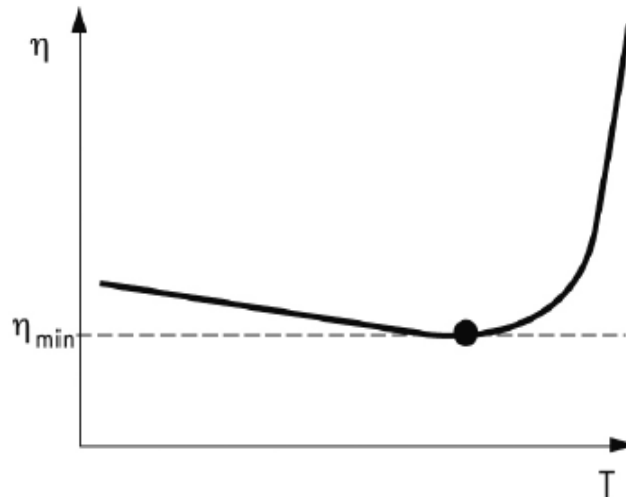


Figure 3.13: Temperature sweep of a gel formation [39].

The objective of the sweep is to measure flow point and physical material changes from elastic to viscous behavior [42, 39].

From a drilling perspective HPHT conditions often occur in wellbores at large depths. The temperature sweep test therefore can state a drilling fluids viscoelastic property at high temperatures. This is beneficial information especially for barite sag and particle settling issues during drilling and hence for gel strength evaluation [41].

3.3.2.2 Amplitude sweep

Amplitude sweep is an oscillatory test where temperature and frequency are held constant while the amplitude is increased as a function of time. The strain amplitude, $\gamma_A(t)$ is gradually increased under isothermal conditions with the constant angular frequency pre-set to $\omega = 10 \left(\frac{\text{rad}}{\text{s}}\right)$, from the same corresponding frequency value in the temperature sweep test from section 3.3.2.1 [39].

Figure 3.14 presents a material sample that exhibit elastic solid or gel behavior because the amplitude sweep test performs $G'' < G'$, and the point of modulus interaction where $G'' = G'$ (gel point). The gel point shows the 50/50 ratio of viscous and elastic portions of the test sample and exhibits the flow stress value (τ_f) [39].

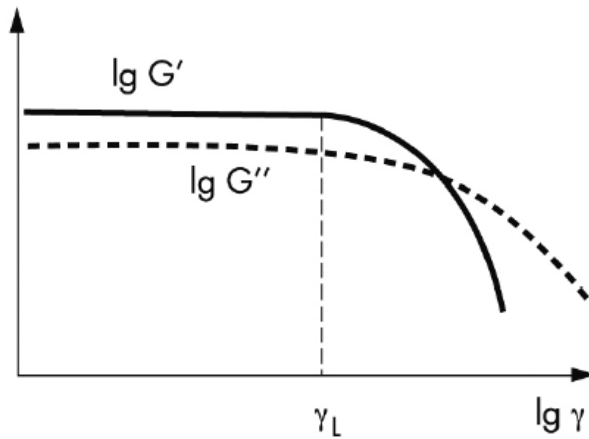


Figure 3.14: Strain amplitude sweep of a sample showing elastic and/or gel behavior in the LVE range [39].

Figure 3.15 presents the fluids flow stress (gel point) and is the stress where the material starts to flow (elastic to viscous material deformation). For all $\tau > \tau_f$, exhibits the flow range where the material behaves like a liquid. The flow point is calculated by linear interpolation between the materials shear stress and the materials phase angle at the gel point (i.e., $\delta = 45^\circ$). The yield stress (τ_y) is determined at the point where the material goes from linear elastic to plastic deformation behavior, hence the limit of the LVE range at the y-axis. The yield zone is the range for all shear stresses in-between $\tau_y < \tau < \tau_f$, and is referred to as the materials transition phase. In this zone, the material still shows gel characteristics. However, partially irreversible plastic deformation may occur for shear stresses in this range [39].

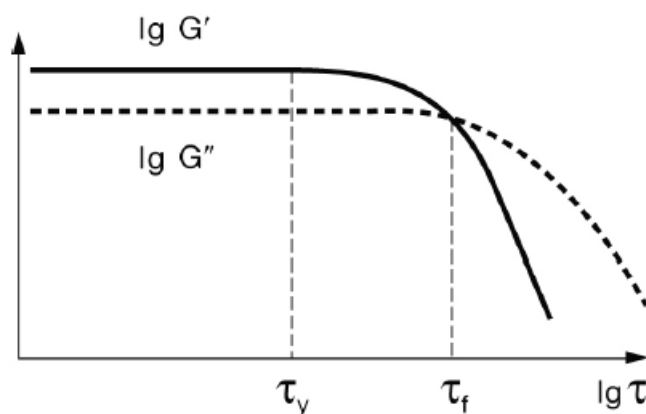


Figure 3.15: Stress amplitude sweep showing yield stress, yield-zone, and flow point of a sample [39].

3.4 Well program

The major problem in well operations are well instability issues. The main objective is to maintain a stable borehole in drilling and completion operations. Wellbore stability is obtained by drilling in-between the well collapse and well fracture gradient. In HPHT wells, the well stability window can be narrow. There are several examples related to instability in wellbores like ductile formations squeezed into hole, slumping and caving shales with consequent hole enlargement. The benefits with wellbore stability are reduced drilling non-productive time and avoidance of stuck pipe, sidetrack-wells and blow out [1, 22].

3.4.1 Equivalent circulating density

The safe operational drilling window between the collapse and fracture gradient is controlled by the drilling fluids equivalent circulating density (ECD). ECD are mainly controlled by a drilling fluids mud weight but also adds wellbore frictional pressure loss. ECD are presented in equation 3.32 [1].

$$ECD = MW + \frac{\Delta P_{\text{friction}}}{g_{\text{TVD}}} \quad (3.32)$$

Where:

- MW= Static mud weight [kg/m³]
- $\Delta P_{\text{friction}}$ = Dynamic frictional pressure loss in annulus [Pa]
- g = Gravitational acceleration [m/s²]
- TVD = True vertical depth [m]

3.4.2 Pump pressure

The pump pressure is calculated as the sum of the frictional pressure losses in the whole hydraulic circulation system. This includes the dynamic frictional pressure loss in the surface flowlines at the rig site, drill pipe, drill collar, bit nozzles and the annular spacing around drill collar and drill pipe in well annulus. This is illustrated in figure 3.16 [43]. Hence the pump pressure is formulated in equation 3.33 [44].

$$P_{\text{pump}} = \Delta P_{\text{total}} = \Delta P_{\text{surface}} + \Delta P_{\text{pipe}} + \Delta P_{\text{drillcollar}} + \Delta P_{\text{bit}} + \Delta P_{\text{annulus,dc}} + \Delta P_{\text{annulus,dp}} \quad (3.33)$$

Where:

- P_{pump} = Pump pressure [psi]
- ΔP_{total} = Total dynamic frictional pressure loss [psi]
- $\Delta P_{\text{surface}}$ = Dynamic frictional pressure loss in the surface flowlines [psi]
- ΔP_{pipe} = Dynamic frictional pressure loss in the drill pipe [psi]
- $\Delta P_{\text{drillcollar}}$ = Dynamic frictional pressure loss in drill collar [psi]
- ΔP_{bit} = Dynamic frictional pressure loss in drill bit nozzles [psi]
- $\Delta P_{\text{annulus,drillcollar}}$ = Dynamic frictional pressure loss in the annular spacing between the wellbore and the drill collar [psi]
- $\Delta P_{\text{annulus,drillpipe}}$ = Dynamic frictional pressure loss in the annular spacing between the wellbore and the drill pipe [psi]

Figure 3.16 illustrates the frictional pressure components in the hydraulic circulation system [43].

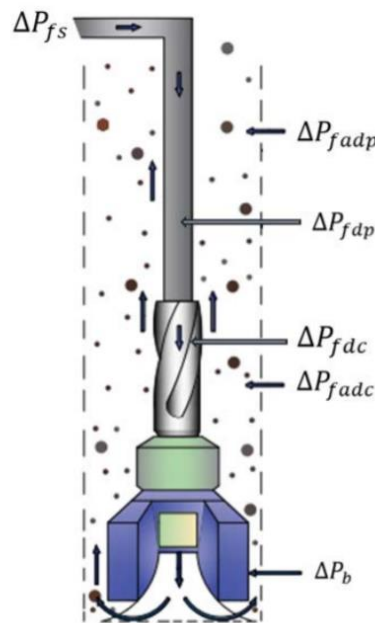


Figure 3.16: Illustrative sketch of the dynamic frictional pressure losses in the hydraulic system [43].

J. Sadigov et al analyzed the predictive power of hydraulics models [45]. Field and laboratory hydraulics data were implemented for the study, and the results showed that the unified hydraulics model was found to be better for most drilling fluids [45]. Therefore, in this thesis, the unified hydraulics model was selected to evaluate ECD and pump pressure for the nano-based sodium and potassium fluid systems in section 6. Table 3.2 presents the summary of the parameters in the unified hydraulics model [38].

Unified Hydraulics Model		
Pipe flow		Annular flow
$\mu_p = R_{600} - R_{300}$	$\tau_y = R_{300} - \mu_p$	$\tau_0 = 1.066(2R_3 - R_6)$
$n_p = 3.32 \log\left(\frac{2\mu_p + \tau_y}{\mu_p + \tau_y}\right)$		$n_p = 3.32 \log\left(\frac{2\mu_p + \tau_y - \tau_y}{\mu_p + \tau_y - \tau_y}\right)$
$k_p = 1.066\left(\frac{\mu_p + \tau_y}{511}\right)$		$k_p = 1.066\left(\frac{\mu_p + \tau_y - \tau_0}{511}\right)$
$\alpha = 0$ for pipe	$G = \left(\frac{(3 - \alpha)n + 1}{(4 - \alpha)n}\right)\left(1 + \frac{\alpha}{2}\right)$	$\alpha = 1$ for annuli
$V_p = \frac{24.51q}{D_p^2} \left[\frac{\text{ft}}{\text{min}}\right]$		$V_a = \frac{24.51q}{D_2^2 - D_1^2} \left[\frac{\text{ft}}{\text{min}}\right]$
$\gamma_w = \frac{1.6 * G * v}{D_R} [\text{sec}^{-1}]$		
$\tau_w = \left[\frac{(4 - \alpha)}{(3 - \alpha)}\right] \tau_0 + k \gamma_w^n [\text{lb}/100\text{ft}^2]$		
$N_{Re} = \frac{\rho V_p}{19.36 \tau_w}$		$N_{Re} = \frac{\rho V_e}{19.36 \tau_w}$
$f_{\text{laminar}} = \frac{16}{N_{Re}}$		$f_{\text{laminar}} = \frac{24}{N_{Re}}$
$f_{\text{transient}} = \frac{16N_{Re}}{(3470 - 1370n_p)}$		$f_{\text{transient}} = \frac{16N_{Re}}{(3470 - 1370n_p)}$
Turbulent: $f_{\text{turbulent}} = \frac{a}{N_{Re}^b}$		Turbulent: $f_{\text{turbulent}} = \frac{a}{N_{Re}^b}$
$a = \frac{\log(n) + 3.93}{50}$ $b = \frac{1.75 - \log(n)}{7}$		$a = \frac{\log(n) + 3.93}{50}$ $b = \frac{1.75 - \log(n)}{7}$
$f_{\text{partial}} = (f_{\text{transient}}^{-8} + f_{\text{transient}}^{-8})^{-\frac{1}{8}}$		
$f_p = (f_{\text{partial}}^{12} + f_{\text{laminar}}^{12})^{\frac{1}{12}}$		$f_a = (f_{\text{partial}}^{12} + f_{\text{laminar}}^{12})^{\frac{1}{12}}$
$\left(\frac{dp}{dL}\right) = 1.076 \cdot \frac{f_p \cdot v_p \cdot \rho}{10^5 \cdot D_p} = \left[\frac{\text{psi}}{\text{ft}}\right]$		$\left(\frac{dp}{dL}\right) = 1.076 \cdot \frac{f_a \cdot v_a \cdot \rho}{10^5 \cdot (D_2 - D_1)} = \left[\frac{\text{psi}}{\text{ft}}\right]$
$\Delta p = \left(\frac{dp}{dL}\right) \cdot \Delta L = [\text{psi}]$		$\Delta p = \left(\frac{dp}{dL}\right) \cdot \Delta L = [\text{psi}]$
$\Delta p_{\text{nozzles}} = \frac{156 \cdot \rho \cdot q^2}{(D_{N1}^2 - D_{N2}^2 - D_{N3}^2)^2} = [\text{psi}]$		

Table 3.2: Summary of parameters for the Unified hydraulics model [38].

3.5 Well fracture models

When the well pressure exceeds the fracture gradient limit, the wellbore is fractured and hence fluid is lost to the formation ($P_{\text{well}} > P_{\text{formation}}$). Hydraulic fracturing of wellbore rock material in drilling operations are identified as rock tensile strength. The formation rock fractures when the minimum effective principal wellbore stress exceeds the rock tensile strength [46, 22]. The following subsections presents the non-penetrating and penetrating fracture models.

3.5.1 Non-Penetrating fracture model

The boundary condition at the wellbore assume that there is no communication between the wellbore and the formation. This is because the fluid creates an impermeable filter cake (flow barrier) at the wellbore wall to prevent fluid flow into formation. This is typical for drilling fluids containing high solid content where the particles will plug and then bridge at the fracture opening. Figure 3.17 illustrates the non-penetrating model situation where the left side of the flow barrier is well pressure (P_w) and the right side of the barrier describes the formation pore pressure (P_o). Each pressure remains constant due to no leak-off effect through the impermeable flow barrier [11].

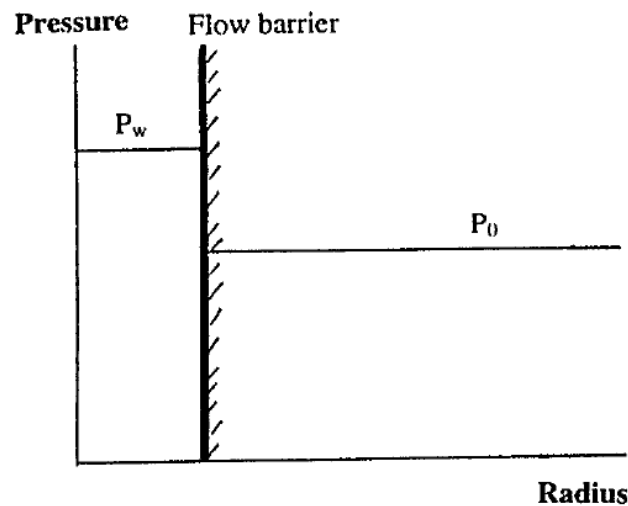


Figure 3.17: Non-penetrating fracture model [11].

In anisotropic state of stress, the fracture initiates at the normal direction (perpendicular) to the minimum horizontal stress. Fractures propagate in the direction of the maximum horizontal stress. Equation 3.34 defines the fracture pressure for a non-penetrating with different horizontal stresses [11].

$$P_{wf} = 3\sigma_h - \sigma_H - P_o + \sigma_t \quad (3.34)$$

Where:

- P_{wf} = Well fracture pressure [specific gravity]
- σ_H = Maximum horizontal in-situ stress [specific gravity]
- σ_h = Minimum horizontal in-situ stress [specific gravity]
- P_o = Formation pore pressure [specific gravity]
- σ_t = Tangential (Hoop) in-situ stress [specific gravity]

It is a common practice to assume that the tensile rock strength is very small or negligible. For stress relaxed sedimentary rock, isotropic in-situ horizontal stress of state is commonly assumed, the non-penetrating fracture model can be described from equation 3.35 [47].

$$P_{wf} = 2\sigma_h - P_o \quad (3.35)$$

Where:

- P_{wf} = Well fracture pressure [specific gravity]
- σ_h = Minimum horizontal in-situ stress [specific gravity]
- P_o = Formation pore pressure [specific gravity]

3.5.2 Penetrating fracture model

The boundary condition at the wellbore is penetrating such that the drilling fluid will leak from the wellbore into the formation rock. As a result, the well pressure is equal the formation pressure at the well barrier as illustrated in figure 3.18. For the model to be applied it requires a clean Newtonian fluid with no filtrate control that creates no filter cake at the wellbore wall. It is mostly applied in drilling operations for hydraulic fracturing and acid stimulation. In the penetrating case, the tensile rock strength is negligible [46, 22, 47].

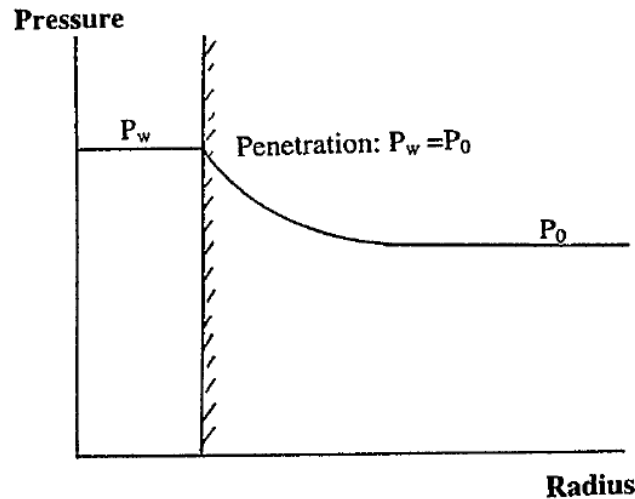


Figure 3.18: Penetrating fracture model [11].

By setting the well pressure equal to the pore pressure in the isotropic stress state fracture equation (Eq. 3.35), the penetrating model is given by equation 3.36 [47].

$$P_{wf} = \sigma_h \quad (3.36)$$

3.6 Lost circulation material

Lost circulation material (LCM) is all material added to the drilling fluid to prevent mud loss to the formation. The main objective of LCM treatment is to effectively seal fractures and the fluid losses are stopped at differential pressures. LCM particles are often chosen based on bridging theory and the pore size of the formation. The main goal of LCM interpretation in drill-in fluids is to minimize formation damage caused by fluid invasion through the formation. A correct selection of LCM is important to ensure wellbore strength because of its ability to act as bridging material at the fracture opening (stress cage effect). Hence LCM functions both as materials to prevent fluid loss and strengthen the wellbore (WSM). Examples of LCM's are graphite, quartz, feldspar, nutshells, mica, CaCO_3 and cellulose fiber [48].

The Moh's scale states the materials compressive hardness. Whether the material is hard or soft. CaCO_3 is a soft LCM and is good for wells with low pressure overbalance. However, quartz and feldspar are stronger LCM particles to resist high mud cake collapse pressures [47]. Figure 3.19 presents the fracture pressures vs. the Moh's scale [47].

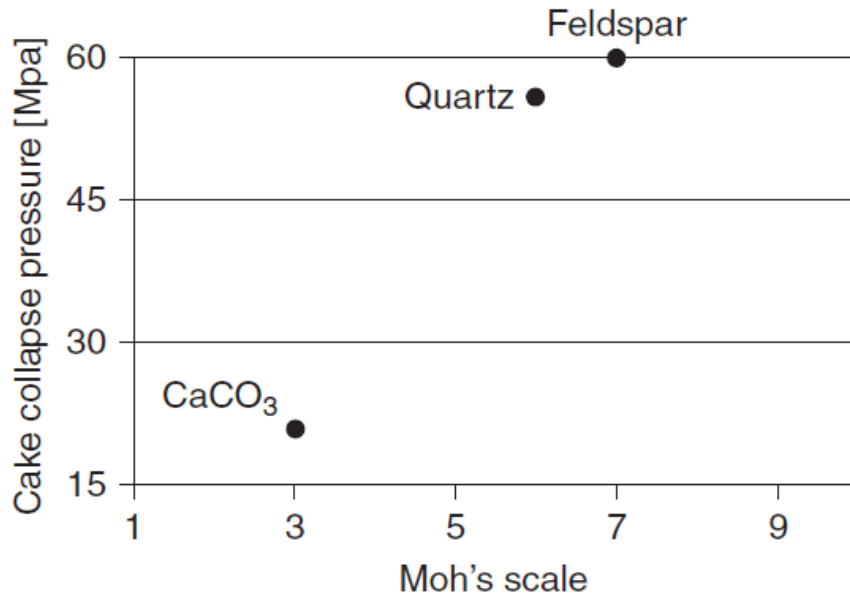


Figure 3.19: Fracture pressure vs. Moh's scale [47].

3.7 Particle size of bridging materials

Particle size distribution (PSD) is essential when designing LCM treatments. Especially for drill-in fluids which are the first fluid in contact with the reservoir section. Hence an optimal bridging material needs to be selected to prevent solid plugging, hydration swelling of reservoir rock, particle migration etc. Larger particles like barite enhances skin on the reservoir rock and hence cannot be selected as bridging material in a drill-in fluid. Calcium carbonate are an optimal bridging material due to the materials ability to resist differential well pressures and are non-damaging to formation permeability. CaCO₃ are also suitable based on its solubility in acids. This creates a wipe-off effect of calcium carbonate on the porous wellbore wall after acid treatment [49].

Figure 3.20 represents an external mud cake with large pore spaces for fluid migration. The particles are too large to effectively plug the pores. Hence well instability issues may occur [49].



Figure 3.20: Incorrect sized CaCO_3 in drill-in fluid [49].

Figure 3.21 represents an internal mud cake with correctly sized particles to prevent fluid invasion [49].

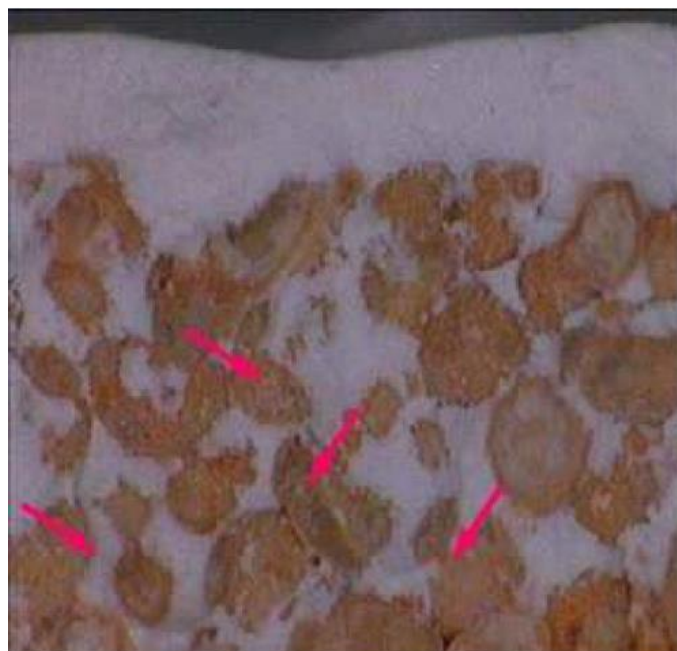


Figure 3.21: Correct sized CaCO_3 in drill-in fluid [49].

3.8 Fracture propagation process

Figure 3.22 presents the hydraulic fracturing process of the wellbore wall due to increased mud weight above the fracture resistance pressure. The illustration presents quantitatively the process of mud cake formation, fracture initiation, fracture growth and mud cake formations collapse along with the main controlling parameters [47].

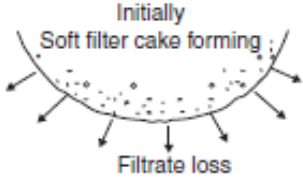
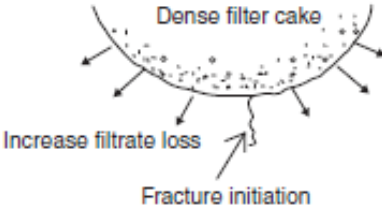
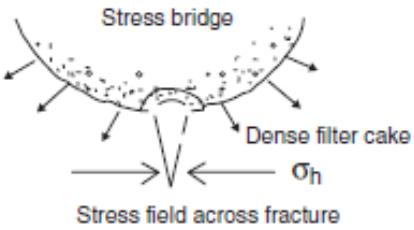
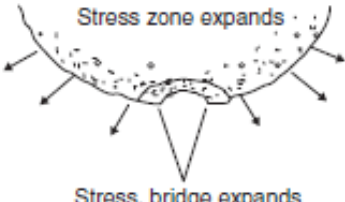
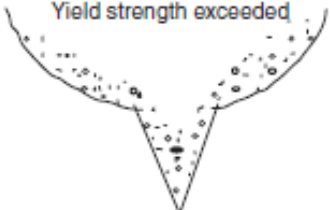
Event	Fig	Main controlling parameters
Filter cake formation	 <p>Initially Soft filter cake forming Filtrate loss</p>	Filtrate loss
Fracture initiation	 <p>Dense filter cake Increase filtrate loss Fracture initiation</p>	Filtrate loss, Stress
Fracture growth	 <p>Stress bridge Dense filter cake σ_h Stress field across fracture</p>	Bridge stress Rock stress
Further fracture growth	 <p>Stress zone expands Stress, bridge expands</p>	Bridge/rock stress Particle strength
Filter cake collapse	 <p>Yield strength exceeded</p>	Particle strength

Figure 3.22: Illustration of the fracture propagation process [47].

4 Experimental work

This section describes the experimental work performed in this thesis. Section 4.1 presents the materials and methods being used and includes the CaCO₃ LCM particle size distribution. The characterization methods present the experimental equipment's and procedure formulated in section 4.2. Section 4.3 presents the sodium, potassium, sodium/potassium, and cesium/potassium-based drill-in fluids formulated in this thesis.

4.1 Materials and methods

This subsection is a general description of the drilling fluid additives added to the mud compositions formulated in section 4.3.

4.1.1 Materials

The materials used for the Na, K, Na/K and Cs/K drill-in fluid compositions is presented in the following subsections.

4.1.1.1 Sodium formate

The chemical formula for sodium formate is HCOONa. A free positive electron circulates in its outer shell. This is a chemical reaction made from neutralization of formic acid (HCOO⁻) with an oxidizing metal (Na⁺). Sodium is an alkali metal in group 1A column of the periodic table with molecular mass equals 23.0 u. The solubility of sodium formate in water equals 47 weight% and density of sodium formate is 1.33 specific gravity relative to water [50, 14, 51].

4.1.1.2 Potassium formate

The chemical formula for potassium formate is CHKO₂. Potassium is an alkali metal in group 1A column of the periodic table and therefore operates with a free positive electron in its outer shell. The molecular mass of potassium alkaline salt equals 39.1 u. Potassium formate is a result of the chemical reaction between the acidic component (HCOO⁻) and alkali metal (K⁺). In contrast to sodium formate, potassium formate has one single and one double molecular bonding to each oxygen atom. The solubility for potassium formate in water equals 77 weight% and the density is 1.59 specific gravity relative to water [51, 14, 50].

4.1.1.3 Cesium formate

The chemical formula for cesium formate is HCOOCs . This is an alkaline salt in the alkali metal group 1A from the periodic table. Cesium formate is a result of the chemical reaction between the acidic molecule (HCOO^-) and alkali metal (Cs^+). The solubility in water for cesium formate equals 82wt% and the density relative to water equals 2.4 specific gravity. However, cesium formate blended with potassium formate can reduce the density to 1.8-2.4 specific gravity range. Hence cesium formate is heavy and the molecular mass for the alkaline salt equals 132.9 u [52, 51].

4.1.1.4 Starch

Starches are carbohydrates defined from the general formula $(\text{C}_6\text{H}_{10}\text{O}_5)_n$ and are extracted from foods like rice, wheat, corn, potatoes etc. For example, in fishing or tomato soup addition of starch can make the soup thicker with increased temperature. In drill-in fluids, starches from methyl groups like carboxymethyl cellulose are normally applied and functions as a filtrate controlling agent in the mud composition [53].

4.1.1.5 Xanthan gum

Xanthan gum (XG) is a polymer additive. XG is an anionic polysaccharide produced from the micro organismic bacteria *Xanthomonas campestris*. It is soluble in cold water and one of its chemical characteristics to fluid is to create pseudoplastic flow, therefore application of XG in drilling fluids is to enhance a Non-Newtonian fluid behavior to effectively transport cuttings in annular flow. XG are also widely used to enhance oil recovery (EOR) in reservoirs. As an important industrial biopolymer, XG functions as an EOR agent in oil drilling, fracturing and pipeline cleaning. Its ability to enhance viscosity, excellent thermal and saline stability and properly functions under high mechanical shear conditions, makes it a suitable polymer additive in HPHT compatible drilling fluids and EOR operations [54, 55, 56].

4.1.1.6 CaCO_3

Calcium carbonate is a biogenetic rock like limestone, and most widely used filler in polymer formulations. Calcium carbonates density ranges from 2.7-2.9 specific gravity, pH of water suspension is 9, oil absorption 13-21 g/100g and surface area ranges from 5-24 m^2/g . It acts as a weighting material preferable to barite because of its solubility to hydrochloric acids and easy to clean up the production zone. However, its primary function is as a bridging material in workover, completion, and drill-in fluids [57, 58].

LCM particle size distribution

This subsection presents the particle size distribution (PSD) and mass percentage obtained from the sieving analysis for both CaCO₃ type 1 and CaCO₃ type 2. These are two different types of CaCO₃ received from the industry with the same purpose to function as LCM in drilling fluids. Figure 4.1 presents the mass percentage plotted as the difference in measured mass CaCO₃ before and after sieving on different particle micron sizes. The PSDs are plotted as cumulative functions from the mass percentages. From the PSDs, it was further investigated that D10 were in the <63 microns range for both the type 1 and type 2 CaCO₃. The mass concentration of CaCO₃ type 2 is higher in the <63 microns range, but the type 1 is higher in the ranges 63-71, 71-90 and crosses at 90-125 microns. From this point of intersection, the mass concentration of type 2 is higher for 125-150, 180-250 and 250-355 microns.

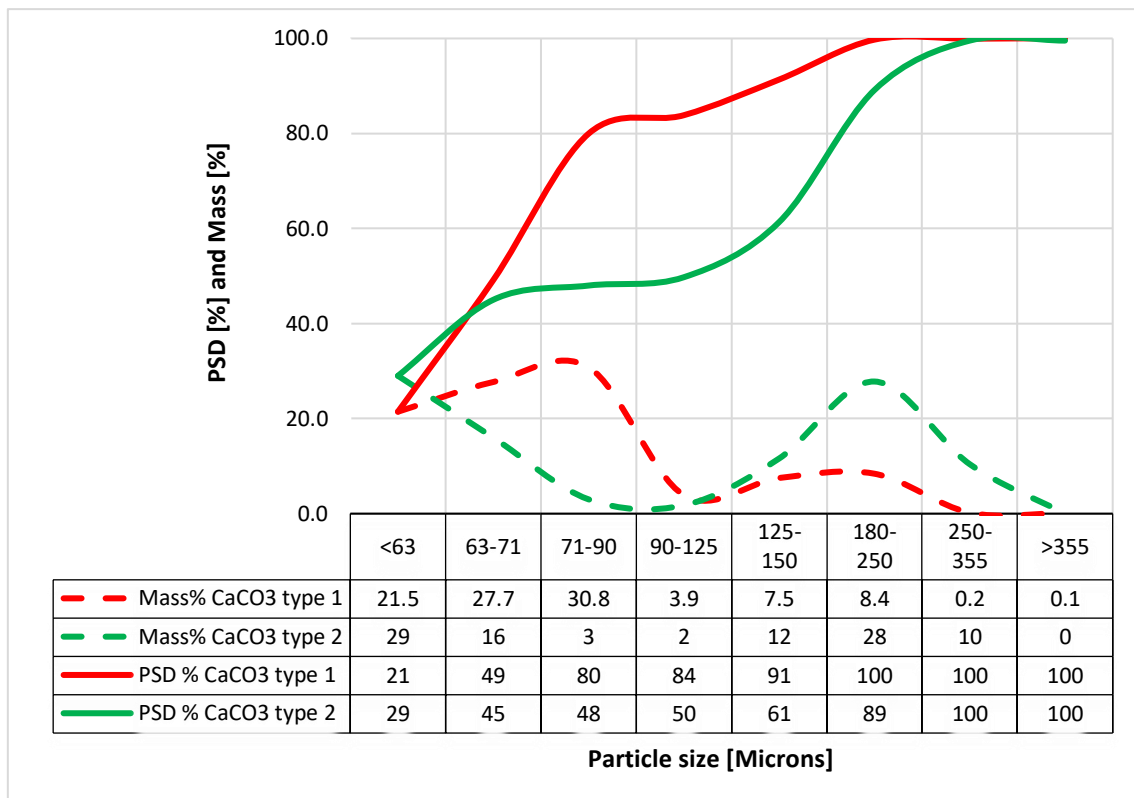


Figure 4.1: Particle size distribution for CaCO₃ type 1 and CaCO₃ type 2 (mass% and cumulative PSD).

4.1.1.7 Quartz

The chemical formula for quartz minerals is SiO₂. This is also referred to as silica. The density for quartz ranges from 2.6-2.7 specific gravity and the minerals Moh's hardness number equals 7. Quartz particles are often chosen for high overbalance situations in drilling [47, 59]. In this thesis, the 100-150- and 150-250-micron sized quartz particles were chosen to increase the wellbore strength in cesium/potassium drill-in fluid.

4.2 Characterization methods

This section is a general description of the experimental equipment and test procedure performed in this thesis. The testing was done systematically starting with the Haver EML 200 digital shaker for CaCO₃ sieving analysis before mixing each fluid system in accordance to section 4.3. Hence, each fluid mixed system was exposed to API static filter press, OFITE model 800 viscometer and Anton Paar rheometer for fluid characterization. The sonics vibra cell was applied for breaking the surface tension in the cesium/potassium fluid, and the Enerpac equipment was used for hydraulic fracturing performance.

4.2.1 Haver EML 200 digital shaker and sieve procedure

Both the CaCO₃ type 1 and CaCO₃ type 2 particles were sieved by using the Haver EML 200 digital shaker, presented in figure 4.2. It consists of 8 metal sieves with different mesh grid sizes in microns (μm), with the largest micron at the top ($>355 \mu\text{m}$) and smallest micron at the bottom ($<63 \mu\text{m}$). From bottom to top the different sieves are presented as follows: $<63 \mu\text{m}$ (bottom), $63-71 \mu\text{m}$, $71-90 \mu\text{m}$, $90-125 \mu\text{m}$, $125-150 \mu\text{m}$, $180-250 \mu\text{m}$, $250-355 \mu\text{m}$ and $>355 \mu\text{m}$ (top). From figure 4.2, the shaker originally consists of 10 metal sieves. However, the mesh grid size of $106 \mu\text{m}$ and $150 \mu\text{m}$ were removed due to very low CaCO₃ particle settling. The $106 \mu\text{m}$ were then added to $90 \mu\text{m}$, and $150 \mu\text{m}$ added to $180 \mu\text{m}$. This was done to make a continuous particle size distribution for 200 g sieved CaCO₃.

The mesh grid sizes are presented as ranges between two absolutes because some particles with diameter equal to the mesh grid size above can be sieved through and layer in the metal sieve below. These sieves are attached together and locked at the top with screws from two metal rods. The sieves and metal rods are placed on the shaker base. This base is the part of the shaker that makes the vibration mechanism to sieve the particles well through the different sieve layers from top to bottom.

The sieving procedure started by placing 200 grams of CaCO₃ at the top sieve ($>355 \mu\text{m}$). The shaker was then adjusted for vibration intensity, intervals, and time. In contrast to the values from figure 4.2, the sieving procedure were performed with intensity equal to 8, zero intervals and sieving period equal to 10 minutes. Instead of splitting the sieve test procedure into more intervals and at low vibration intensity, the shaker were set to the mentioned values to sieve the CaCO₃ well through all the different mesh grid sizes, and hence to prevent larger particles to

block the small particles coming through the sieves. The sieves were weighted before and after sieving of CaCO_3 particles.



Figure 4.2: Haver EML 200 digital shaker for sieving the CaCO_3 particles.

4.2.2 API static filter press and filtrate procedure

The function of the API filter press is to measure the fluid loss for the different fluid systems at ambient conditions under 100 psi of applied pressure. Filtrate control is an important parameter in drilling and completion operations to avoid fluid loss to the formation.

The metallic cell before connected to the pressure tubing are put together by several mechanical components. The metallic bottom consists of a base cap with a filtrate tube. Then a circle formed mesh screen with a filter paper sized 2.7 microns is placed at the base cap in between two rubber rings to seal the mesh screen and filter paper together. Thereafter the cell body is placed upon the base cap and fluid filled to the marked line at the cell body wall. A rubber ring seals the cell body and the top cap. Hence, the mechanical setup is complete and ready for pressure testing.

From figure 4.3, the base cap with a filtrate tube, cell body, top cap (attached to pressure tubing) and measuring cylinder are presented.

The filtrate procedure started by putting a fluid filled and sealed cell body into the API static filter press. A metal rod is then screwed into the cell body to keep it tight. A measuring cylinder were put under the filtrate tube to constantly measure the fluid loss volume during testing. Then 100 psi of pressure were applied to the system and filtrate testing time set to 7 minutes and 30 seconds. From figure 4.3, the spurt loss can be seen from the bottom of the measuring cylinder and was established right after applied pressure. Then fluid drops were constantly filling the measuring cylinder to a desired level for 7.5 minutes. The fluid loss volume was measured from the cylinder, and the filter paper were taken out of the cell body to identify mud cake characteristics.



Figure 4.3: API static filter press with measuring cylinder.

4.2.3 OFITE Model 800 viscometer and rheology measurement procedure

The rheological measurements were performed using a OFITE model 800 8-speed viscometer. The viscometer consists of a rotational bob connected to the measuring apparatus. At the top of the measuring apparatus there are eight different shear rates: 600, 300, 200, 100, 60, 30, 6 and

3 (gel) rpm. The OFITE model 800 Viscometer also has a STIR function to stir the fluid with a shear rate higher than 600 rpm.

Each fluid system was prepared for rheology measurements by fluid mixing for 2 minutes using the Hamilton Beach mixer to prevent particle segregation and maintain a homogeneous fluid system after the API static filter press testing. Additionally, the STIR function at the viscometer apparatus were applied to stir the fluid well before starting the rheological measuring procedure.

The rheological measurements for all fluid systems were done at 20, 50 and 80°C. All rheological measurements for the 3 different temperatures were done starting from top (600 rpm) and measured at all eight shear rates down to 3 rpm. As a rule of thumb, it was decided to wait 3 seconds for the viscometer to stabilize at each reading value before taking notes. This procedure was performed consequently for all shear rates. The measuring procedure were done once for each temperature, starting at room temperature, hence increase the temperature to 50°C and then 80°C using a heating cup. The temperature was controlled by a digital thermometer during heating. Figure 4.4 presents the OFITE model 800 viscometer with heating cup.



Figure 4.4: OFITE model 800 viscometer with heating cup.

4.2.4 Anton Paar MCR 302 Rheometer and viscoelastic test procedure

All oscillatory viscoelastic measurements performed in this thesis were done by using the Anton Paar MCR 302 rheometer. The rheometer consists of several advanced rotational and oscillatory functions and is a highly accurate equipment for the fluid systems viscoelastic performance. The mechanical setup is different based on the test performed. In this thesis, the rotational bob and cup setup for temperature sweep, and the mechanical plate-against-plate setup for oscillatory amplitude sweep (back-and-forth movement) were used. For any test the flow valves from the nearby fluid tank had to be switched open to circulate cooling fluid through the flow tube connecting the fluid tank and rheometer. The cooling fluid is a blend of water and glycol and its function is to prevent the rheometer to overheat during testing.

The temperature sweep test was performed using a rotational bob and cup setup. The bob was carefully attached into the open space under the black top cap, and fluid were filled to the marked line in the cup and placed into the rheometer open hole. The test was set to perform linear temperature increase from 20°C to 80°C and measure the viscosity at a constant shear rate equal to 50 s⁻¹. The temperature increase was decided to end at 80°C regarding safety issues because of no information about the fluids boiling point. The choice of shear rate was based on the rheometers ability to create turbulence at high shear rates. Hence 50 s⁻¹ were applied to obtain laminar flow conditions. The bob was then set from lift position to measuring position and test started.

After the measurements were complete, the rheometer was set to cool down the cup containing measured fluid volume from 80°C to 20°C, to prepare the rheometer for a new test with another fluid. Figure 4.5 presents the MCR 302 rheometer where the temperature sweep and amplitude sweep tests were performed. Figure 4.5 indicates that the rheometer is adjusted for plate-against-plate setup for amplitude sweep tests. In this test procedure, the strain increases in % and correspondingly measure the fluid systems storage and loss moduli.



Figure 4.5: Anton Paar MCR 302 rheometer.

4.2.5 Sonics vibra-cell and ultrasonic test procedure

The purpose behind the application of the sonics vibra-cell is to break the surface tension in highly concentrated fluids by ultrasonic waves. This makes the organic solvents to dissolve into a uniform system. A solid probe is put into the fluid system obtained in a mixing cup. The probe is tuned in to resonate at 20kHz (with $\pm 50\text{Hz}$ deviation).

Figure 4.6 presents the sonics vibra cell. The solid probe is put into the fluid system and ultrasonic waves is pulsating in 2-seconds intervals into the system. The total elapsed time to make the starch dissolve and to break the surface tension of the highly concentrated cesium/potassium brine were 30 minutes (as required).



Figure 4.6: Sonics vibra-cell.

4.2.6 Enerpac hydraulic fracturing setup and fracking procedure

The Enerpac applied power equipment were applied for hydraulic fracturing. The max hydraulic pressure for Enerpac equals 10,000 psi. Figure 4.7 presents the Enerpac hydraulic fracturing experimental setup. After the core is put into the cell, there is a gap filled with water (H₂O) between the cell-wall and core referred to as “well annulus”. In the core there is a hollow cylinder referred to as “well”, which equals 15 ml. The core simulates the formation and is sealed with a metallic block that has a hydraulic fluid connection to the hose with a red tip in figure 4.7. Two metallic blocks are additionally put onto the metallic seal, and the black metallic block creates axial load by pushing onto the block system.

The setup is divided into a circulating (open system) and non-circulating system (closed system). The experimental procedure for both circulating and non-circulating system is described in the following numerical order:

1. The fluid cell in the top-left of the picture is filled with mud. From this cell the fluid will be circulated downwards to another flow line that connects the well with pump.
2. Underneath this connection point, there is a valve that can be switched Open/ Closed.
3. If the valve is switched Open, the fluid is hydraulically pumped upwards, and hence circulate the well system dynamically from the red hose tip.
4. If the valve in 2. is switched Closed, the fluid fills the well directly from the mudline and hence hydraulic fracturing occurs at static conditions (sketched blue line in figure 4.7).
5. After the valve is either switched Open or Closed, distilled water is pumped continuous from two pumping units into the fluid cell in 1., and the well system is pressurized.

The pros with circulate the well system during fracturing, is that this scenario simulates real operational drilling with overpressure and continuous flow, hence a mud cake will be established at the wellbore wall. The con is that this procedure needs more mud in the system (i.e., approximately 1.5 liter) and the Cs/K brine is expensive.

The pros with hydraulic fracturing at static conditions, is that less mud is needed and can be re-used for several tests. However, it is still possible to create a mud cake by lubricating the well with mud from a syringe spray before filling mud into the whole well system. In real-life drilling operations, the mud pumps are turned off during a drill pipe connection. Therefore, there are several time periods in a drilling operation were the well is at static conditions, and hence simulating fracturing at static conditions are very reasonable.

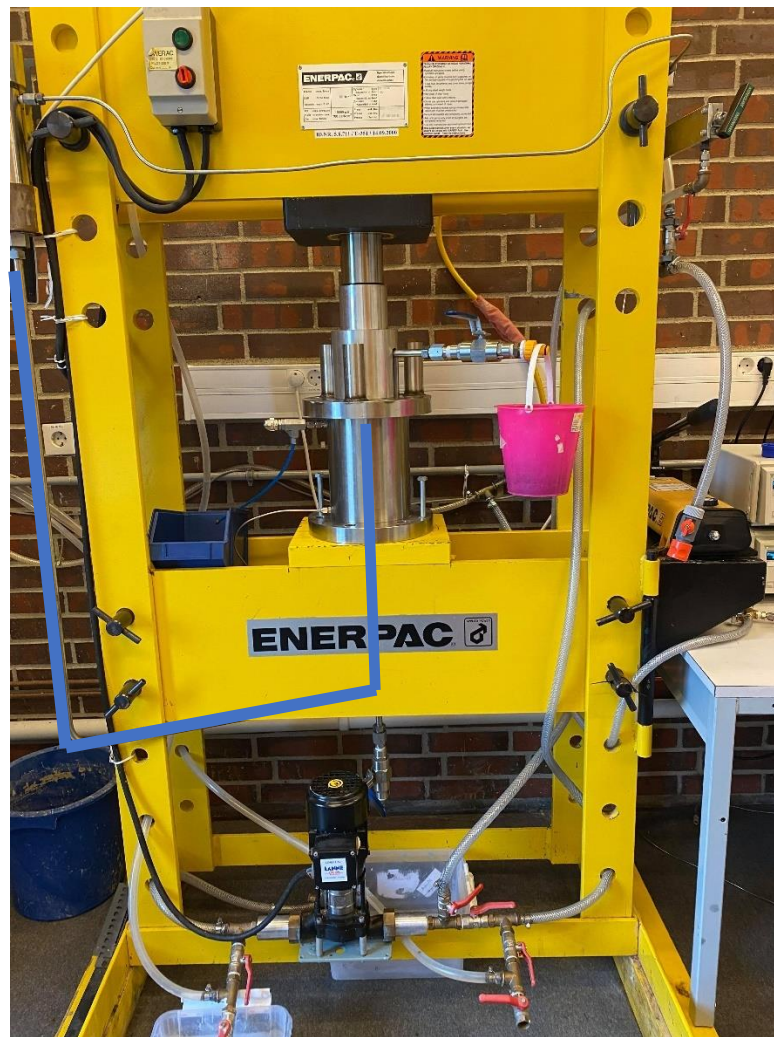


Figure 4.7: Enerpac hydraulic fracturing experimental setup.

4.3 Laboratory drilling fluid formulation

This subsection presents the drilling fluid formulation for the sodium, potassium, sodium/potassium, and cesium/potassium laboratory drill-in fluids. It describes the mixing steps, mixed chemicals, mixing method and time for all the fluid systems.

4.3.1 Na-formate drilling fluid formulation

4.3.1.1 Na-formate mixing method and time

The sodium formate drill-in fluid formulated in this thesis were mixed and characterized at the University of Stavanger. It is based on the Martin Linge formulation from table 2.1 [12]. Table 4.1 presents the Na-formate fluid system with chemicals and additional mixing steps, mixing method and time. The fluid system was mixed in the following steps and consists of water

(H₂O), 45 weight% Na-formate, starch, xanthan gum and micron sized CaCO₃. This represents the Na-formate fluid system without nanoparticles.

Steps	Chemical	Mixing method	Mixing time
1A.	H ₂ O	-	7-8 minutes
1B.	45 weight% Na ⁺ formate	Stirred manually with spoon into water until uniform distributed	
2.	Starch	Stirred manually with spoon into brine until uniform distributed, and mixed at medium speed	
3.	Xanthan Gum In-situ	Mixed at medium speed	
Add defoamer (as required)			
4.	CaCO ₃	Mixed at high speed	10 minutes
Add defoamer (as required)			
5.	Xanthan Gum Ex-situ	Mixed at medium speed	2 minutes

Table 4.1: Na-formate fluid system with mixing steps, mixed chemicals, mixing method and time.

A Mettler Toledo precision weight were used to accurately achieve the desired weights of the different materials added to the chemical composition. Firstly, Na-formate were added to water and rotated with a spoon to achieve a uniform distribution of solid salt particles in water. Starch were then added to the brine and the fluid system were rotated with a spoon and mixed at medium speed to maintain the distribution homogeneous. Xanthan gum were then carefully added in-situ to avoid flocculation and mixed at medium speed using a Hamilton Beach mixer. Medium mixing speed were chosen because some fluid can spill out of the cup under high rotations. This is because the fluid is too little viscous at this mixing step. Another reason for medium mixing speed is for the starch to dissolve and react with the polymer in the fluid system. The mixing time for these steps are not time dependent to achieve a homogeneous blend. However, the mixing time for this process were approximately 7-8 minutes. 5-6 droplets of defoamer were carefully added by pipette to reduce amount of air in the fluid system. CaCO₃ were then added and mixed at high speed for 10 min to maintain a uniform distribution. At this point in time, the fluid was viscous enough to deal with high speed mixing without spilling out

of the cup. The purpose of mixing CaCO₃ at high speed for 10 minutes is therefore only to mix it well into a uniform fluid system. After mixing step no. 4, 5-6 droplets of defoamer were again added to the fluid system. The total amount of defoamer droplets added to the system is as required to reduce air. Finally, xanthan gum was carefully added ex-situ and mixed at medium speed for 2 min. This were done to avoid breaking the bonding's in the polymer structure. The decision to proceed with the in-situ/ex-situ polymer treatment is to easily control the total polymer concentration added to the system after the system is already in-situ mixed. Subsection 5.1 presents the ex-situ polymer treatment after the fluid system was mixed in-situ. The system was then added more polymers ex-situ to reduce the filtrate loss to acceptable values, hence the ex-situ polymer procedure is more like a controllable parameter if the results indicate high filtrate loss.

All the fluid systems created foam in the system after CaCO₃ were mixed into the system. The reason for this perhaps originates from hydrolysis, were CaCO₃ particles reacts with water (i.e., H₂O) and separates the CaCO₃ molecule into other molecules. The chemical reaction could for example be described from the following equation: $\text{CaCO}_3 + \text{H}_2\text{O} \rightarrow \text{CO}_2 + \text{H}_2 + \text{other elements}$, were carbon dioxide and hydrogen are gas molecules. Still, the air was removed by adding defoamer.

CMC polymers has a higher ability to establish clumps in the system (i.e., create polymer balls), and hence not create a uniform distributed fluid system. Therefore, xanthan gum was chosen as polymer additive for all the fluid systems to avoid this issue.

4.3.1.2 Test design 1: Effect of CaCO₃ particle size in Na-formate drill-in fluid

The aim for test design 1 was to investigate the best performing CaCO₃ particle size. 25g CaCO₃ particle concentration were used for the analysis. CaCO₃ type 2 were chosen, and 3 particle size ranges were selected: <63 microns, 71-90 microns and 0-<355 microns (whole CaCO₃ spectrum). The <63 microns size are according to Martin Linge in section 2.1.5. The mixing method and time for test design 1 is presented in section 4.3.1.1. Table 4.2 presents the fluid composition for test design 1, were the CaCO₃ type 2 particle size is the varying component while others remain constant.

Chemical	Fluid 1	Fluid 2	Fluid 3
H ₂ O [g]	250	250	250
45wt% Na ⁺ formate [g]	250	250	250
Starch [g]	7.9	7.9	7.9
Xanthan Gum [g] In-situ	0.79	0.79	0.79
CaCO ₃ type 2 [g]	25 (<63 microns)	25 (71-90 microns)	25 (0-<355 microns)
Xanthan Gum [g] Ex-situ	0.6	0.6	0.6

Table 4.2: Composition for the Na-formate test design 1 with <63, 71-90 and 0-<355 microns CaCO₃ particle sizes.

4.3.1.3 Test design 2: Effect of CaCO₃ particle concentration in Na-formate drill-in fluid

The aim for test design 2 was to analyze how different CaCO₃ LCM concentrations behave in sodium formate fluid systems. Based on the results from test design 1 in section 5.1, <63-micron CaCO₃ particle size was selected. The total concentration of xanthan gum polymer was reduced to achieve filtrate loss values closer to 10 ml and the polymers were mixed in-situ. A further analysis of the effect of polymer concentration in Na-formate fluid is presented in test design 3. CaCO₃ type 1 was used to increase the particle concentration in the fluid system. This decision was based on that the UIS lab ran out of type 2 CaCO₃ and a large amount of CaCO₃ type 1 were available at the UIS lab. Table 4.3 presents the fluid composition for test design 2, where CaCO₃ type 1 particle concentration is the varying component while others remain constant.

Chemical	Fluid 1	Fluid 2	Fluid 3
H ₂ O [g]	250	250	250
45wt% Na ⁺ formate [g]	250	250	250
Starch [g]	7.9	7.9	7.9
Xanthan Gum [g] In-situ	0.79 + 0.4	0.79 + 0.4	0.79 + 0.4
CaCO ₃ type 1 [g]	25 (<63 microns)	45 (<63 microns)	65 (<63 microns)

Table 4.3: Composition for Na-formate test design 2 with increased CaCO₃ particle concentration.

4.3.1.4 Test design 3: Effect of polymer concentration in Na-formate drill-in fluid

The aim for test design 3 was to observe the effect of polymer concentration. The 45g particle concentration was selected for the study based on that a 45g fluid had already been made from subsection 4.3.1.3. The decision-making was based on to save the amount of CaCO₃ type 1 at the lab for further test designs, hence the 65g were not selected. The 25g from subsection 4.3.1.3 was selected for test design 4. The xanthan gum polymers in test design 3 were treated 0.79 + 0.4 in-situ mixed for fluid 1, and 0.79 + 0.6 in-situ mixed for fluid 2. Table 4.4 presents the fluid composition for test design 3, were xanthan gum polymer concentration is the varying component while others remain constant.

Chemical	Fluid 1	Fluid 2
H ₂ O [g]	250	250
45wt% Na ⁺ formate [g]	250	250
Starch [g]	7.9	7.9
Xanthan Gum [g] In-situ	0.79 + 0.4	0.79 + 0.6
CaCO ₃ type 1 [g]	45 (<63 microns)	45 (<63 microns)

Table 4.4: Composition for Na-formate test design 3 with increased polymer concentration.

4.3.1.5 Test design 4: Comparison between CaCO₃ type 1 and CaCO₃ type 2 in Na-formate drill-in fluid

The aim for test design 4 was to investigate which particle type that could be used for the cesium/potassium brine. The 25g particle concentration was selected to save the amount of CaCO₃ (25g type 1 CaCO₃ had already been made from section 4.3.1.3). Xanthan gum polymers were treated 0.79 + 0.4 in-situ. This was based on that the already made 25g type 1 CaCO₃ had 0.79 + 0.4 in-situ XG polymer treatment, and hence for comparison reasons the XG polymers had to be treated the same way. Table 4.5 presents the fluid composition for test design 4, were CaCO₃ particle type is the varying component while others remain constant.

Chemical	Fluid 1	Fluid 2
H ₂ O [g]	250	250
45wt% Na ⁺ formate [g]	250	250
Starch [g]	7.9	7.9
Xanthan Gum [g] In-situ	0.79 + 0.4	0.79 + 0.4
CaCO ₃ type 1 [g]	25 (<63 microns)	0
CaCO ₃ type 2 [g]	0	25 (<63 microns)

Table 4.5: Composition for Na-formate test design 4 with CaCO₃ type 1 and CaCO₃ type 2 comparison.

4.3.2 K-formate drilling fluid formulation

4.3.2.1 Test design 5: Effect of CaCO₃ particle concentration in K-formate drill-in fluid

The aim for test design 5 was to observe how increased amount of CaCO₃ particle concentration performed in potassium formate drill-in fluid. It has the same mixing method and time as the reference fluid system presented in section 4.3.1.1. However, 250 gram of 45 weight% Na formate is substituted with 250 gram of 45 weight% K formate, while the other components remain constant. The polymer treatment is mixed in-situ and ex-situ, and the <63 microns sized CaCO₃ were selected based on the results in section 5.1. The mud composition for the potassium formate drill-in fluid systems based on increased type 1 CaCO₃ concentrations is presented in table 4.6.

Chemical	Fluid 1	Fluid 2	Fluid 3
H ₂ O [g]	250	250	250
45wt% K ⁺ formate [g]	250	250	250
Starch [g]	7.9	7.9	7.9
Xanthan Gum [g] In-situ	0.79	0.79	0.79
CaCO ₃ type 1 [g]	25 (<63 micron)	45 (<63 micron)	65 (<63 micron)
Xanthan Gum [g] Ex-situ	0.4	0.4	0.4

Table 4.6: Composition for K-formate test design 5 with increased CaCO₃ particle concentration.

4.3.3 Nano-based Na and K-formate drilling fluid formulation

4.3.3.1 Nano-based K-formate mixing method and time

Table 4.7 presents the nano-based K-formate fluid system with chemicals and additional mixing steps, mixing method and time. The fluid system was mixed in the following steps in-situ: water (H₂O), 45 weight% K-formate, starch, nano sized CaCO₃, xanthan gum and <63 microns sized CaCO₃. The nanoparticles were dispersed in water (50nm, 40wt%). This subsection in addition represents the mixing method and time for the nano-based Na-formate fluid system, as 45wt% Na-formate is substituted with 45wt% K-formate in step 1B.

Steps	Chemical	Mixing method	Mixing time
1A.	H ₂ O	-	7-8 minutes (as required)
1B.	45 weight% K ⁺ formate	Stirred manually with spoon into water until uniform distributed	
2.	Starch	Stirred manually with spoon into brine until uniform distributed, and mixed at medium speed	
3.	Nano CaCO ₃	Mixed at low speed	
4.	Xanthan Gum in-situ	Mixed at medium speed	
Add defoamer (as required)			
5.	CaCO ₃	Mixed at high speed	10 minutes
Add defoamer (as required)			
6.	Xanthan Gum Ex-situ	Mixed at medium speed	2 minutes

Table 4.7: Nano-based K-formate fluid system with mixing steps, mixed chemicals, mixing method and time.

45wt% K-formate were first added to water and rotated with a spoon to uniformly distribute the solid salt particles in water. Starch were then added to the brine. The brine solution with starch were firstly rotated with a spoon and secondly mixed at medium speed with the Hamilton beach mixer. This was performed to maintain a homogeneous distribution. The fluid system consisted of some air bubbles after starch mix. This could be surfactants. There was no buoyancy from the brine solution, hence the starch bits could easily dissolve into water without any additional mechanical mix. Therefore, the sonicate vibration cell was not applied.

It was observed that the sodium formate created more air compared to the potassium formate in the mix process. However, the addition of CaCO₃ NP's reduced the amount of air in the system compared to the sodium systems without nanoparticles, before defoamer were added as required. The reason for this perhaps originates from the LCM theory that nanosized CaCO₃ additives may plug the open pore spaces in the micron sized CaCO₃ systems, and hence the originally open cross-sectional area for air bubbles to form in Na-formate mud is reduced. Consequently, less foam is created. Still, the amount of air was removed by adding defoamer as required.

4.3.3.2 Test design 6: Effect of CaCO₃ NP's in K-formate drill-in fluid

The aim for test design 6 was to investigate how CaCO₃ nanoparticles performed in potassium formate drill-in fluids. The mixing method and time is according to subsection 4.3.3.1. CaCO₃ type 1 was chosen because we ran out of type 2 CaCO₃ in test design 4. Less than 63 microns particle size was chosen from test design 1 results, in addition to see how CaCO₃ NP's could plug the open pore spaces in <63 microns sized CaCO₃. The nanosized CaCO₃ particles were added as 1wt%, 2.05wt% and 3wt% following fluid 1 from the K-formate reference system in test design 5 that was already made. The polymers were mixed in-situ/ex-situ. The mud composition for the CaCO₃ nanoparticle-based potassium systems is presented in table 4.8.

Chemical	REF	REF + 1wt% NP	REF + 2.05wt% NP	REF + 3wt% NP
H ₂ O [g]	250	250	250	250
45wt% K ⁺ formate [g]	250	250	250	250
Starch [g]	7.9	7.9	7.9	7.9
Nano CaCO ₃ [g]	0	5.3	11.0	16.0
Xanthan Gum [g] In-situ	0.79	0.79	0.79	0.79
CaCO ₃ type 1 [g]	25 (<63 micron)	25 (<63 micron)	25 (<63 micron)	25 (<63 micron)
Xanthan Gum [g] Ex-situ	0.4	0.4	0.4	0.4

Table 4.8: Composition for nano-based K-formate in test design 6.

4.3.3.3 Test design 7: Effect of CaCO₃ NP's in Na-formate drill-in fluid

The aim for test design 7 was to investigate how CaCO₃ nanoparticles performed in sodium formate drill-in fluids. The mixing method and time is according to subsection 4.3.3.1. However, 45wt% Na-formate is substituted with 45wt% K-formate in mixing step 1B. Nanosized CaCO₃ particles were added as 1wt%, 2wt% and 3wt% and the XG polymers were mixed in-situ/ex-situ. The mud composition for the NP based Na-formate drill-in fluid systems is presented in table 4.9.

Chemical	REF	REF + 1wt% NP	REF + 2wt % NP	REF + 3wt % NP
H ₂ O [g]	250	250	250	250
45wt% Na ⁺ formate [g]	250	250	250	250
Starch [g]	7.9	7.9	7.9	7.9
Nano CaCO ₃ [g]	0	5.3	10.7	16.0
Xanthan Gum [g] In-situ	0.79	0.79	0.79	0.79
CaCO ₃ type 1 [g]	25 (<63 micron)	25 (<63 micron)	25 (<63 micron)	25 (<63 micron)
Xanthan Gum [g] Ex-situ	0.4	0.4	0.4	0.4

Table 4.9: Composition for the nano-based Na-formate systems in test design 7.

4.3.4 Na/K-formate drilling fluid formulation

4.3.4.1 Na/K ratios mixing method and time

The sodium/potassium ratios were blended and mixed at University of Stavanger. Table 4.10 presents the Na/K fluid system with chemicals and additional mixing steps, mixing method and time. The fluid system was mixed in the following steps in-situ: water (H₂O), 45 weight% Na-formate, 45 weight% K-formate, starch, xanthan gum and 63-71 microns sized type 1 CaCO₃.

Steps	Chemical	Mixing method	Mixing time
1A.	H ₂ O	-	7-8 minutes (as required)
1B.	45 weight% Na ⁺ formate	-	
1C.	45 weight% K ⁺ formate	Stirred manually with spoon into water until uniform distributed	
2.	Starch	Stirred manually with spoon into brine until uniform distributed, and mixed at medium speed	
3.	Xanthan Gum in-situ	Mixed at medium speed	
Add defoamer (as required)			
4.	CaCO ₃	Mixed at high speed	10 minutes
Add defoamer (as required)			
5.	Xanthan Gum ex-situ	Mixed at medium speed	2 minutes

Table 4.10: sodium/potassium fluid system with mixing steps, mixed chemicals, mixing method and time.

45wt% Na-formate and 45wt% K-formate were added to water and rotated with a spoon to uniformly distribute the solid salt particles in water. Starch were then added to the brine, rotated with a spoon and hence the fluid system was mixed at medium speed at the Hamilton Beach mixer. The xanthan gum was added in small amounts to prevent polymer balls in the system while mixing at medium speed. Some air bubbles were visible after mixing. To reduce the amount of air in the Na/K fluid system, 5-6 droplets of antifoam were added as required. All the CaCO₃ particles were added at the same time and mixed at high speed for 10 minutes. Another 2-3 droplets of antifoam were added after CaCO₃ mixing to prevent air bubbles, as required. Finally, xanthan gum was carefully added ex-situ and mixed at medium speed for 2 minutes. The mixing procedure was the same for all Na/K ratios.

4.3.4.2 Test design 8: Effect of Na/K ratios

The aim for test design 8 was to investigate how sodium and potassium chemically interacts together. As seen from table 4.11, the Na/K blending ratios is based on percentage (i.e., 50% sodium formate/ 50% potassium formate etc.). It was chosen to start with increase in percentage

of sodium formate (i.e., 60%, 70%), because the sodium formate brine is cheaper than potassium brine. 63-71 microns of CaCO₃ type 1 was chosen to save the amount of <63 microns type 1 CaCO₃ particle size for the cesium/potassium brine. The xanthan gum polymers added in-situ/ex-situ. The mud composition for the Na/K ratios is presented in table 4.11.

Chemicals	Na/K 50/50	Na/K 60/40	Na/K 70/30
H ₂ O [g]	250	250	250
45wt% Na ⁺ formate [g]	125	150	175
45wt% K ⁺ formate [g]	125	100	75
Starch [g]	7.9	7.9	7.9
Xanthan Gum [g] in-situ	0.79	0.79	0.79
CaCO ₃ type 1 [g]	25 (63-71 micron)	25 (63-71 micron)	25 (63-71 micron)
Xanthan Gum [g] ex-situ	0.4	0.4	0.4

Table 4.11: Composition for the Na/K ratios in test design 8.

4.3.5 Cs/K-formate drilling fluid formulation

4.3.5.1 Cs/K mixing method and time

The cesium/potassium brine received from the industry were modified and characterized at the University of Stavanger. Table 4.12 presents the drilling fluid formulation for the cesium/potassium fluid system.

Steps	Chemical	Mixing method	Mixing time
1.	Cs/K/water (Sinomine)	-	Sonicate starch into brine for 30 min (as required)
2.	Starch	Stirred manually with spoon and sonicated	
3.	Xanthan gum in-situ	Mixed at medium speed	2-3 min (as required)
Add defoamer (as required)			
4.	CaCO ₃	Mixed at high speed	10 min
Add defoamer (as required)			

Table 4.12: Cs/K-formate fluid system with mixing steps, mixed chemicals, mixing method and time.

A specific amount of brine from the Sinomine jug were taken out and put into a mix cup. Hence the starch was added into the brine. The starch bits did not dissolve well when manually stirred with a spoon because the Sinomine brine was heavily concentrated. It was then decided to sonicate the starch into the brine, to break the surface tension with application of ultrasonic waves from the vibrational cell. Elapsed time for the 1st round of pulsating waves was 8 minutes. The starch particles had now dissolved better into the Sinomine, but not 100%. Hence a 2nd round of pulsating waves from the sonicate were applied. Elapsed time for the 2nd wave was 22 minutes. This was enforced to be completely sure that the starch bits had dissolved 100% into the brine solution. The xanthan gum polymers were added carefully and mixed at medium speed for approximately 2-3 minutes, to avoid polymer balls. Antifoam were added as required. The CaCO₃ particles were finally added and mixed at high speed for 10 minutes to create a uniform distributed cesium/potassium system.

4.3.5.2 Test design 9: Characterization of modified Cs/K drill-in fluid

The aim for test design 9 was to modify the Sinomine fluid to a drill-in reservoir fluid applicable for hydraulic fracturing. The fluid design was based on the mud components from the Martin Linge paper in table 2.1 [12]. In contrast to the weight percentages of cesium and potassium added at Martin Linge, the Sinomine blending ratio between cesium, potassium, and water is unknown. It was then decided to design 2 separate fluids; one mud based on mass scaling and another mud based on volume scaled components. The density is known and equals 2.0 specific gravity for the Sinomine brine.

From table 4.13, the high viscous Cs/K fluid is based on mass scaled components, and the less viscous Cs/K is based on volume scaled components. It was decided to use 350 ml, which equals 700g in the Sinomine, to make enough mud to perform all the fluid characterization tests (i.e., density, API filtrate loss, viscometer, and rheometer).

The calculation procedure is based on that the Martin Linge “brine” equals 500g for the mass scaled and 460 ml for the volume scaled Cs/K, since the weight percentages from table 2.1 is not defined. However, the Martin Linge starch and xanthan gum components equals 7.9g and 0.79g respectively. It was decided to use 45g CaCO₃ for the high viscous Cs/K, and 50g CaCO₃ for the less viscous Cs/K according to Martin Linge. Both the 11- and 24-microns particle sized CaCO₃ from table 2.1 are within the <63 microns particle spectrum applied. The mud

components in table 4.13 are hence calculated from the brine ratio of Martin Linge and Sinomine for the high viscous Cs/K and less viscous Cs/K respectively.

In addition, a leftover mud of the high viscous and less viscous Cs/K were designed. This design was based on measuring the total height of a cylindrical plastic cup, hence measure half of the total height containing high viscous Cs/K, and half of the total height containing less viscous Cs/K and add them together. Thus, the leftover Cs/K fluid system is referred to as the 50/50 Cs/K ratio. However, the leftover mud is precisely blended in a 1:1 ratio.

For particle stability analysis in Cs/K drill-in fluids, another leftover mud was made based on percentage mud mix, between 2/3 of the 100% less viscous Cs/K + 1/3 of the 100% high viscous Cs/K. The mud was taken out of both samples by a syringe spray. The 2/3 + 1/3 Cs/K mix were blended 14 ml of the 100% high viscous Cs/K and 28 ml of the 100% less viscous Cs/K which equals 42 ml total mud mix.

Chemicals	High viscous Cs/K	Less viscous Cs/K	50/50 Cs/K ratio	2/3 + 1/3 Cs/K mix
Cs/K/water (Sino)	700 [g]	350 [ml]	Less viscous + High viscous (1:1) Cs/K mud mix	2/3 less viscous + 1/3 High viscous Cs/K mud mix
Starch	11 [g]	5.97 [g]		
Xanthan gum in-situ	1.1 [g]	0.6 [g]		
CaCO ₃ type 1	63 (<63 microns) [g]	38.04 (<63 microns) [g]		

Table 4.13: Mud composition for the high viscous Cs/K and less viscous Cs/K drill in fluids.

4.3.5.3 Test design 10: Hydraulic fracturing of Cs/K drill-in fluid

The aim for test design 10 was to characterize Cs/K brine-based drill-in fluids on hydraulic fracturing. Hence it was designed one base mud without LCM, and one design mud with LCM. The mud composition was based on the 100% less viscous Cs/K from test design 9 in section 4.3.5.2.

The 100% less viscous Cs/K mud were blended with a new less viscous Cs/K made for the particle stability test in section 5.9.5, aged for 2 days + the new less viscous Cs/K aged for 1

day. These two muds were blended and referred to as the “light viscous Cs/K” for hydraulic fracturing. This is the base mud in the hydraulic fracturing experiments. The mud was designed based on the same composition and mixing method and time according to section 4.3.5.1 and 4.3.5.2, for the less viscous Cs/K fluid system. The light viscous Cs/K drill-in fluid were applied for hydraulic fracturing since the 100% less viscous Cs/K (i.e., same composition) fluid could possess penetrating characteristics (higher filtrate loss).

In addition, a design mud was made based on the same mud composition as the Cs/K base mud, with quartz particles as wellbore strength material. The quartz particles were mass scaled as 2 weight% of the total mud composition and added ex-situ after 3 days ageing at static conditions. LCM were added 0.5% from the 100-150 microns and 1.5% from the 150-250 microns from the quartz particle spectrum. This decision was justified based on that the 100 microns may plug the 250 microns quartz open pore spaces thus provide wellbore strengthening effect. The mud composition for the Cs/K base and Cs/K design mud for hydraulic fracturing performance is presented in table 4.14.

Chemicals	Base mud	Design mud
Cs/K/water (Sino)	350 [ml]	350 [ml]
Starch	5.97 [g]	5.97 [g]
Xanthan gum in-situ	0.6 [g]	0.6 [g]
CaCO ₃ type 1	38.04 (<63 microns) [g]	38.04 (<63 microns) [g]
2 weight% Quartz ex-situ	0	13.6 [g]

Table 4.14: Mud composition for the Cs/K base mud and Cs/K design mud for hydraulic fracturing.

5 Results and discussion

This section presents all the results in this thesis obtained from the experimental work in section 4. The viscometer measurements were performed at 20, 50 and 80°C for all the sodium and potassium fluid systems. Test design 1-8 is based on micron sized (i.e., <63 microns and 63-71 microns) CaCO₃ LCM concentration and CaCO₃ nanoparticle performance in sodium, potassium, and sodium/potassium formate blended drill-in fluids. Test design 9-10 presents the results obtained for the cesium/potassium formate mixed fluids characterization and hydraulic fracturing performance.

5.1 Test design 1: Effect of CaCO₃ particle size in Na-formate drill-in fluid

This subsection presents the results obtained from the laboratory designed sodium formate drill-in fluid formulation in section 4.3.1.2.

5.1.1 Effect of CaCO₃ particle size on polymer mix and filtration properties

Initially, 0.79g XG in-situ polymer treatment were used according to the Martin Linge scaling. The API static filtrate loss test was performed as described in section 4.2.2. From figure 5.1, the results showed that the fluid system with in-situ treatment exhibited 7.5 min filtrate loss at 18.5, 20.5 and 21.5 ml, for the <63, 71-90 and 0-<355 microns sized type 2 CaCO₃ respectively.

The fluid system was then additionally treated with 0.6g XG ex-situ. This resulted in more filtrate control and can be observed from figure 5.1. The 7.5 min filtrate loss reduced to 6, 6.25 and 7.25 ml for the <63, 71-90 and 0-<355 microns sized fluid systems. This indicates that larger CaCO₃ particle sizes in microns provides penetrating fluid properties. By adding more polymer to the fluid composition one can obtain reduced filtrate loss. For both in-situ and in-situ + ex-situ polymer treatment, the filtrate loss increased by increase in CaCO₃ particle size in microns.

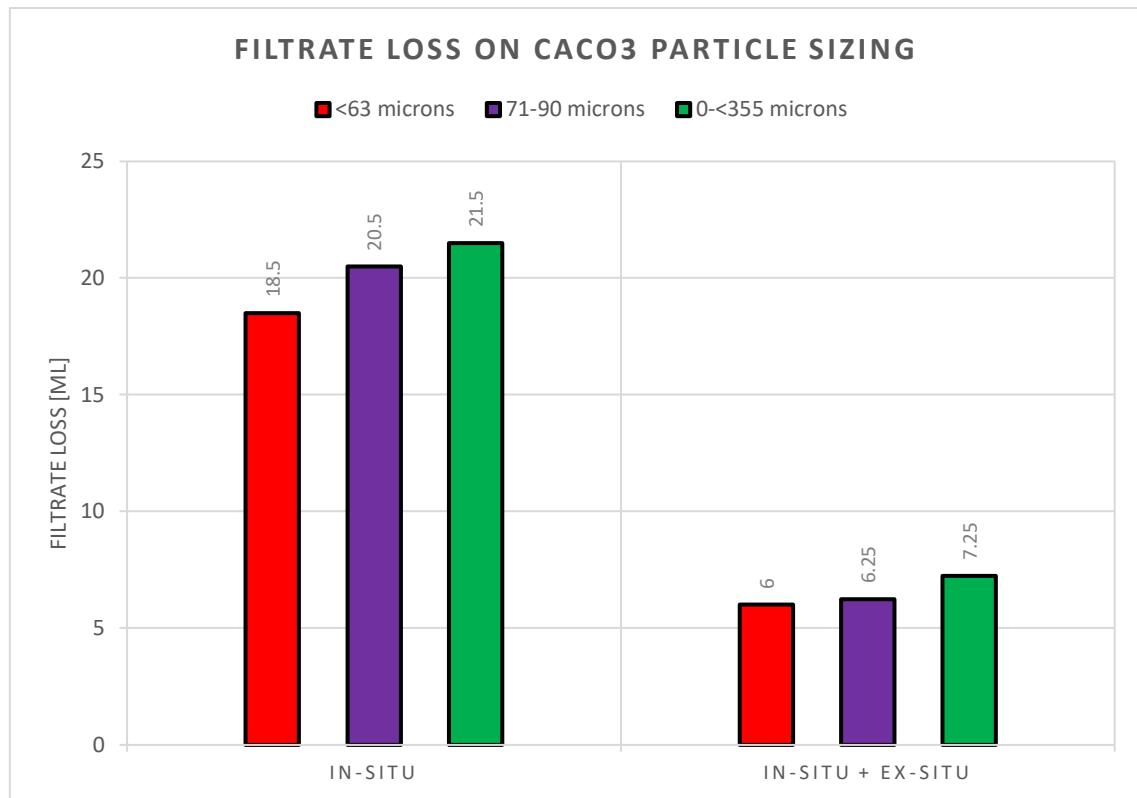


Figure 5.1: API Filtrate loss for <63, 71-90 and 0-<355 microns with in-situ vs. in-situ + ex-situ polymer treatment.

5.1.2 Effect of CaCO₃ particle size on rheological properties

The rheology was measured after 0.79g XG in-situ + 0.6g XG ex-situ polymer treatment as presented in section 5.1.1. The viscometer data were measured according to the test procedure in section 4.2.3.

Figure 5.2 presents the rheology for the <63, 71-90 and 0-<355 microns CaCO₃ particle sizes at ambient conditions. The results show that different CaCO₃ sizes in microns does not show any significant impact on the viscometer responses, and hence behaves approximately equal for all rpms. However, the 0-<355 microns size occurs with a higher max shear stress value compared to the other fluid systems. Still, the deviation is minimal between the <63, 71-90 and 0-<355 microns particle sizes.

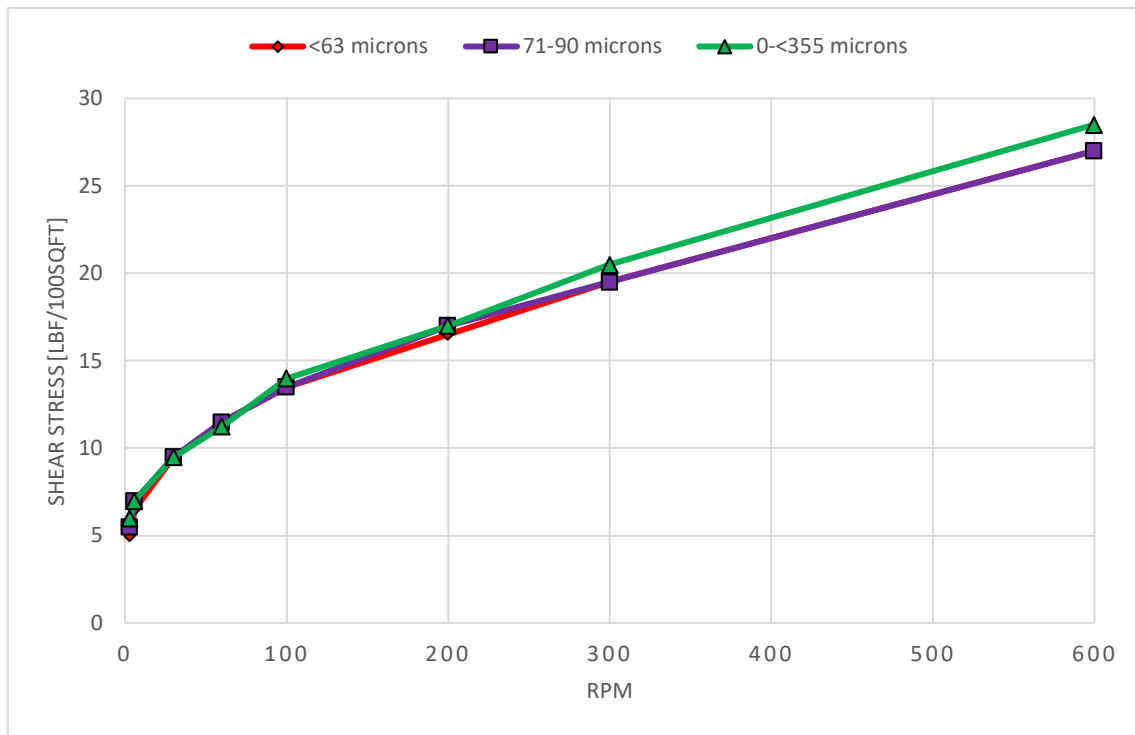


Figure 5.2: Shear stress on rpm for <63, 71-90 and 0-<355-micron sized CaCO₃ at 20°C.

The viscometer responses at 50°C does not express any significant impact on the rheology. Hence the shear stress values are roughly equal for the <63, 71-90 and 0-<355 microns CaCO₃ particle size. Figure 5.3 presents shear stress of the different CaCO₃ particle size spectrum fluid systems.

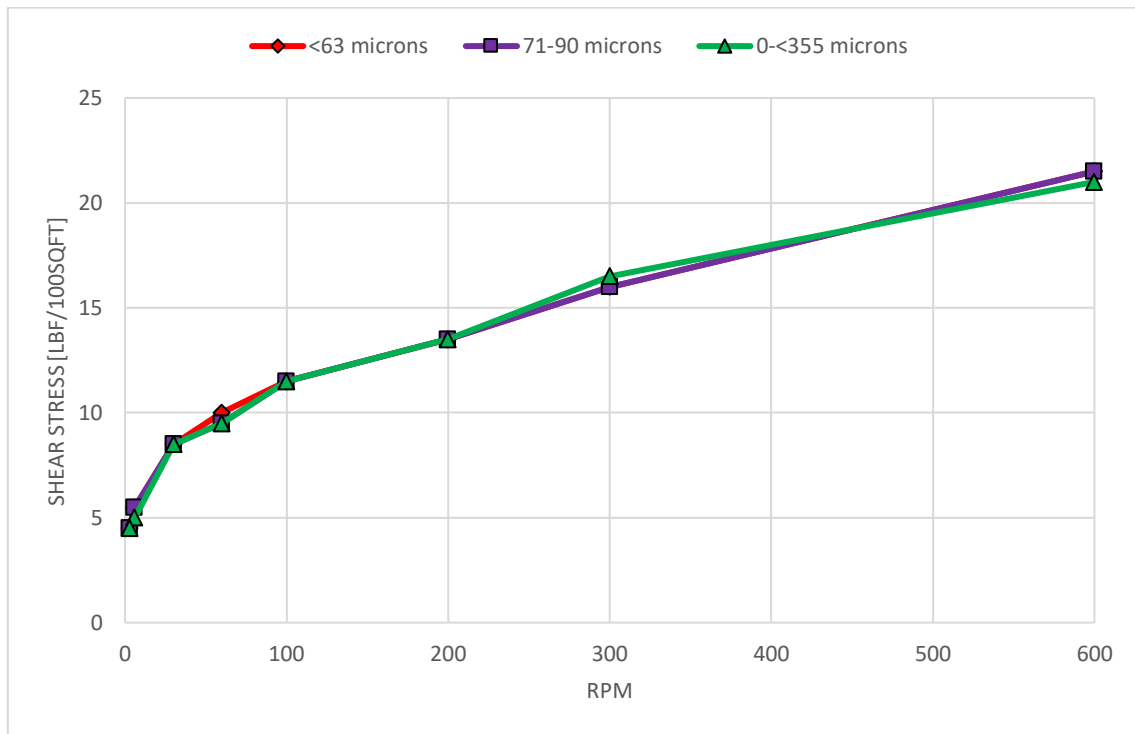


Figure 5.3: Shear stress on rpm for <63, 71-90 and 0-<355-micron sized CaCO₃ at 50°C.

The rheology increases from 50°C to 80°C for all CaCO₃ particles sizes in Na-formate drill-in fluid. However, the viscometer responses exhibit relatively the same rheology for the <63, 71-90 and 0-<355 microns particle sizes. Figure 5.4 presents the viscometer response for the <63, 71-90 and 0-<355 microns from the CaCO₃ particle spectrum in figure 5.4.

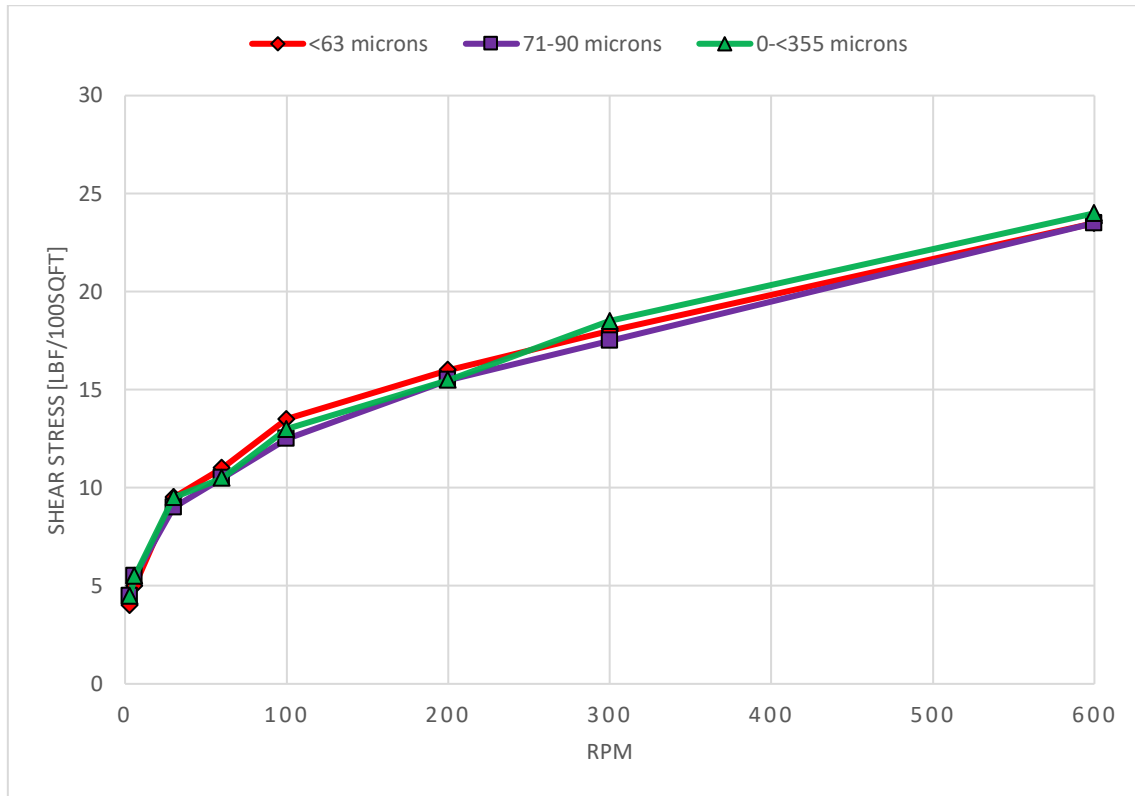


Figure 5.4: Shear stress on rpm for <63, 71-90 and 0-<355-micron sized CaCO₃ at 80°C.

The fluid systems have a Non-Newtonian fluid behavior since the apparent viscosity is not constant and both the <63, 71-90 and 0-<355 microns CaCO₃ systems acts shear-thinning with a lower shear rate yield stress > 0. However, there is a trend that both the plastic viscosity and Bingham yield stress decreases from room temperature down to 50°C and hence increases up to 80°C for nearly all the fluid systems. The <63 microns plastic viscosity at 50°C and 80°C is equal at 5.5 centipoise and therefore behaves more thermal stable compared to the other systems. Still, the deviation in other rheological parameters like flow and consistency index is insignificant. This could be since the fluids mainly consist of Na-brine with light atomic weight, hence the different sizes of CaCO₃ does not have any chemical but mechanical interaction with the other mud components in the system. The rheological parameters for the <63, 71-90 and 0-<355 microns are presented in table 5.1.

Rheological parameters	<63 microns			71-90 microns			0-<355 microns		
	20°C	50°C	80°C	20°C	50°C	80°C	20°C	50°C	80°C
AV [cP]	13.5	10.75	11.75	13.5	10.75	11.75	14.25	10.5	12
PV [cP]	7.5	5.5	5.5	7.5	5.5	6	8	4.5	5.5
YS [lbf/100sqft]	12	10.5	12.5	12	10.5	11.5	12.5	12	13
LSYS [lbf/100sqft]	3.5	3.5	3	4	3.5	3.5	5	4	3.5
n	0.469	0.426	0.348	0.469	0.426	0.425	0.475	0.348	0.375
k [lbf ⁿ /100sqft]	1.05	1.12	1.64	1.05	1.12	1.24	1.06	1.89	1.78

Table 5.1: Rheological parameters for the <63, 71-90 and 0-<355-micron sized CaCO₃ at 20, 50 and 80°C.

5.1.3 Effect of CaCO₃ particle size on viscoelastic properties

5.1.3.1 Effect of CaCO₃ particle size on amplitude sweep

From table 5.2, the most important parameters obtained from the amplitude sweep tests is summarized. The fluid systems containing <63 and 71-90 microns occur with the same LVE range at 37.3%. This could be since the polymer structures in these fluids are elongated in contrast to the 0-<355 CaCO₃ particle size, hence the LVE range is increased. However, the yield stress for the 71-90 microns is 0.04 pascals higher compared to the <63 microns particle sizes, and hence stay longer in the elastic range. The flow point for the 71-90 microns occurs at 4.77 pascals compared to 4.08 pascals for the <63 microns. For the 0-<355 microns CaCO₃ particles range, the strain limit is 19.3%, and the fluid system occurs the lowest yield point at 0.99 Pa. However, the fluid system performs the largest transition zone from 0.99 to the flow point at 4.84 Pa respectively, compared to the <63 and 71-90 microns fluid systems. Hence the <63 and 71-90 microns are less affected to material deformation compared to the 0-<355 microns sized CaCO₃.

Fluid systems	Strain, γ_L [%]	Yield point, τ_y [Pa]	Flow point, τ_f [Pa]
<63 microns	37.3	1.79	4.08
71-90 microns	37.3	1.83	4.77
0-<355 microns	19.3	0.99	4.84

Table 5.2: Important parameters obtained from the amplitude sweeps for <63, 71-90 and 0-<355-micron sized CaCO_3 .

5.2 Test design 2: Effect of CaCO_3 particle concentration in Na-formate drill-in fluid

This subsection presents the results obtained from the sodium formate drill-in fluid formulation in section 4.3.1.3. The CaCO_3 particle size selected for this test design is <63 micron since this particle size exhibited the lowest filtrate loss independent of polymer treatment, more thermal stable at rheological properties and less affect by material deformation from the amplitude sweeps tests. The aim for test design 2 is to study the effect of CaCO_3 LCM particle concentration on filtration, rheological and viscoelastic properties.

5.2.1 Effect of CaCO_3 particle concentration on filtration properties

The fluid systems were treated with in-situ polymer treatment as presented in section 4.3.1.3. From figure 5.5, the results showed that the fluid systems exhibited 7.5 min filtrate loss at 8.0, 8.5 and 11.5 ml, for the 25g, 45g and 65g particle concentrations respectively. These results show that increase in CaCO_3 particle concentration increase the API static filtrate loss in sodium drill-in fluid systems, hence the results show that larger CaCO_3 particle concentrations provides penetrating fluid characteristics.

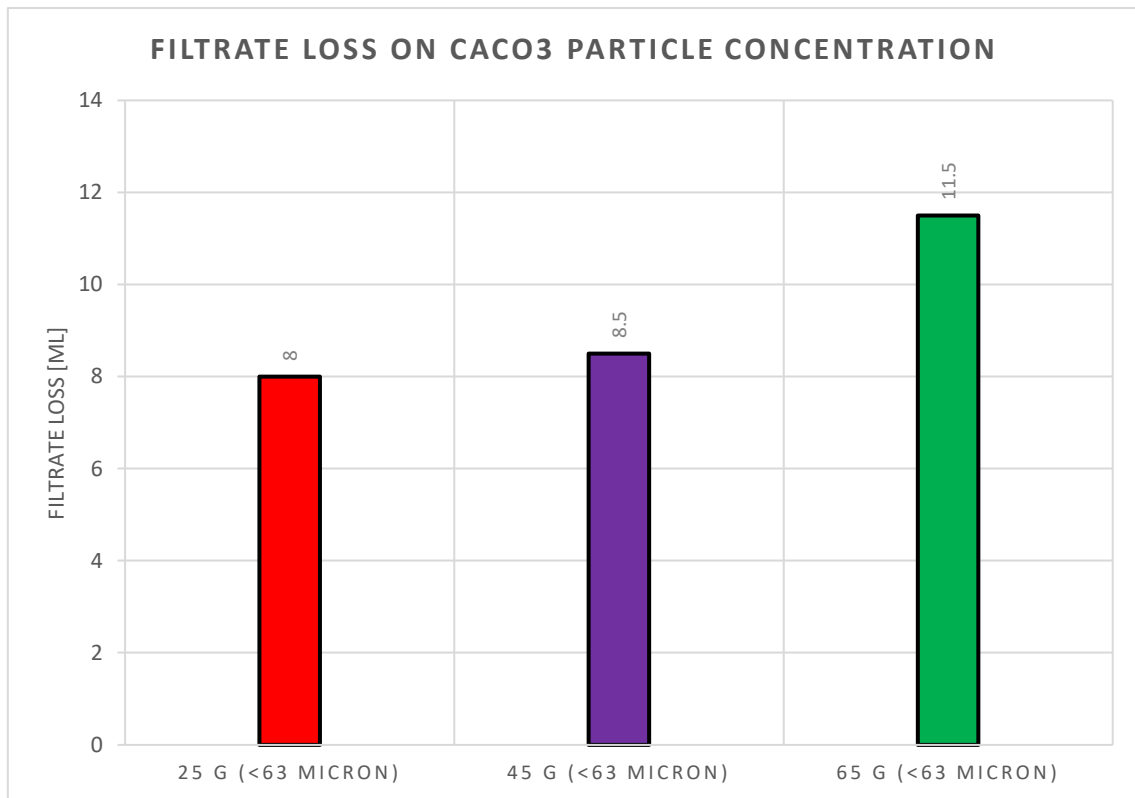


Figure 5.5: API filtrate loss for the 25g, 45g and 65g CaCO₃ particle concentration in Na-formate fluid.

5.2.2 Effect of CaCO₃ particle concentration on rheological properties

The rheology for the 25g, 45g and 65g CaCO₃ particle concentrations at room temperature is presented in figure 5.6. The viscometer responses look almost the same for all particle concentrations in sodium systems. However, the max shear stress occurs for the 65g particle concentration at 26.5 lbf/100sqft and is the highest shear stress compared to the other particle concentrations. Still, the max shear stress is lower than the viscometer responses from figure 5.2 at ambient conditions. This could be since the mud were treated with in-situ and not in-situ + ex-situ polymer treatment. Hence some polymers particles may create a “fluid film” around the solid particles and enhance the fluid properties with additional ex-situ polymer treatment. However, this effect would still be very small or negligible.

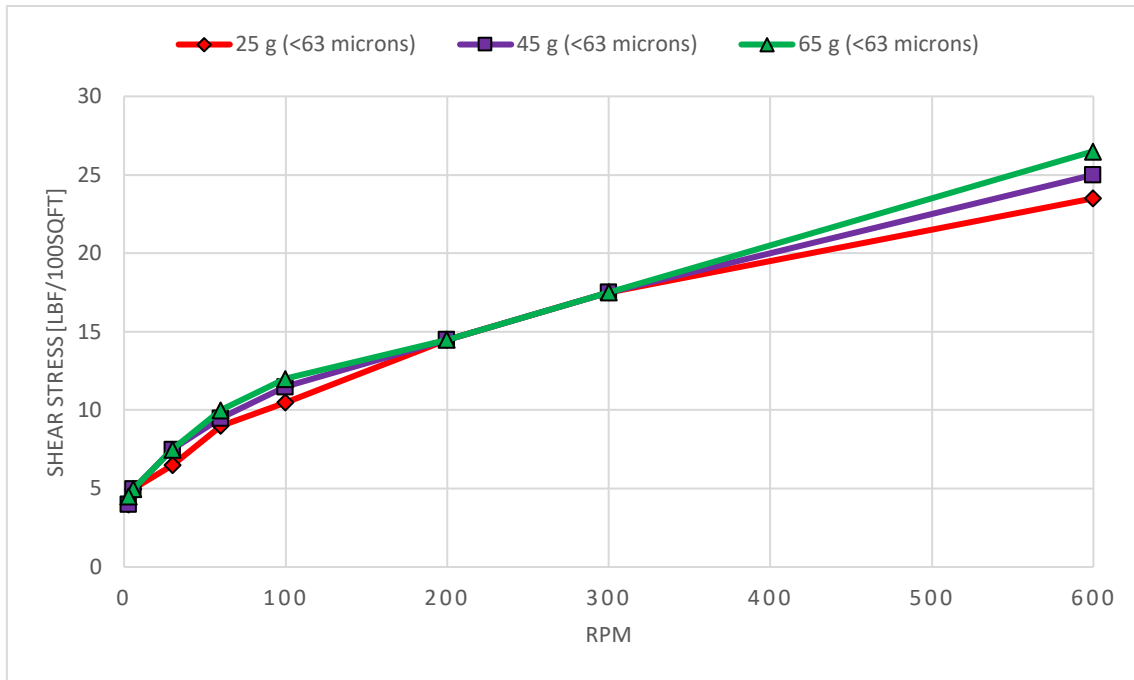


Figure 5.6: Shear stress on rpm for 25g, 45g and 65g CaCO₃ particle concentration at 20°C.

The viscometer responses show roughly the same for the 45g and 65g particle concentration over the whole shear rate range at 50°C. However, the 25g certainly exhibits a lower shear stress compared to the other CaCO₃ particle concentrations. This could indicate a trend that more CaCO₃ concentration provides a higher viscous fluid system in Na-formate fluid. The 45g tends to have higher shear stress at lower rpms compared to the 25g and 65g. Figure 5.7 presents the viscometer responses for the 25g, 45g and 65g particle concentrations at 50°C.

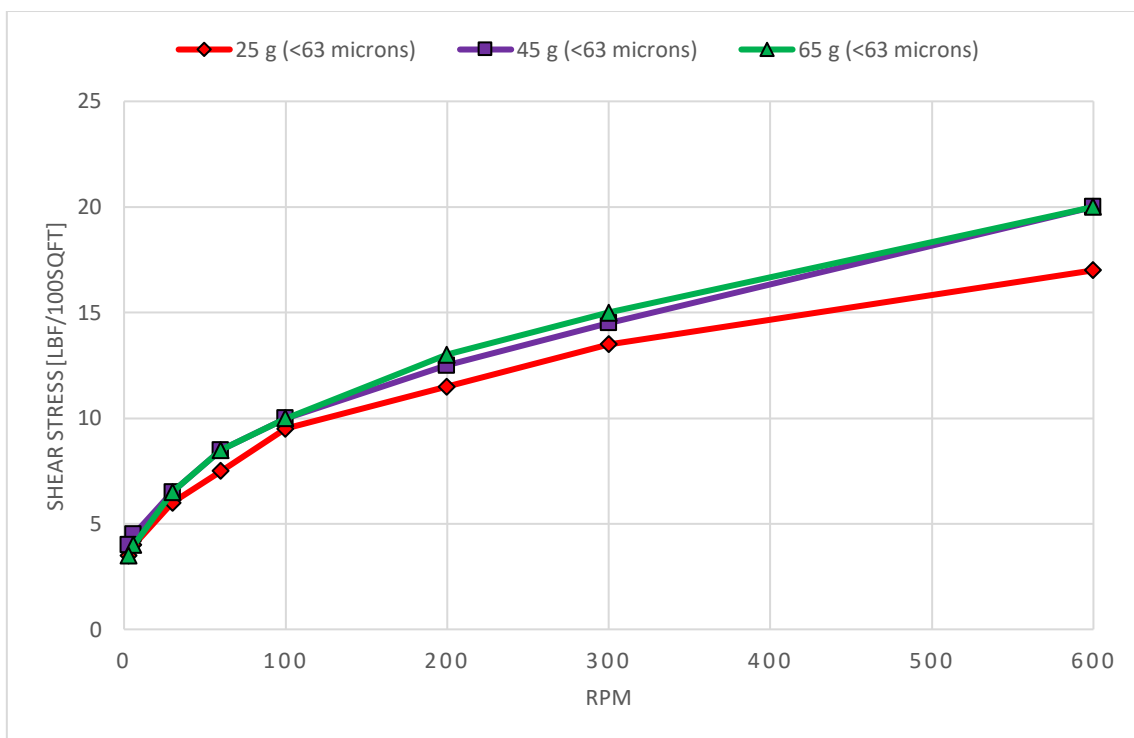


Figure 5.7: Shear stress on rpm for 25g, 45g and 65g CaCO₃ particle concentration at 50°C.

The same trend occurs for the fluid systems at 80°C, as the shear stress for the 45g and 65g are higher for all rpms compared to the 25g CaCO₃ concentration. Figure 5.8 presents the rheology for the 25g, 45g and 65g particle concentrations at 80°C.

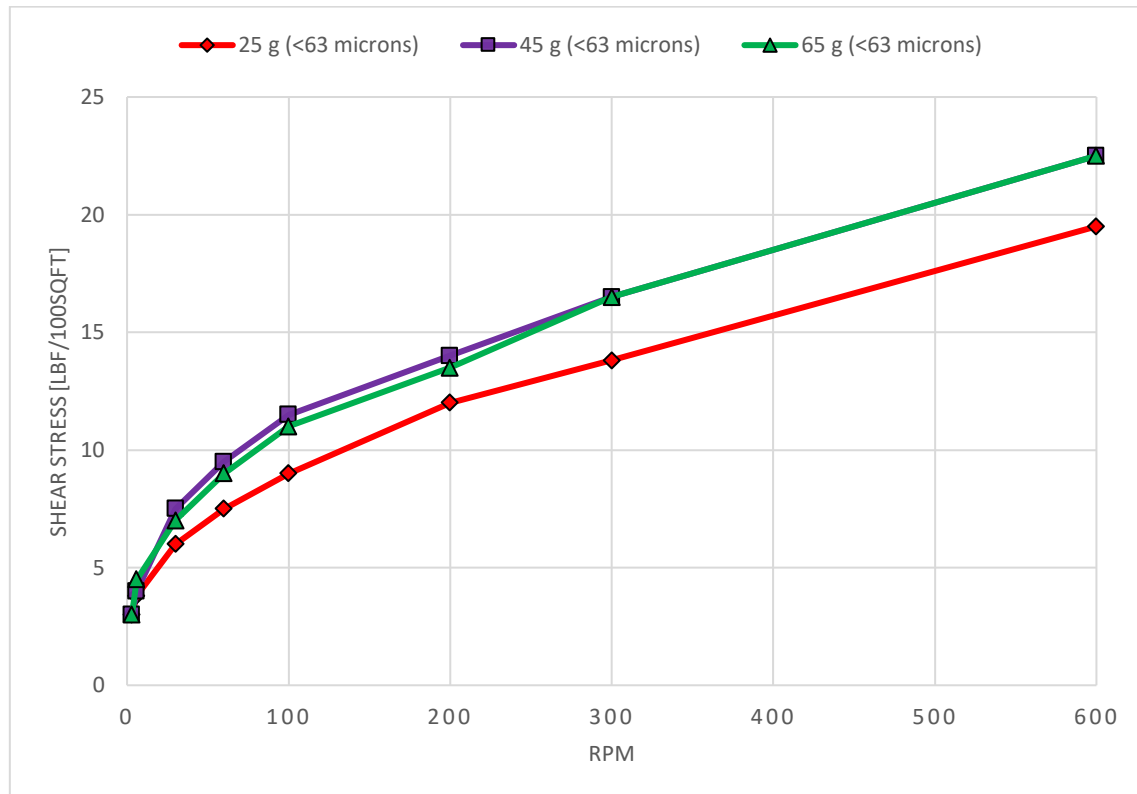


Figure 5.8: Shear stress on rpm for 25g, 45g and 65g CaCO₃ particle concentration at 80°C.

The rheological parameters at three different temperatures for the 25g ,45g and 65g CaCO₃ particle concentrations is presented in table 5.3. Regarding whether CaCO₃ systems provides a thermally stable fluid or not, the apparent and plastic viscosity tends to increase from 50°C to 80°C for all the concentrated fluid systems. However, the Bingham yield stress for the 25g is within the limits for good cuttings transport at ambient conditions (i.e., 11-20 lbf/100sqft). Still, the 65g occurs most thermal stable at higher temperatures from YS calculations. From the flow index it is shown that all the fluids exhibit a shear-thinning characteristic. Yet, the consistency index depends on the flow index, hence the 45g and 65g CaCO₃ particle concentrations are thermal stable in sodium brines at higher temperatures.

Rheological parameters	25g (<63 microns)			45g (<63 microns)			65g (<63 microns)		
	20°C	50°C	80°C	20°C	50°C	80°C	20°C	50°C	80°C
AV [cP]	11.75	8.5	9.75	12.5	10	11.25	13.25	10	11.25
PV [cP]	6	3.5	5.7	7.5	5.5	6	9	5	6
YS [lbf/100sqft]	11.5	10	8.1	10	9	10.5	8.5	10	10.5
LSYS [lbf/100sqft]	3	3	2.2	3	3.5	2	4	3	1.5
n	0.425	0.332	0.499	0.514	0.464	0.447	0.598	0.415	0.447
k [lbf ⁿ /100sqft]	1.235	1.699	0.616	0.708	0.805	1.015	0.419	1.129	1.015

Table 5.3: Rheological parameters for the 25g, 45g and 65g CaCO₃ particle concentrations at 20, 50 and 80°C.

5.2.3 Effect of CaCO₃ particle concentration on viscoelastic properties

5.2.3.1 Effect of CaCO₃ particle concentration on temperature sweep

Temperature sweeps for the 25g, 45g and 65g CaCO₃ particle concentrations is presented in figure 5.9. The viscosity increases with increase in CaCO₃ particle concentration in Na-formate drill-in fluid. However, all the curves decrease linearly for all the particle concentrations with temperature increase to the minima at approximately 70°C. At this temperature, the gel starts to active in the fluid system, hence the viscosity increases due to structural gel formation between the polymer bonding's and other solid content in the Na-brine. This could indicate that the CaCO₃ based fluid systems are thermal stable at temperatures > 80°C (i.e., could be well suitable for HPHT drilling operations).

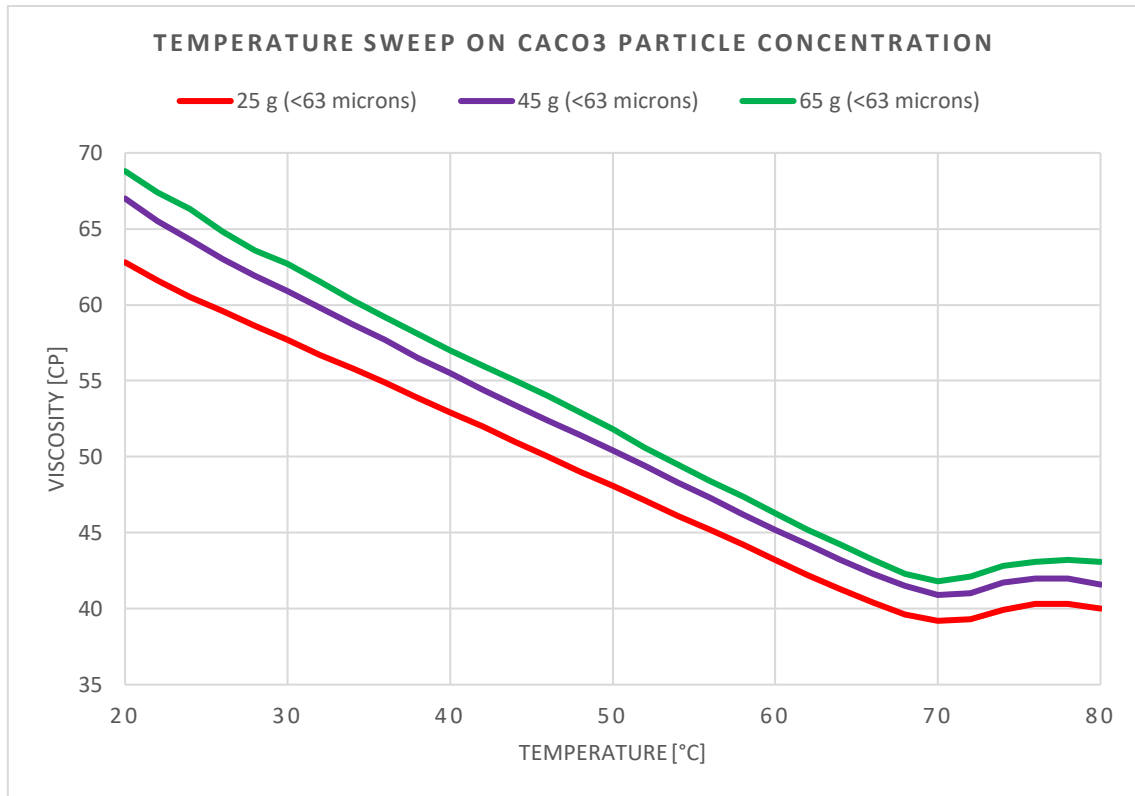


Figure 5.9: Temperature sweeps for 25g, 45g and 65g CaCO₃ particle concentrations.

5.2.3.2 Effect of CaCO₃ particle concentration on amplitude sweep

From figure 5.10, strain amplitude sweep is plotted on storage and loss modulus for increased amount of CaCO₃ particle concentrations. The results show that the 65g exhibits the highest amount of store and loss moduli compared to the 25g and 45g fluid systems. This is expected, since the total amount of solid particles is higher for the 65g compared to the other fluid systems, and hence shows higher storage modulus in the LVE range.

At strain values approximately in-between $0.1 < \gamma < 0.15$, the 45g shows higher viscous behavior than the 65g particle concentration. However, the strain values are so low that the samples exhibit zig-zag characteristic. For higher strain values, the 65g shows a slightly higher loss moduli in the LVE range compared the 45g. The 25g performs the lowest both storage and loss modulus compared to the 45g and 65g fluid systems. This is expected since this is the fluid system with the least amount of solid content.

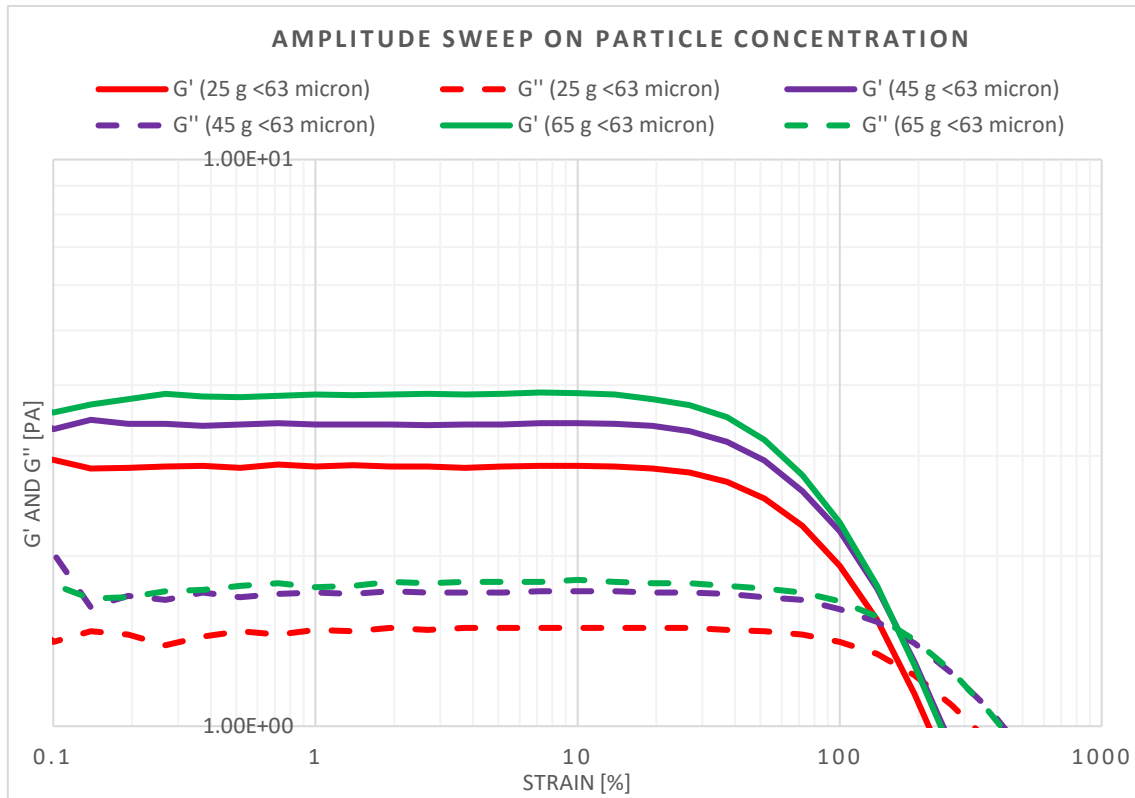


Figure 5.10: Strain amplitude sweep for 25g, 45g and 65g CaCO₃ particle concentrations.

From table 5.4, the most important parameters from figure 5.10 is presented. All fluid systems show equal strain limits at 37.3%. However, the yield point is higher for the 45g compared to both the 25g and 65g, even though the yield stress deviation between the 45g and 65g is only 0.01 Pa. The flow points for the fluid systems is higher for the 45g, compared to both the 25g and 65g. Hence the 45g CaCO₃ particle concentration occurs with the longest yield-zone before it starts to flow in sodium systems.

Fluid systems	Strain, γ_L [%]	Yield point, τ_y [Pa]	Flow point, τ_f [Pa]
25 g (<63 microns)	37.3	1.15	3.10
45 g (<63 microns)	37.3	1.35	3.53
65 g (<63 microns)	37.3	1.34	3.26

Table 5.4: Important parameters obtained from the amplitude sweeps for 25g, 45g and 65g CaCO₃ particle concentrations.

5.3 Test design 3: Effect of polymer concentration in Na-formate drill-in fluid

This subsection presents the results obtained from the sodium drill-in fluid formulation in section 4.3.1.4. The aim is to investigate the behavior of xanthan gum polymer concentrations in Na-formate drill-in fluids. The polymer concentrations are presented as 0.79g + 0.4g for the 1.19g total XG polymer concentration, and 0.79g + 0.6g for the 1.39g total XG polymer concentration. Both the fluid systems were treated equally in-situ.

5.3.1 Effect of polymer concentration on filtration properties

From figure 5.11, the filtrate loss for the 1.19g XG polymer concentration exhibited 8.5 ml filtrate loss in contrast to the 1.39g XG polymer concentration which resulted in a 7.6 ml filtrate loss respectively. This indicates that increasing the polymer amount in the fluid system reduces the API static filtrate loss at ambient conditions.

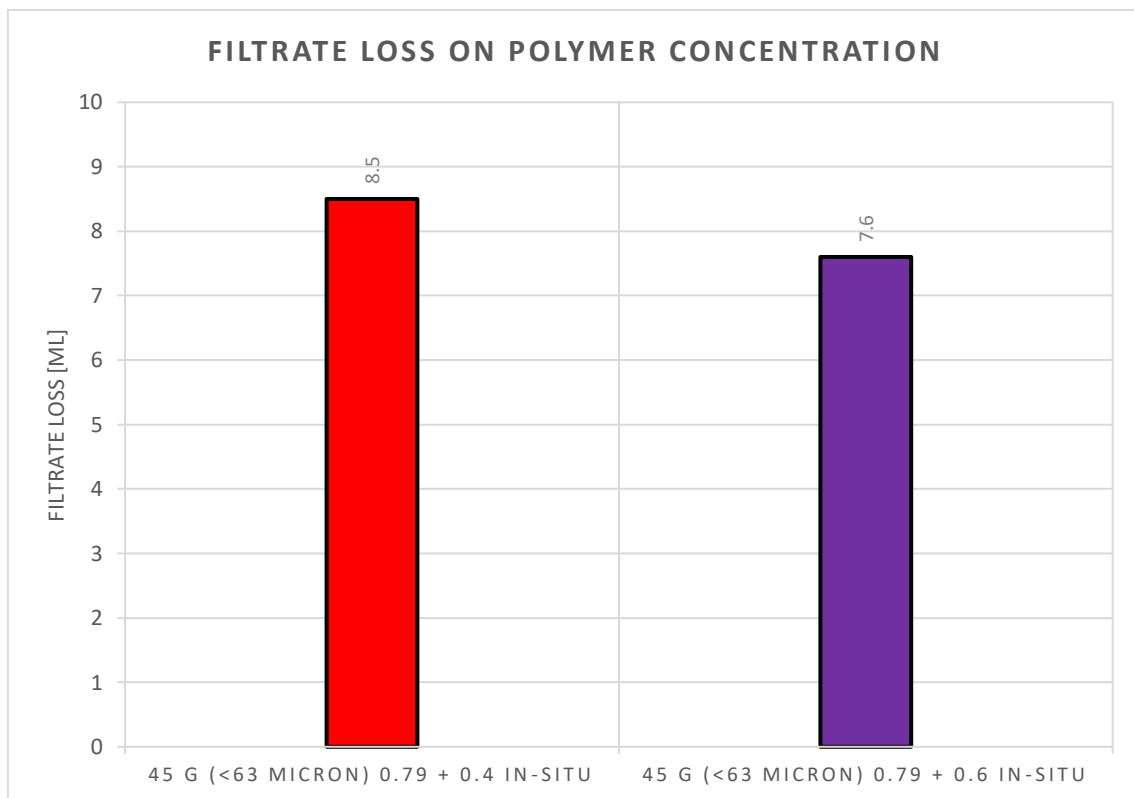


Figure 5.11: API filtrate loss for the 1.19g XG and 1.39g XG polymer concentrations.

5.3.2 Effect of polymer concentration on rheological properties

Figure 5.12 presents the viscometer responses for the 1.19g XG and 1.39g XG polymer concentrations at room temperature. The results show that the 1.39g xanthan gum polymers exhibits a higher shear stress over the whole rpm range compared to the other sodium systems with lower polymer concentrations. However, this result is expected, since it is known that polymers increases the viscosity in drilling fluids.

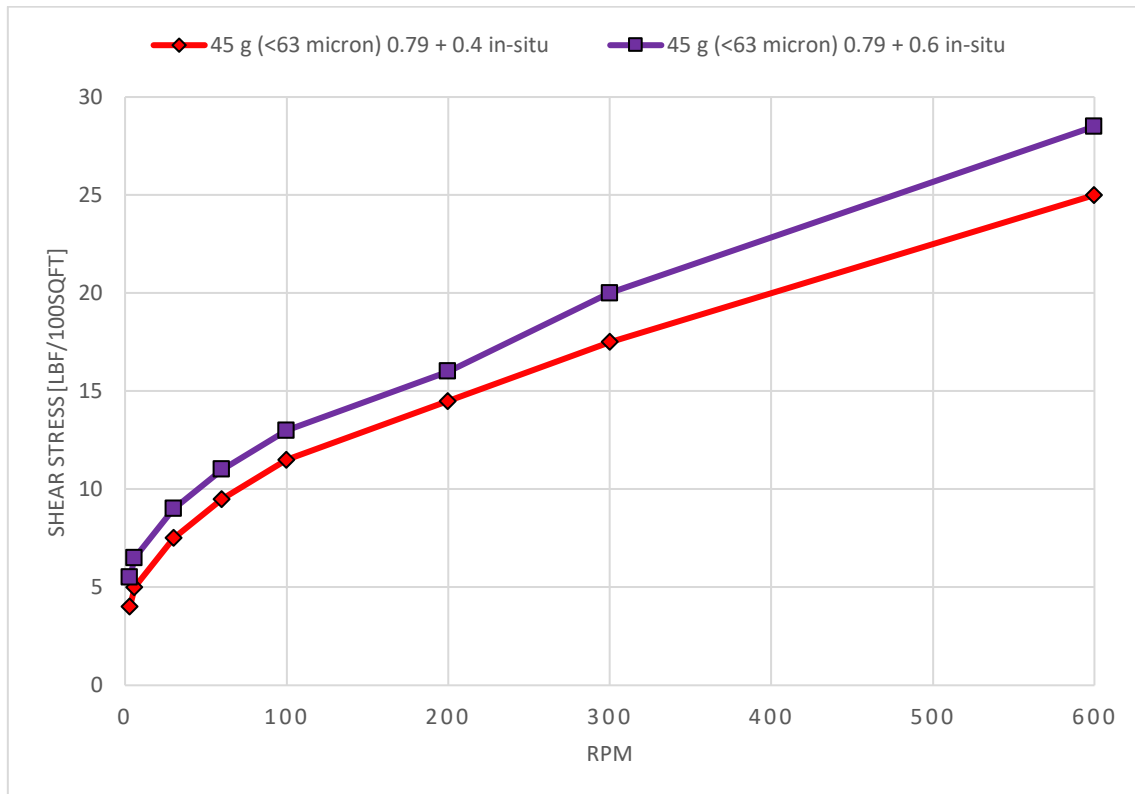


Figure 5.12: Shear stress on rpm for the 1.19g XG and 1.39g XG polymer concentrations at 20°C.

Figure 5.13 and 5.14 presents the rheology for the 1.19g XG and 1.39g XG polymer concentrations at 50°C and 80°C respectively. The xanthan gum polymers are not affected by temperature increase, hence the 1.39g XG exhibit higher rheological behavior compared to lower polymer concentrations. However, the shear stress values are not the same with increase in temperature. This could be because heated Na-brines could weaken the chemical interaction in-between the polymer structure, brine atoms and the other solid content, hence the shear stress decreases. Another explanation could also be that the kinetic energy in the fluid system increases with increase in temperature, then some turbulence in the system may occur at higher temperatures that weakens the rheological structure.

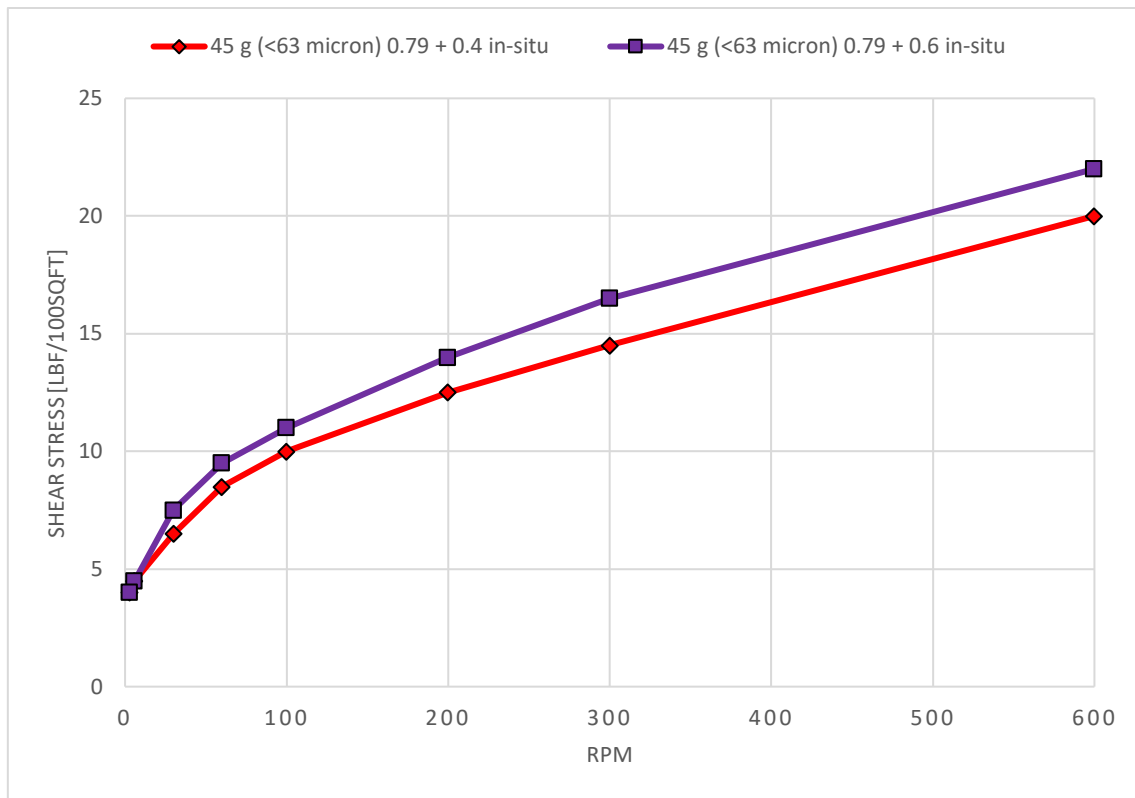


Figure 5.13: Shear stress on rpm for the 1.19g XG and 1.39g XG polymer concentrations at 50°C.

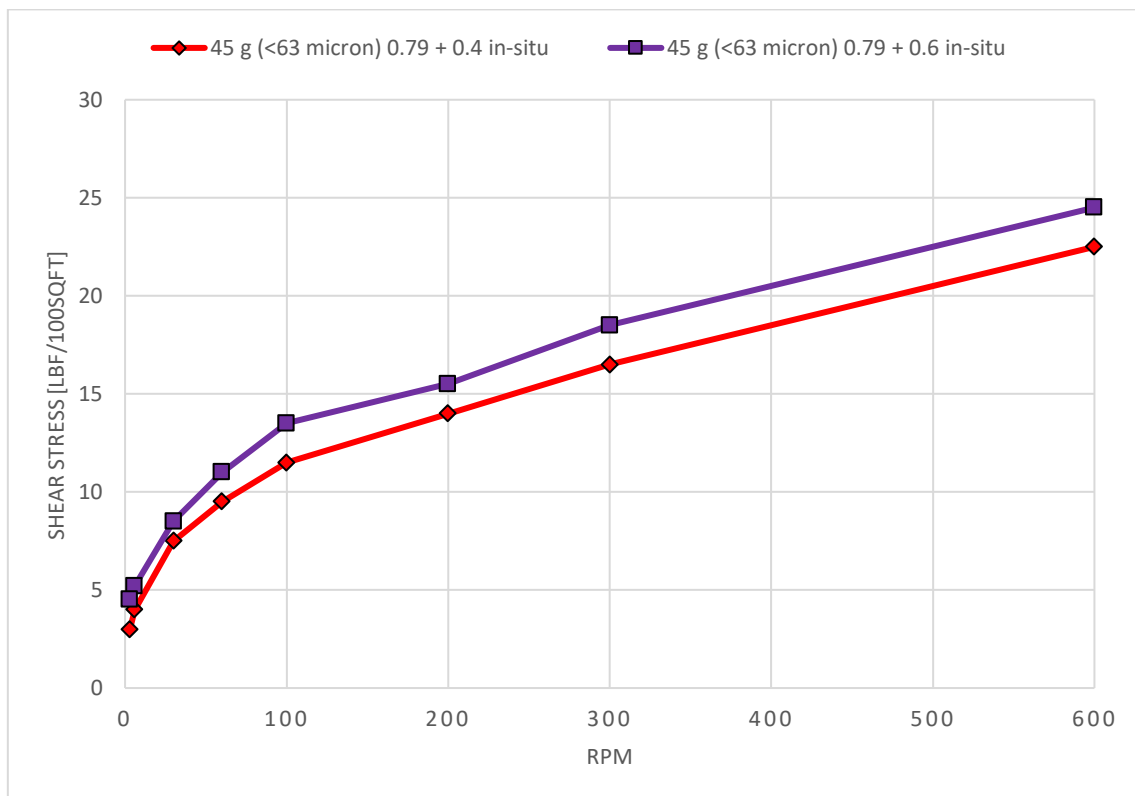


Figure 5.14: Shear stress on rpm for the 1.19g XG and 1.39g XG polymer concentrations at 80°C.

Table 5.5 presents the rheological parameters for the 1.19g XG and 1.39g XG polymer concentrations. The apparent viscosity is not constant with increase in temperature as this exhibits a polynomial trend. However, the AV is higher for the 1.39g XG compared to the 1.19g XG polymers at all temperatures. The Bingham yield stress is within the limits for good transport of drilled cuttings for the 1.39g XG. For both polymer concentrations, the plastic viscosity, flow index and consistency index are thermal stable at higher temperatures. Therefore, it can be justified that xanthan gum polymers as a viscosity agent are modified to withstand higher temperature conditions. In addition, increase in xanthan gum polymer concentration tends to increase the Bingham yield stress and the fluids consistency index.

Rheological parameters	1.19g XG			1.39g XG		
	20°C	50°C	80°C	20°C	50°C	80°C
AV [cP]	12.5	10	11.25	14.25	11	12.25
PV [cP]	7.5	5.5	6	8.5	5.5	6
YS [lbf/100sqft]	10	9	10.5	11.5	11	12.5
LSYS [lbf/100sqft]	3	3.5	2	4.5	3.5	3.8
n	0.514	0.464	0.447	0.511	0.415	0.405
k [lbf ⁿ /100sqft]	0.708	0.805	1.015	0.828	1.242	1.480

Table 5.5: Rheological parameters for the 1.19g XG and 1.39g XG polymer concentrations at 20, 50 and 80°C.

5.3.3 Effect of polymer concentration on viscoelastic properties

5.3.3.1 Effect of CaCO₃ polymer concentration on temperature sweep

Figure 5.15 presents the temperature sweeps for the 1.19g XG and 1.39g XG polymer concentrations. The temperature sweep tests further justify that increase in XG polymer concentration increases the fluid systems viscosity. Both fluid systems tend to decrease linearly to the viscous minima at roughly 70°C. The same trend occurred for the different CaCO₃ particle concentrations in Na-formate muds from test design 2; the gel forms and establish a higher viscous system at temperatures above 70°C. However, the viscosity at temperature above 75°C for the 1.39g XG concentration, tends to be established at consistent change in shear-

plateau viscosity = 0 (i.e., the viscosity is constant at high temperatures). This could again be justified with that the xanthan gum polymers are thermal stable at higher temperatures.

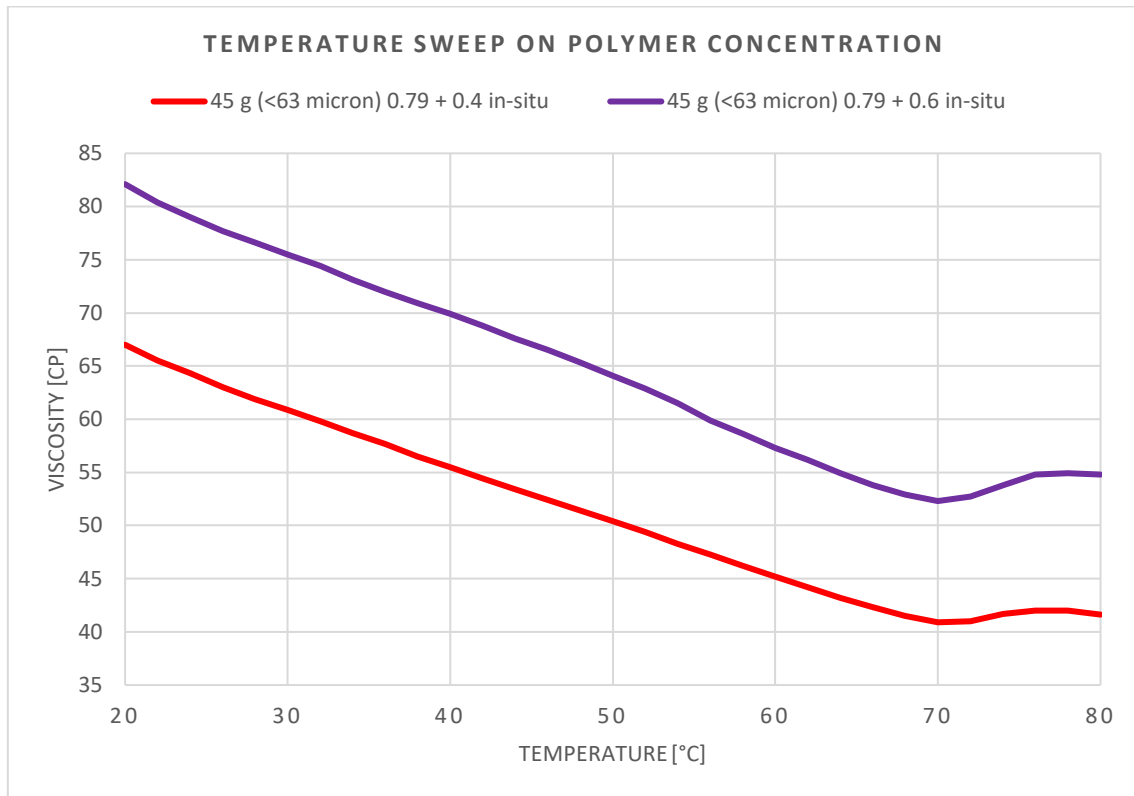


Figure 5.15: Temperature sweeps for the 1.19g XG and 1.39g XG polymer concentrations.

5.3.3.2 Effect of CaCO₃ polymer concentration on amplitude sweep

From table 5.6, the most important parameters obtained from the amplitude sweep tests is summarized. The limit strain for both polymer concentrations are equal at 37.3%. However, the yield stress and flow point are higher for the 1.39g XG compared to the 1.19g XG polymer concentration at 1.98 and 4.75 pascals respectively. This indicates that the stress required for elastic to plastic deformation is higher for the 1.39g XG compared to the 1.19g XG polymer concentration.

Fluid systems	Strain, γ_L [%]	Yield point, τ_y [Pa]	Flow point, τ_f [Pa]
45 g (<63 micron) 1.19 g XG in-situ	37.3	1.35	3.53
45 g (<63 micron) 1.39 g XG in-situ	37.3	1.98	4.75

Table 5.6: Important parameters obtained from the amplitude sweeps for the 1.19g XG and 1.39 XG polymer concentrations.

5.4 Test design 4: Comparison between CaCO₃ type 1 and CaCO₃ type 2 in Na-formate drill-in fluids

This subsection presents the results obtained from the sodium drill-in fluid formulation in section 4.3.1.5. The CaCO₃ particle concentration is 25g and the particle size were decided to <63 microns for both fluid systems.

5.4.1 Effect of CaCO₃ particle type on filtration properties

Figure 5.16 shows that the CaCO₃ type 1 exhibited an 8.0 ml filtrate loss. The API static filtrate loss for the type 2 CaCO₃ was 7.8 ml. From these results it is shown that the type 2 CaCO₃ had a 0.2 ml lower filtrate loss than the 25g CaCO₃ type 1. However, both fluid systems could indicate a penetrating characteristic since the filtrate loss is relatively high.

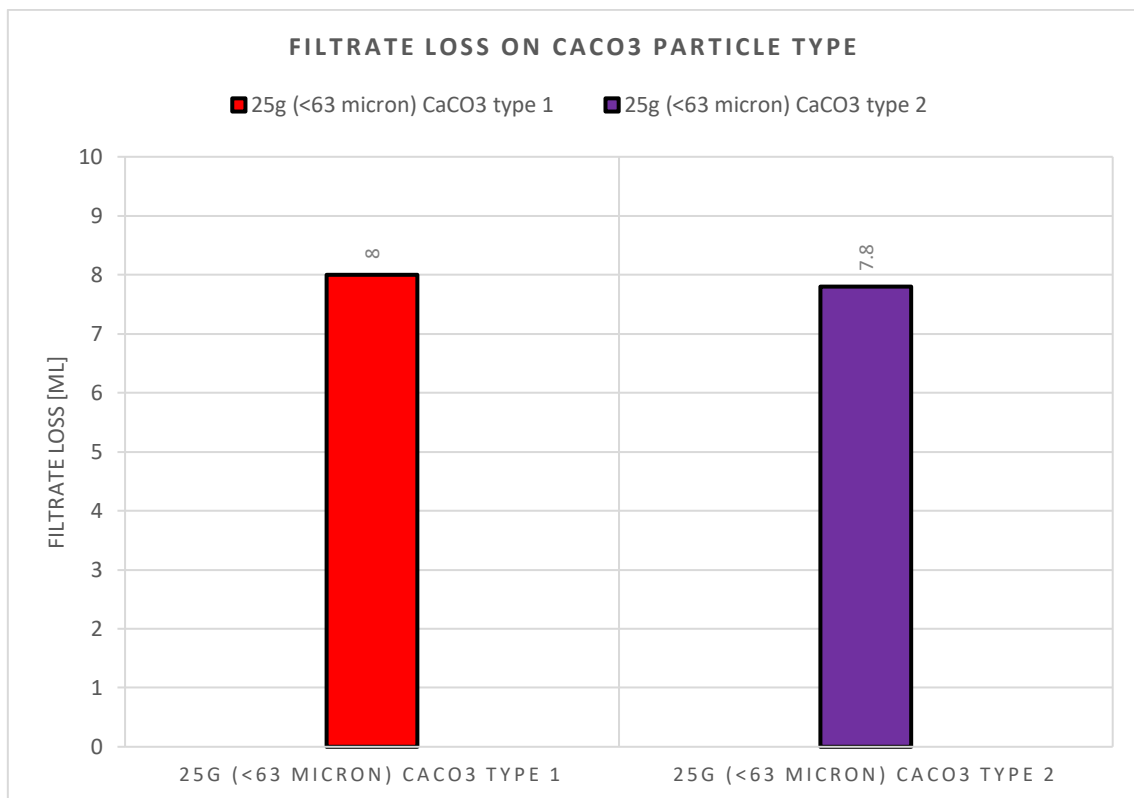


Figure 5.16: API filtrate loss for the 25g CaCO₃ type 1 and 25g CaCO₃ type 2.

5.4.2 Effect of CaCO₃ particle type on rheological properties

Figure 5.17 presents the viscometer response for the CaCO₃ particle types at ambient conditions. The results show that the shear stress is higher for the type 1 CaCO₃ compared to

CaCO₃ type 2 at higher shear rates. However, at the lower rpms the results show an opposite trend.

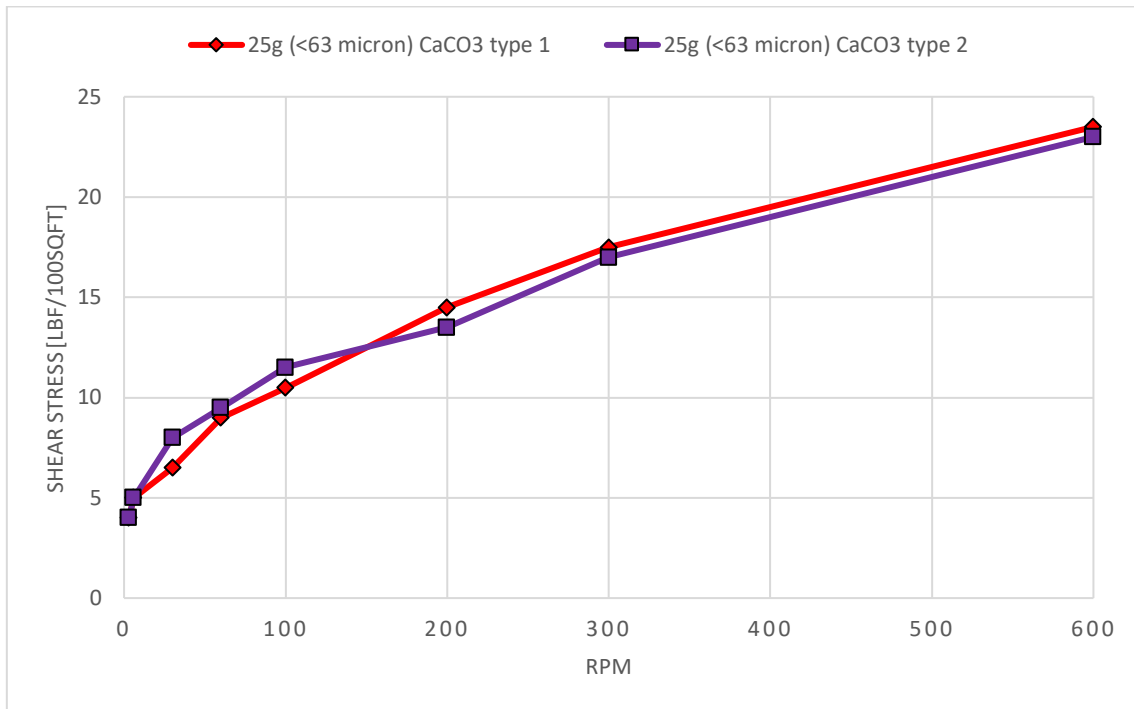


Figure 5.17: Shear stress on rpm for the CaCO₃ type 1 and CaCO₃ type 2 at 20°C.

The viscometer responses at 50°C show a higher shear stress performance for the type 1 CaCO₃ compared to CaCO₃ type 2. Figure 5.18 presents the rheology for the type 1 and type 2 CaCO₃ at 50°C.

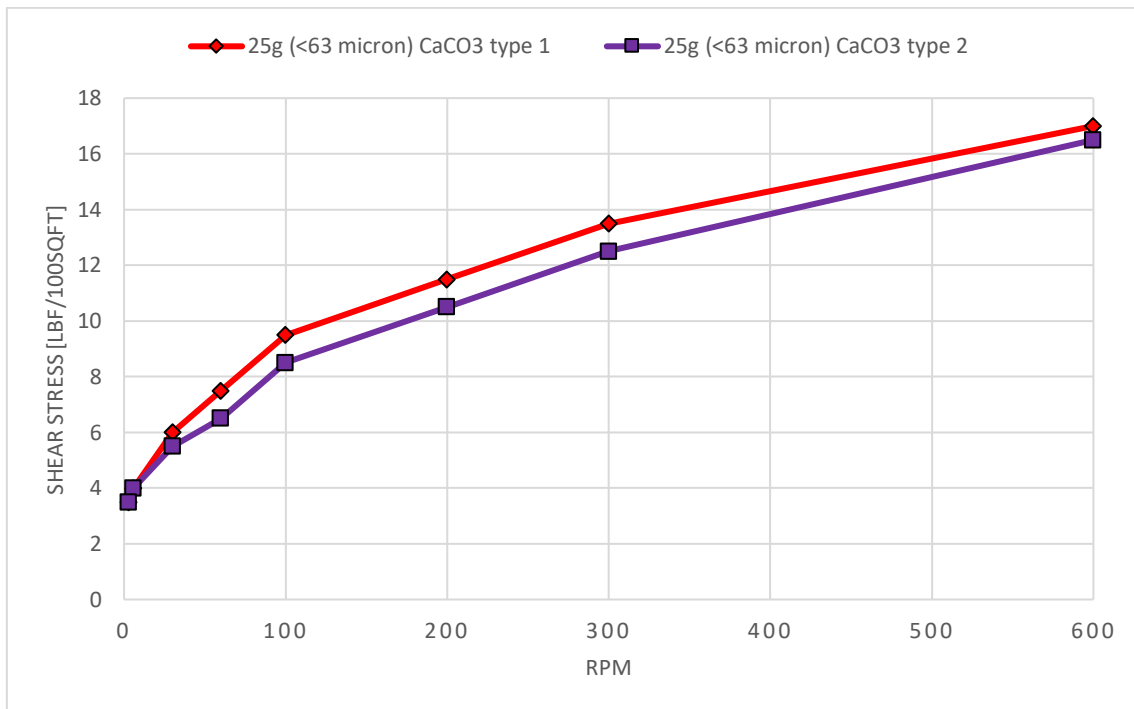


Figure 5.18: Shear stress on rpm for the CaCO₃ type 1 and CaCO₃ type 2 at 50°C.

The rheological trend shifts with temperature increase. By increasing the temperature from 50°C to 80°C, the CaCO₃ type 2 fluid system express higher shear stress over the whole rpm range compared to the type 1 CaCO₃ system. Figure 5.19 presents the viscometer responses for the CaCO₃ type 1 and CaCO₃ type 2 at 80°C.

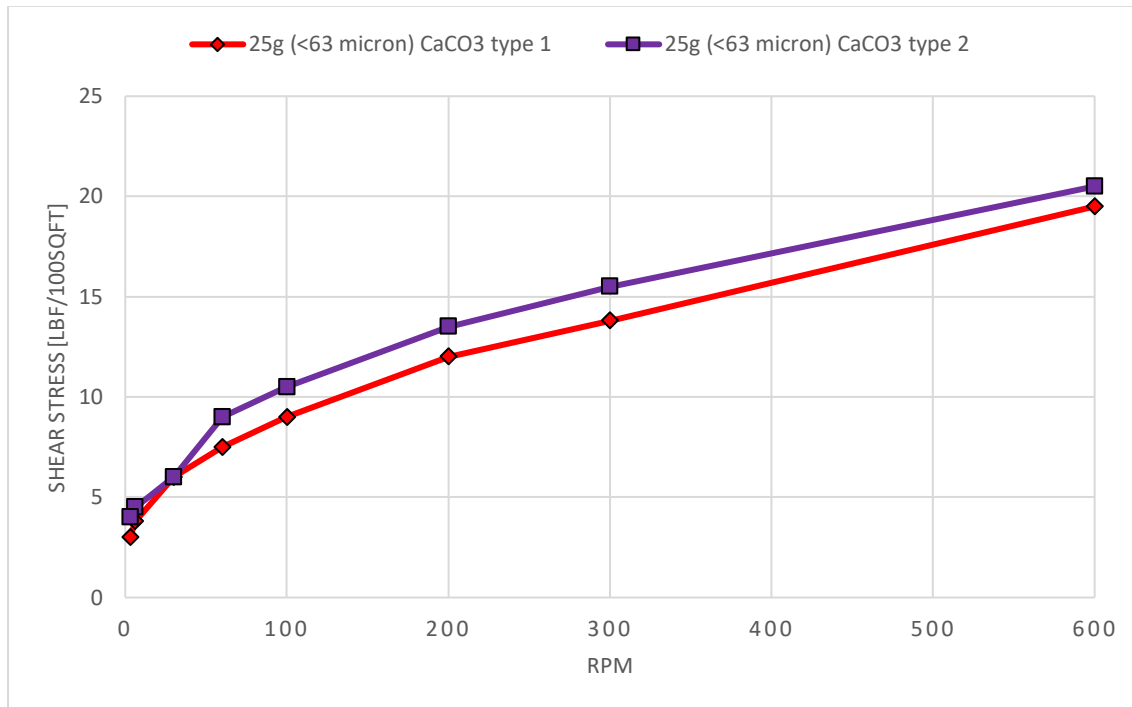


Figure 5.19: Shear stress on rpm for the CaCO₃ type 1 and CaCO₃ type 2 at 80°C.

The apparent and plastic viscosity exhibits a polynomial trend since the viscosity decreases from 20°C to 50°C, hence increases to 80°C, for both the type 1 and type 2 CaCO₃ fluid systems. However, the flow index for the CaCO₃ type 2 are approximately the same at 50°C and 80°C viscometer responses. Hence the type 2 CaCO₃ is thermal stable at higher temperatures justified by minimal deviation in parameter. However, the consistency index depends on the n parameter, and the CaCO₃ type 2 rheological performance is frequently more constant independent of high temperatures compared to the type 1 CaCO₃. Table 5.7 summarizes the rheological parameters obtained for the CaCO₃ type 1 and CaCO₃ type 2 systems.

Rheological parameters	CaCO ₃ type 1			CaCO ₃ type 2		
	20°C	50°C	80°C	20°C	50°C	80°C
AV [cP]	11.75	8.5	9.75	11.5	8.25	10.25
PV [cP]	6	3.5	5.7	6	4	5
YS [lbf/100sqft]	11.5	10	8.1	11	8.5	10.5
LSYS [lbf/100sqft]	3	3	2.2	3	3	3.5
n	0.425	0.332	0.499	0.436	0.400	0.403
k [lbf ⁿ /100sqft]	1.235	1.699	0.616	1.122	1.030	1.255

Table 5.7: Rheological parameters for the CaCO₃ type 1 and CaCO₃ type 2 at 20, 50 and 80°C.

5.4.3 Effect of CaCO₃ particle type on viscoelastic properties

5.4.3.1 Effect of CaCO₃ particle type on temperature sweep

The type 2 CaCO₃ is more viscous than the CaCO₃ type 1 over the whole temperature range. All the sodium brines exhibit gel formation at approximately 70°C. However, the CaCO₃ LCM particles does not show a significant impact on the fluids tensile gel strengthening. This could be justified since the xanthan gum polymers are the substance that activates the gel in the system, hence the explanation whether the CaCO₃ type 1 or CaCO₃ type 2 performs a thermal stable fluid system or not is insignificant since the polymer amount are equal. Figure 5.20 presents the temperature sweeps for the type 1 CaCO₃ and type 2 CaCO₃ fluid systems.

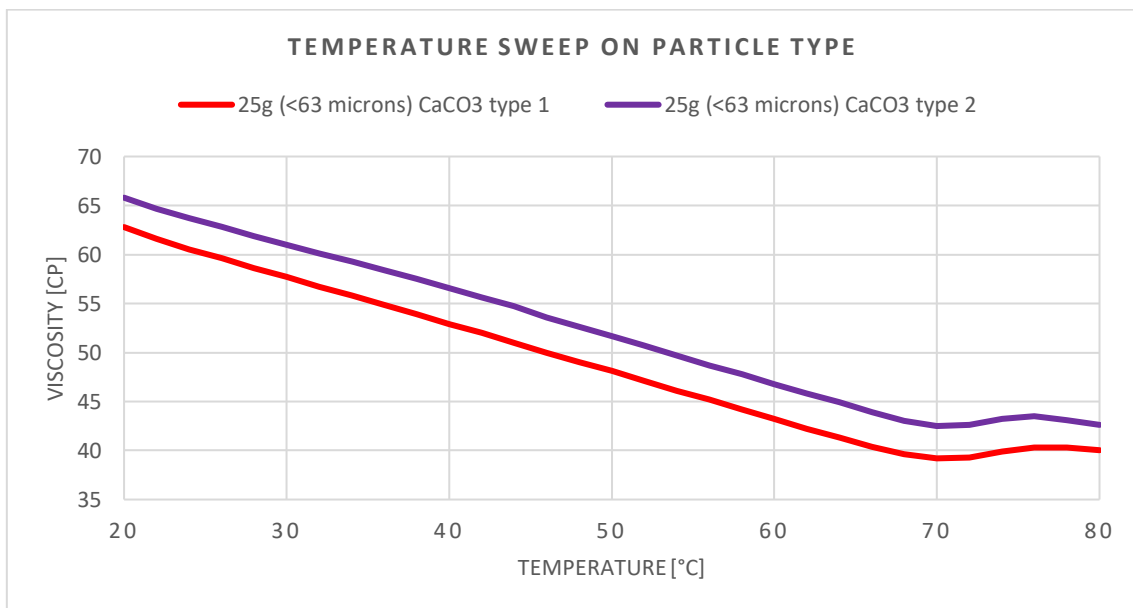


Figure 5.20: Temperature sweeps for the CaCO₃ type 1 and CaCO₃ type 2.

5.4.3.2 Effect of CaCO₃ particle type on amplitude sweep

From table 5.8, the most important parameters obtained from the amplitude sweep tests is summarized. The limit strain is equal for the type 1 and type 2 CaCO₃ at 37.3%. This indicates that the elongated LVE is the same independent of CaCO₃ particle type. Yet, the type 2 CaCO₃ occurs with the highest yield and flow point compared to type 1 CaCO₃, thus are more withstand able towards material deformation. This is expected from the temperature sweep tests since the CaCO₃ type 2 fluid system performs a higher viscous characteristic.

Fluid systems	Strain, γ_L [%]	Yield point, τ_y [Pa]	Flow point, τ_f [Pa]
25 g (<63 micron) CaCO₃ type 1	37.3	1.36	3.59
25 g (<63 micron) CaCO₃ type 2	37.3	1.79	4.08

Table 5.8: Important parameters obtained from the amplitude sweeps for the CaCO₃ type 1 and CaCO₃ type 2.

5.5 Test design 5: Effect of CaCO₃ particle concentration in K-formate drill-in fluid

This subsection presents the results obtained for the potassium formate drill-in fluid formulation in section 4.3.2.1.

5.5.1 Effect of CaCO₃ particle concentration on filtration properties

Before testing the samples were modified for pH by added 3 droplets of 5% NaOH. The pH was modified to 11.0, 11.1 and 10.98 for the 25g, 45g and 65g CaCO₃ particle concentrations respectively. The purpose behind pH modification is to avoid bacterial forming in the fluid systems that later could affect the rheological properties.

Figure 5.21 presents the results from the API static filtrate loss for the 25g, 45g and 65g CaCO₃ particle concentrations in K-formate fluid. The results show that the 65g CaCO₃ concentration performs the highest filtrate loss at 9.25 ml, compared to the 25g and 45g particle concentrations that exhibits a 7.5 ml and 7.4 ml filtrate loss respectively. However, the API filtrate loss at static conditions deviates with only 0.1 ml from the 25g to the 45g CaCO₃ particle concentration increase. Thus, it could be a trend that particle increase in CaCO₃ LCM increases the filtrate loss and hence possesses penetrating fluid characteristics in K systems. Still, the increase in

CaCO₃ particle concentration in K-formate systems exhibits a lower filtrate loss compared to the same concentrated increase for type 1 CaCO₃ in the Na-based fluid systems. This could be since potassium has a higher atomic weight and lower electronegative charge, thus occurs with weaker bonding abilities with other chemical elements in the mud composition, compared to sodium formate fluids.

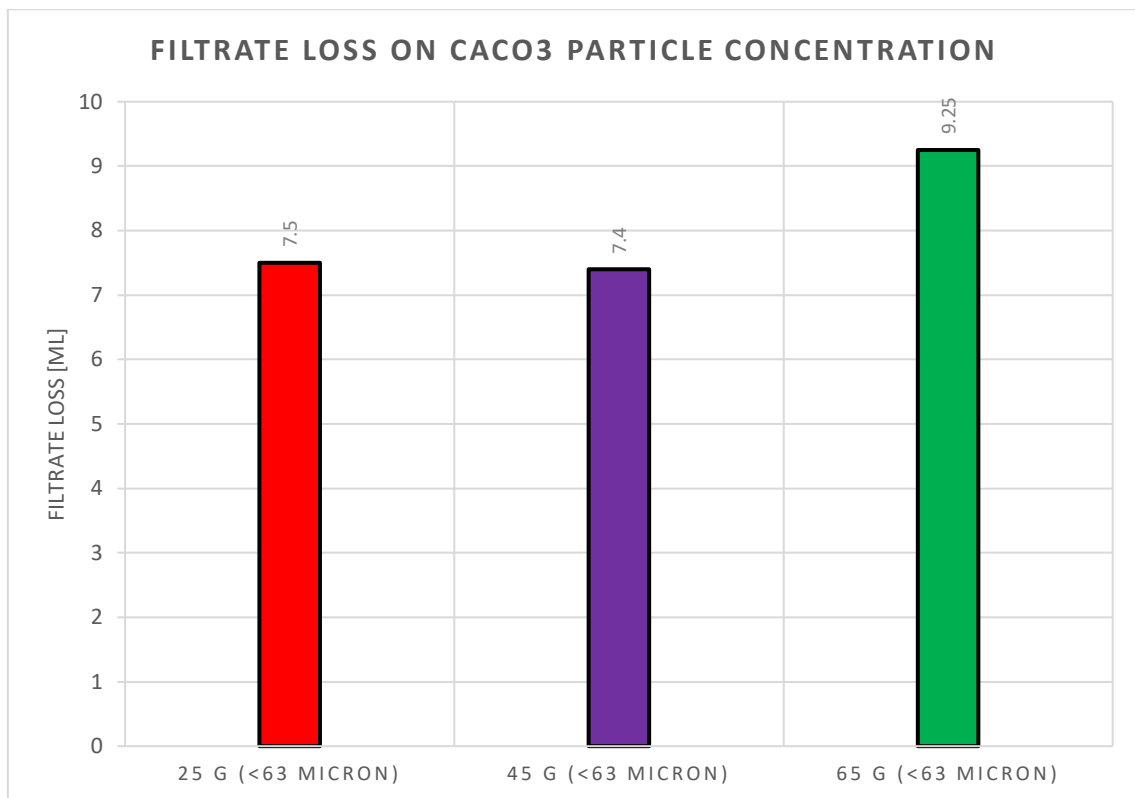


Figure 5.21: API filtrate loss for the 25g, 45g and 65g CaCO₃ particle concentrations.

5.5.2 Effect of CaCO₃ particle concentration on rheological properties

Figure 5.22 presents the viscometer responses at ambient conditions for the 25g, 45g and 65g CaCO₃ particle concentrations. The results clearly show that increase in CaCO₃ particle concentration increases the fluids shear stress. However, this trend is more significant for the K-brines compared to the rheology for Na-fluids at room temperature, where the 45g equaled the 65g CaCO₃ particle concentrations viscous response over the whole rpm range.

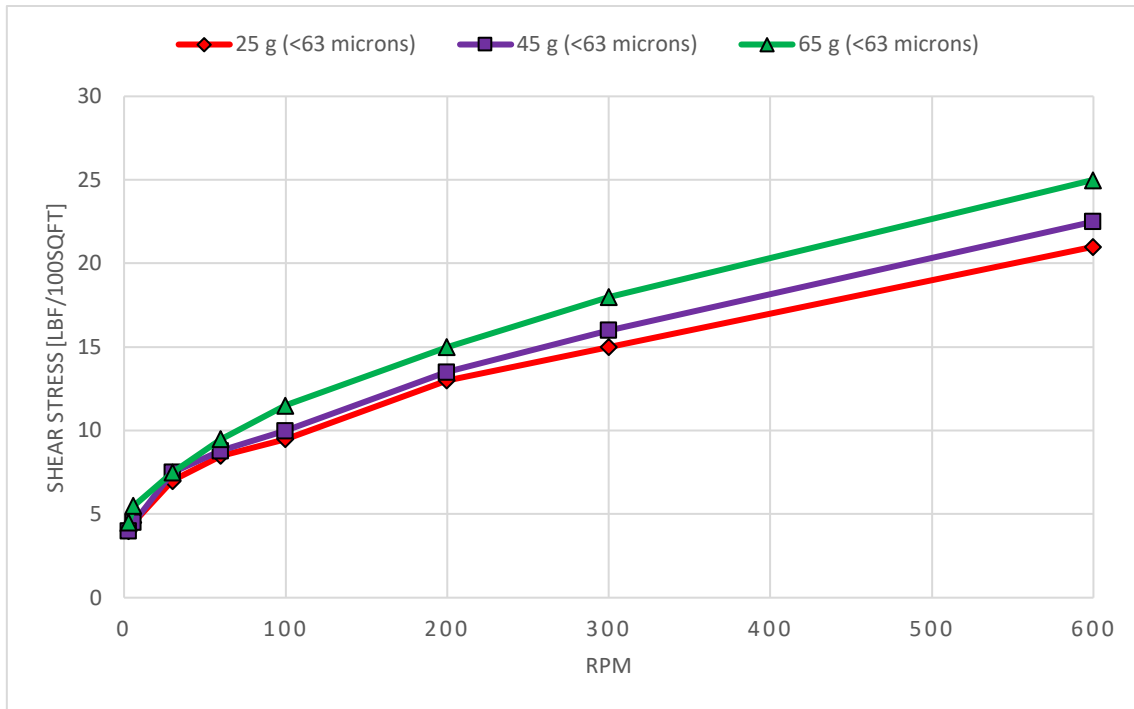


Figure 5.22: Shear stress on rpm for 25g, 45g and 65g CaCO₃ particle concentration at 20°C.

The rheology for the 45g drops down to shear stress responses closer to the 25g CaCO₃ system at 50°C. This could indicate that the 45g CaCO₃ concentration loses its rheological properties at higher temperatures, hence behaves thermally unstable. Figure 5.23 presents the rheological behavior for the 25g, 45g and 65g CaCO₃ particle concentrations at 50°C.

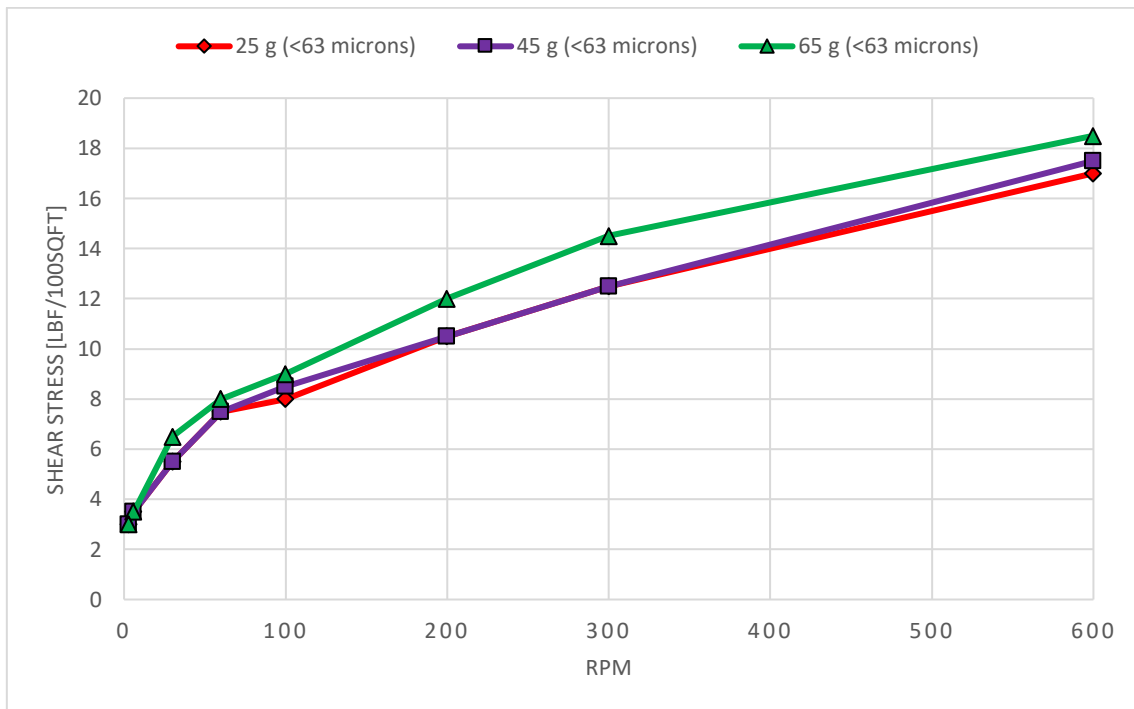


Figure 5.23: Shear stress on rpm for 25g, 45g and 65g CaCO₃ particle concentration at 50°C.

Figure 5.24 presents the K-brines viscometer responses for the 25g, 45g and 65g CaCO₃ particle concentrations at 80°C. The trend is that increase in CaCO₃ LCM particle concentration enhances viscous behavior in K-formate systems at higher temperatures.

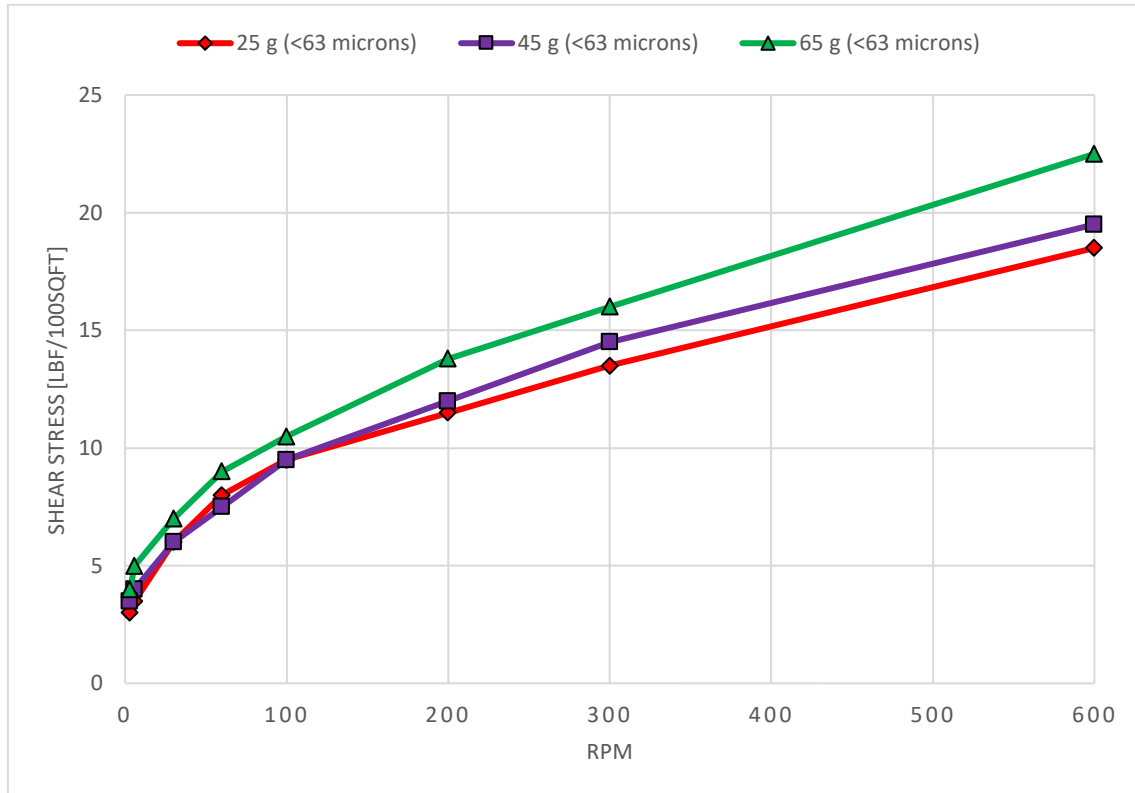


Figure 5.24: Shear stress on rpm for the 25g, 45g and 65g CaCO₃ particle concentrations at 80°C.

Table 5.9 presents the rheological parameters for the 25g, 45g and 65g CaCO₃ particle concentrations. The 25g particle concentration occurred with the lowest viscometer responses compared to higher concentrations, yet this is the concentration that occurs thermal stable as the flow and consistency index performs minimal deviation at higher temperatures. Hence from thermal stability analysis, the trend is opposite in K-formate fluids compared to Na-brines were the 45g and 65g CaCO₃ particle concentrations occurred thermal stable at higher temperatures. This could be since the kinetic energy increases with temperature increase; thus, sodium's electron affinity could keep the system thermal stable and avoid turbulence at higher temperatures compared to K-brines. From the periodic table, potassium has a lower thermal conductivity than sodium [51]. However, the CaCO₃ particles could react mechanically and not chemically with the other mud components. Therefore, the ionization energy for the Na and K-formate brines could express an answer whether the 25g, 45g and 65g CaCO₃ concentrations exhibit thermal stability at higher temperatures.

Rheological parameters	25g (<63 microns)			45g (<63 microns)			65g (<63 microns)		
	20°C	50°C	80°C	20°C	50°C	80°C	20°C	50°C	80°C
AV [cP]	10.5	8.5	9.25	11.25	8.75	9.75	12.5	9.25	11.25
PV [cP]	6	4.5	5	6.5	5	5	7	4	6.5
YS [lbf/100sqft]	9	8	8.5	9.5	7.5	9.5	11	10.5	9.5
LSYS [lbf/100sqft]	3.5	2.5	2.5	3.5	2.5	3	3.5	2.5	3
n	0.485	0.443	0.454	0.492	0.485	0.427	0.474	0.351	0.492
k [lbf ⁿ /100sqft]	0.728	0.787	0.794	0.746	0.607	1.010	0.938	1.622	0.746

Table 5.9: Rheological parameters for the 25g, 45g and 65g CaCO₃ particle concentrations at 20, 50 and 80°C.

5.5.3 Effect of CaCO₃ particle concentration on viscoelastic properties

5.5.3.1 Effect of CaCO₃ particle concentration on temperature sweep

Figure 5.25 presents the temperature sweeps for the 25g, 45g and 65g CaCO₃ particle concentrations in potassium systems. The viscosity increases with increase in CaCO₃ particle concentration. This trend is the same for the Na-based brines and could further justify that CaCO₃ LCM's occurs as a mechanical and not chemical component in brine-based muds, since more CaCO₃ particles makes the fluid systems higher viscous. However, the gel activates at higher temperatures, and the fluids are more viscous for the sodium particle concentrations compared to the potassium formate systems. This could be due to Na and K-formate difference in elemental electron affinity, atomic weights and/or ionization energy. The shear-viscosity for potassium formate tends to drop for temperatures above 80°C. This further supports the theory that higher CaCO₃ particle concentrations in K-formate brines are thermally unstable at higher temperatures.

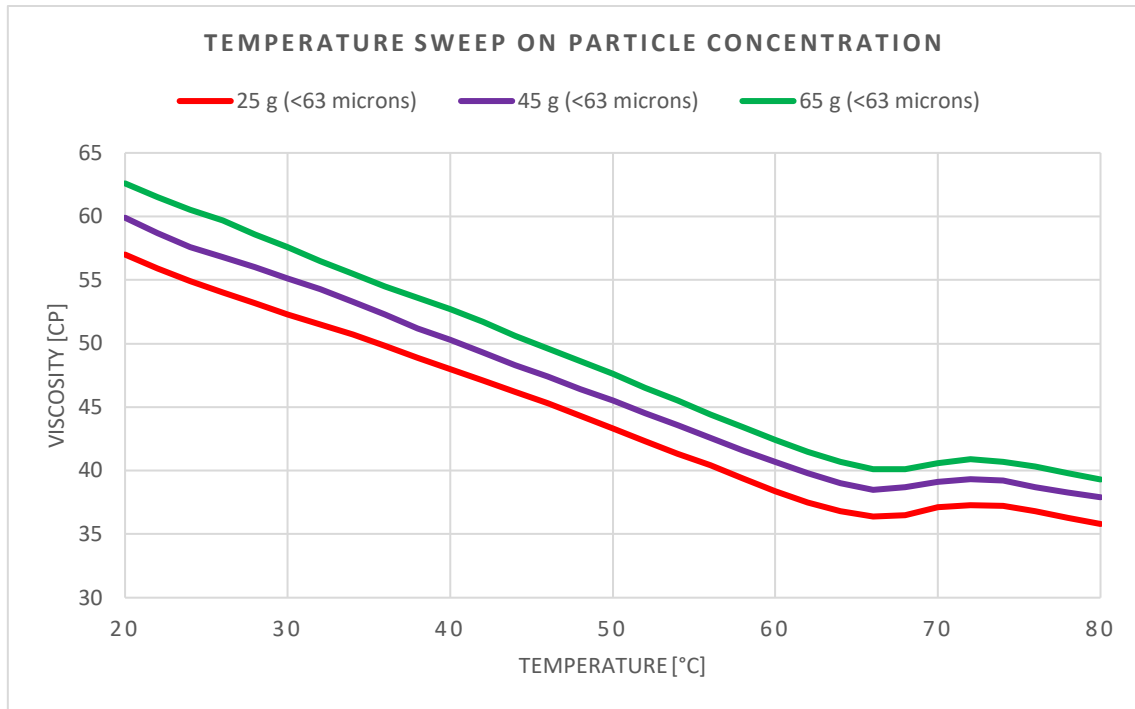


Figure 5.25: Temperature sweeps for the 25g, 45g and 65g CaCO₃ particle concentrations.

5.5.3.2 Effect of CaCO₃ particle concentration on amplitude sweep

The storage and loss moduli increase with increase in CaCO₃ particle concentration. Figure 5.26 presents the strain amplitude sweeps for the 25g, 45g and 65g CaCO₃ particle concentrations.

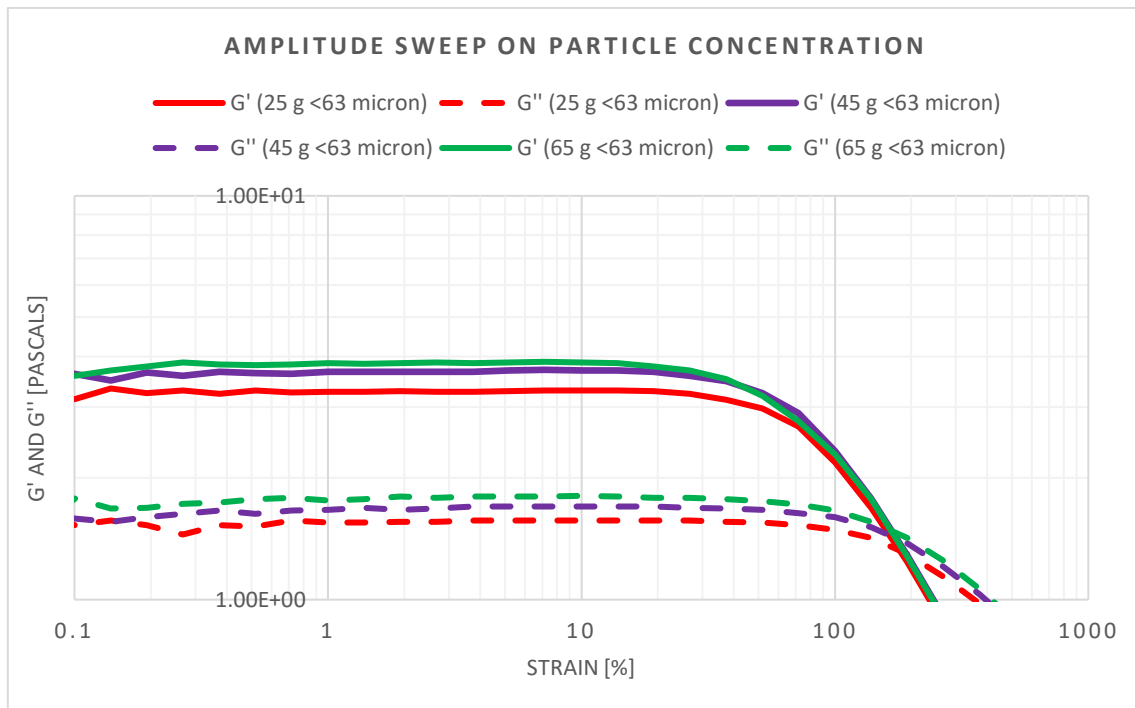


Figure 5.26: Strain amplitude sweeps for 25g, 45g and 65g CaCO₃ particle concentrations.

Important parameters from the strain amplitude sweeps in figure 5.26 is presented in table 5.10. The results show that the LVE range is equal for the two lowest CaCO₃ particle concentrations, hence the 65g are more withstand able to material deformation compared to the other CaCO₃ concentrations. The 65g behaves thermally unstable at higher temperatures based on the rheological properties. However, it still obtains gel-characteristics like the Na-brine based CaCO₃ systems. Increased amount of CaCO₃ particle concentration, increases the yield strengthening effect linearly in K-formate fluids. This trend is not equal for the Na-formate systems where the linear elastic range reaches a plateau value with increase in CaCO₃ particle concentration. This could be since potassium consists of heavier molecules than sodium, hence the mechanical purpose of CaCO₃ particles makes the chemical reaction insignificant with the other mud components, which could improve yield strengthening material effect.

Fluid systems	Strain, γ_L [%]	Yield point, τ_y [Pa]	Flow point, τ_f [Pa]
25 g (<63 microns)	26.8	0.96	3.37
45 g (<63 microns)	26.8	1.07	3.53
65 g (<63 microns)	37.3	1.47	3.51

Table 5.10: Important parameters obtained from the amplitude sweeps for the 25g, 45g and 65g CaCO₃ particle concentrations.

5.6 Test design 6: Effect of CaCO₃ NP's in K-formate drill-in fluid

This subsection presents the results obtained from the nanoparticle-based potassium formate drill-in fluid formulation in section 4.3.3.2.

5.6.1 Effect of CaCO₃ NP's on filtration properties

The fluids were firstly measured for pH before modification. This was to observe whether the CaCO₃ NP's behaved as a pH inhibitor in K-formate fluids. It was observed that the pH did not increase fast enough for the CaCO₃ NP's to possess pH inhibition properties. Hence the samples were modified for pH by addition of 3-4 droplets of 5% NaOH. The modified pH was 11.0, 10.90, 11.12 and 11.48 for the reference fluid, 1wt%, 2.05wt% and 3wt% NP's fluid systems.

Figure 5.27 presents the API filtrate loss at static conditions for the K-formate reference fluid, 1wt%, 2.05wt% and 3wt% NP's. The results show that the filtrate loss increases with increase in NP concentration in K-brines. This could indicate that CaCO₃ NP's compose penetrating

properties in potassium fluids. However, the NP's could have plugged the open pore spaces in-between the micron sized CaCO₃, hence increased the fluids filtrate loss.

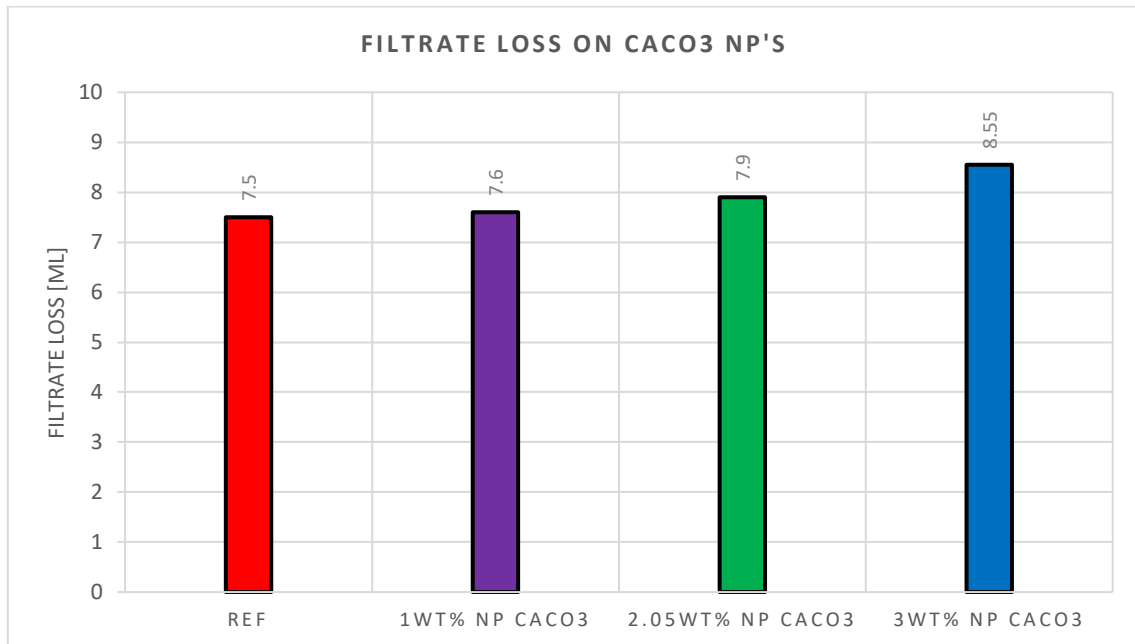


Figure 5.27: API filtrate loss for the reference fluid with 1wt%, 2.05wt% and 3wt% CaCO₃ NP fluid systems.

5.6.2 Effect of CaCO₃ NP's on rheological properties

Figure 5.28 presents the viscometer responses for the NP-based fluid systems at ambient conditions. The results show that the rheology looks approximately the same with increase in CaCO₃ NP's. There is no clear trend in shear stress from the viscometer responses at ambient conditions.

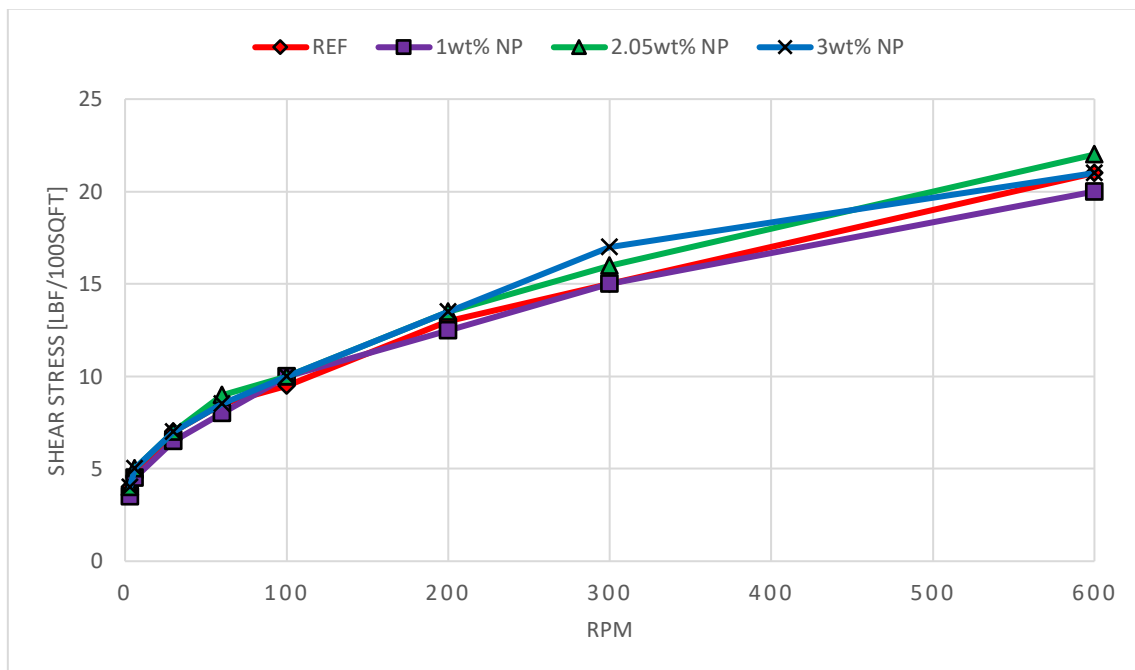


Figure 5.28: Shear stress on rpm for the reference fluid with 1wt%, 2.05wt% and 3wt% CaCO₃ NP's at 20°C.

The max shear stress values from the viscometer responses decreases for all the fluid systems at 50°C. However, CaCO₃ NP's does not show any significant effect on the fluids shear stress. Figure 5.29 presents the rheology for the reference fluid with 1wt%, 2.05wt% and 3wt% NP concentrations at 50°C.

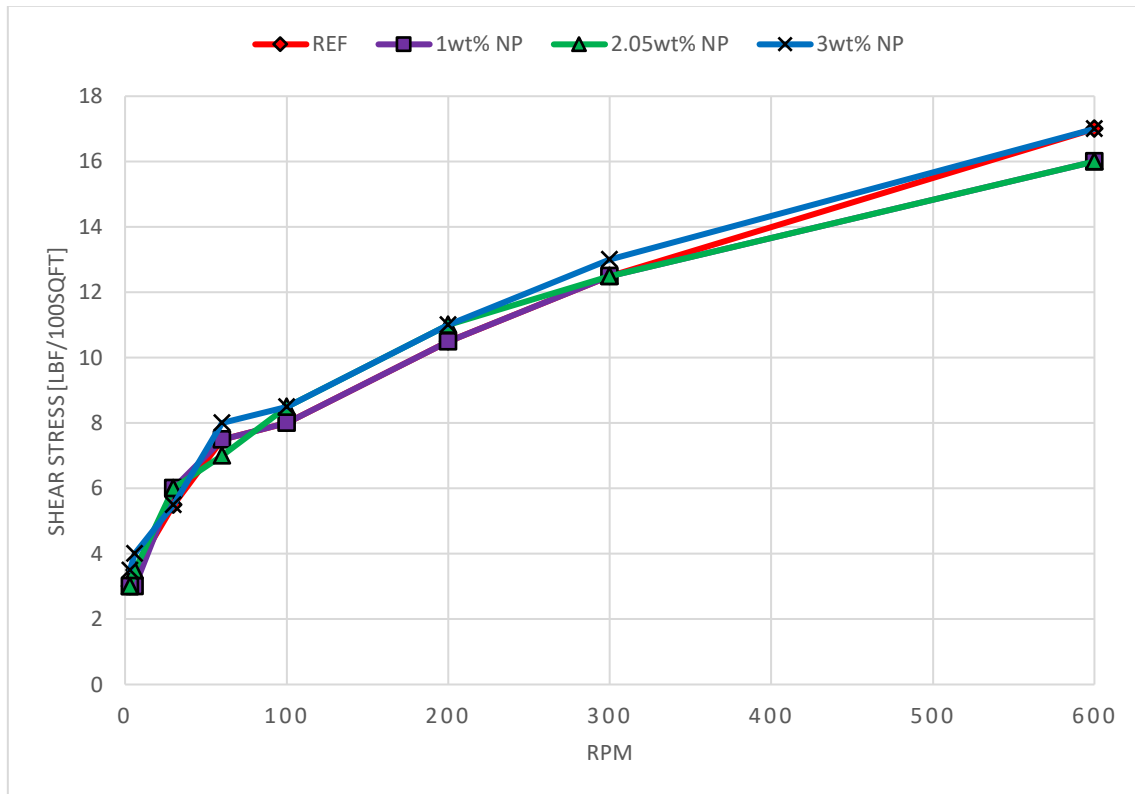


Figure 5.29: Shear stress on rpm for the reference fluid with 1wt%, 2.05wt% and 3wt% CaCO₃ NP's at 50°C.

Figure 5.30 presents the viscometer responses for the reference fluid with 1wt%, 2.05wt% and 3wt% NP's at 80°C. The 2.05wt% and 3wt% NP systems exhibit the highest shear stress compared to the other fluid systems. However, the 1wt% NP concentration shows a less viscous behavior related to the reference fluid. This could indicate that CaCO₃ nanoparticles above a specific weight% are not thermal stable in K-formate systems.

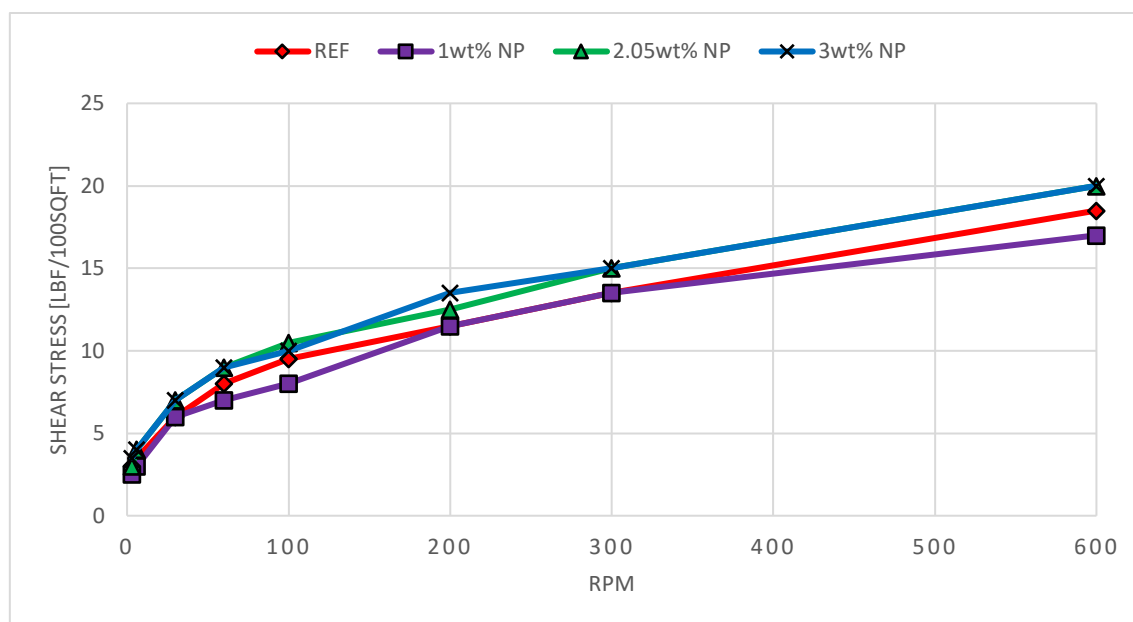


Figure 5.30: Shear stress on rpm for reference fluid with 1wt%, 2.05wt% and 3wt% CaCO₃ NP's at 80°C.

The rheological parameters obtained from the K-formate reference fluid with 1wt%, 2.05wt% and 3wt% CaCO₃ NP's is presented in table 5.11. From the Bingham yield stress, it is shown that none of the fluid systems address optimal cuttings transport performance. The plastic viscosity for the reference fluid and 1wt% NP occurs thermally stable. However, for CaCO₃ NP concentrations >1wt% creates a thermal unstable fluid system in K-brines. This is shown straightforward from the flow and consistency index, were the K-formate reference system occurs as the most thermally stable fluid with temperature increase. Hence increase in CaCO₃ NP concentration tends to decrease the systems thermal stability in potassium.

Rheological parameters	REF			REF + 1wt% CaCO ₃ NP			REF + 2.05wt% CaCO ₃ NP			REF + 3wt% CaCO ₃ NP		
	20°C	50°C	80°C	20°C	50°C	80°C	20°C	50°C	80°C	20°C	50°C	80°C
AV [cP]	10.5	8.5	9.25	10	8	8.5	11	8	10	10.5	8.5	10
PV [cP]	6	4.5	5	5	3.5	3.5	6	3.5	5	4	4	5
YS [lbf/100sqft]	9	8	8.5	10	9	10	10	9	10	13	9	10
LSYS [lbf/100sqft]	3.5	2.5	2.5	2.5	3	2	3	2.5	2	3	3	3
n	0.485	0.443	0.454	0.415	0.356	0.332	0.459	0.356	0.415	0.305	0.387	0.415
k [lbf ⁿ /100sqft]	0.728	0.787	0.794	1.129	1.358	1.699	0.913	1.358	1.129	2.542	1.165	1.129

Table 5.11: Rheological parameters for the reference fluid with 1wt%, 2.05wt% and 3wt% NP's at 20, 50 and 80°C.

5.6.3 Effect of CaCO₃ NP's on viscoelastic properties

5.6.3.1 Effect of CaCO₃ NP's on temperature sweep

Figure 5.31 presents the temperature sweep curves for the K-brines reference fluid with 1wt%, 2.05wt% and 3wt% NP concentrations. CaCO₃ NP's in potassium formate systems does not behave as a viscosity enhancing agent. This justifies the statement that this LCM additive has more mechanical than chemical impact in reservoir drill-in fluids. However, the 2.05wt% and 3wt% nano-based fluids are more viscous over the whole temperature range compared to the reference fluid, and reference + 1wt% NP's. This could be since there is more brine-wetted solid particles in the system. Still, the increase in NP's does not show any significant impact on the apparent viscosity compared to for example increase in xanthan gum polymers.

The structural gel formation starts earlier in the reference system compared to the 1wt% NP concentration in K-brines. Yet, both fluids decrease linearly from ambient conditions measurements, but the 2.05wt% reaches the viscous minima faster than the 3wt% NP's. The gel has formed in all the fluid systems, the 2.05wt% and 3wt% NP's are higher viscous than the reference fluid and 1wt% NP concentration respectively. None of the fluid systems are ideally thermal stable since $\eta \neq \text{constant}$ at higher temperatures.

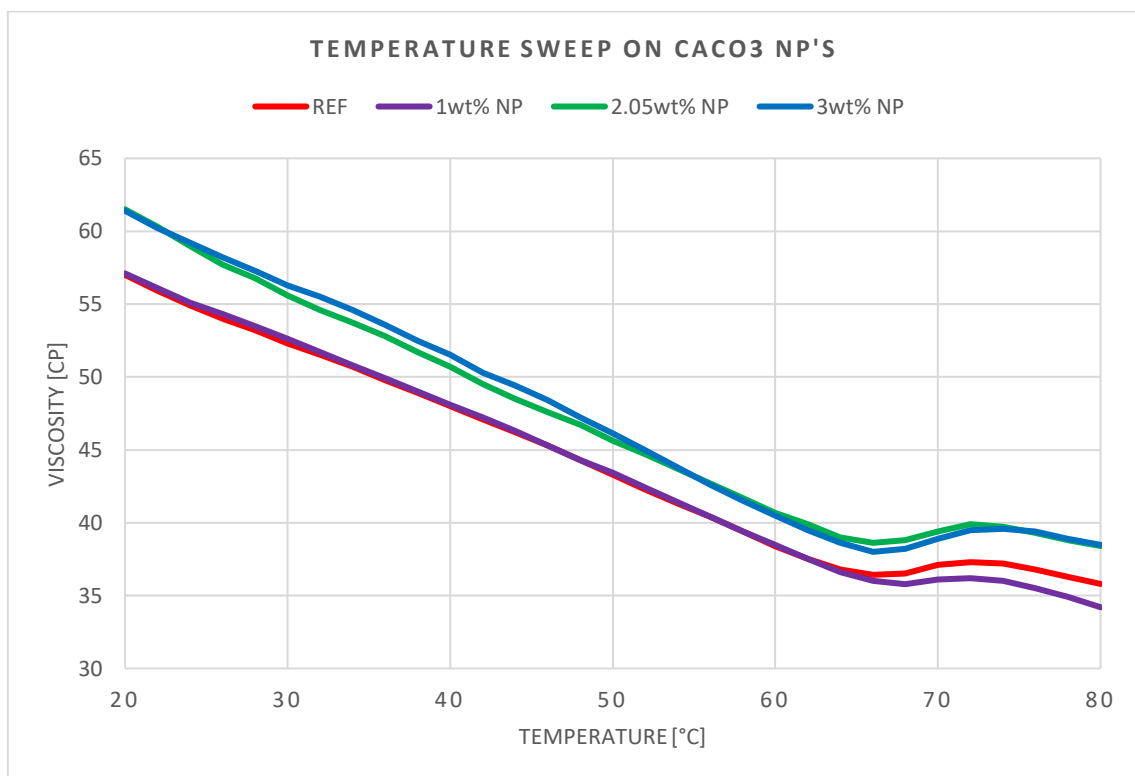


Figure 5.31: Temperature sweeps for the reference fluid with 1wt%, 2.05wt% and 3wt% CaCO₃ NP's.

5.6.3.2 Effect of CaCO₃ NP's on amplitude sweep

The LVE range increases with addition of CaCO₃ NP's in the fluid system, with limit strain equals 26.8% for the reference fluid, and 51.8% for the 1wt%, 2.05wt% and 3wt% NP's respectively. Therefore, CaCO₃ NP's possesses viscoelastic enhancing properties in potassium brines (i.e., more withstand able to material deformation). The most important parameters from the strain amplitude sweeps are summarized in table 5.12.

Fluid systems	Strain, γ_L [%]	Yield point, τ_y [Pa]	Flow point, τ_f [Pa]
REF	26.8	0.96	3.37
1wt% NP	51.8	1.5	3.07
2.05wt% NP	51.8	1.63	3.23
3wt% NP	51.8	1.57	3.07

Table 5.12: Important parameters obtained from the strain amplitude sweeps for the reference fluid, 1wt%, 2.05wt% and 3wt% CaCO₃ NP's.

5.6.4 Effect of CaCO₃ NP's on particle stability

The reference potassium formate-based fluid with 1wt%, 2.05wt% and 3wt% CaCO₃ NP concentrations was cooked after the viscometer measurements at 20, 50 and 80°C. Then the fluid systems were set for 14 days ageing in plastic cups. The solid content in all the uncooked K-brines falls to the bottom in time. Hence two phases are established: one liquid phase and one solid phase.

Figure 5.32 presents the particle stability for the cooked potassium systems. The results show that the K reference fluid, 2.05wt% and 3wt% CaCO₃ NP concentration keeps the solid particles stable in one phase. Hence the solid particles are attached to the brine molecules in the system. However, the reference fluid is in one phase without addition of NP's, and the 1wt% NP addition creates a two-phase fluid system. This could be since the 1wt% NP's does not form enough gel strength to prevent the solid content from settling in time. Yet, from the temperature sweep tests, the 1wt% NP concentration is thermally unstable at higher temperatures and the shear-viscosity drops the most compared to the other nano-based potassium fluids. This could justify that the particle settling speed will increase with correspondingly large fall in viscosity.



Figure 5.32: Particle stability for cooked K-formate reference fluid with 1wt%, 2.05wt% and 3wt% CaCO₃ NP's.

5.7 Test design 7: Effect of CaCO₃ NP's in Na-formate drill-in fluid

This subsection presents the results obtained from the nano-based Na-formate drill-in fluids formulation in section 4.3.3.3.

5.7.1 Effect of CaCO₃ NP's on filtration properties

The fluids were first measured for pH before the API static filtrate loss test. The CaCO₃ NP's did not have pH inhibition properties as the pH did not rise fast enough. Then the fluids were modified for pH by adding 3-4 droplets of 5% NaOH. Hence the fluids pH was 10.78, 10.47 and 11.30 for the 1wt%, 2wt% and 3wt% nano-based Na-brine fluids.

Figure 5.33 presents the API filtrate loss at static conditions for the Na-brine reference fluid with 1wt%, 2wt% and 3wt% NP concentrations. The results express a polynomial trend as the filtrate loss reduces until 2wt% CaCO₃ NP concentration, then the filtrate loss increase to the 3wt% NP's. This could indicate that CaCO₃ LCM possesses non-penetrating characteristics in Na-brine fluids until a certain NP concentration. For CaCO₃ NP concentration >2wt%, the sodium systems could exhibit penetrating properties.

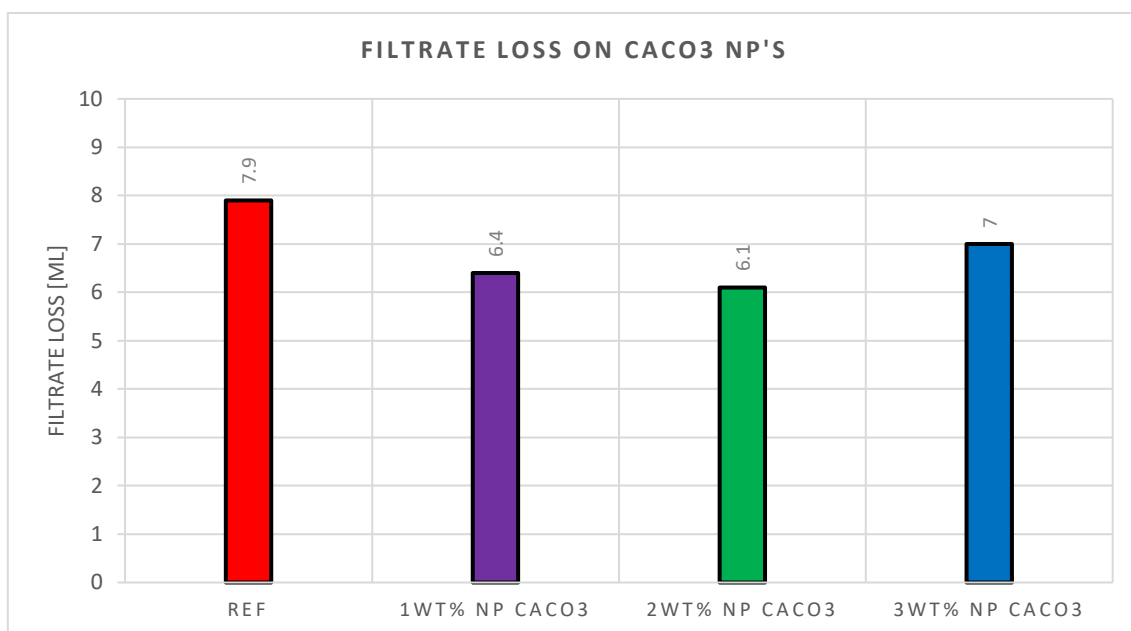


Figure 5.33: API filtrate loss for the reference fluid with 1wt%, 2wt% and 3wt% CaCO₃ NP fluid systems.

5.7.2 Effect of CaCO₃ NP's on rheological properties

Figure 5.34 presents the viscometer responses at ambient conditions for sodium formate reference fluid with 1wt%, 2wt% and 3wt% NP concentrations. Increase in CaCO₃ NP's tends to increase the fluids rheological behavior in Na-brines.

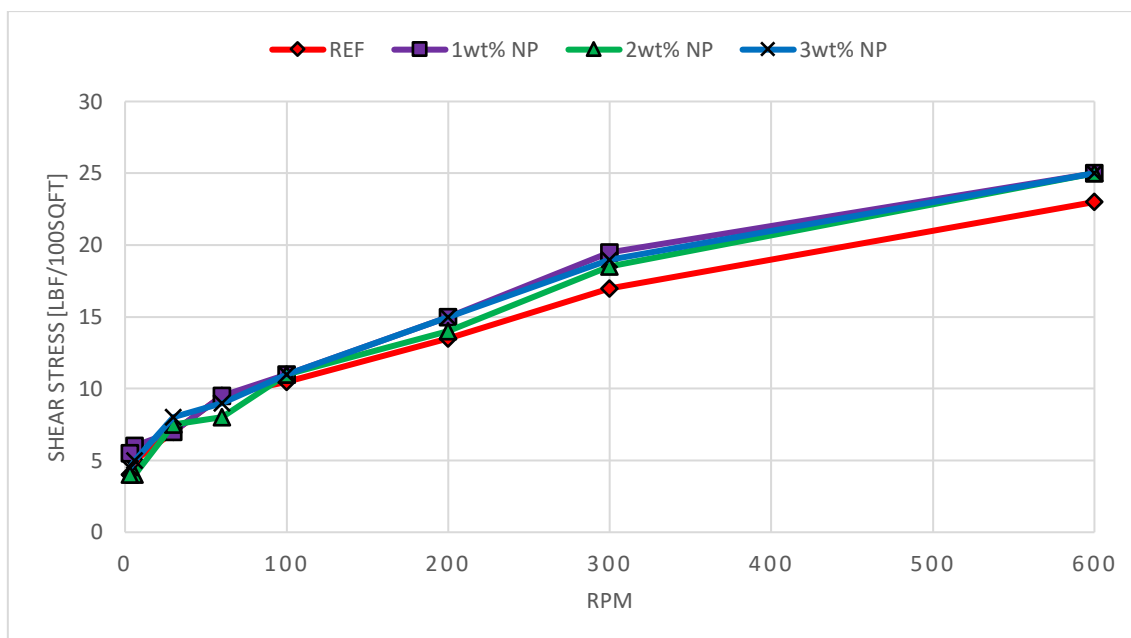


Figure 5.34: Shear stress on rpm for the reference fluid with 1wt%, 2wt% and 3wt% CaCO₃ NP's at 20°C.

The rheology for the nano-based Na-formate fluid looks roughly the same from the viscometer responses at 50°C. Figure 5.35 presents the rheological performance for the sodium reference fluid with additional 1wt%, 2wt% and 3wt% NP concentrations.

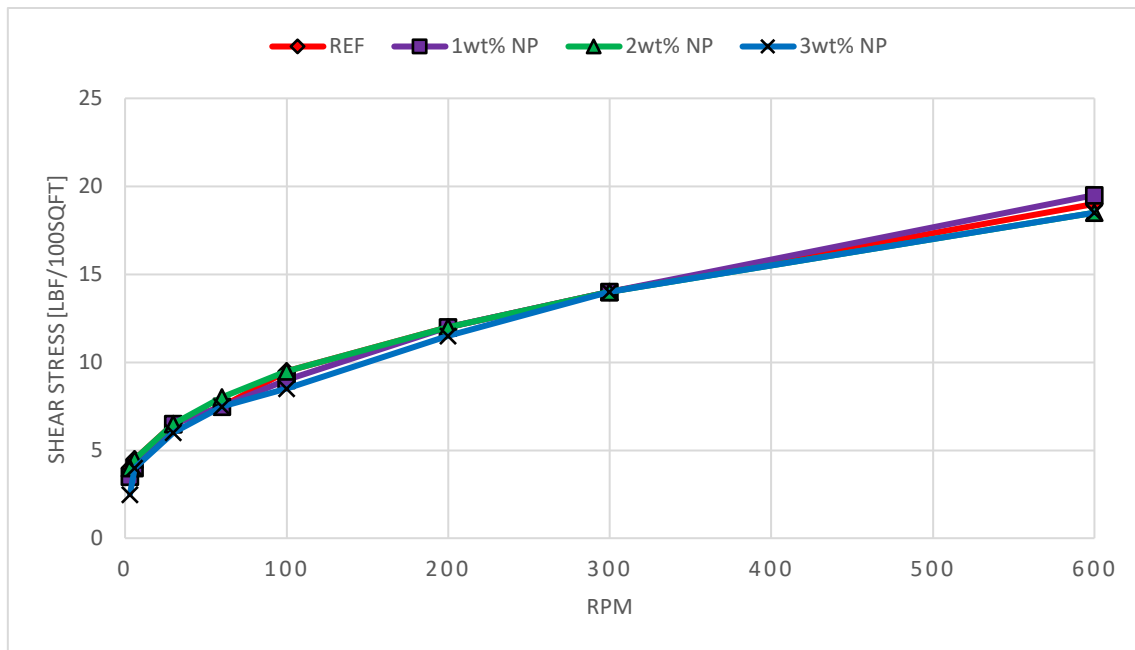


Figure 5.35: Shear stress on rpm for the reference fluid with 1wt%, 2wt% and 3wt% CaCO₃ NP's at 50°C.

Figure 5.36 presents the viscometer responses for the reference fluid with 1wt%, 2wt% and 3wt% NP concentrations at 80°C. The results show that addition of CaCO₃ NP's could make Na-brine systems to behave thermally stable at higher temperatures. However, this needs to be further investigated from the rheological parameters [34, 33, 32]. There is no trend in rheology by increasing CaCO₃ NP's in sodium fluids, hence these nanoparticles do not possess shear stress enhancing properties.

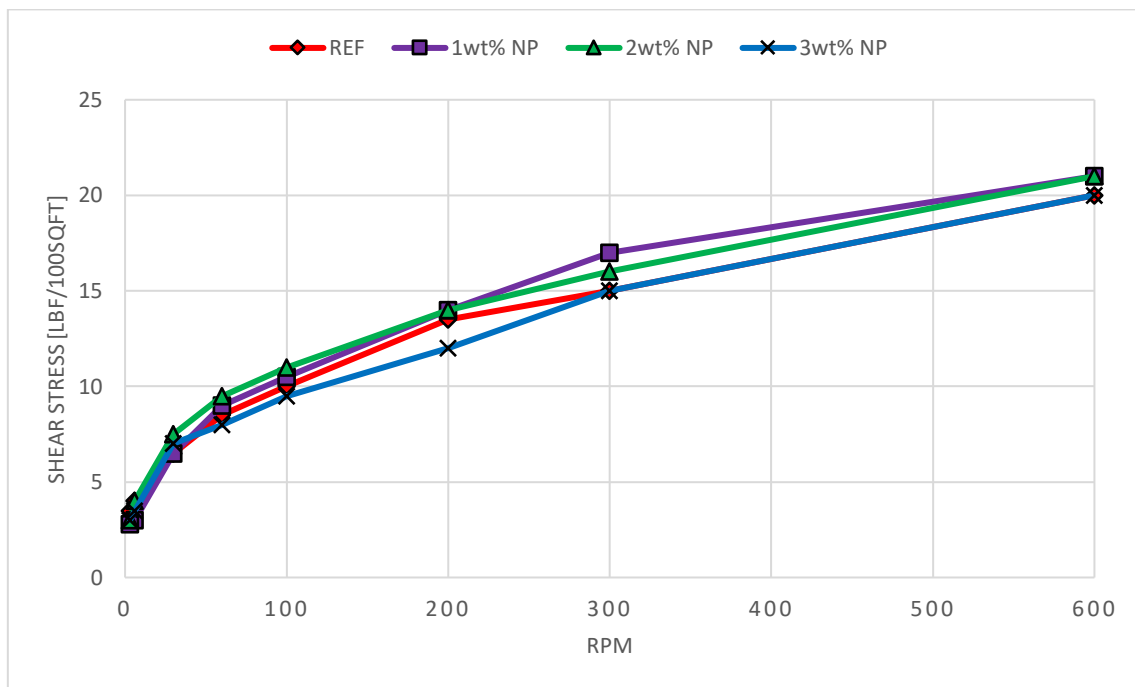


Figure 5.36: Shear stress on rpm for the reference fluid with 1wt%, 2wt% and 3wt% CaCO₃ NP's at 80°C.

From the sodium formate fluids plastic viscosities, more concentrated CaCO₃ NP's in the systems creates a polynomial trended plastic behavior with temperature increase. The Bingham yield stress for the Na 1wt% CaCO₃ and Na 2wt% CaCO₃ NP's at 80°C, are within the optimal range for good cuttings transport from the wellbore. Since the consistency index depends on the fluids flow index, the reference fluid and 1wt% NP concentration are thermally unstable. However, for the 2wt% and 3wt% NP's, the trend seems to be that increase of concentrated CaCO₃ NP's >2wt%, makes the Na-brine systems thermal stable. This trend is straightly opposite in comparison to the nano-based K-formate systems. Thus, whether CaCO₃ NP's could express a thermally stable fluid system or not depends on the brine. The rheological parameters for the nano based CaCO₃ potassium fluids is presented in table 5.13.

Rheological parameters	REF			REF + 1wt% CaCO ₃ NP			REF + 2wt% CaCO ₃ NP			REF + 3wt% CaCO ₃ NP		
	20°C	50°C	80°C	20°C	50°C	80°C	20°C	50°C	80°C	20°C	50°C	80°C
AV [cP]	11.5	9.5	10	12.5	9.75	10.5	12.5	9.25	10.5	12.5	9.25	10
PV [cP]	6	5	5	5.5	5.5	4	6.5	4.5	5	6	4.5	5
YS [lbf/100sqft]	11	9	10	14	8.5	13	12	9.5	11	13	9.5	10
LSYS [lbf/100sqft]	3	3.5	3	5	3	2.6	4	3.5	2	4	1	2.5
n	0.436	0.440	0.415	0.358	0.478	0.305	0.434	0.402	0.392	0.396	0.402	0.415
k [lbf ⁿ /100sqft]	1.122	0.899	1.129	2.088	0.711	2.542	1.234	1.142	1.387	1.611	1.142	1.129

Table 5.13: Rheological parameters for the reference fluid with 1wt%, 2wt% and 3wt% NP's at 20, 50 and 80°C.

5.7.3 Effect of CaCO₃ NP's on viscoelastic properties

5.7.3.1 Effect of CaCO₃ NP's on temperature sweep

Figure 5.37 presents the temperature sweeps for the sodium formate reference fluid with 1 wt%, 2wt% and 3wt% NP concentrations. The fluids shear-viscous performance looks roughly the same to the point where the gel forms in the systems. Then increase in CaCO₃ NP's tends to increase the fluids viscous behavior in Na-brines. Hence the 3wt% CaCO₃ NP concentration reaches a constant viscous plateau value at higher temperatures, hence could possess constant

shear-viscosity for temperatures $> 80^{\circ}\text{C}$. Therefore, these results could justify that CaCO_3 NP's in sodium formate has viscosity enhancing and thermal stability properties. In addition, the nano based systems could exhibit yield strengthening characteristics from the gel formation at higher temperatures.

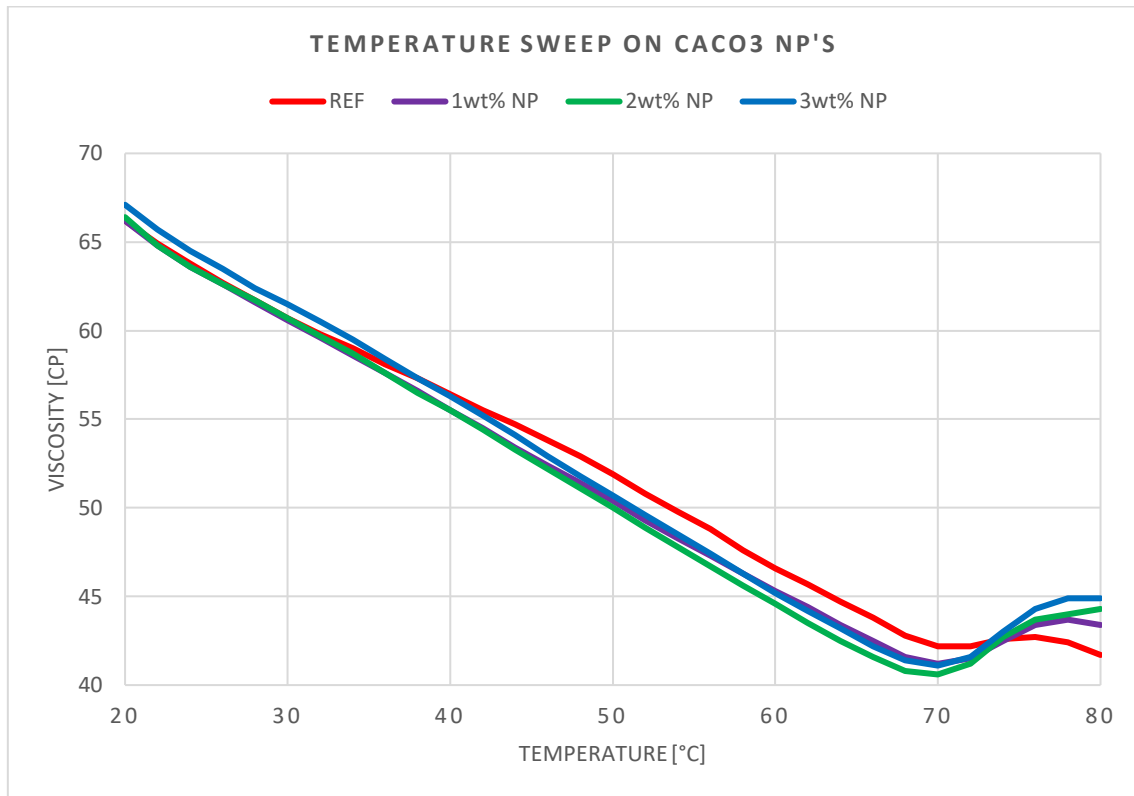


Figure 5.37: Temperature sweeps for the reference fluid with 1wt%, 2wt% and 3wt% CaCO_3 NP's.

5.7.3.2 Effect of CaCO_3 NP's on amplitude sweep

The potassium formate reference fluid and the reference + 1wt% NP system occurs with the same strain limit at the LVE range at 51.8%. In addition, it performs approximately equal values for yield and flow stresses. This could be based on that the chemical bonding is strengthened between cross-linked polymers. For the 2wt% and 3wt% NP's, the strain limit occurs at 37.3%. These results may be justified with respect to that the xanthan gum polymers structures melts, and hence the polymer structure is not bonded in the fluid systems. Therefore, increased amount of CaCO_3 NP's in Na-brines decreases the LVE range, hence drops the fluids flow point. Table 5.14 presents the most important parameters summarized from the strain amplitude sweeps.

Fluid systems	Strain, γ_L [%]	Yield point, τ_y [Pa]	Flow point, τ_f [Pa]
REF	51.8	1.79	3.59
1wt% NP	51.8	1.76	3.58
2wt% NP	37.3	1.48	3.59
3wt% NP	37.3	1.35	3.42

Table 5.14: Important parameters obtained from the strain amplitude sweeps for the reference fluid with 1wt%, 2wt% and 3wt% CaCO₃ NP's.

5.7.4 Effect of CaCO₃ NP's on particle stability

The sodium formate and nano-based CaCO₃ Na-brines were cooked after viscometer measurements and aged for 14 days at ambient conditions. For all the uncooked sodium systems; the particles settled at the bottom in time, hence a two-phase fluid system was established.

Figure 5.38 presents the particle stability for the sodium reference fluid with 1wt%, 2wt% and 3wt% NP concentrations. The results show that CaCO₃ NP's prevents the solid content from falling to the bottom in sodium formate drill-in fluids. This may be since sodium has a high ability to form chemical bonds with other elements. However, the CaCO₃ NP's could enhance gel strengthening effect after the fluid systems have experienced higher temperatures.



Figure 5.38: Particle stability for the cooked Na-formate reference fluid with 1wt%, 2wt% and 3wt% CaCO₃ NP's.

5.8 Test design 8: Effect of Na/K ratios

This subsection presents the results obtained from the Na/K ratio formulations in section 4.3.4.2.

5.8.1 Effect of Na/K ratios on filtration properties

The Na/K blended formate brines were measured for pH before modification of the drill-in fluids. Results showed that the blending and the individual sodium and/or the potassium brine systems measured to be a pH of around 8.5. Hence 3 droplets of 5% NaOH were added to the drill-in fluid systems to modify the pH of the drill-in fluid to a desired range. The modified pH was measured to be 10.36, 10.38 and 10.34 for the Na/K 50/50, 60/40 and 70/30 systems respectively. Figure 5.39 presents the API static filtrate loss test for the Na/K 50/50, 60/40 and 70/30 fluid systems. The 50/50 ratio exhibited the lowest filtrate loss compared to the Na/K 70/30 and 60/40 ratios. This could indicate that all the Na/K ratios behave as penetrating fluids under ambient conditions. It is an interesting observation that there is no trend on filtrate loss for decreased amount of potassium formate in the Na/K brine blending. However, a chemical reaction of the Na/K 60/40 blending resulted in high filtrate loss. The Na/K fluid systems consists of 63-71 microns sized CaCO_3 . This will increase the fluids API filtrate loss independent of brine ratio compared to the <63 microns sized CaCO_3 systems. Due to the unavailability of equipment, the micro-structure and ionic concentrations of the mud cake and the filtrate loss were not further investigated to answer why high filtrate loss occurred for the Na/K 60/40 fluid system.

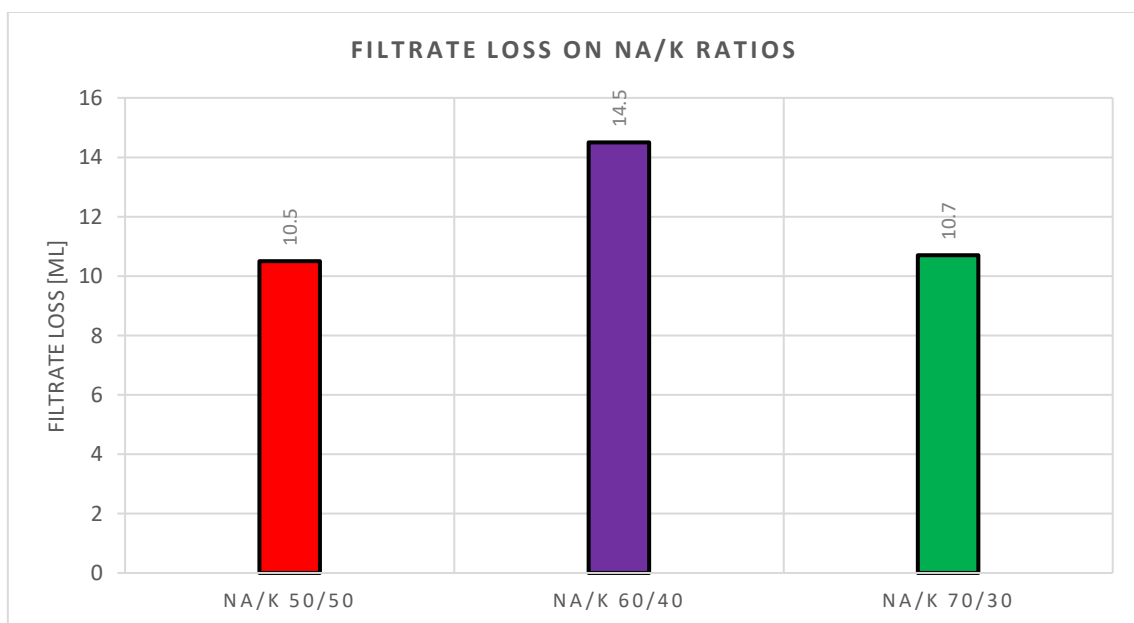


Figure 5.39: API filtrate loss for the Na/K 50/50, 60/40 and 70/30 fluid systems.

5.8.2 Effect of Na/K ratios on rheological properties

The viscometer responses show that the rheology is approximately the same for all the Na/K fluid systems. The rheology at ambient conditions for the Na/K ratios is presented in figure 5.40.

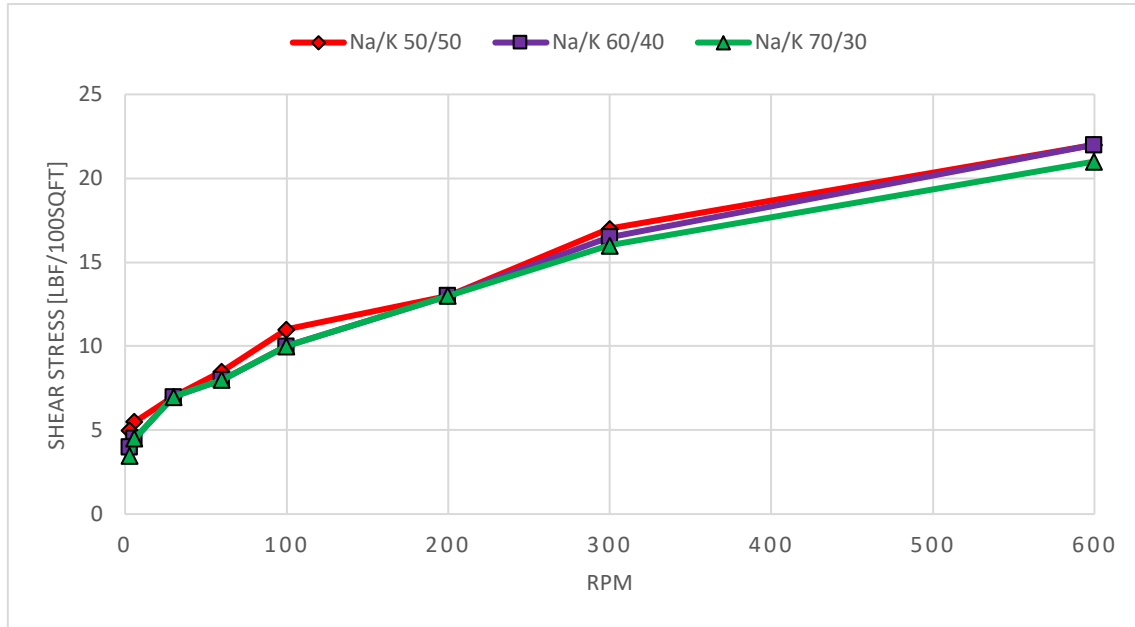


Figure 5.40: Shear stress on rpm for the Na/K 50/50, 60/40 and 70/30 ratios at 20°C.

Figure 5.41 presents the rheological behavior for the Na/K ratios at 50°C. The max shear stress value has decreased for all the brine blended fluids. However, the Na/K 60/40 ratios max shear stress is relatively more affected to temperature increase compared to the other ratios observed from the viscometer responses.

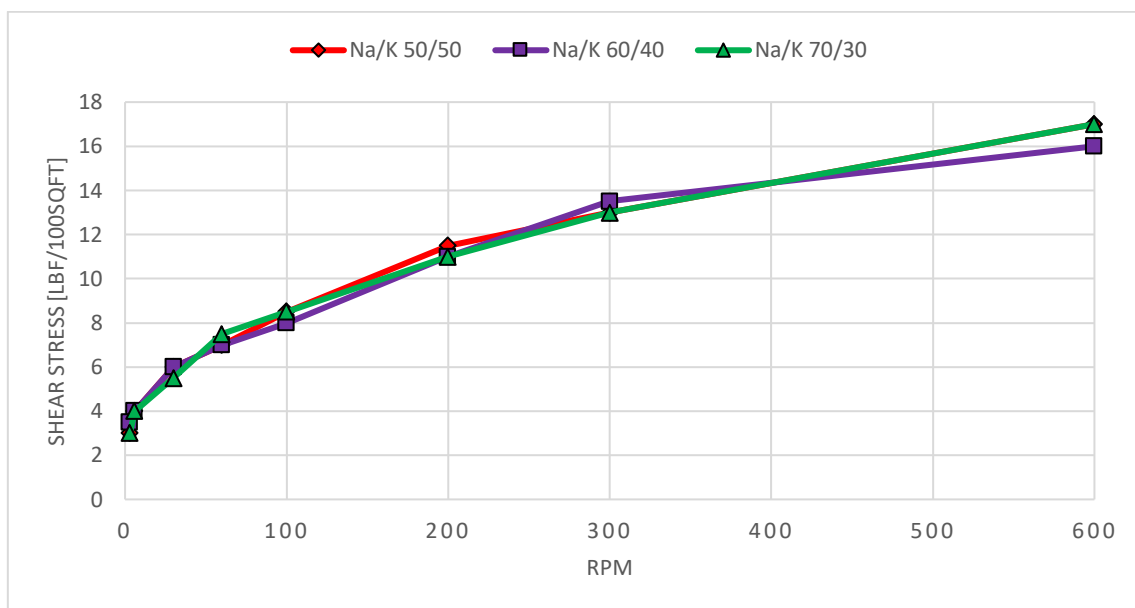


Figure 5.41: Shear stress on rpm for the Na/K 50/50, 60/40 and 70/30 ratios at 50°C.

The viscometer responses express roughly the same shear stress at higher temperatures. Figure 5.42 presents the rheology for the Na/K 50/50, 60/40 and 70/30 ratios at 80°C.

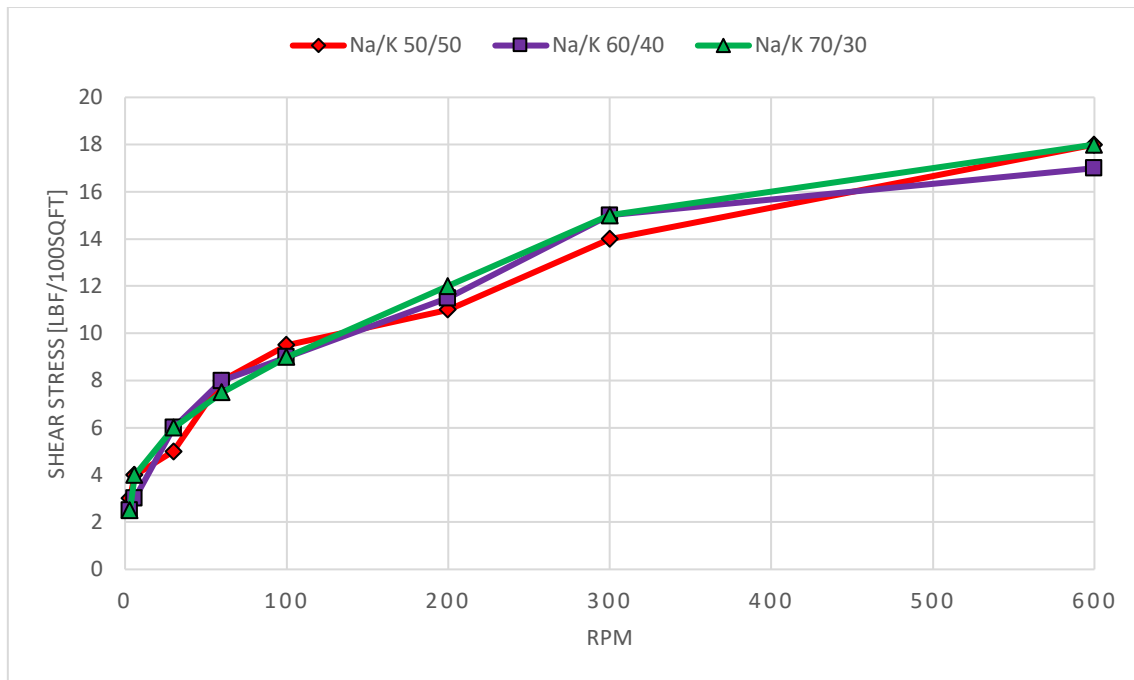


Figure 5.42: Shear stress on rpm for the Na/K 50/50, 60/40 and 70/30 ratios at 80°C.

Rheological parameters for the Na/K 50/50, 60/40 and 70/30 ratios are presented in table 5.15. The plastic viscosity tends to linearly decrease with more sodium formate in the system. However, the fluids flow and consistency index express a less thermal stable system at higher temperatures with more sodium brine present. Since the CaCO_3 particle concentration is 25g from the D50 range (63-71 microns) and equal for all fluids, the chemical reaction between sodium and potassium at molecular level could be the explanation regarding thermal instability issues at higher temperatures. However, from the CaCO_3 particle concentration (<63 microns) analysis separately in sodium and potassium systems; these results are expected since the 25g CaCO_3 particle concentration behaved thermally stable in potassium formate, and not thermally stable in sodium formate. Therefore, in Na/K ratio-based drill-in fluids at low CaCO_3 LCM concentrations, the increased amount of sodium reduces the systems thermal stability at higher temperatures.

Rheological parameters	Na/K 50/50			Na/K 60/40			Na/K 70/30		
	20°C	50°C	80°C	20°C	50°C	80°C	20°C	50°C	80°C
AV [cP]	11	8.5	9	11	8	8.5	10.5	8.5	9
PV [cP]	5	4	4	5.5	2.5	2	5	4	3
YS [lbf/100sqft]	12	9	10	11	11	13	11	9	12
LSYS [lbf/100sqft]	4.5	2	2	3.5	3	2	2.5	2	1
n	0.372	0.387	0.362	0.415	0.245	0.180	0.392	0.387	0.263
k [lbf ⁿ /100sqft]	1.673	1.165	1.461	1.242	2.930	4.868	1.387	1.165	2.911

Table 5.15: Rheological parameters for the Na/K 50/50, 60/40 and 70/30 ratios at 20, 50 and 80°C.

5.8.3 Effect of Na/K ratios on viscoelastic properties

5.8.3.1 Effect of Na/K ratios on temperature sweep

Figure 5.43 presents the temperature sweeps for the Na/K 50/50, 60/40 and 70/30 ratios. Increased percentage of Na-formate in the Na/K-formate blending decreases the systems shear-viscosity. This could be since the atomic weight of potassium is larger than sodium formate, consequently the reduction of potassium atoms itself could reduce the viscosity in the Na/K blend. However, sodium has a higher electronegativity than potassium, and hence the chemical reaction should gel-strengthen the fluids due to higher ability to form chemical bonds. Since all the fluids consists of 25g CaCO₃ (63-71 microns), the Na/K 70/30 ratio exhibits thermally stable viscosity at higher temperatures. This could be since larger CaCO₃ particle sizes expressed minimal thermal stability properties. The Na/K 70/30 and 50/50 ratios show better yielding effect than the 60/40 ratio from temperature sweep analysis.

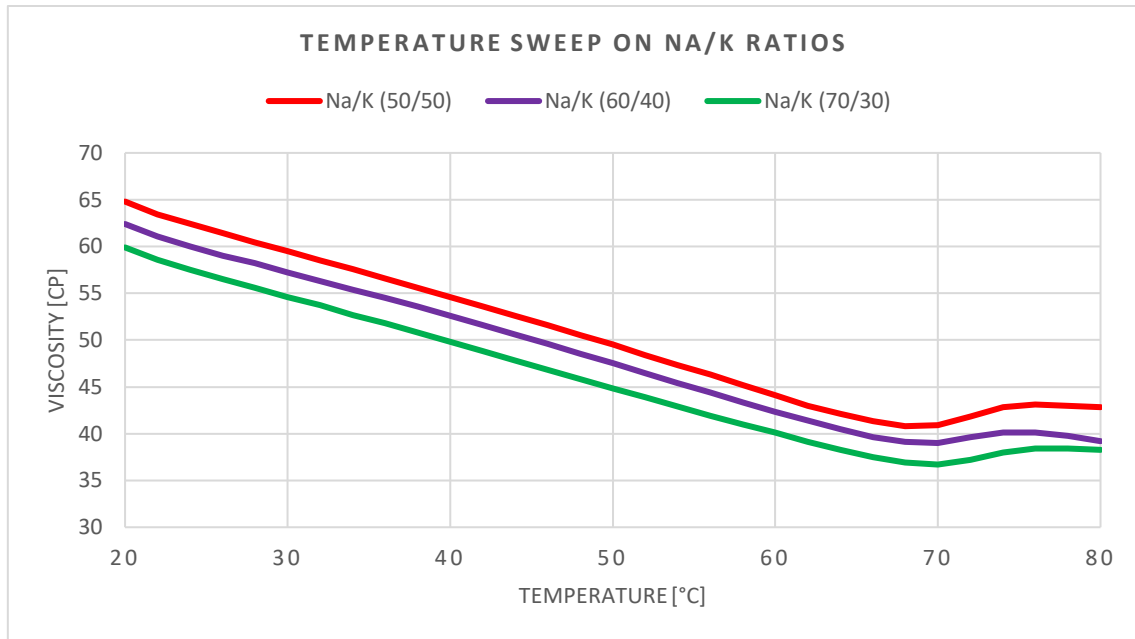


Figure 5.43: Temperature sweeps for the Na/K 50/50, 60/40 and 70/30 ratios.

5.8.3.2 Effect of Na/K ratios on amplitude sweep

Increased amount of sodium formate in the Na/K blending does not show a linear trend on the storage and loss moduli. The storage and loss modulus for the Na/K 60/40 ratio is accordingly below the 70/30 moduli. Nonetheless, the Na/K 50/50 ratio shows higher gel-like consistency in the LVE range compared to the Na/K 70/30 and 60/40 ratios. Strain amplitude sweep tests for the Na/K ratios are presented in figure 5.44.

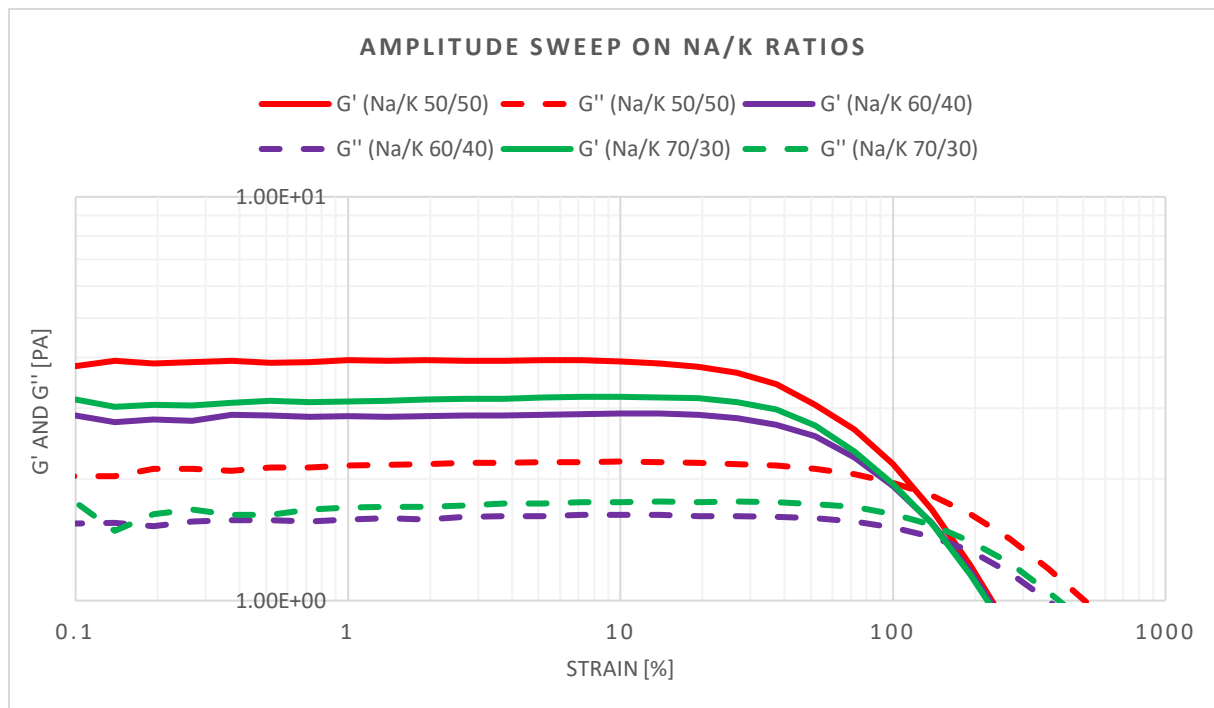


Figure 5.44: Strain amplitude sweeps for the Na/K 50/50, 60/40 and 70/30 ratios.

The LVE range for the Na/K 50/50 ratio is elongated to 51.8% compared to the 60/40 and 70/30 ratios at 37.3% respectively. Increased percentage of sodium formate atoms in the Na/K blending decreases the flow point. However, the yield point does not show a linear trend for the same Na/K ratios. The most important parameters obtained from strain amplitude sweep tests is summarized in table 5.16.

Fluid systems	Strain, γ_L [%]	Yield point, τ_y [Pa]	Flow point, τ_f [Pa]
Na/K 50/50	51.8	1.93	3.23
Na/K 60/40	37.3	1.18	3.14
Na/K 70/30	37.3	1.29	3.04

Table 5.16: Important parameters obtained from the strain amplitude sweeps for the Na/K 50/50, 60/40 and 70/30 ratios.

5.9 Test design 9: Characterization of modified Cs/K drill-in fluid

5.9.1 Effect of Cs/K on pH and density properties

The fluid systems were measured for pH and density before the API static filtrate loss test were applied. Both the high viscous and less viscous Cs/K fluid systems behaved as a pH inhibitor, and hence no addition of 5% NaOH were added. Then the density was measured by use of a traditional mud weight. The density of the high viscous Cs/K were higher compared to the less viscous Cs/K. This is expected since there are more solid particles in the higher viscous than the less viscous system. The pH and density for the Cs/K fluid systems is presented in table 5.17.

Fluid systems	pH	Density (s.g)
High viscous Cs/K	10.61	2.02
Less viscous Cs/K	10.84	2.00

Table 5.17: pH and density for the high viscous Cs/K and less viscous Cs/K fluid systems.

5.9.2 Effect of polymer mix on filtration and rheological properties

During the fluid characterization process, it was observed that the polymer particles were attached to the wall at the fluid bottles. Then it was decided to mix the Cs/K fluid systems 15 min extra to dissolve the polymers better. Figure 5.45 presents the high viscous Cs/K observed before and after 15 min extra polymer mix during the amplitude sweep tests. The polymers are

well uniform distributed into the fluid system in the right picture, in contrast to the left picture where the polymers are not homogenous blended.

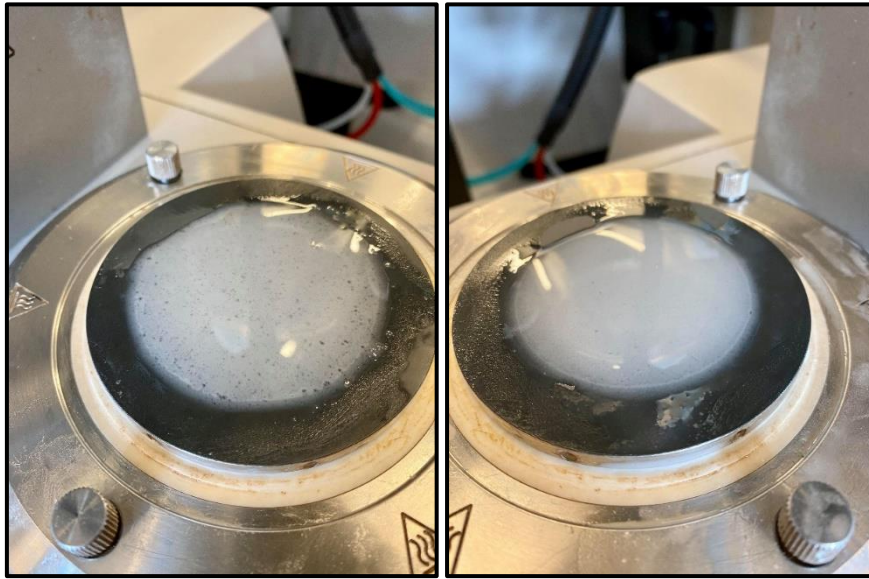


Figure 5.45: Left: High viscous Cs/K before extra mix. Right: High viscous Cs/K after 15 min extra mix.

Figure 5.46 presents the API static filtrate loss test performed for the high viscous and less viscous Cs/K before and after extra polymer mix. The results show that when more polymers are uniformly blended into the fluid system, the filtrate loss is reduced. However, this result is expected from the results in API filtrate loss performance in test design 1 and test design 3. The filtrate loss for the high viscous Cs/K system is reduced compared to the less viscous Cs/K fluid system, both before and after extra polymer mix.

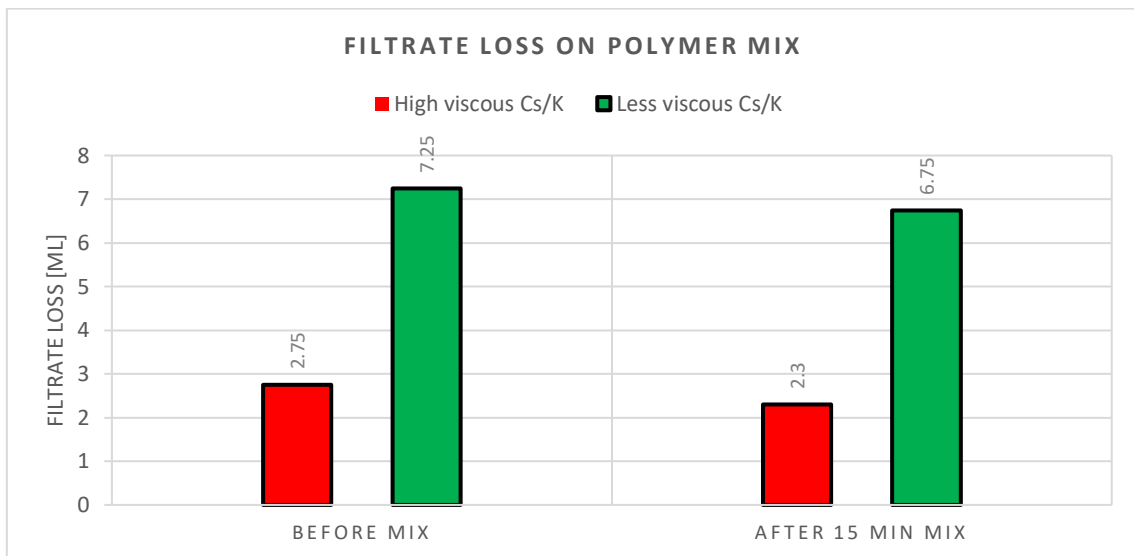


Figure 5.46: API filtrate loss test performed before and after extra polymer mix for the high viscous and less viscous Cs/K fluids.

The rheology for the high viscous Cs/K is presented in figure 5.47. The viscometer measurements were performed at room temperature, to avoid unnecessary waste of the cesium/potassium fluid after cooking at 50°C and 80°C. Hence the fluid could be re-used for rheometer tests. It is shown from figure 5.47, that the viscosity increases for the high viscous Cs/K with uniformly blended polymers, contra non-uniformly blended polymers.

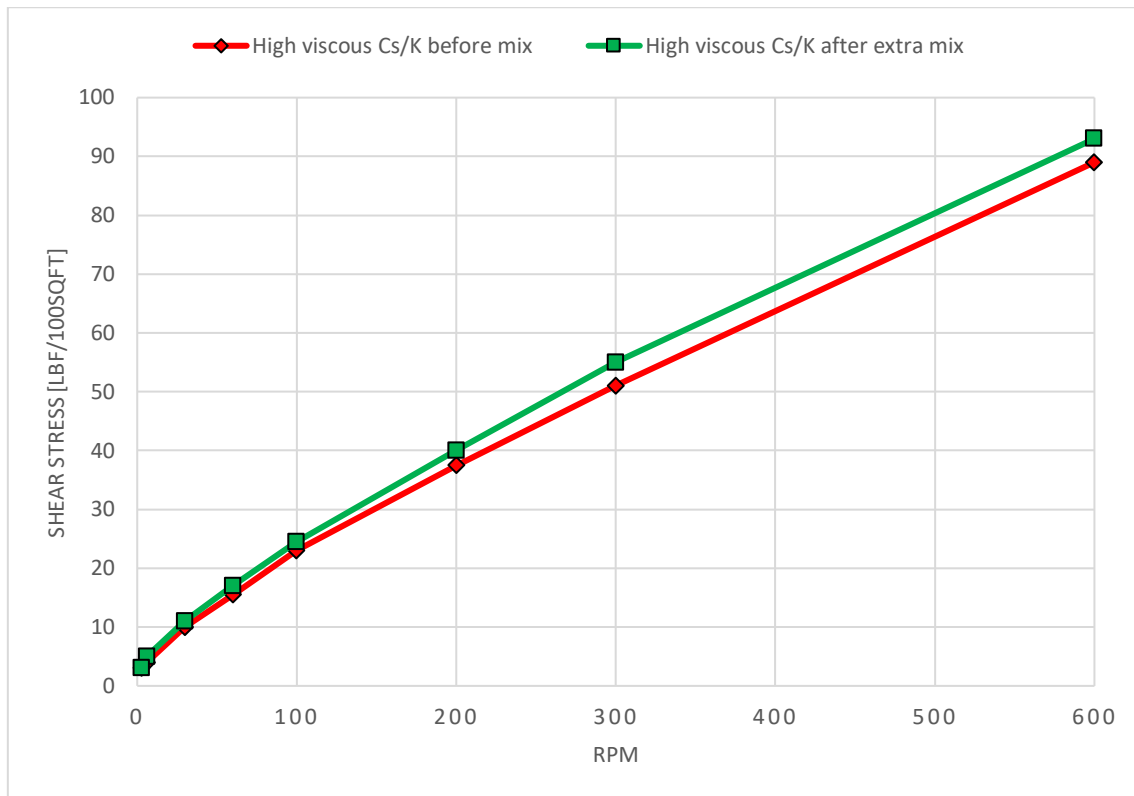


Figure 5.47: Shear stress on rpm for the high viscous Cs/K fluid system at 20°C.

The less viscous Cs/K system exhibit a higher shear stress after extra polymer mix, except from the maximum shear stress for the fluid system at 600 rpm reading. Hence the uniform distribution of polymers within the system has a better impact on the high viscous Cs/K compared to the less viscous Cs/K system at ambient conditions. Figure 5.48 presents the viscometer responses for the less viscous Cs/K system before and after 15 min extra polymer mix.

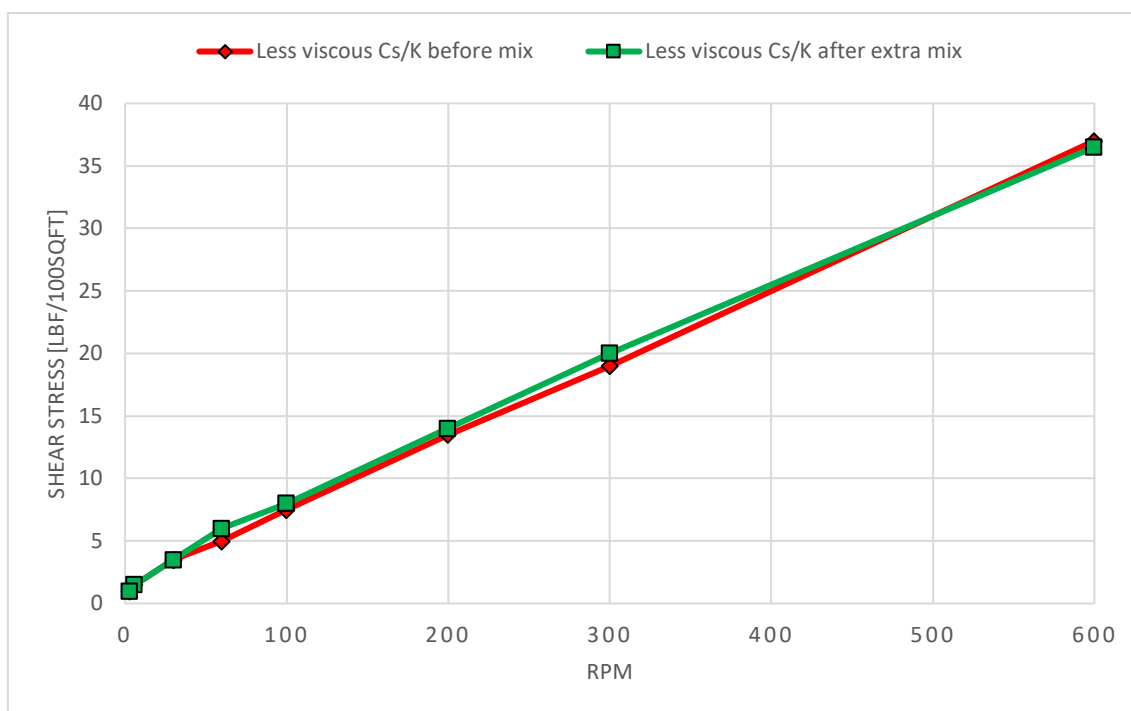


Figure 5.48: Shear stress on rpm for the less viscous Cs/K fluid system at 20°C.

The rheological parameters for the high viscous and less viscous Cs/K before and after extra xanthan gum mix are summarized in table 5.18. The plastic viscosity for the high viscous Cs/K is the same before and after extra polymer mix, compared to the less viscous Cs/K fluid system where the PV decreases after extra mixing. However, the Bingham yield stress increases for both cesium/potassium-based fluid systems after 15 min extra polymer mix.

Rheological parameters	High viscous Cs/K before mix	High viscous Cs/K after extra mix	Less viscous Cs/K before mix	Less viscous Cs/K after extra mix
AV [cP]	44.5	46.5	18.5	18.25
PV [cP]	38	38	18	16.5
YS [lbf/100sqft]	13	17	1	3.5
LSYS [lbf/100sqft]	2	1	0.5	0.5
n	0.803	0.757	0.961	0.867
k [lbf ⁿ /100sqft]	0.341	0.489	0.047	0.089

Table 5.18: Rheological parameters for the high viscous and less viscous Cs/K before and after extra polymer mix.

5.9.3 Effect of Cs/K ageing on rheological properties

The high viscous fluid system was tested right away after mixing containing air in the system and after 3 days of ageing at ambient conditions. The results show that the high viscous Cs/K are much higher viscous after 3 days of ageing. This could be since the additives may undergo chemical reactions in time and forming a gel structure. Figure 5.49 presents the 3 days static ageing effect for the high viscous Cs/K at room temperature.

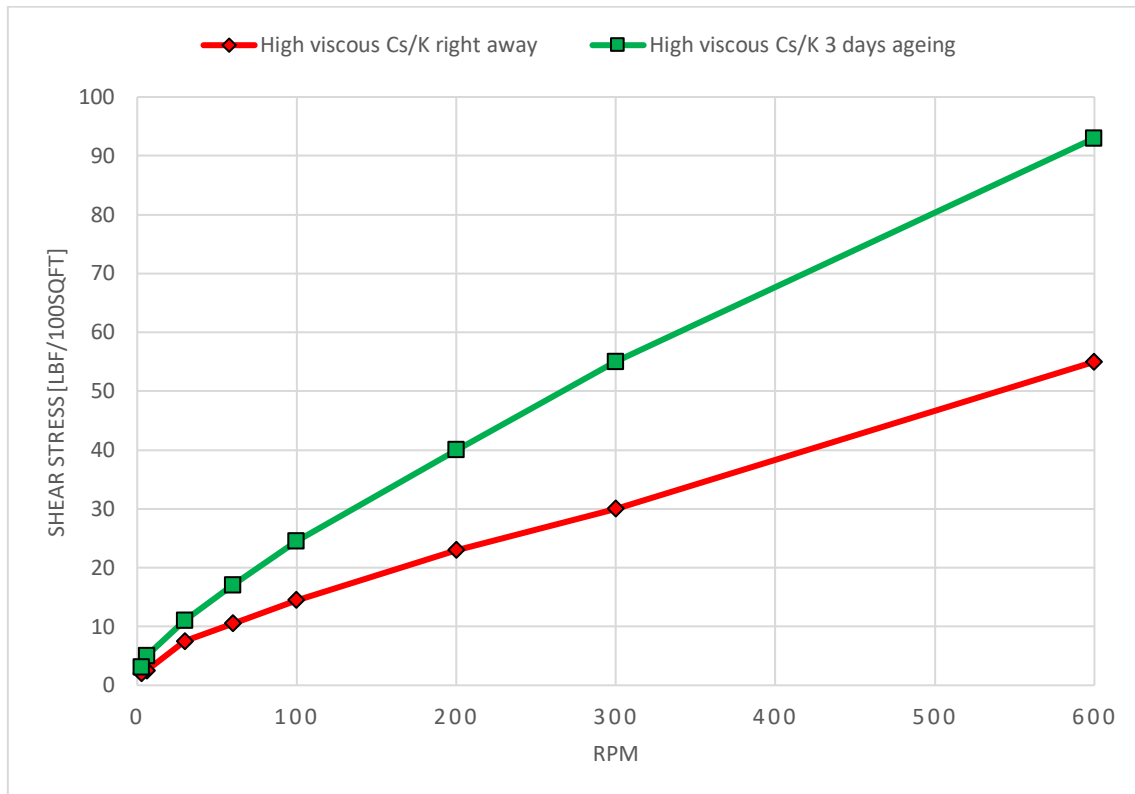


Figure 5.49: Shear stress on rpm for the high viscous Cs/K tested right away and after 3 days of ageing at 20°C.

Table 5.19 presents the rheological parameters obtained from the viscometer responses for the high viscous Cs/K. The results show that cesium/potassium systems possess ageing effect at static conditions. This could be justified as the AV, PV, and Bingham yield stress increases in time. Hence the Bingham yield stress is within the Martin Linge range after 3 days of ageing.

Rheological parameters	High viscous Cs/K tested right away	High viscous Cs/K 3 days ageing
AV [cP]	27.5	46.5
PV [cP]	25	38
YS [lbf/100sqft]	5	17
LSYS [lbf/100sqft]	1.5	1
n	0.874	0.757
k [lbfⁿ/100sqft]	0.129	0.489

Table 5.19: Rheological parameters for the high viscous Cs/K tested right away and after 3 days static ageing.

5.9.4 Effect of modified Cs/K on viscoelastic and rheological properties

5.9.4.1 Effect of modified Cs/K on temperature sweep

The Sinomine brine received from industry, were modified for drilling according to table 4.10 and 4.11. It was performed temperature sweeps for the modified Cs/K fluid to compare with the unmodified cesium/potassium brine. The results show that both the modified Cs/Ks are higher viscous than the unmodified brine. However, the higher viscous Cs/Ks apparent viscosity are much higher compared to the less viscous Cs/K. The higher viscous cesium/potassium system shows stronger gel strength at higher temperatures compared to the less viscous Cs/K. Figure 5.50 presents the temperature sweep performance for the unmodified Sinomine brine, high viscous modified Cs/K, and less viscous modified Cs/K.

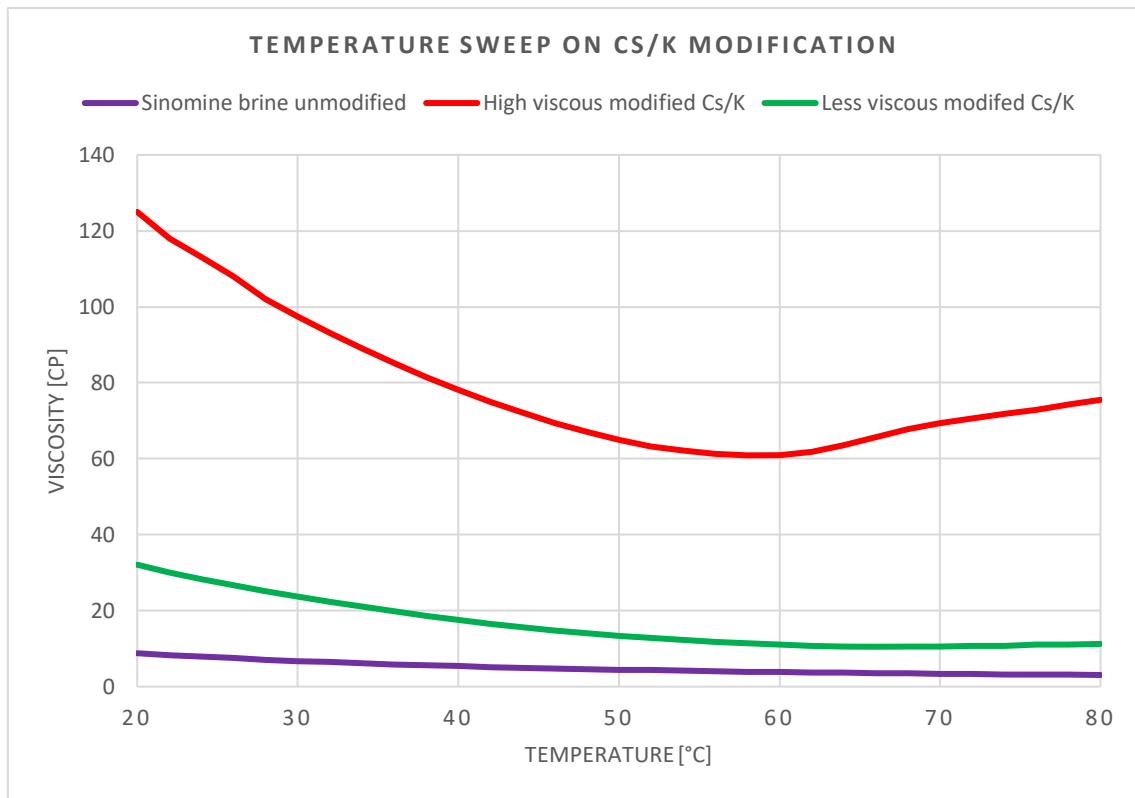


Figure 5.50: Temperature sweeps for the unmodified Sinomine, high viscous modified Cs/K, and less viscous modified Cs/K fluids.

5.9.4.2 Effect of modified high viscous Cs/K on temperature

The modified high viscous Cs/K were further tested for shear stress on shear rate for 50°C and 80°C at the rheometer. Figure 5.51 presents the viscosity for the high viscous Cs/K on a logarithmic scale. In addition, the fluids shear stress is plotted linearly for increased shear rates. The high viscous Cs/K is more viscous at 80°C than 50°C for the whole shear rate range. However, for shear rate values $> 400 \text{ s}^{-1}$, turbulence may occur in the fluid system. Therefore, the x-axis is limited to approximately 500 s^{-1} shear rate.

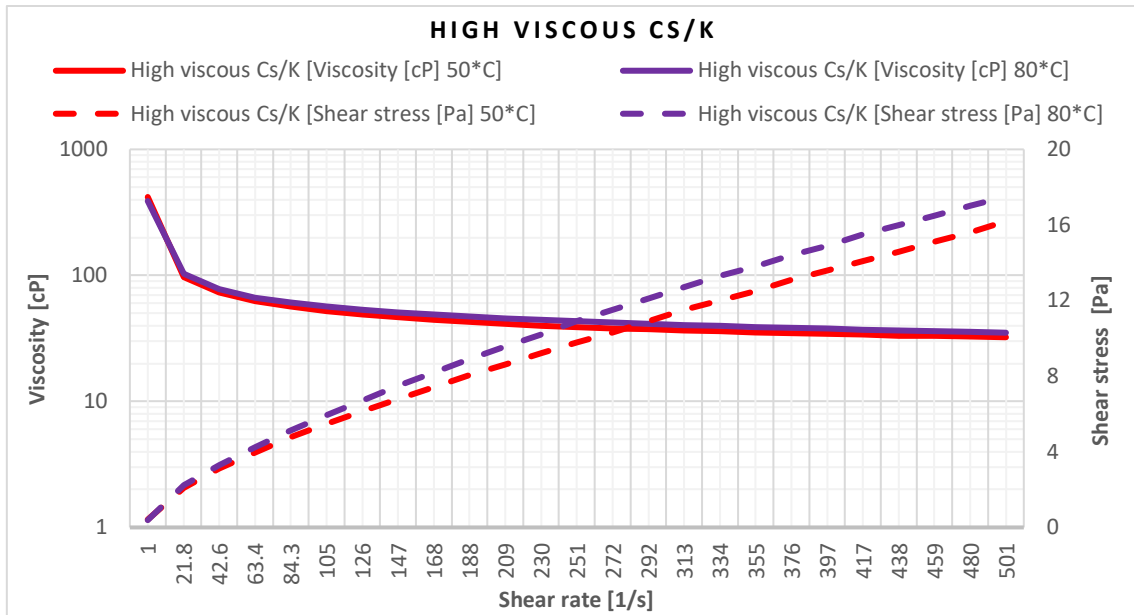


Figure 5.51: Shear stress on shear rate for the high viscous modified Cs/K fluid at 50°C and 80°C.

5.9.4.3 Effect of modified less viscous Cs/K on temperature

Figure 5.52 presents the temperature effect for the less viscous Cs/K fluid system. The results show that the fluid system is higher viscous at 50°C compared to 80°C at lower shear rates (i.e., until approximately 168 s⁻¹ shear rate). Hence the trend shifts, and the fluid system is relatively higher viscous at 80°C than 50°C for increasing shear rates. The less viscous Cs/K seems to have a Newtonian fluid behavior for both temperatures to the 459 s⁻¹ shear rate. However, from this point the shear stress at 80°C starts to increase.

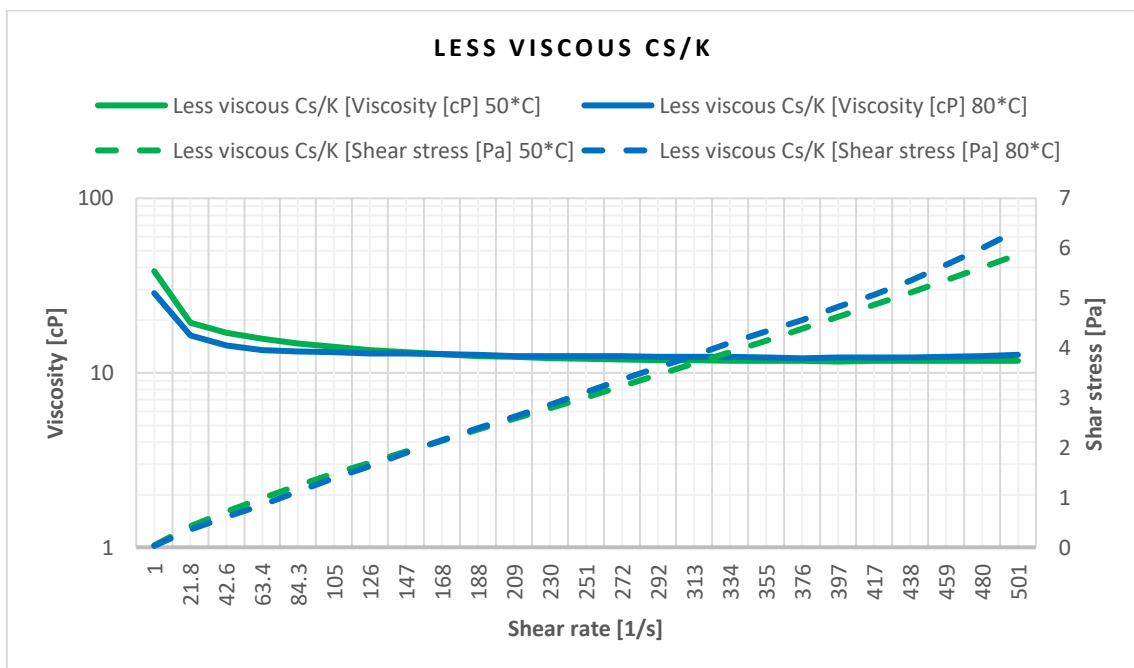


Figure 5.52: Shear stress on shear rate for the less viscous modified Cs/K fluid at 50°C and 80°C.

5.9.4.4 Effect of modified Cs/K leftover mud on temperature

The modified Cs/K leftover mud is based on that an equal amount of the less viscous Cs/K + high viscous Cs/K (1:1 ratio) is blended. Hence it is referred to as the less viscous/ high viscous 50/50 Cs/K ratio. Figure 5.53 presents the shear stress flow curve for the Cs/K 50/50 ratio. The fluid systems shear stress is slightly lower at 50°C compared to 80°C with increased shear rates.

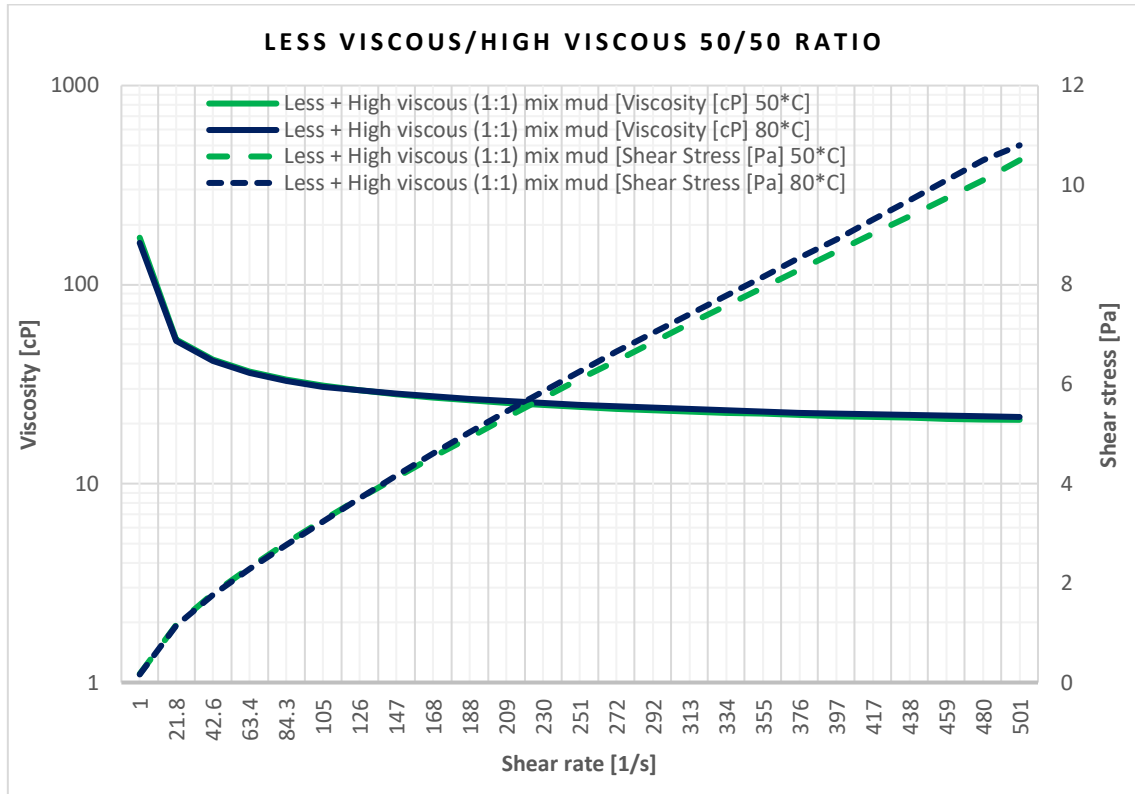


Figure 5.53: Shear stress on shear rate for the Cs/K 50/50 ratio at 50°C and 80°C.

5.9.4.5 Viscosity comparison between modified Cs/K fluids on lower shear rates

Figure 5.54 presents the viscosity for the less viscous Cs/K, high viscous Cs/K and Cs/K 50/50 ratio at the lower shear rates. The results show that the viscous behaviour of the 50/50 Cs/K ratio lies in-between the higher viscous and less viscous Cs/K fluid systems. With increasing shear rates, the viscosity gap shrinks between the fluid systems. The 50/50 Cs/K ratio is the most thermal stable system at lower shear rates, compared to the higher viscous Cs/K and less viscous Cs/K fluids.

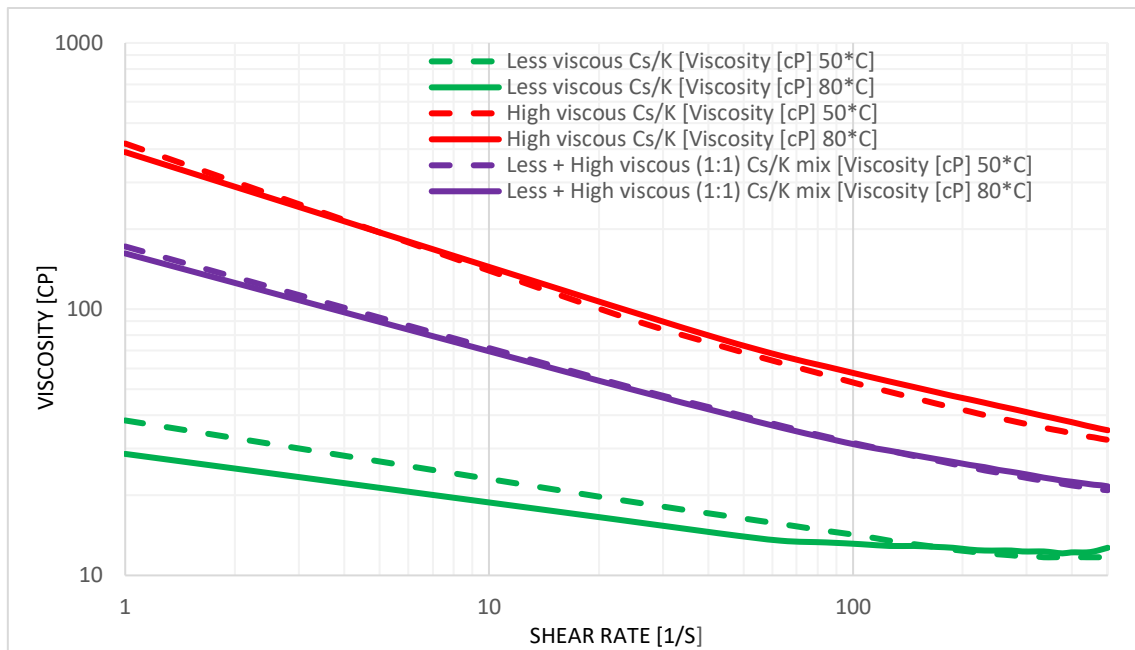


Figure 5.54: Viscosity comparison between the high viscous Cs/K, less viscous Cs/K and 50/50 Cs/K ratio for lower shear rates at 50°C and 80°C.

5.9.4.6 Flow comparison between modified Cs/K fluids at higher temperatures

Figure 5.55 presents the flow comparison between the high viscous Cs/K, less viscous Cs/K and 50/50 Cs/K ratio at higher temperatures. The flow curve of the 50/50 ratio lies in-between the higher viscous and less viscous Cs/K fluid systems. The 50/50 Cs/K ratio is still the most thermal stable fluid system over the whole shear rate spectrum.

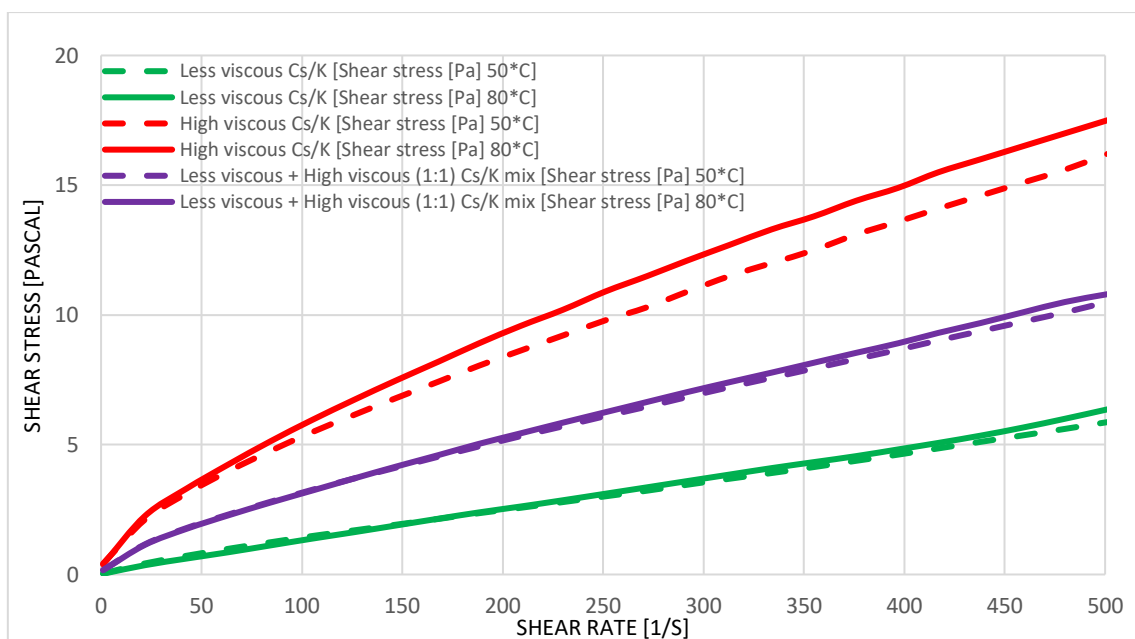


Figure 5.55: Flow comparison between high viscous Cs/K, less viscous Cs/K and 50/50 Cs/K ratio at 50°C and 80°C.

5.9.4.7 Flow comparison between modified Cs/K fluids at ambient conditions

The viscometer responses show that the 50/50 Cs/K ratio lies in-between the higher viscous and less viscous Cs/K at ambient conditions. This result is expected since equal volume of the high viscous Cs/K and less viscous Cs/K is blended. Figure 5.56 presents the flow curves at room temperature for the high viscous Cs/K, less viscous Cs/K and 50/50 Cs/K ratio fluid systems.

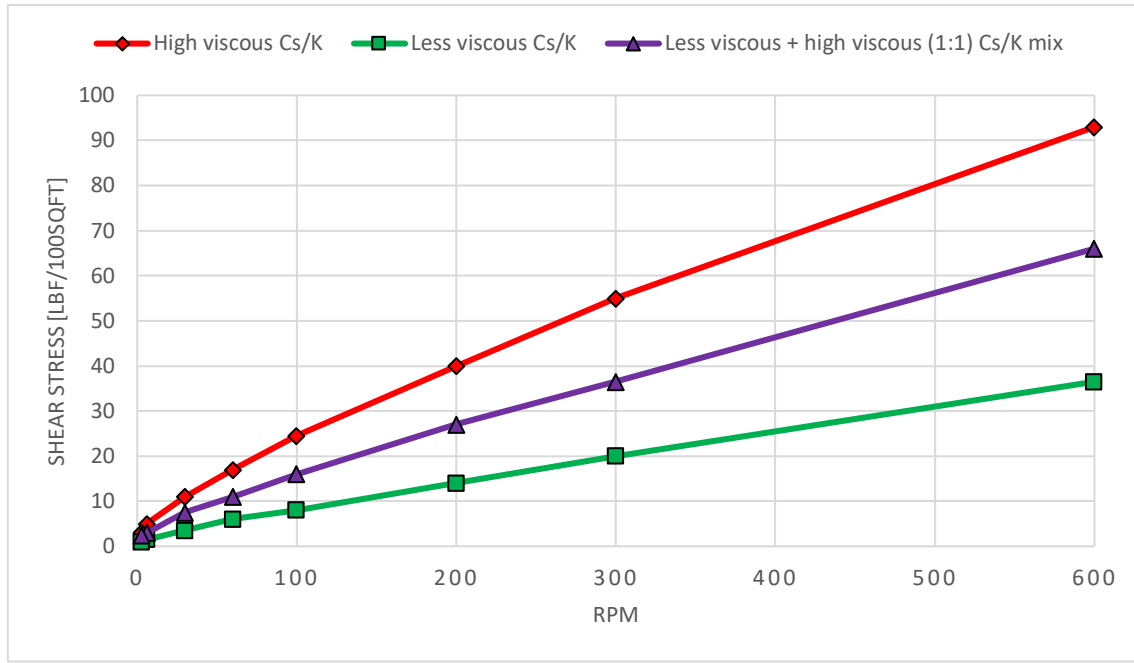


Figure 5.56: Shear stress on rpm for the high viscous Cs/K, less viscous Cs/K and 50/50 Cs/K ratio at 20°C.

Table 5.20 presents the rheological parameters obtained from the viscometer responses at ambient conditions. The results show that the fluids plastic viscosity and Bingham yield stress is linearly reduced. However, this is expected since there are fewer solid particles in the less viscous Cs/K fluid compared to the other systems.

Rheological parameters	High viscous Cs/K	Less viscous + High viscous (1:1) Cs/K mix	Less viscous Cs/K
AV [cP]	46.5	33	18.25
PV [cP]	38	29.5	16.5
YS [lbf/100sqft]	17	7	3.5
LSYS [lbf/100sqft]	1	2	0.5
n	0.757	0.854	0.867
k [lbf ⁿ /100sqft]	0.489	0.177	0.089

Table 5.20: Rheological parameters for the high viscous Cs/K, less viscous Cs/K and Cs/K 50/50 ratio at 20°C.

5.9.5 Particle stability in Cs/K drill-in fluid

The particle stability in the 100% less viscous Cs/K and the 2/3 + 1/3 Cs/K mud mix, were analyzed in a 1-hour time frame, to observe if CaCO₃ particle settling occurred or not under static conditions.

Figure 5.57 presents the particle stability for the 100% less viscous Cs/K fluid. The particles do not fall to the bottom for the 100% less viscous Cs/K drill-in fluid. Therefore, the CaCO₃ LCM material remains stable being in suspension the drilling fluid. This could be due to the fact that Cs/K is a high-density brine, hence the particle settling speed is slow, and the particles up-thrust force could be greater than the gravitational forces.

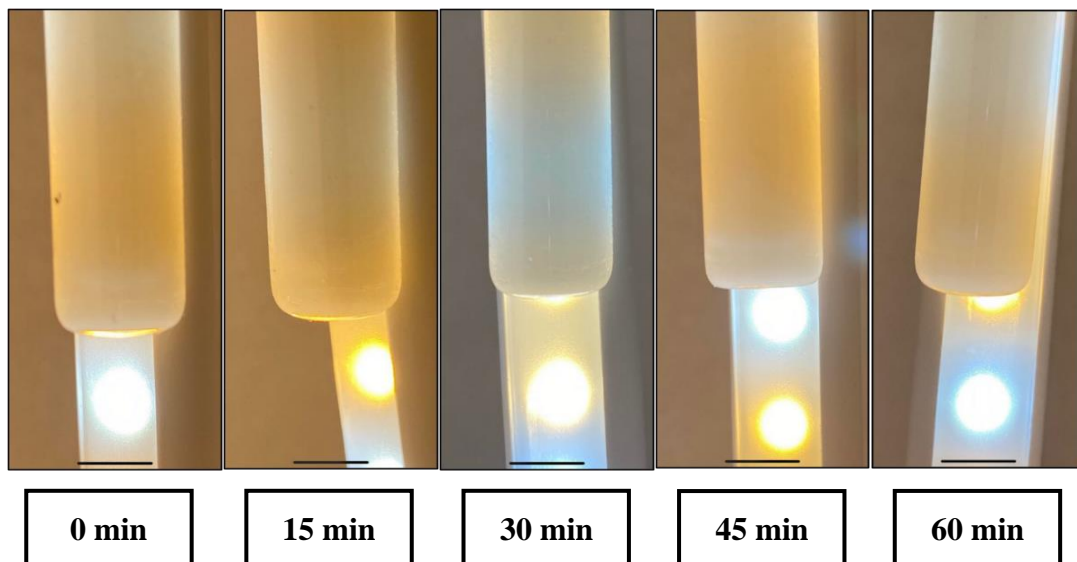


Figure 5.57: Particle stability for the 100% less viscous Cs/K in a 1-hour time frame.

The CaCO₃ particles are stable, and the fluid was being one phase for the 2/3 less viscous Cs/K + 1/3 high viscous Cs/K mud mix. The settling speed will be reduced compared to the 100% less viscous Cs/K, since this fluid is more viscous with a higher density. This indicates that the particles in the 100% less viscous Cs/K will fall faster to the bottom compared to the 2/3 less viscous + 1/3 high viscous Cs/K. Figure 5.58 presents the particle stability for the 2/3 less viscous Cs/K + 1/3 high viscous Cs/K fluid system.

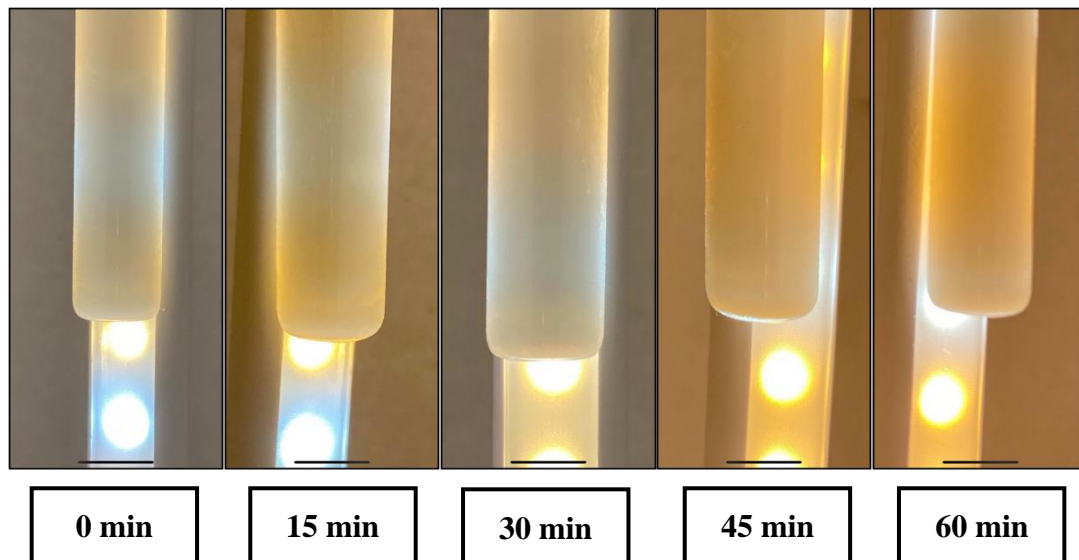


Figure 5.58: Particle stability for the 2/3 less viscous Cs/K + 1/3 high viscous Cs/K in a 1-hour time frame.

5.10 Test design 10: Hydraulic fracturing characterization on Cs/K drill-in fluid

A light viscous Cs/K were made to have enough fluid for hydraulic fracturing characterization. This mud was blended with a new less viscous Cs/K made for particle stability test, aged for 2 days + the new less viscous Cs/K aged for 1 day. These two muds were blended and referred to as the “light viscous Cs/K” for hydraulic fracturing. The mud was designed based on the same composition and mixing method and time according to section 4.3.5.1 and 4.3.5.2 for less viscous Cs/K fluid system.

5.10.1 Cs/K drill-in fluid for fracking on rheological properties

Even though the aim for test design 10 was to make enough mud of the 100% less viscous Cs/K as a penetrating case for hydraulic fracturing, the viscometer responses were tested at ambient conditions right before fracturing experiments. The viscometer responses show that the fluid exhibited a higher shear stress closer to the Cs/K 50/50 ratio which were clearly not expected. However, this rheology describes the Cs/K fluid for fracturing closer to the Martin Linge fluid properties, and hence could be a better fluid to perform fracturing experiments. Still, it seems like the Cs/K mud designed for fracturing gives a penetrating fluid description compared to the high viscous non-penetrating Cs/K. Yet, the API static filtrate loss test were not applied for this fluid characterization. The viscometer responses at room temperature for the light viscous Cs/K

for fracturing compared to the earlier designed 100% less viscous Cs/K and Cs/K 50/50 ratio is presented in figure 5.59.

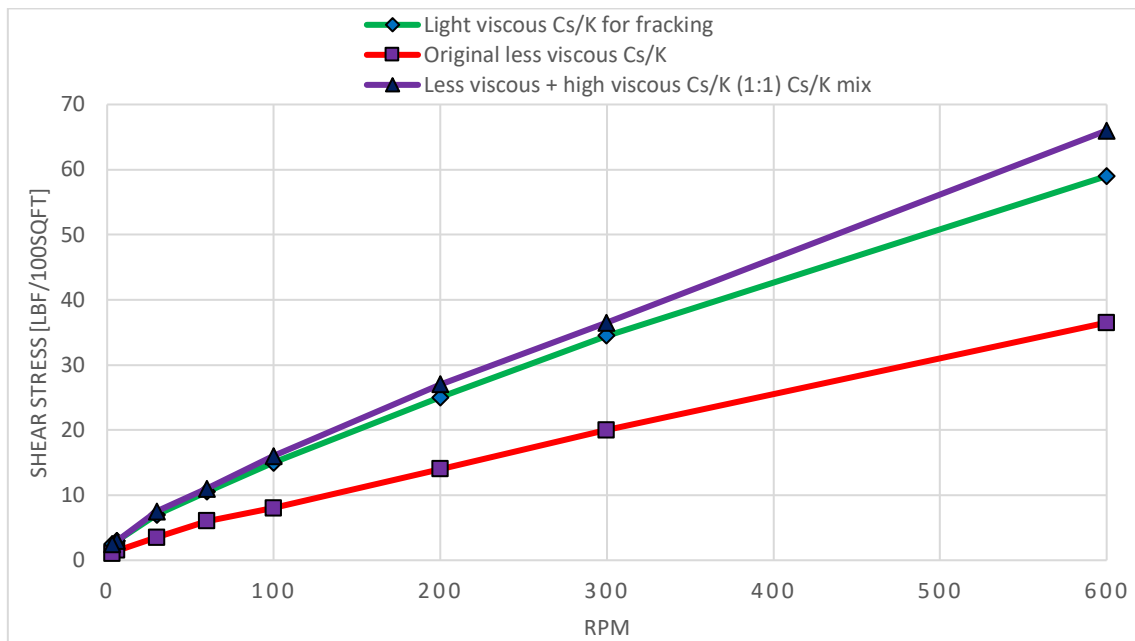


Figure 5.59: Shear stress on rpm for the light viscous Cs/K for fracturing, original 100% less viscous Cs/K and Cs/K 50/50 ratio at 20°C.

The rheological parameters for the viscometer responses in figure 5.59 is presented in table 5.21. Both the original less viscous Cs/K, light viscous Cs/K for fracturing and Cs/K 50/50 ratio acts shear-thinning. However, the fracking muds plastic viscosity is closer to the rheological properties obtained at Martin Linge, and its Bingham yield stress is close to the range of efficient cuttings transport (i.e., 11-20 lbf/100sqft).

Rheological parameters	Less viscous + high viscous Cs/K (1:1) mix	Light viscous Cs/K for fracturing	Original less viscous Cs/K
AV [cP]	33	29.5	18.25
PV [cP]	29.5	24.5	16.5
YS [lbf/100sqft]	7	10	3.5
LSYS [lbf/100sqft]	2	2	0.5
n	0.854	0.774	0.867
k [lbf ⁿ /100sqft]	0.177	0.277	0.089

Table 5.21: Rheological parameters for the Cs/K 50/50 ratio, Cs/K for fracturing and 100% less viscous Cs/K at 20°C.

5.10.2 Cs/K drill-in fluid for hydraulic fracturing on viscoelastic properties

Figure 5.60 presents the temperature sweep tests performed for the light viscous Cs/K for hydraulic fracturing compared with the original 100% less viscous Cs/K from the modification section. The results show that the light viscous Cs/K are higher viscous compared to the original less viscous Cs/K, and the fracturing mud does not define a clear minima at the sweep curve. This could be since the light viscous Cs/K for fracking may not perform gel-like tendency at temperatures below and/or equal to 80°C. However, the gel could activate at temperatures > 80°C. From the viscometer responses and rheological parameters, the fluid is Non-Newtonian, and hence the decreasing trend for the fracking mud is most likely justified with dynamic gel activation at high temperature conditions.

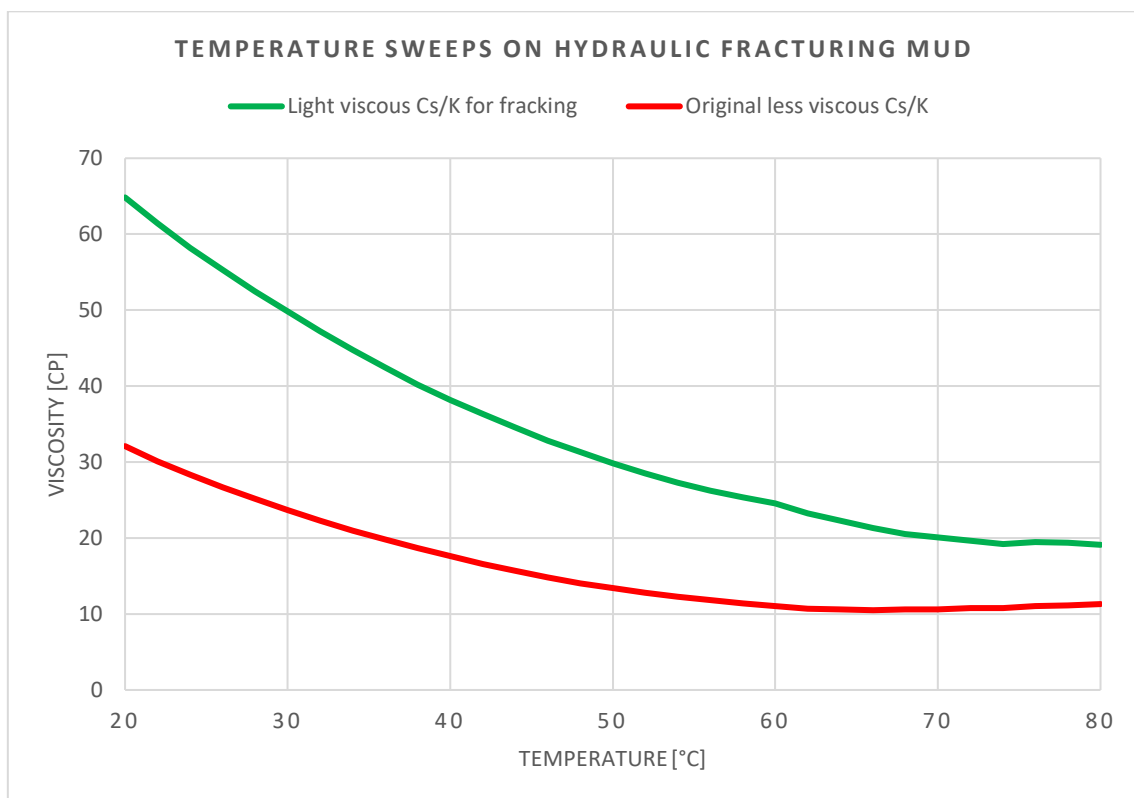


Figure 5.60: Temperature sweeps for the light viscous Cs/K for fracking and original 100% less viscous Cs/K at 20°C.

The rheometer responses at shear rate values above 500 s^{-1} could form turbulence in the fluid systems at higher temperatures. Hence the shear stress for the light viscous Cs/K for fracking, original 100% less viscous Cs/K and Cs/K 50/50 ratio is presented linearly in figure 5.61, with a shear rate interval between 0 and 500 1/s. The results show that the light viscous Cs/K fracking mud is less thermal stable compared to the designed 100% less viscous Cs/K and Cs/K 50/50

ratio. This is justified since there occurs larger gap between the 50°C and 80°C measurements compared to the other fluid systems. An interesting observation is that the fluids shear stress for the light viscous Cs/K fracking mud decreases with increase in temperature. This is a contradicting effect correlated with the other fluid systems presented in figure 5.61. However, the 100% less viscous Cs/K and Cs/K 50/50 ratio seems to form turbulence at lower shear rates compared with the light viscous Cs/K for hydraulic fracturing.

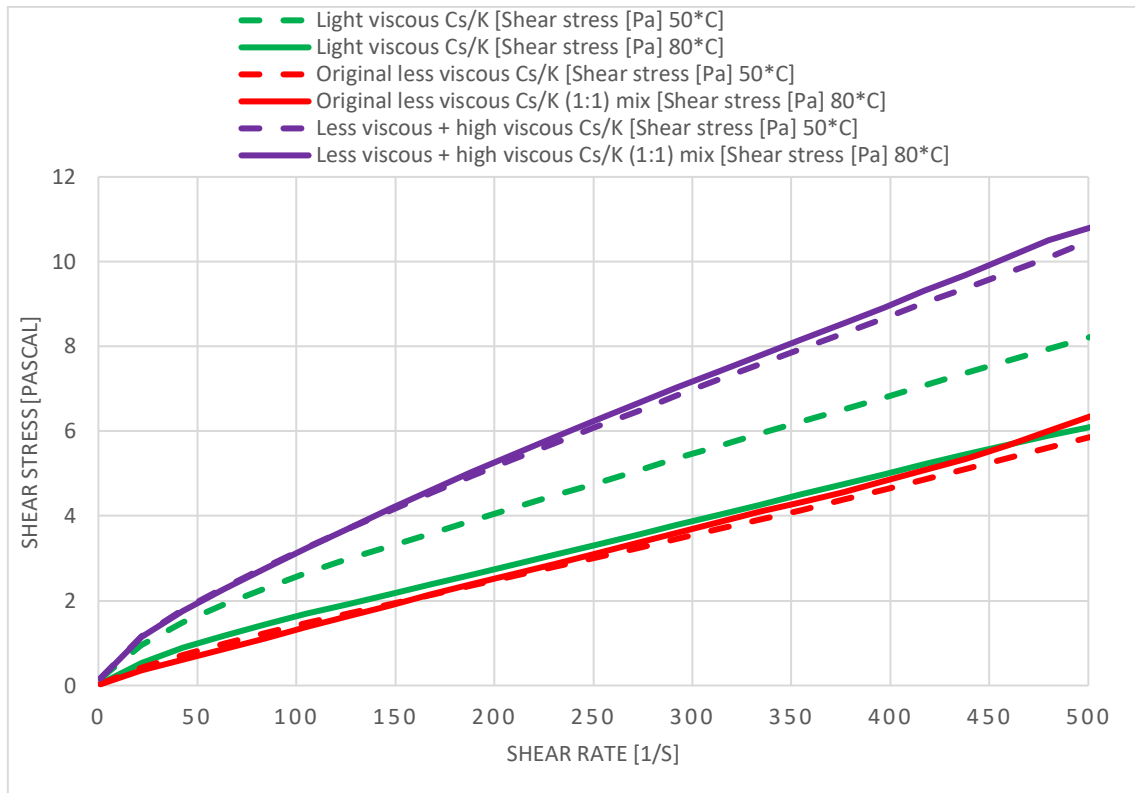


Figure 5.61: Shear stress on shear rate for the light viscous Cs/K fracking mud, 100% less viscous Cs/K and Cs/K 50/50 ratio at 50°C and 80°C.

The thermal instability issue for the light viscous Cs/K for fracturing is studied on a logarithmic scale in figure 5.62. The viscosity at lower shear rates is equal for the light viscous Cs/K and Cs/K 50/50 ratio from rheometer analysis at 50°C. However, the viscosity gap decreases between 50°C and 80°C measurements for the light viscous Cs/K with increasing shear rates. The original less viscous Cs/K at both temperatures has a breakpoint where the viscosity increases approximately equal to the light viscous Cs/K fracking mud at 80°C. This could be since the polymer bonding's stretches out and gathers in the fluid structure, hence the viscosity

increases earlier for the 100% original less viscous Cs/K at 50°C and 80°C, and light viscous hydraulic fracturing fluid at 80°C, compared to the fracking mud at 50°C.

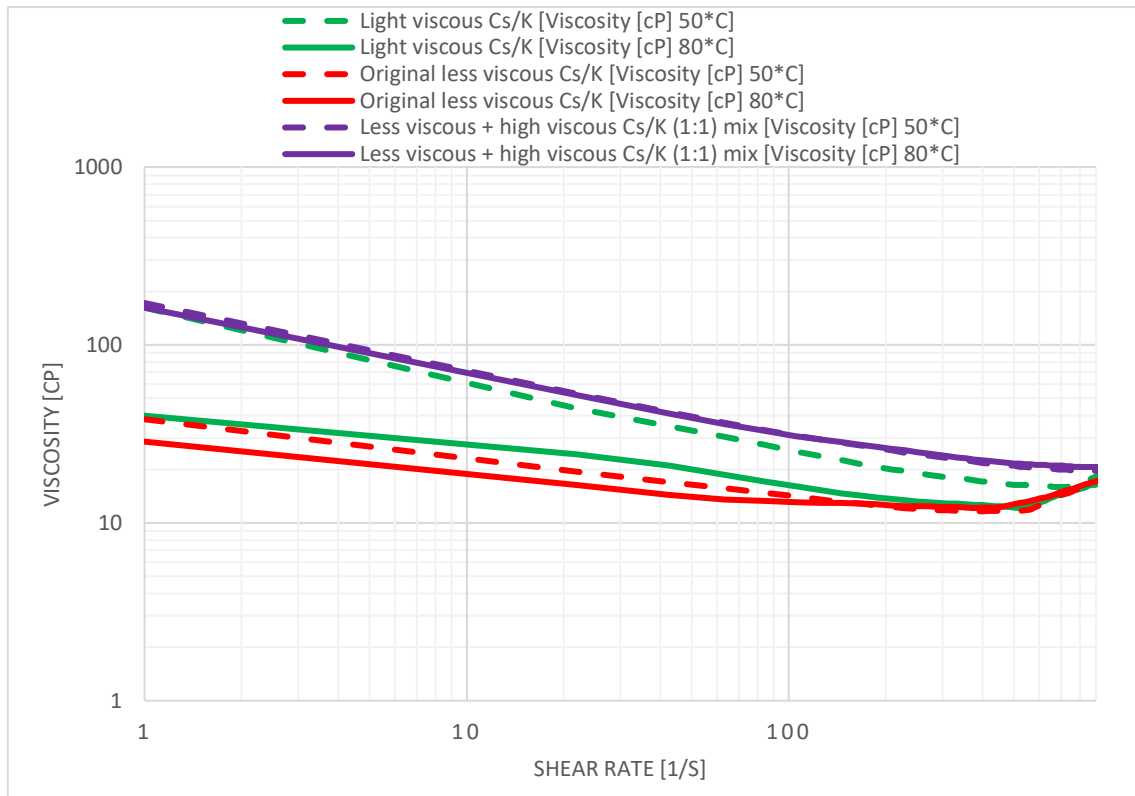


Figure 5.62: Viscosity on shear rate for the light viscous Cs/K fracking mud, original 100% less viscous Cs/K and Cs/K 50/50 ratio at 50°C and 80°C.

5.10.3 Particle stability on Cs/K design mud

The particle stability for the light viscous Cs/K + quartz (design mud) were observed in a 1-hour time frame. This analysis was performed to see whether the solid quartz particles settled in the light viscous Cs/K fluid or not. The results show that 2wt% quartz particles do not settle in the cesium/potassium brine system. This could be justified since the viscous mud components in the Cs/K brine reduced the particle velocity. Figure 5.63 presents the particle stability for the Cs/K design mud.

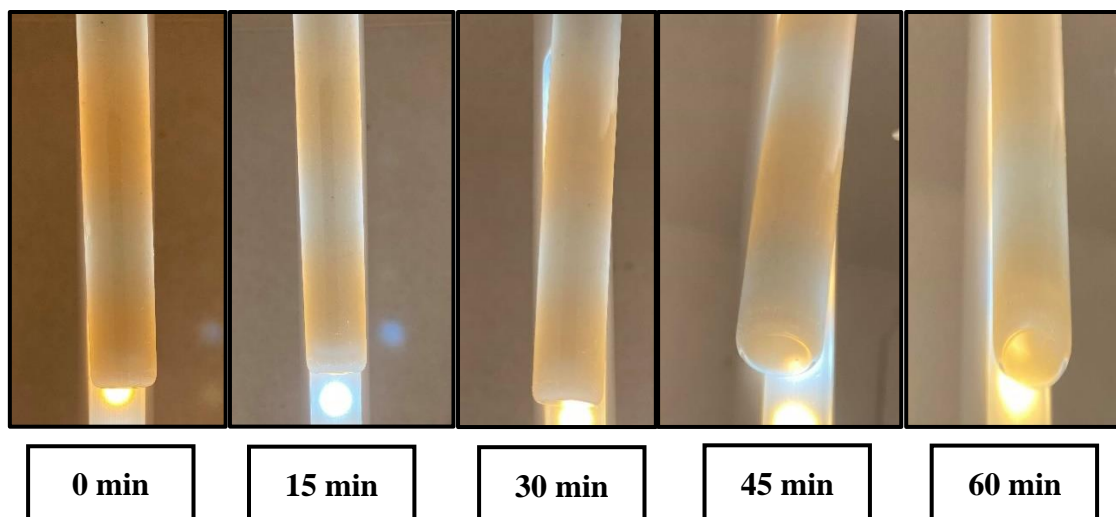


Figure 5.63: Particle stability for the design mud in a 1-hour time frame.

5.10.4 Effect of Cs/K design mud on density and rheological properties

The Cs/K design muds density were measured and compared with the base mud (i.e., 100% less viscous Cs/K) and high viscous Cs/K densities. The results show that the quartz wellbore strength material does not affect the fluid systems mud weight. Hence possesses no weighting components that exceeds the Cs/K brines established high-density system. The density for the base mud, design mud and high viscous Cs/K is presented in table 5.22.

Fluid systems	Density (s.g)
Base mud (without quartz)	2.00
Design mud (with quartz)	2.015
High viscous Cs/K	2.02

Table 5.22: Density for the base mud, design mud and high viscous Cs/K fluid systems.

Rheological properties for the base mud and design mud were obtained from the viscometer responses at ambient conditions. The rheology looks precisely the same for the light viscous Cs/K without quartz particles and the light viscous Cs/K with 2wt% quartz measured at the same temperature. This could be since the solid particles is well suspended in the liquid phase and does not possess viscosity enhancing properties. The rheology for the base and design mud is presented in figure 5.64.

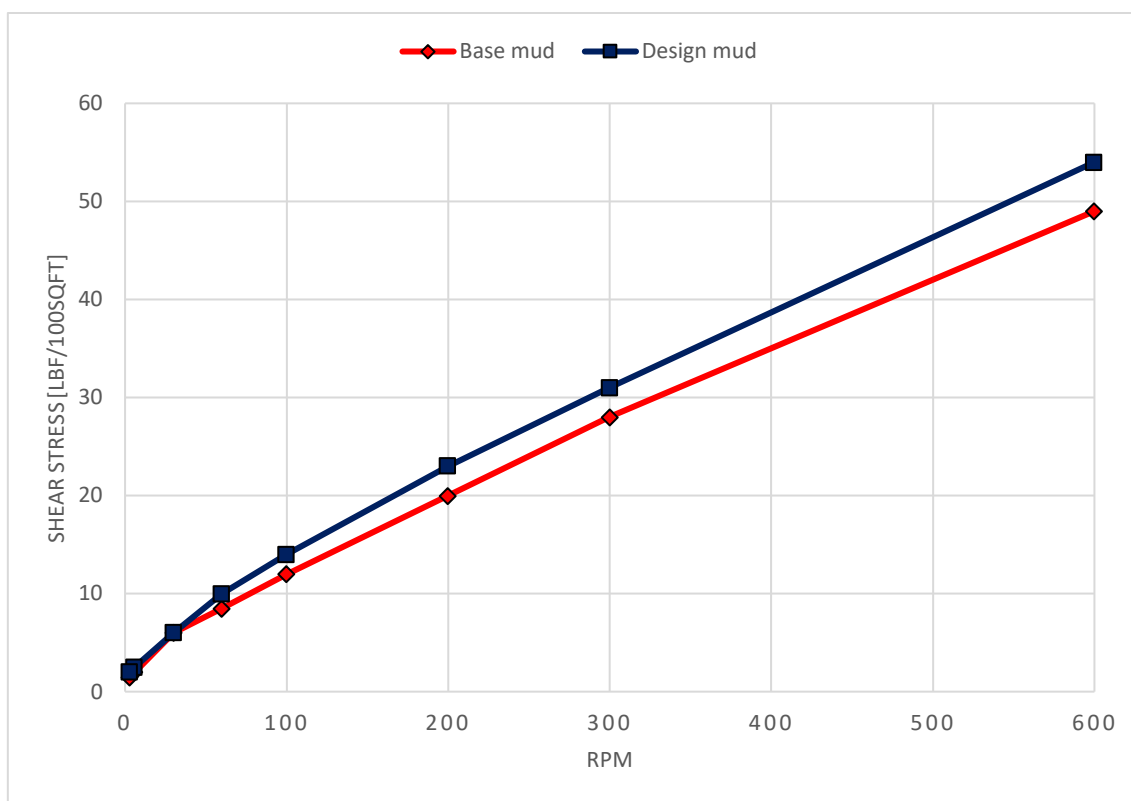


Figure 5.64: Shear stress on rpm for the Cs/K base mud and Cs/K design mud at 20°C.

Table 5.23 presents the rheological parameters for the Cs/K base mud and Cs/K design mud. All the rheological parameters are approximately the same at ambient conditions. The 2wt% quartz minimally affects the Cs/K base muds flow characteristic. This could indicate that quartz particles possess mechanical properties, hence the chemical reaction with the cesium/potassium brine is minimal.

Rheological parameters	Base mud	Design mud
AV [cP]	24.5	27
PV [cP]	21	23
YS [lbf/100sqft]	7	8
LSYS [lbf/100sqft]	1	1.5
n	0.807	0.800
k [lbf ⁿ /100sqft]	0.183	0.211

Table 5.23: Rheological parameters for the Cs/K base mud and Cs/K design mud.

5.10.5 Hydraulic fracturing of Cs/K drill-in fluids

The light viscous Cs/K for fracking (base mud) and the base mud + 2wt% quartz (Cs/K design mud) were applied with the aim to characterize the mud on hydraulic fracturing. The hydraulic fracturing was performed using a non-circulation setup since the circulation system at the equipment had too many leakage points. These were tested on two different cores: core 1 and core 2 respectively. The cement material for these cores have two different rock strengths since both cores were re-used from earlier fracturing experiments in 1998 and 2004 [60, 61]. From a drilling perspective this could simulate a worst-case scenario were the well is already fractured, hence whether LCM have a repairing effect to improve the wellbore strength or not.

5.10.5.1 Test 1: Core 1

The results show that the wellbore is strengthened with addition of 2wt% quartz, compared to the Cs/K base mud, for both the initial fracturing, 10 min re-fracturing and 1-hour re-fracturing tests. This could be since the quartz particles are hard and CaCO₃ possesses soft lost circulation material properties. Hence the 100-150 microns + 150-250-micron sized quartz particles would establish a more compact bridge at the fracture opening to enhance seal effect and prevent leakage into the fracture compared to CaCO₃. Figure 5.65 presents the fracture breakdown pressures for the Cs/K base mud and Cs/K design mud at core 1.

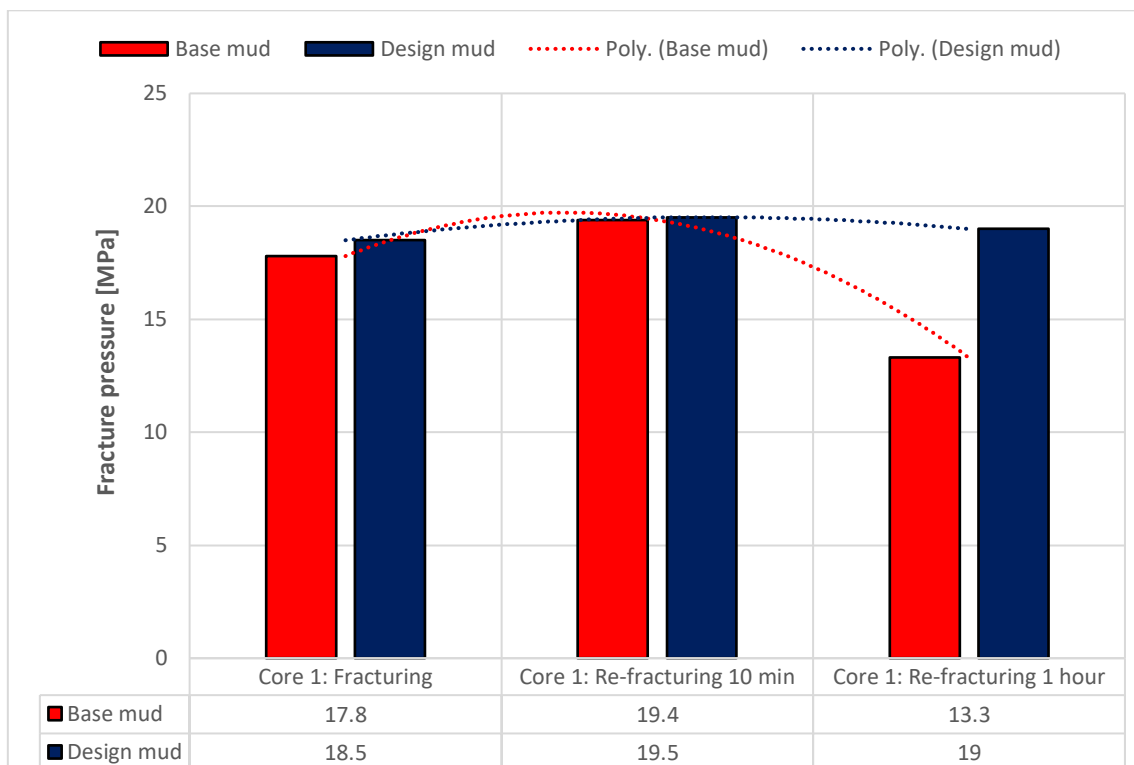


Figure 5.65: Fracture breakdown pressures for the Cs/K base mud and Cs/K design mud at core 1.

5.10.5.2 Test 2: Core 2

The well pressure for the Cs/K base mud builds up slowly for the 10 min re-fracturing test. This could be since the injection rate were 1 ml/min for the initial phase and 2 ml/min from the point where the pressure builds up before the minimum horizontal in-situ stress exceeds the tensile rock strength. Hence the mud compressibility is high from the cesium/potassium filter cake at the wellbore wall. However, fracturing occurs at a higher well pressure for the Cs/K design mud compared to the Cs/K base mud.

The CaCO₃ particles shows a clear self-healing seal effect for the Cs/K base mud after fracture breakdown has been established in the core's plastic zone. Therefore, the well pressure is roughly maintained in time as the Cs/K base mud flows into the fractures, then the CaCO₃ particles bridge the opening, hence the well is again fractured. Then the mud again flows into the fractures and fine grained CaCO₃ particles again bridges the opening. This process is repeated in time, and most likely due to the lost circulation materials mechanical properties. The process could also be justified with stress cage theory as the hoop stress increases due to other particles like starch or xanthan gum polymers interacts with the wellbore wall. However, the CaCO₃ particles have a more mechanical than chemical impact on formation properties.

Coarse quartz enhances the wellbore strength compared to fine CaCO₃ particles. However, quartz occur with repairing wellbore properties before but not after fracture propagation compared to CaCO₃. This could be since the hard quartz particles have already broken the formation, the <63 microns CaCO₃ particles in the Cs/K design mud are not able the repair the fracture opening. Figure 5.66 presents the 10 min re-fracturing well pressure curves for the Cs/K base mud and Cs/K design mud.

Figure 5.67 presents the fracture breakdown pressures for the Cs/K base mud and Cs/K design mud at core 2. The fracture and 10 min re-fracture pressures are higher for the design mud compared to the base mud. This is expected from the theory in section 3.6, that quartz LCM shall strengthen the mud compressibility in the filter cake [47]. However, the 1-hour re-fracture pressure presents the opposite. This could be since it occurred leakage during testing and the design mud fracture pressure is the same as the 10 min re-fracture pressure with clean water. Hence leakage occurred trough the gasket (i.e., leaking well). This is shown from the constant plateau pressure value in appendix were an equal amount of mud volume leaving the system as entering the system. In addition, the 1-hour repeat test for the design mud showed an equal

leakage effect at constant 6.3 MPa which strengthens this mechanical failure argument. Therefore, the 1-hour re-fracturing pressure for the Cs/K design mud in core 2 is not clearly representative.

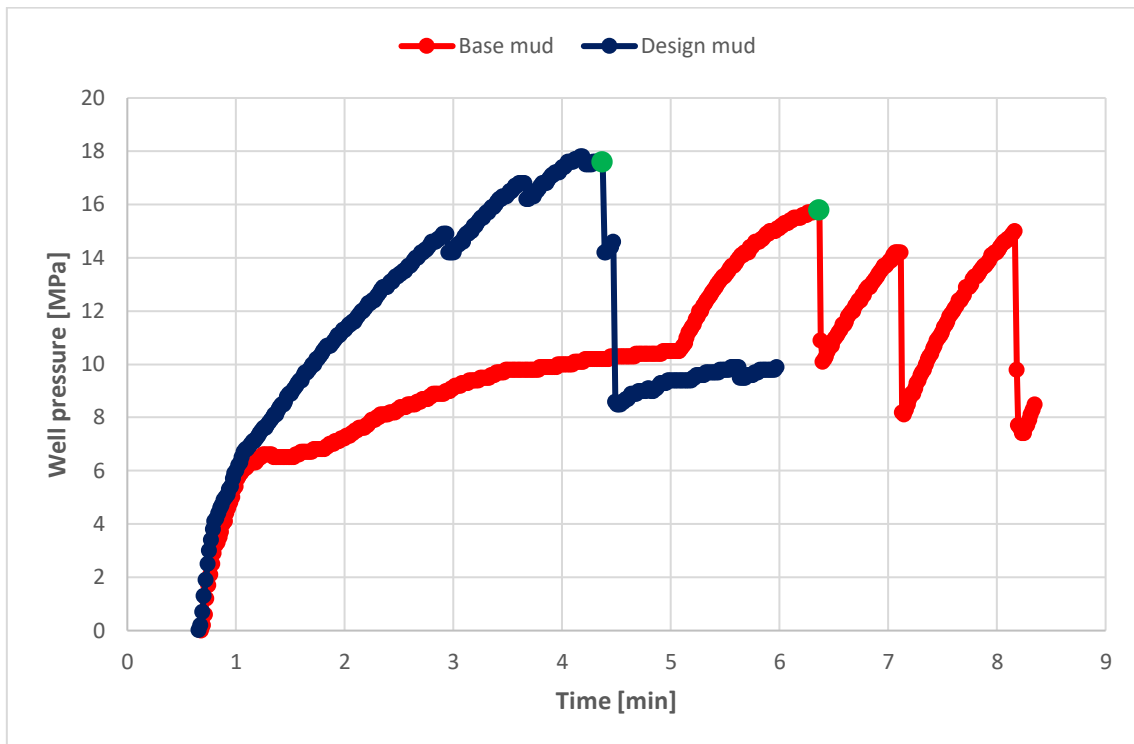


Figure 5.66: 10 min re-fracturing pressure for the Cs/K base mud and Cs/K design mud at core 2.

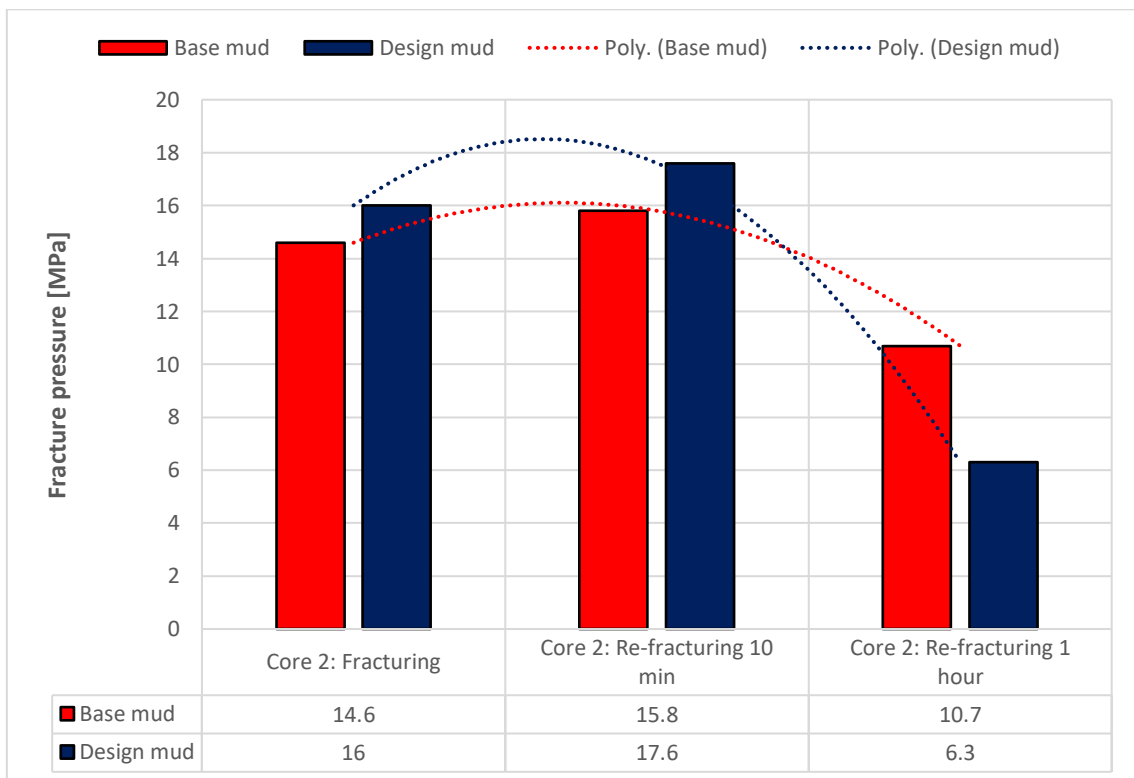


Figure 5.67: Fracture breakdown pressures for the Cs/K base mud and Cs/K design mud at core 2.

5.10.5.3 Average fracture breakdown pressures

Average fracture breakdown pressures between the Cs/K base mud and Cs/K design mud is presented in figure 5.68. The average is presented independent of core type. The results show that the quartz lost circulation material in the Cs/K design mud improves the wellbore strength for both the fracturing, 10 min re-fracturing and 1-hour re-fracturing experiments, independent of formation type in cesium/potassium reservoir drill-in fluid.

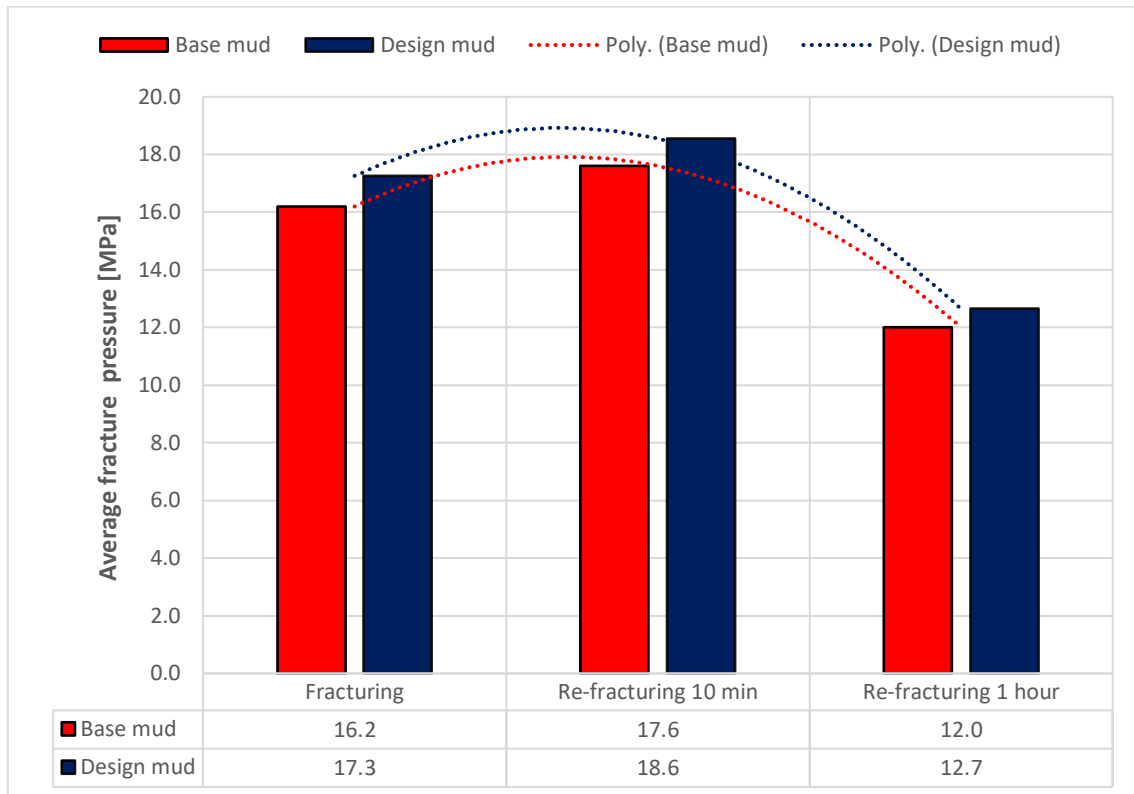


Figure 5.68: Average fracture breakdown pressures between the Cs/K base mud and Cs/K design mud.

5.10.5.4 Deviation between Cs/K design mud and Cs/K base mud

The % change in average maximum fracture pressure further confirms that the quartz particles in the design mud composition improves wellbore strength independent of core type in cesium/potassium reservoir drill-in fluids. Still, the 6.3 MPa fracture pressure for the design mud in core 2 (i.e., equal to water) decreases the value for % change for the 1-hour re-fracturing pressure. The deviation trend shows that the initial fracture is higher compared to the extended leak-off test at 10 min and 1-hour refracturing. However, with a representative fracture pressure for the Cs/K design mud at 1-hour re-fracturing in core 2, would have a major increase in % quartz LCM effect on wellbore strengthening. Figure 5.69 presents the % change in average fracture pressure between the Cs/K design mud and Cs/K base mud.

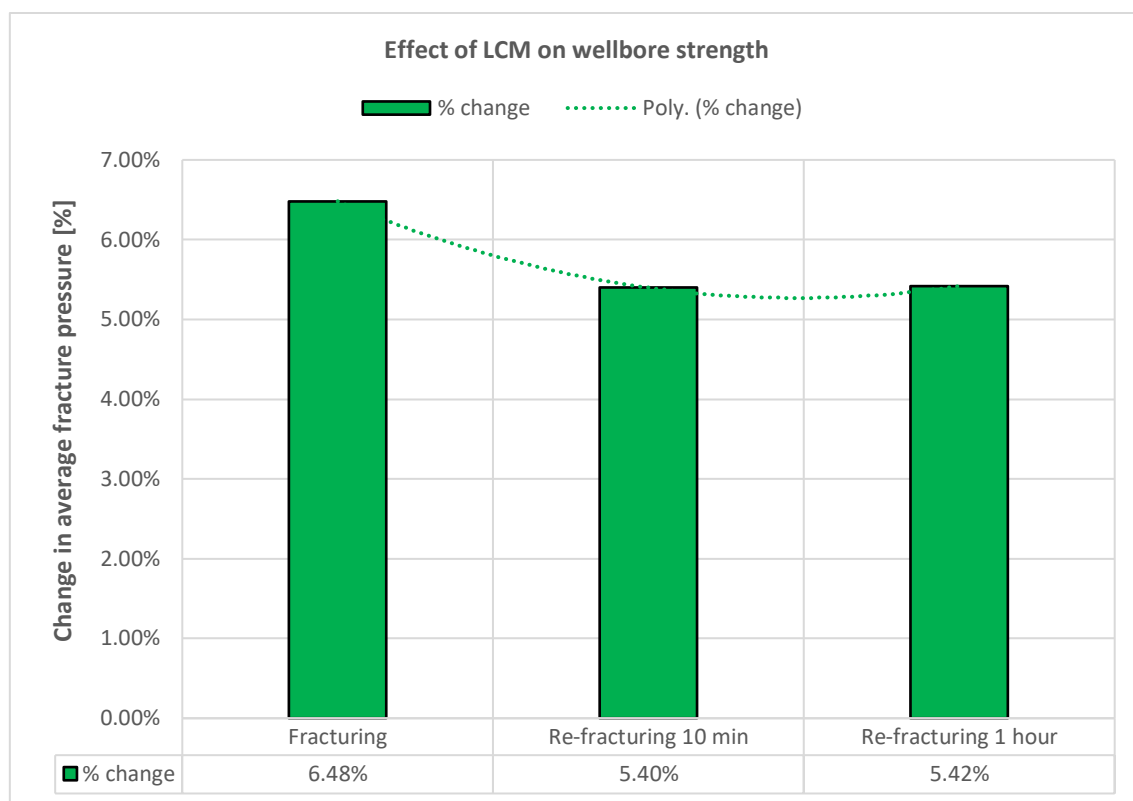


Figure 5.69: % change in average fracture pressure between the Cs/K design mud and Cs/K base mud.

Whether the cesium/potassium drill-in fluids behave penetrating or non-penetrating on hydraulic fracturing is relative since the limits are not defined. The cores used for the hydraulic fracturing experiments are over 20 years old. Hence the tensile rock strength of the cement material is reduced from earlier tests with WBM and OBM in 1998 and 2004 [60, 61]. However, the non-penetrating and penetrating fracture models is based on that the tensile strength is very small or negligible [47]. The solid quartz particles alone possess non-penetrating properties since the design mud strengthens the wellbore. Still, this effect could be even more definitely based on a representative result for the 1-hour re-fracturing pressure for the Cs/K design mud in core 2. The % change between the Cs/K base mud and Cs/K design mud is independent of core type and hence presents an imperceptible tensile strength scenario. Therefore, the Cs/K base mud may possess penetrating characteristics and the Cs/K design mud non-penetrating characteristics on hydraulic fracturing.

2wt% quartz strengthens the wellbore with 6.5% and 5.4% for the average fracturing and re-fracturing pressures in Cs/K reservoir drill-in fluids.

6 Simulation work

This section presents the simulation work performed in this thesis. The simulation work is based on hydraulic performance calculations related to ECD and pump pressure. This is done as supportive information with the aim to identify whether CaCO₃ nanoparticles in Na- and K-formate fluid systems are thermal stable or not. The following statements were assumed for simplification: vertical well (i.e., no deviated well) with no bottomhole assembly. It is a closed system consisting of a drill pipe, drill bit and well annulus only. Surface pressure from the flowlines is set equal to zero. The drill bit consists of 3 nozzles with equal diameter, and the well depth is 10 000 feet. The hydraulic calculations are based on the unified hydraulic model from theory section 3.4.2.

6.1 Nano-based potassium system

The density was set to 1.59 specific gravity for the K-formate system according to figure 2.1 [14]. The rheological data for the ECD and pump pressure calculations is summarized in table 6.1.

RPM	K-formate REF			K-formate REF + 1wt% CaCO ₃ NP		
	20°C	50°C	80°C	20°C	50°C	80°C
600	21	17	18.5	20	16	17
300	15	12.5	13.5	15	12.5	13.5
200	13	10.5	11.5	12.5	10.5	11.5
100	9.5	8	9.5	10	8	8
6	4.5	3.5	3.5	4.5	3	3
3	4	3	3	3.5	3	2.5

Table 6.1: Summarize of the viscometer data applied for K-formate hydraulic performance simulations.

6.1.1 ECD thermal stability analysis

Figure 6.1 presents the ECD simulations for the K-formate reference fluid with and without 1wt% CaCO₃ NP concentration.

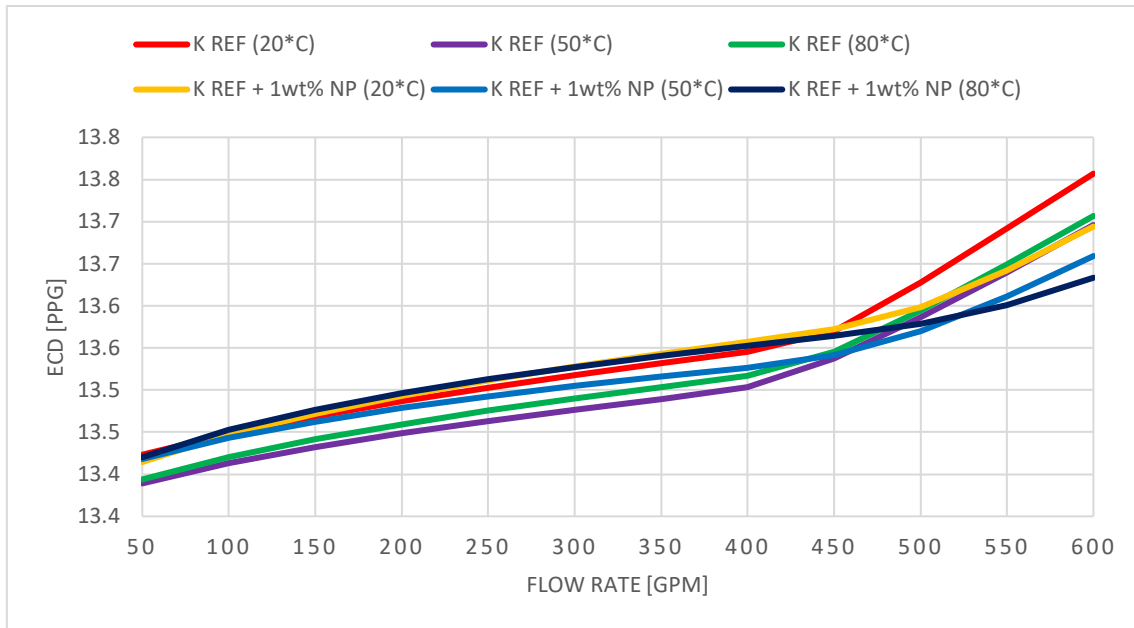


Figure 6.1: Thermal stability analysis on ECD for the K-formate reference fluid and 1wt% CaCO₃ NP.

The lowest % change in ECD occurs at ambient conditions for the K reference + 1wt% CaCO₃ NP concentration. However, the ECD at higher temperatures are the most interesting to evaluate whether the fluid system is thermal stable or not. Therefore, for the K-formate system at 50°C, the ECD are more thermal stable with increasing flow rates compared to the same fluid system at 80°C. However, the K reference + 1wt% nanoparticle concentration is within the limit in <1% ECD deviation, hence are thermally stable. The % change in ECD for the K-formate system is presented in figure 6.2.

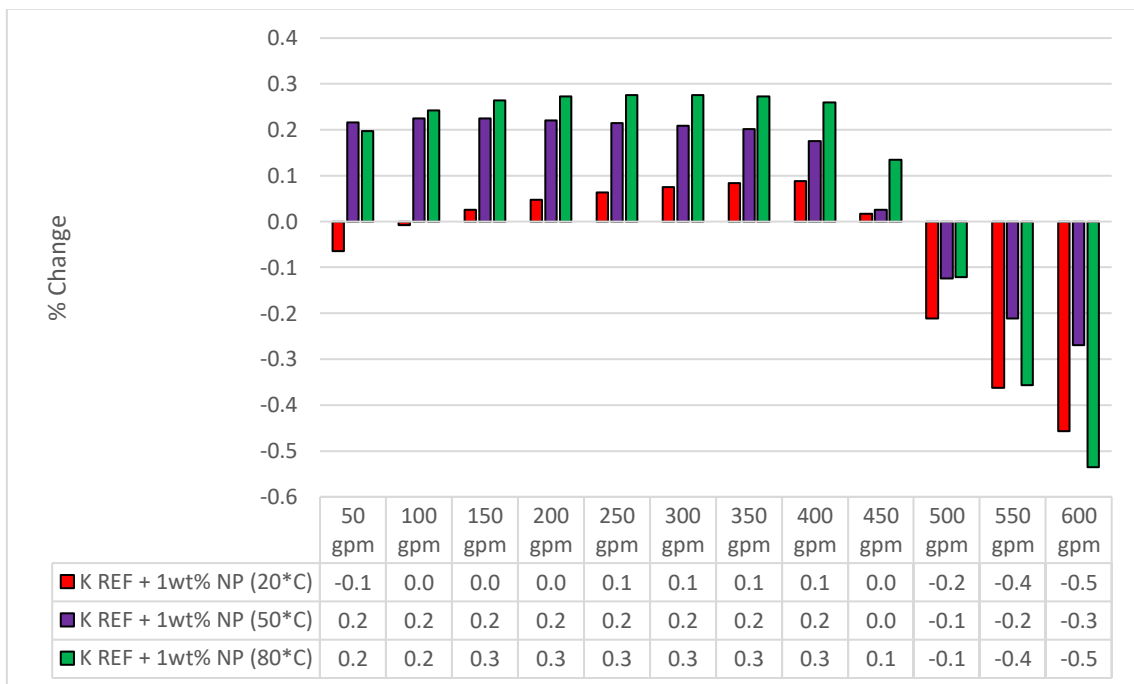


Figure 6.2: Thermal stability analysis on ECD for the K-formate reference fluid and 1wt% CaCO₃ NP.

6.1.2 Pump pressure thermal stability analysis

The pump pressure for the K reference + 1wt% CaCO₃ NP fluid system is presented in figure 6.3. The curves look almost the same for the K-formate systems at all three temperatures before the curves starts to spread with increasing flow rate.

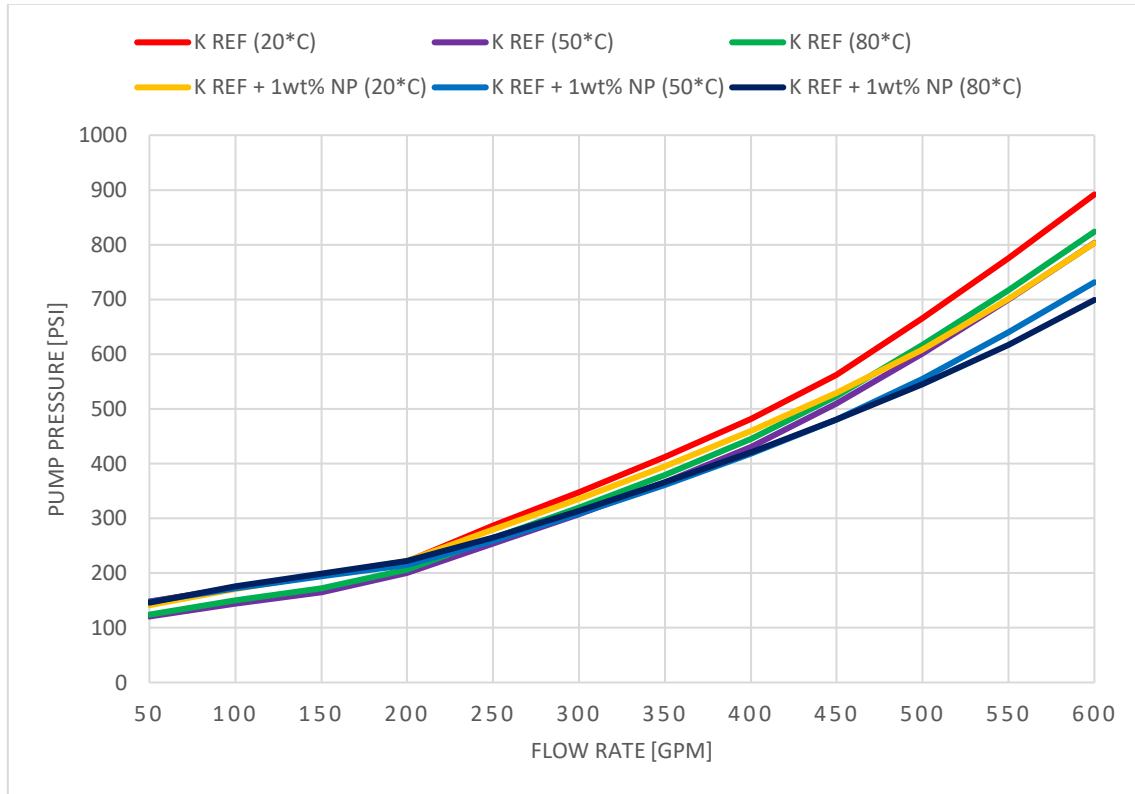


Figure 6.3: Thermal stability analysis on pump pressure for the K-formate reference fluid and 1wt% CaCO₃ NP.

The % change in pump pressure for the K-formate fluids is presented in figure 6.4. Except from the pump pressure simulations at room temperature, the K reference + 1wt% NP concentration at 50°C is the most thermal stable with increasing flow rate compared with the simulations at 80°C. Even though the K-formate fluid is more thermal stable for 80°C than 50°C at lower flowrates. This corresponds with the ECD simulations for the K-formate fluids in section 6.1.1. However, the % deviation in pump pressure is within the $\pm 30\%$ limit.

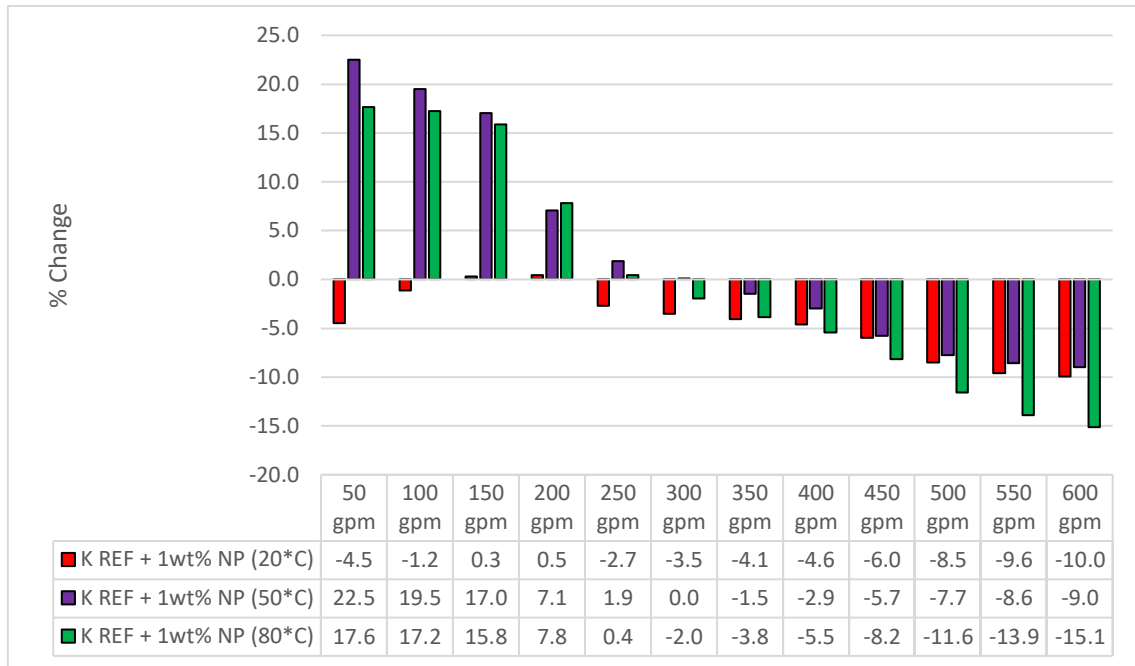


Figure 6.4: Thermal stability analysis on pump pressure for the K-formate reference fluid and 1wt% CaCO₃ NP

6.2 Nano-based sodium system

The density for the Na-formate drill-in fluid system is set equal to 1.33 specific gravity for the hydraulic calculations according to the density for Na-formate in figure 2.1 [14]. However, the density is constant in both ECD and pump pressure calculations. Still, the rheological data are the interesting parameters for thermal stability challenges. The rheological data for the ECD and pump pressure calculations is summarized in table 6.2.

RPM	Na-formate REF			Na-formate REF + 1wt% CaCO ₃ NP		
	20°C	50°C	80°C	20°C	50°C	80°C
600	23	19	20	25	19.5	21
300	17	14	15	19.5	14	17
200	13.5	12	13.5	15	12	14
100	10.5	9.5	10	11	9	10.5
6	5	4.5	4	6	4	3
3	4	4	3.5	5.5	3.5	2.8

Table 6.2: Summarize of the viscometer data applied for Na-formate hydraulic performance simulations.

6.2.1 ECD thermal stability analysis

From ECD simulations, the results show that the ECD are higher for the 1wt% nanoparticle at ambient conditions and 80°C, compared to the other Na-formate fluid systems respectively.

Figure 6.5 presents thermal stability analysis on ECD simulations for the Na-formate fluids.

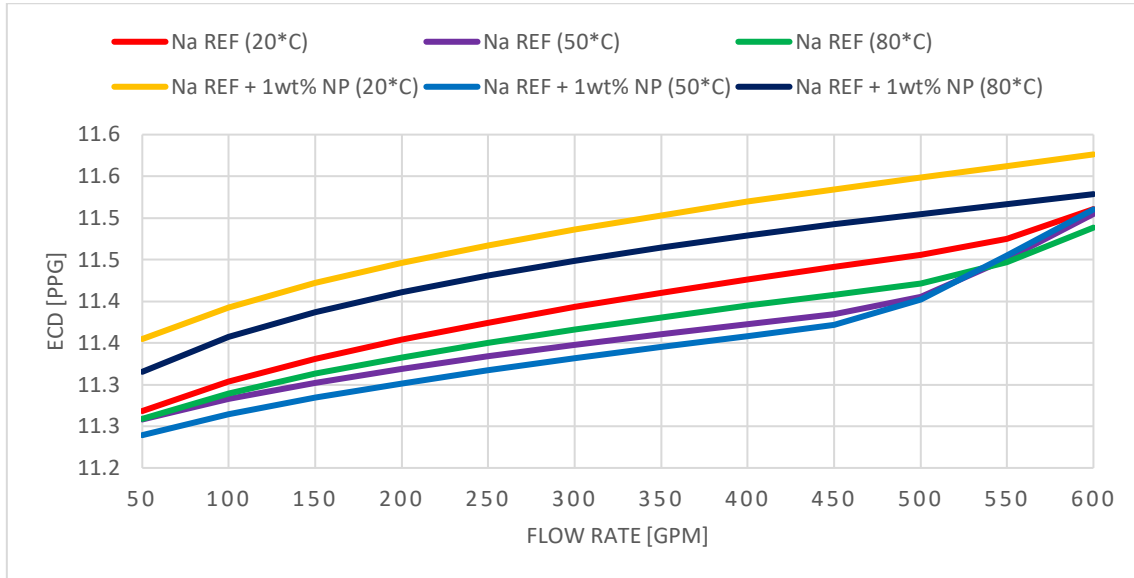


Figure 6.5: Thermal stability analysis on ECD for the Na-formate reference fluid and 1wt% CaCO₃ NP

From figure 6.6, the % change in ECD from the 1wt% NP concentration to the reference fluid is presented. All the sodium fluid systems exhibit <1% change in ECD. This statement indicates thermal stability. However, the sodium systems are less thermal stable on ECD compared to the 1wt% CaCO₃ nano-based potassium systems.

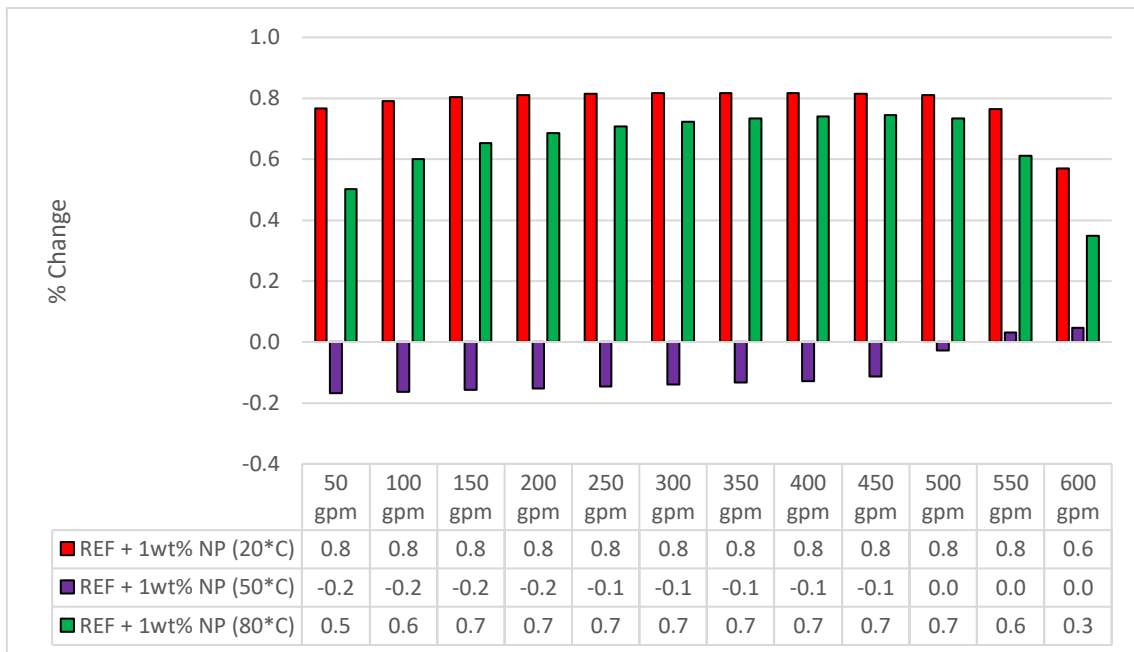


Figure 6.6: Thermal stability analysis on ECD for the Na-formate reference fluid and 1 wt% CaCO₃ NP.

6.2.2 Pump pressure thermal stability analysis

The pump pressure is further analysed on thermal stability for the sodium systems. Figure 6.7 presents the thermal stability analysis on pump pressure for the Na-formate reference fluid and 1wt% CaCO₃ NP concentration.

The % change in pump pressure from the reference fluid to the 1wt% NP's is presented in figure 6.8. The results show that the % change in pump pressure decreases by increase in flow rate for all the Na-formate systems. However, the Na reference + 1wt% CaCO₃ NP concentration exhibits more thermal stability at 50°C compared to the other Na-brines. This corresponds with the thermal stability analysis on ECD in section 6.2.1. Both the fluid systems at 50°C and 80°C are within ± 30 % deviation in pump pressure at higher temperatures. However, the 1wt% CaCO₃ nanoparticle sodium systems are less thermal stable both on ECD and pump pressure compared to the 1wt% CaCO₃ nanoparticle potassium systems. This verifies that CaCO₃ NP concentrations less than or equal to 1wt% creates a thermal stable system in potassium formate from the results section. In addition, it indicates that CaCO₃ nanoparticle concentrations >2wt% performs a more thermal stable fluid system at higher temperatures in sodium brines.

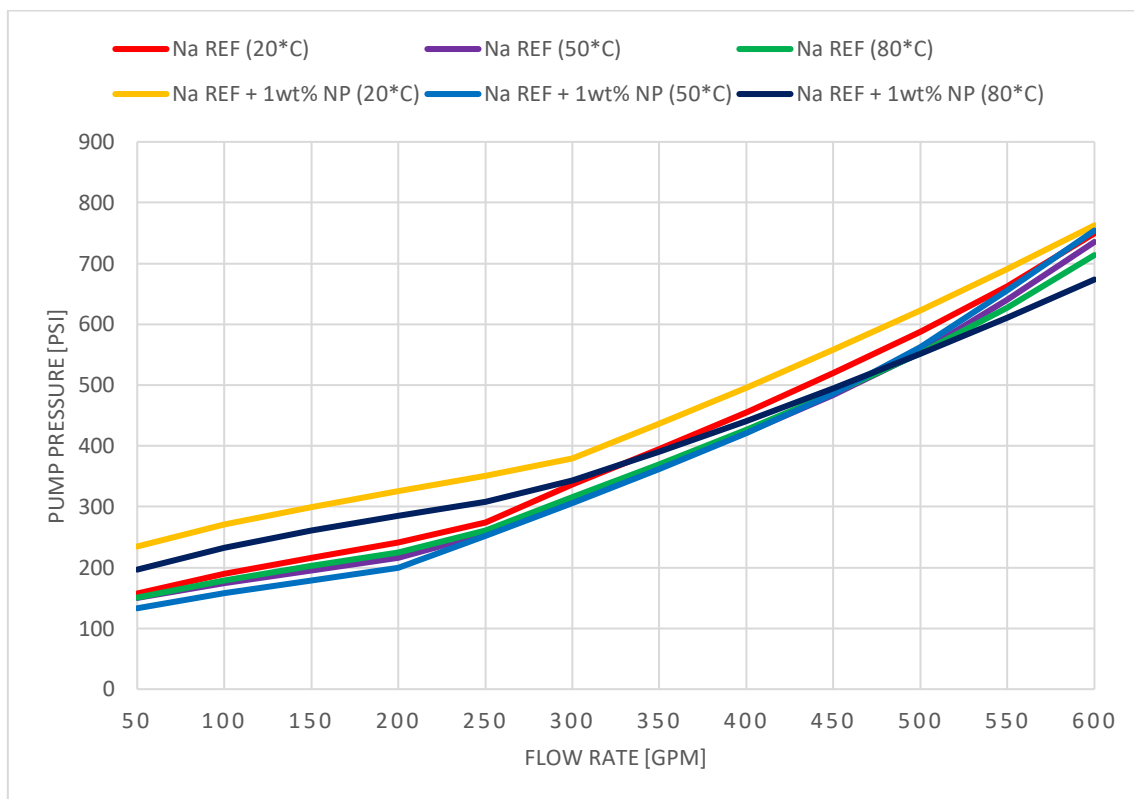


Figure 6.7: Thermal stability analysis on pump pressure for the Na-formate reference fluid and 1wt% CaCO₃ NP.

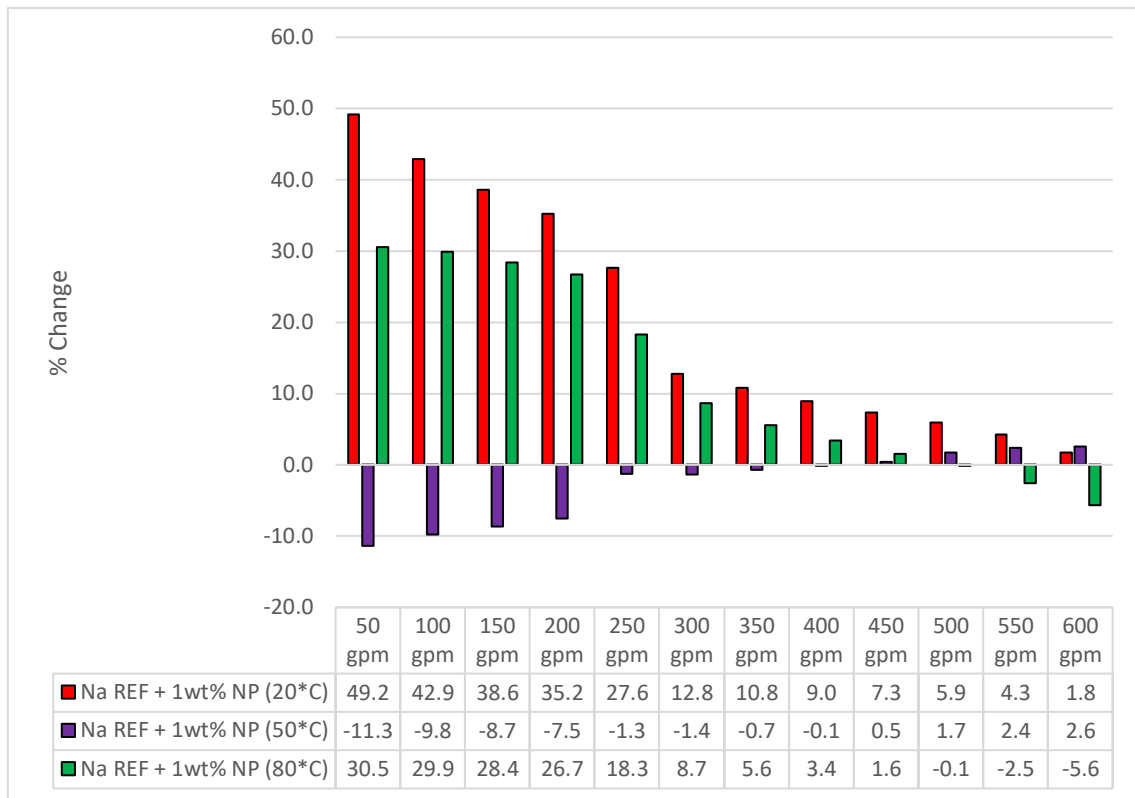


Figure 6.8: Thermal stability analysis on pump pressure for the Na-formate reference fluid and 1wt% CaCO₃ NP.

7 Conclusion

The main objective in this thesis work was to design formate (Na, K and Na/K blending) based drill-in fluids and characterize their properties at 20, 50 and 80°C. Their characterization was with respect to the fluids rheological, viscoelastic, API filtrate loss and particle stability in the presence of CaCO₃ nanoparticles. Moreover, the wellbore strength properties of lost circulation material were tested in Cs/K formate mixed drill-in fluids. The selected fluids were circulated in the considered simulation well to investigate the fluids hydraulic performance and thermal stability.

The following presents the main investigations obtained from the experimental and simulation work:

Conclusion for the sodium formate drill-in fluid system:

- ✓ Particle sizes less than 63 microns CaCO₃ was found out to be the optimal particle size range to reduce fluid loss.
- ✓ Based on the rheological flow and consistency index behaviours, the 45g and 65g CaCO₃ particle concentration treated fluids performed a thermally stable system.
- ✓ From the temperature sweep tests, the apparent viscosity increases with increase in CaCO₃ particle concentration.
- ✓ From the amplitude sweeps, the CaCO₃ type 2 exhibits the highest flow point and yield stress compared to CaCO₃ type 1. It shows higher viscous and lower filtrate loss from the temperature sweeps and API filtrate loss test.
- ✓ CaCO₃ nanoparticles performance on the rheological flow and consistency index indicates that CaCO₃ nanoparticle concentrations higher than 2wt% creates a thermally stable system at higher temperatures.
- ✓ The blending of CaCO₃ nanoparticles in the sodium formate fluid decreases the API filtrate loss.

- ✓ ECD and pump pressure simulations showed that the sodium formate reference fluid and 1wt% CaCO₃ nanoparticle blended fluids are less thermal stable than the 1wt% CaCO₃ nano-based potassium formate fluid system.
- ✓ The microparticles blended in the sodium-formate fluid becomes stable in suspension up on treating the fluid with 1wt%, 2wt% and 3wt% CaCO₃ nanoparticles resulting in a one phase fluid system. On the other hand, the nanoparticle untreated sodium-formate based fluids showed two phases separating the fluid from the additives.

Conclusion for the potassium formate drill-in fluid system:

- ✓ Results from the rheological flow and consistency index indicated that the 25g CaCO₃ particle concentration exhibited a thermally stable system at higher temperatures.
- ✓ The blending of CaCO₃ nanoparticles in the potassium-formate fluid system increases the API filtrate loss.
- ✓ The high temperature experienced potassium formate reference fluid with the 2.05wt% and 3wt% CaCO₃ nanoparticles kept the drill-in fluids particle additives stable in suspension and maintained a one phase fluid system.
- ✓ The concentration of CaCO₃ nanoparticles higher than 1wt% make the rheological flow and consistency index behaviours of potassium-formate drill-in fluid systems thermally unstable.
- ✓ From the strain amplitude sweeps, increase in CaCO₃ particle concentration performs elongated LVE range.
- ✓ Simulation work on ECD and pump pressure confirms that the reference fluid and 1wt% CaCO₃ nanoparticle systems perform a thermal stable fluid system at higher temperatures as the change in hydraulic parameters are nearly negligible.

Conclusion for the sodium/potassium formate drill-in fluid system:

- ✓ From the rheological flow and consistency index, increased concentration of sodium formate brine exhibits a thermally unstable fluid system at higher temperatures.

- ✓ Temperature sweep experiments indicated that the viscosity decreases with more sodium formate in the system, hence potassium brines owns viscosity enhancing properties.
- ✓ The strain amplitude sweeps indicate that more sodium in the Na/K formate fluid system decreases the fluids LVE range and flow stress.

Conclusion for the cesium/potassium drill-in fluid system on hydraulic fracturing:

- ✓ The Cs/K formate-based fluid that contains micron sized CaCO_3 showed a self-healing (i.e., fracture seal) effect after the well was fractured.
- ✓ 2wt% micron sized quartz LCM blending with Cs/K formate-based drill-in fluid formulated micron sized CaCO_3 , effectively increased the fracturing and re-fracturing pressures by 6.5% and 5.4% respectively.

8 References

- [1] H. C. H. D. G. R. G. Ryen Caenn, *Composition and properties of drilling and completion fluids*, Houston, Laguna beach, Texas, California: Oxford: Elsevier Science & Technology, 2016.
- [2] H. Halvorsen, H. J. Blikra, S. S. Grelland, A. Saasen and M. Khalifeh, "Viscosity of oil-based drilling fluids," p. 9, June 2019.
- [3] A. H. S. a. H. Bilgesu, "Investigation of Rheological and Filtration Properties of Water-Based Drilling Fluids Using Various Anionic Nanoparticles," *SPE-185638-MS*, p. 21, 23 April 2017.
- [4] Z. Vryzas, L. Nalbandian, V. T. Zaspalis and V. C. Kelessidis, "How different nanoparticles affect the rheological properties of aqueous Wyoming sodium bentonite suspensions," *Journal of Petroleum Science and Engineering*, pp. 941-954, February 2019.
- [5] A. R. Ismail, A. Aftab, Z. H. Ibupoto and N. Zolkifile, "The novel approach for the enhancement of rheological properties of water-based drilling fluids by using multi-walled carbon nanotube, nanosilica and glass beads," *Journal of Petroleum Science and Engineering*, pp. 264-275, 9 February 2016.
- [6] J. Zhang, L. Lie, S. Wang, J. Wang, H. Yang, Z. Zhao, J. Zhu and Z. Zhang, "Novel Micro and Nano Particle-Based Drilling Fluids: Pioneering Approach to Overcome the Borehole Instability Problem in Shale Formations," *SPE-176991-MS*, p. 13, November 2015.
- [7] N. M. Taha and S. Lee, "Nano Graphene Application Improving Drilling Fluids Performance," in *International Petroleum Technology Conference*, Doha, 2015.
- [8] J. K. M. William, S. Ponmani, R. Samuel, R. Nagarajan and J. S. Sangwai, "Effect of CuO and ZnO nanofluids in xanthan gum on thermal, electrical and high pressure rheology of water-based drilling fluids," *Journal of Petroleum Science and Engineering*, pp. 15-27, May 2014.
- [9] G. H. M. H. R. N. M. F. Z. Charles O. Nwaoji, "Wellbore Strengthening - Nano-Particle Drilling Fluid Experimental Design Using Hydraulic Fracture Apparatus," *SPE/IADC 163434*, p. 12, 5-7 March 2013.
- [10] P. Anne Marie Helmenstine, "ThoughtCo.," 03 July 2019. [Online]. Available: <https://www.thoughtco.com/how-to-use-a-periodic-table-608807>. [Accessed 26 April 2021].
- [11] B. S. Aadnøy, "Geomechanical Analysis for Deep-Water Drilling," *IADC/SPE 39339*, p. 16, 3-6 March 1998.
- [12] E. Jøntvedt, M. Fjeldheim, J. Løchen, S. Howard, S. Leon, C. Busengdal and K. R. Gyland, "Deployment of Cesium Formate Drill-in and Openhole Completion Fluid in the Martin Linge High Pressure, High Permeability Gas Reservoir Enhances Total's Operation Efficiency and Radically Improves Well Performance," *SPE-189550-MS*, p. 28, 7-9 February 2018.
- [13] N. GAURINA-MEĐIMUREC, B. PAŠIĆ, K. SIMON and M. M. DAVORIN MATANOVIĆ, "FORMATE-BASED FLUIDS: FORMULATION AND APPLICATION," p. 10, 2008.
- [14] J. Downs, "Drilling Point," 18 December 2014. [Online]. Available: <https://www.drillingpoint.com/p2793/why-brine-is-the-next-best-thing/>.

- [15] Oljedirektoratet, "Norsk Petroleum," 28 April 2021. [Online]. Available: <https://www.norskpetroleum.no/fakta/felt/martin-linge/>. [Accessed 29 April 2021].
- [16] Oljedirektoratet, "Norsk petroleum," 2021. [Online]. Available: <https://www.norskpetroleum.no/05-nordsjoen-n-n-08032017/>.
- [17] E. S. P. Å. L. N. B. S. H.-J. S. H. G. O. J. D. D. J. T. M. H. Per Cato Berg, "Drilling and Completing High-Angle Wells in High-Density, Cesium Formate Brine - Kvitebjørn Experience, 2004-2006," p. 10, March 2009.
- [18] R. Sorkhabi, "GEOExPro," 2010. [Online]. Available: <https://www.geoexpro.com/articles/2010/04/the-king-of-giant-fields>.
- [19] S. A.-R. D. F. J. G. M. A.-F. a. P. V. Michael A. Simpson, "Application and Recycling of Sodium and Potassium Formate Brine Drilling Fluids for Ghawar Field HT Gas Wells," no. OTC 19801, 2009.
- [20] N. K. a. S. Salehi, "Experimental Investigation of Inhibitive Drilling Fluids Performance: Case studies United States Shale Basins," *Energies*, p. 21, 2 October 2020.
- [21] "Shale experts," 2021. [Online]. Available: <https://www.shaleexperts.com/plays/tuscaloosa-marine-shale/Overview>.
- [22] M. A. M. M. H. d. J. a. K. A. M.S. Aston, "Drilling Fluids for Wellbore Strengthening," *IADC/SPE 87130*, p. 8, 2-4 March 2004.
- [23] J. Parker, "Oklahoma Minerals," 20 November 2017. [Online]. Available: <https://www.oklahomaminerals.com/arkoma-basin-sooner-later-everything-old-becomes-new-simply-become-less-old>. [Accessed 23 February 2021].
- [24] F. Irgens, *Rheology and Non-Newtonian Fluids*, 1st edition ed., Cham: Springer, 2014.
- [25] G. Kolle og R. Mesel, *Brønnvæsker: for VK1 brønnteknikk*, Nesbru: Vett & viten, 1998.
- [26] A. P. L. A. P. O. E. F. B. Folayan J. Adewale, "Selecting the Most Appropriate Model for Rheological Characterization of Synthetic Based Drilling Mud," *International Journal of Applied Engineering Research*, p. 16, 2017.
- [27] A. Paar, "Basics of rheology," [Online]. Available: <https://wiki.anton-paar.com/en/basics-of-rheology/>.
- [28] K. S. a. T. M. Rafał Wiśniowski, "Selection of a Suitable Rheological Model for Drilling Fluid Using Applied Numerical Methods," *Energies*, p. 17, 19 June 2020.
- [29] "Drillingformulas.com," 14 February 2016. [Online]. Available: <http://www.drillingformulas.com/types-of-flow-and-rheology-models-of-drilling-mud/>.
- [30] T. Sochi, "Flow of Non-Newtonian Fluids in Porous Media," *Wiley Online Library*, p. 31, 2010.
- [31] M. Tabatabaei, A. D. Taleghani, G. Li and T. Zhang, "Shape Memory Polymers as Lost Circulation Materials for Sealing Wide-Opened Natural Fractures," *SPE Drill & Compl*, no. SPE-205514-PA, pp. 1-12, 4 June 2021.
- [32] E. v. Oort, J. Lee, J. Friedheim and B. Toups, "New Flat-Rheology Synthetic-Based Mud for Improved Deepwater Drilling," *SPE 90987*, p. 11, 26 September 2004.
- [33] A. Salih, T. Elshehabi and H. Bilgesu, "Impact of Nanomaterials on the Rheological and Filtration Properties of Water-Based Drilling Fluids," *SPE-184067-MS*, p. 14, 13-15 September 2016.

- [34] L. Xu, M.-b. Xu, L. Zhao, S.-c. Wen, W.-h. Liu, J. Xu, F.-c. You and C. Gong, "Experimental Investigations Into the Performance of a Flat-Rheology Water-Based Drilling Fluid," *SPE-163107-PA*, pp. 69-77, 23 May 2013.
- [35] E. A. Al-Khdheawi and D. S. Mahdi, "Apparent Viscosity Prediction of Water-Based Muds Using Empirical Correlation and an Artificial Neural Network," *Energies*, p. 12, 9 August 2019.
- [36] M. V. OCHOA, "ANALYSIS OF DRILLING FLUID RHEOLOGY AND TOOL JOINT EFFECT TO REDUCE ERRORS IN HYDRAULICS CALCULATIONS," August 2006.
- [37] D. Power and M. Zamora, "Making a Case for AADE Hydraulics and the Unified Rheological Model," in *AADE 2002 Technology Conference "Drilling & Completion Fluids and Waste Management"*, Houston, Texas, 2002.
- [38] R. Robertson and H. Stiff, "An Improved Mathematical Model for Relating Shear Stress to Shear Rate in Drilling Fluids and Cement Slurries," *Society of Petroleum Engineers Journal*, pp. 31-36, 1 February 1976.
- [39] T. G. Mezger, *The Rheology Handbook: For users of rotational and oscillatory rheometers*, 4th Edition, Hanover: Vincentz Network, 2014.
- [40] B. Welch, *Rheology and Viscoelasticity*, Espoo: Aalto University, School of Chemical Technology, 2015.
- [41] B. Bui, A. Saasen, J. Maxey, M. E. Ozbayoglu, S. Z. Miska, M. Yu and N. E. Takach, "Viscoelastic Properties of Oil-Based Drilling Fluids," *ANNUAL TRANSACTIONS OF THE NORDIC RHEOLOGY SOCIETY*, p. 16, January 2012.
- [42] S. M. Strømø, "Formulation of New Drilling Fluids and Characterization in HPHT," University of Stavanger, Stavanger, 2019.
- [43] T. Zeynalov, "Effect of Boron nitride (BN) and surface modified BN on the properties of laboratory water-based drilling fluid formulated in Duovis/XG polymers: Experimental and Simulation studies," University of Stavanger, Stavanger, 2018.
- [44] R. F. Mitchell and S. Miska, *Fundamentals of drilling engineering*, Richardson, Texas: Society of Petroleum Engineers, 2010.
- [45] J. Sadigov and M. Belayneh, "Analyses of Field Measured Data With Rheology and Hydraulics Models," *International Journal of Fluids Engineering*, pp. 1-12, 2016.
- [46] B. Aadnøy and L. Reza, *Petroleum Rock Mechanics: Drilling Operations and Well Design*, San Diego: Elsevier Science & Technology, 2019.
- [47] B. S. Aadnøy, *Modern Well Design*, Second edition ed., Stavanger: Taylor & Francis Group, 2010.
- [48] M. Alsaba, M. F. Al Dushaishi, R. Nygaard, O.-M. Nes and A. Saasen, "Updated criterion to select particle size distribution of lost circulation materials for an effective fracture sealing," *Journal of Petroleum Science and Engineering*, p. 8, 20 January 2017.
- [49] A. ODABAŞI, "EFFECTS OF CALCIUM CARBONATE ON RHEOLOGICAL AND FILTRATION PROPERTIES OF DRILL-IN FLUIDS," Turkey, 2015.
- [50] "Schlumberger Oilfield Glossary," Schlumberger, 2021. [Online]. Available: <https://www.glossary.oilfield.slb.com/en/Terms/f/formate.aspx>. [Accessed 19 March 2021].
- [51] M. Dayah, "Ptable," 20 November 2020. [Online]. Available: <https://ptable.com/#Egenskaper/Atomvekt>. [Accessed 19 March 2021].
- [52] "Schlumberger Oilfield Glossary," Schlumberger, 2021. [Online]. Available: https://glossary.oilfield.slb.com/en/terms/c/cesium_formate. [Accessed 8 June 2021].

- [53] "Schlumberger Oilfield Glossary," Schlumberger, 2021. [Online]. Available: <https://www.glossary.oilfield.slb.com/en/terms/s/starch>. [Accessed 19 March 2021].
- [54] "Schlumberger Oilfield Glossary," Schlumberger, 2021. [Online]. Available: https://www.glossary.oilfield.slb.com/en/terms/x/xanthan_gum. [Accessed 23 March 2021].
- [55] G.Sworn, "Handbook of Hydrocolloids (Second Edition)," *Woodhead Publishing Series in Food Science, Technology and Nutrition*, pp. 186-203, 2009.
- [56] H. Y. Yang, K. Zhang, B. H. Chon and H. J. Choi, "Enhanced oil recovery performance and viscosity characteristics of polysaccharide xanthan gum solution," *Journal of Industrial and Engineering Chemistry*, pp. 741-745, 13 April 2014.
- [57] "Schlumberger Oilfield Glossary," Schlumberger, 2021. [Online]. Available: https://www.glossary.oilfield.slb.com/en/terms/c/calcium_carbonate. [Accessed 23 March 2021].
- [58] JOSÉ MIGUEL MARTÍN-MARTÍNEZ, "Surfaces, Chemistry & Applications," *Adhesion Science and Engineering*, 2002.
- [59] H. M. King, "Geology.com," 2005. [Online]. Available: <https://geology.com/minerals/quartz.shtml>. [Accessed 8 June 2021].
- [60] M. Belayneh, Experimental and analytical borehole stability study, Stavanger, Rogaland: Stavanger University College, Department of Petroleum Engineering, 2004.
- [61] S. B. Drangeid, «Eksperimentell studie av borehulls frakturering,» S.B. Drangeid, Stavanger, 1998.

APPENDICES

APPENDIX A– Sinomine brine

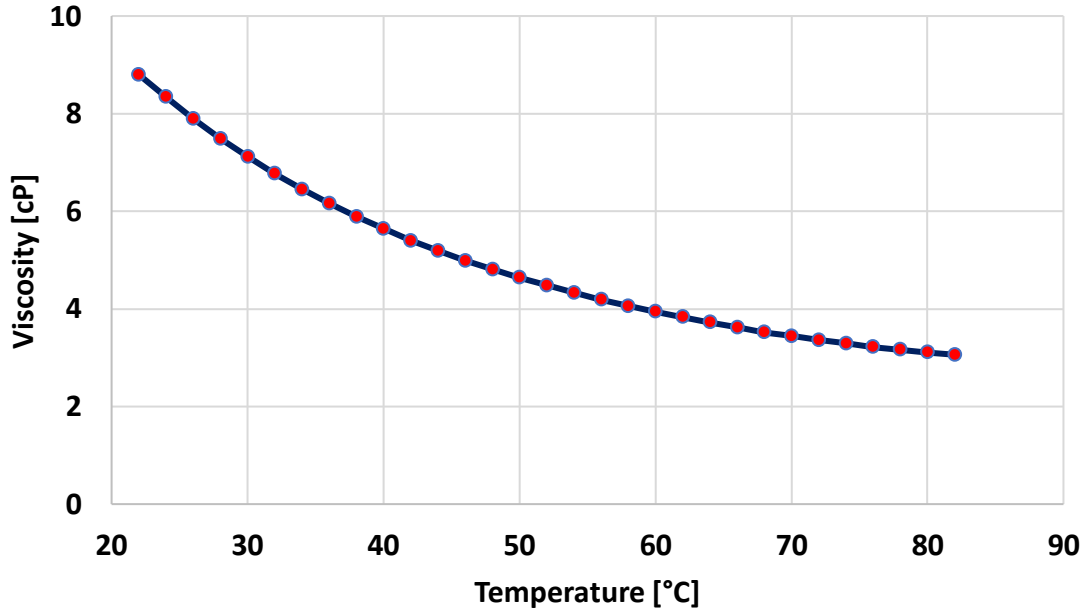


Figure A.1: Temperature sweep of Sinomine fluid.

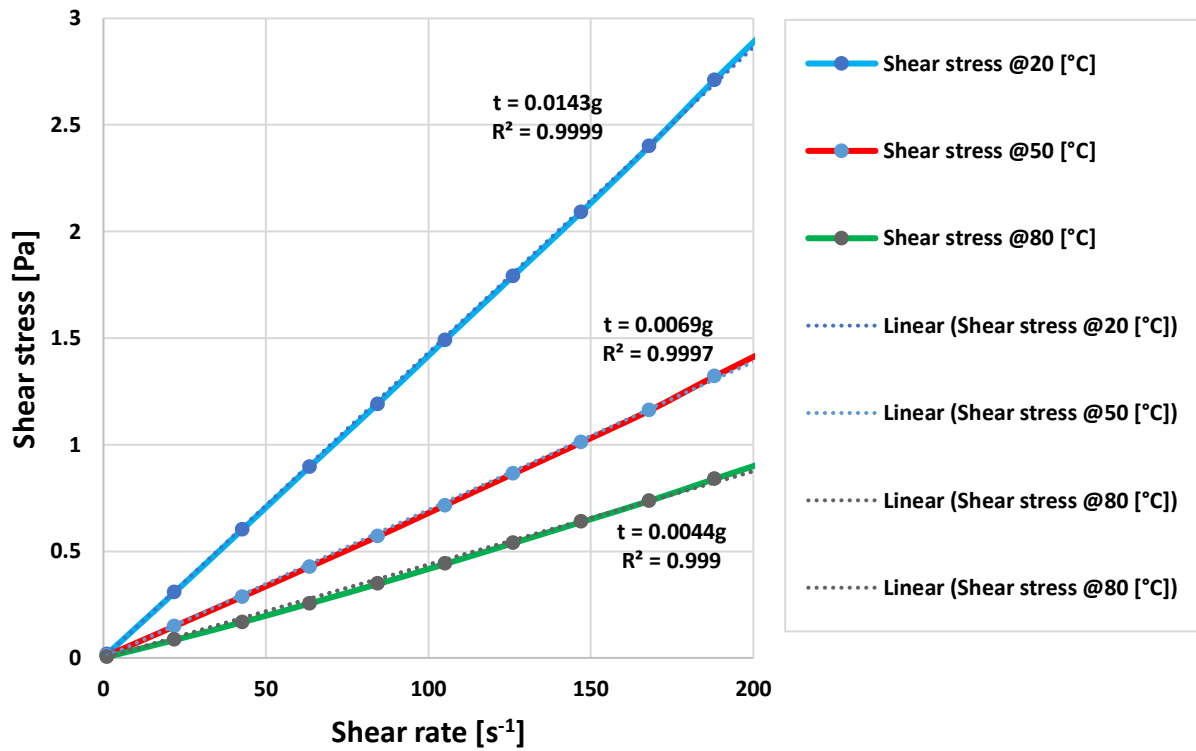


Figure A.2: Flow curve of Sinomine fluid.

APPENDIX B – Mud cakes for the nano-based sodium and potassium systems

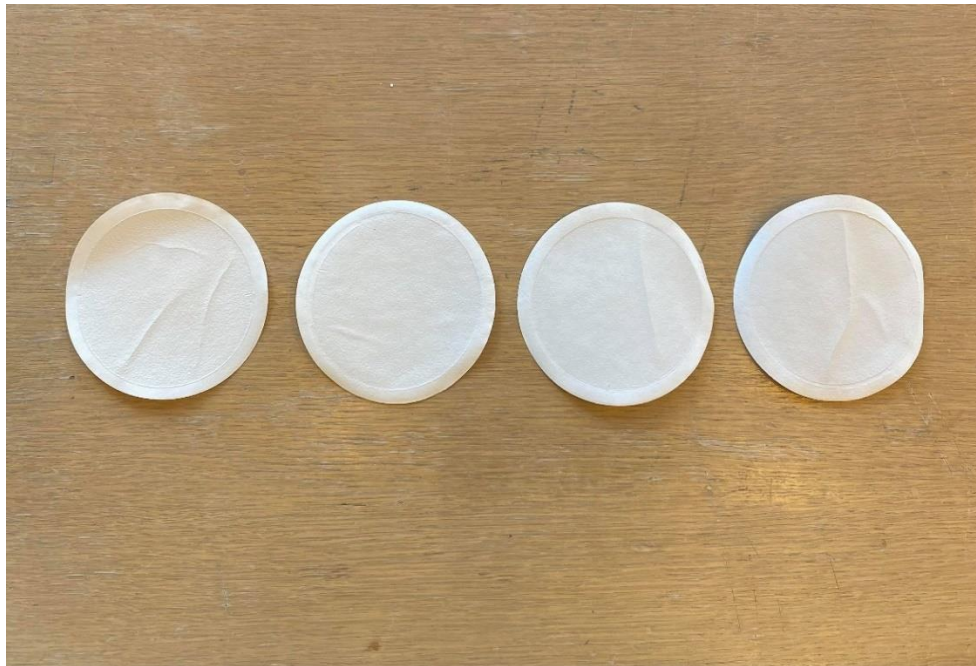


Figure B.1: Mud cakes for the Na reference fluid with 1wt%, 2wt% and 3wt% CaCO₃ nanoparticle concentrations.

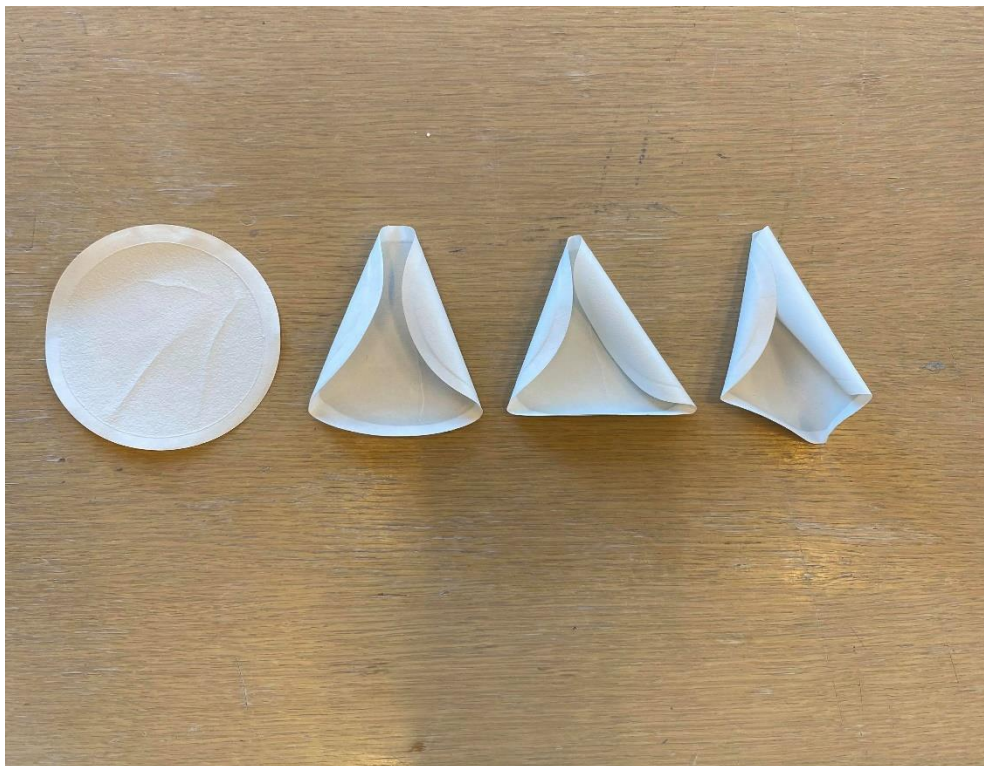


Figure B.2: Mud cakes for the K reference fluid with 1wt%, 2.05wt% and 3wt% CaCO₃ nanoparticle concentrations.



Figure B.3: Mud cakes for the Na/K 50/50, 60/40 and 70/30 ratios.

APPENDIX C – Hydraulic fracturing of Cs/K fluid systems and water

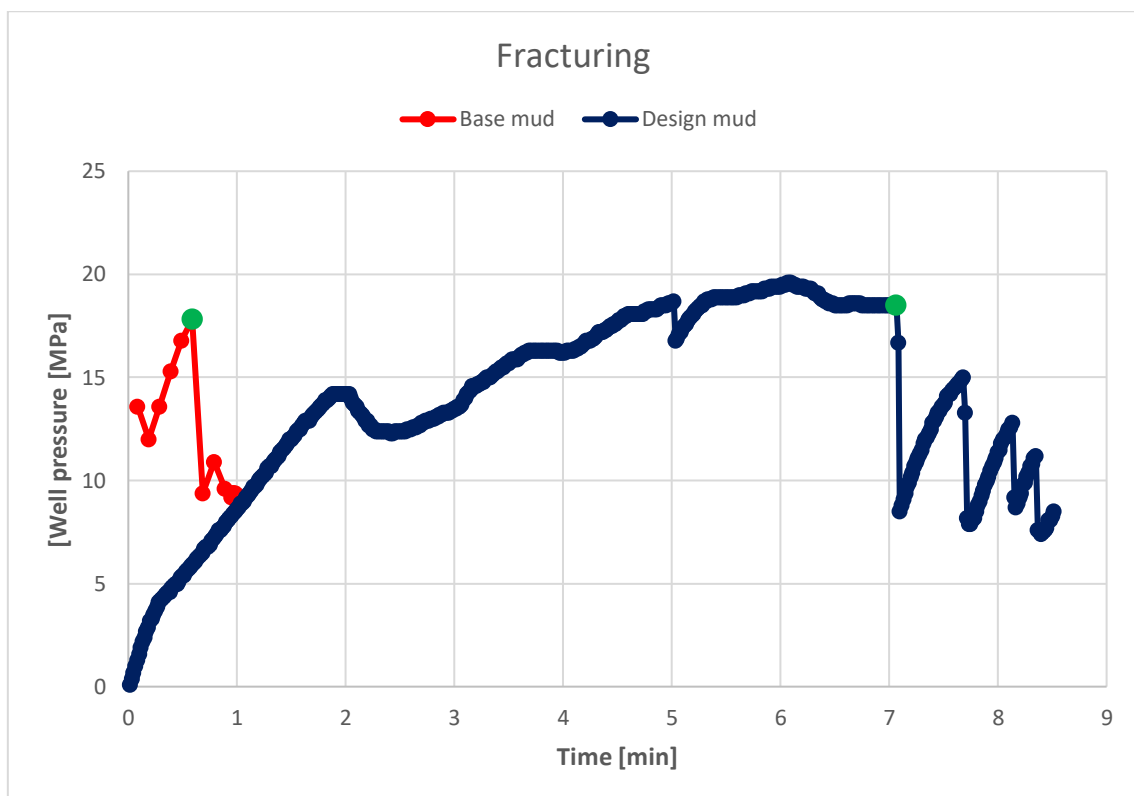


Figure C.1: Fracturing for the Cs/K base mud and Cs/K design mud at core 1.

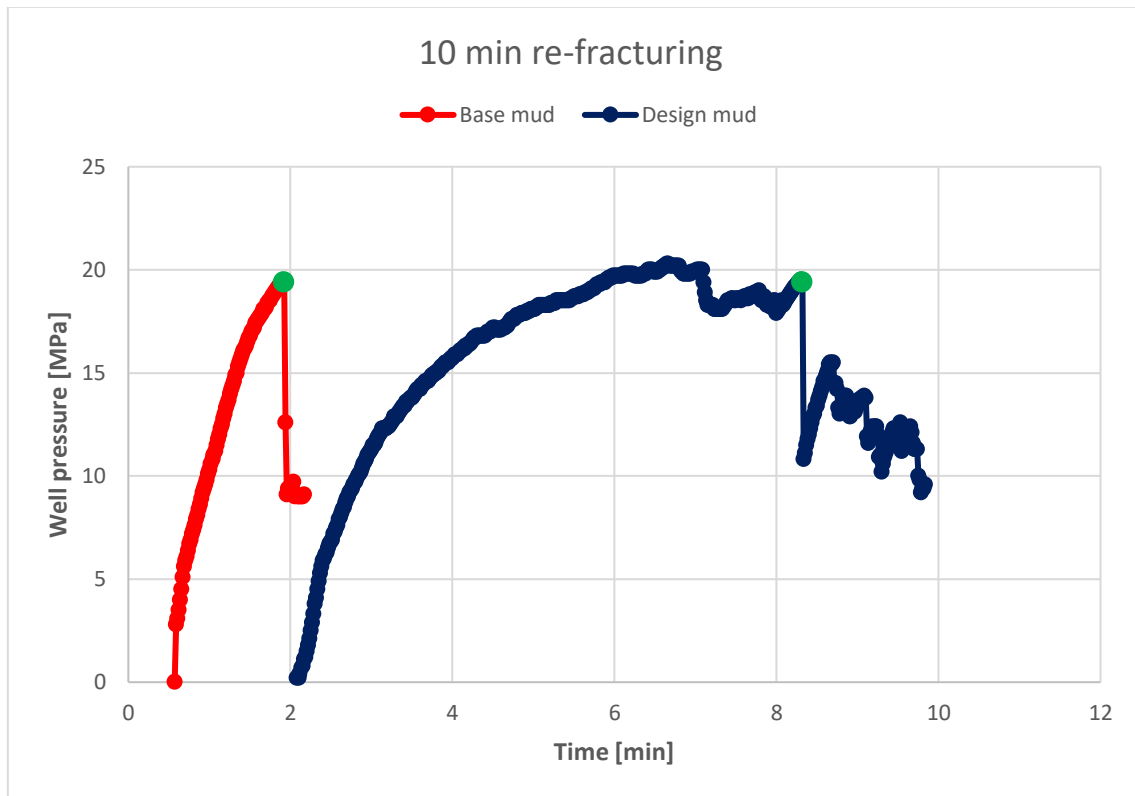


Figure C.2: 10 min re-fracturing for the Cs/K base mud and Cs/K design mud at core 1.

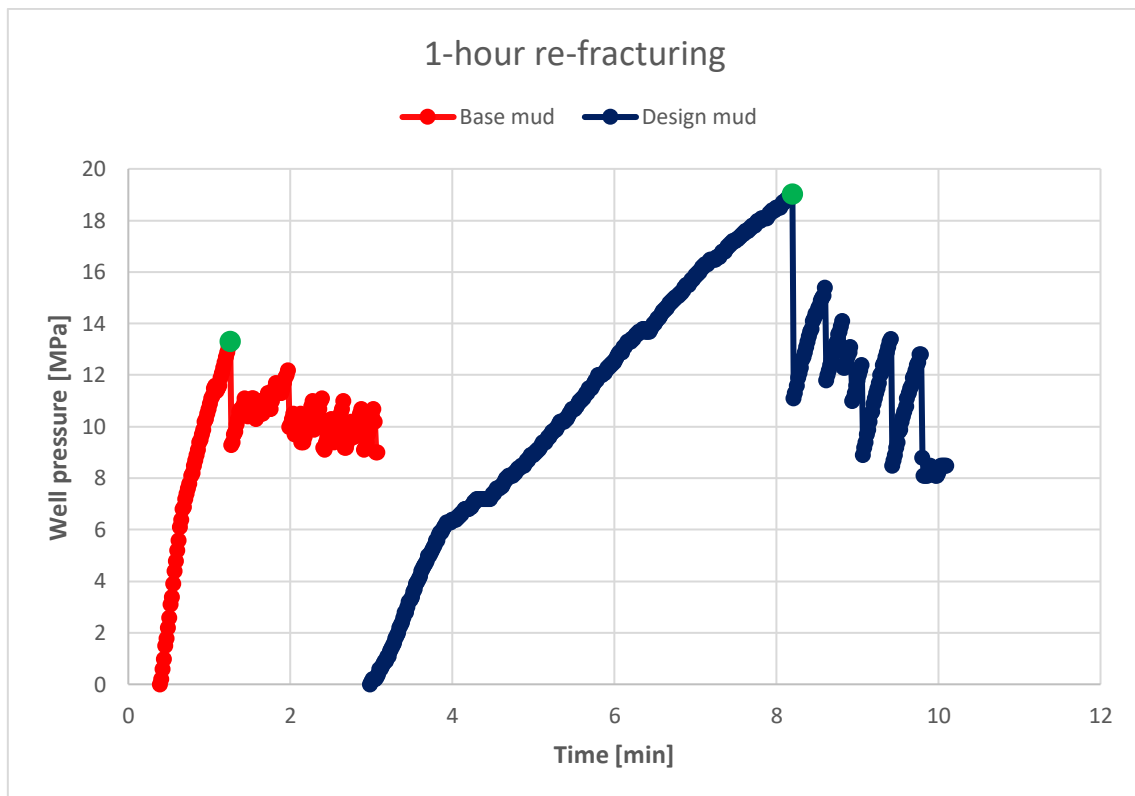


Figure C.3: 1-hour re-fracturing for the Cs/K base mud and Cs/K design mud at core 1.

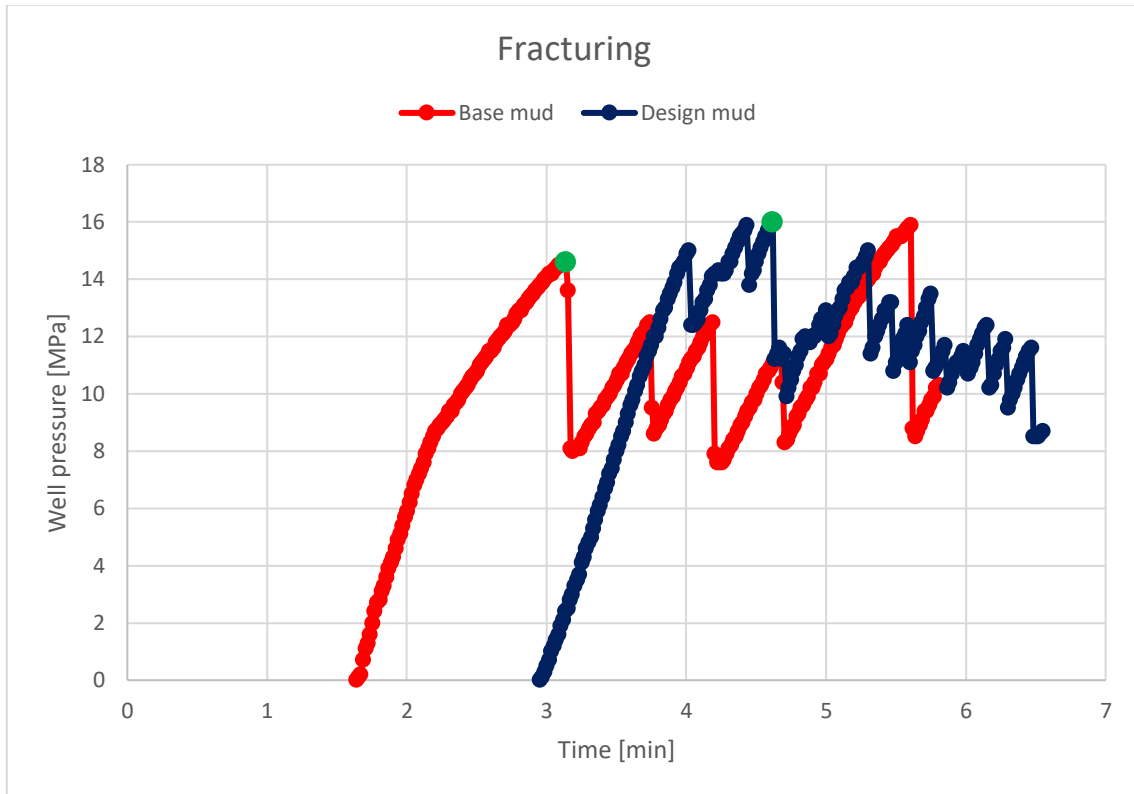


Figure C.4: Fracturing for the Cs/K base mud and Cs/K design mud at core 2.

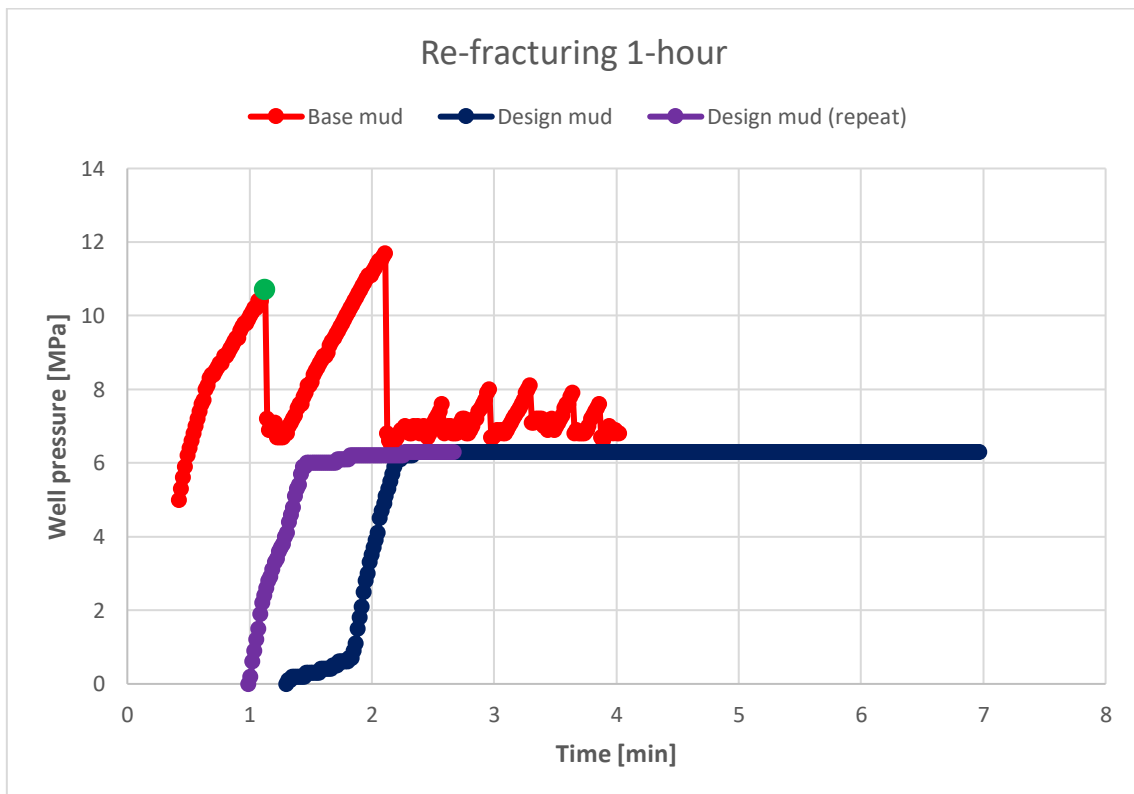


Figure C.5: 1-hour re-fracturing pressure for the Cs/K base mud and Cs/K design mud with repeat test for the design mud at core 2.

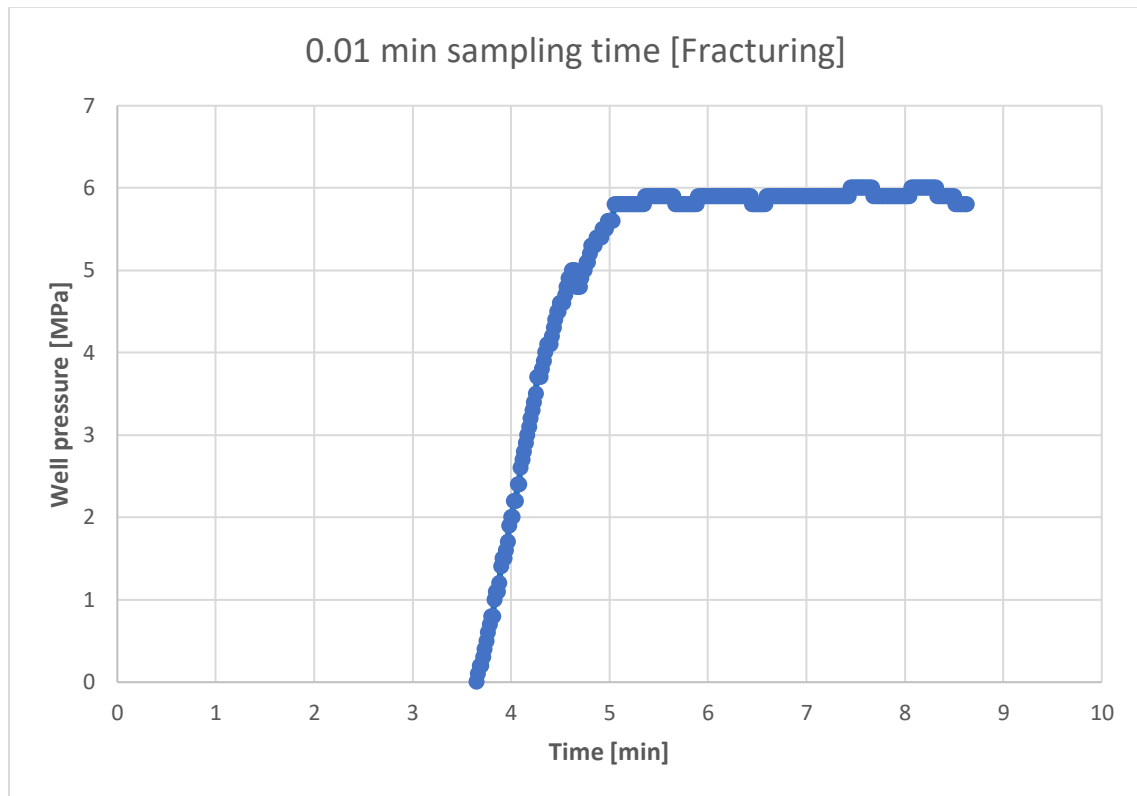


Figure C.6: Fracturing of water at core 1.

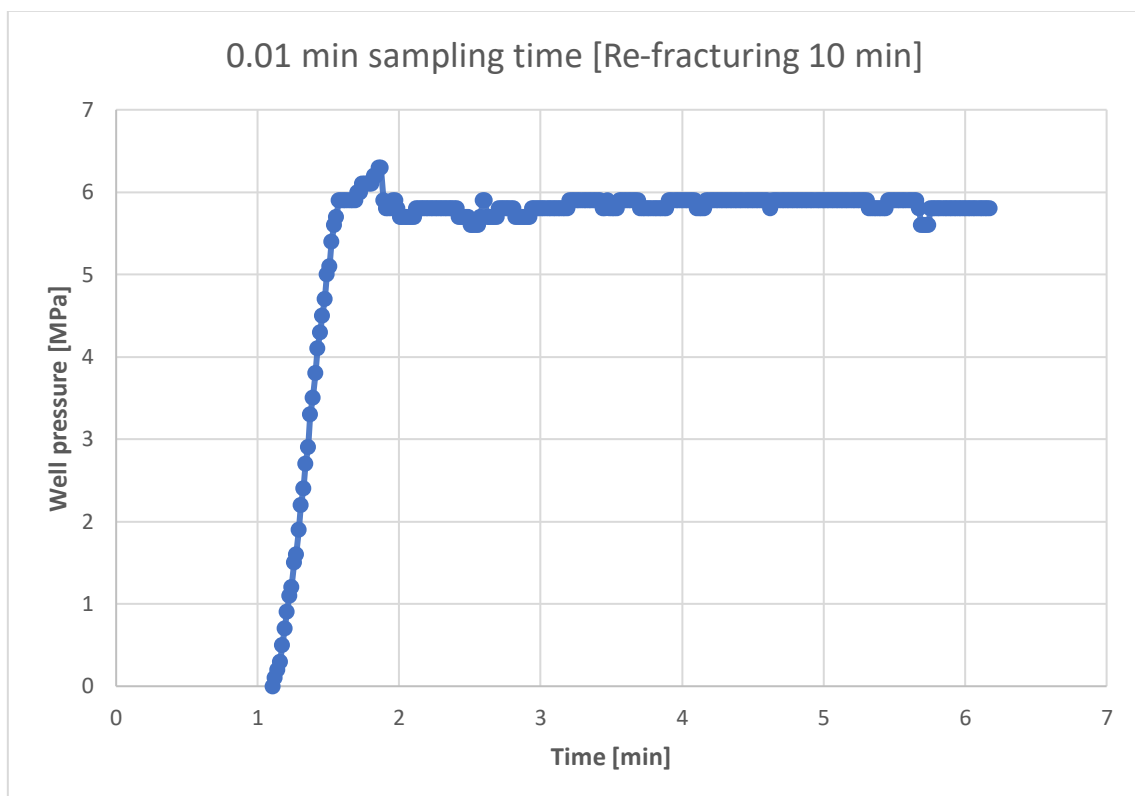


Figure C.7: 10 min re-fracturing of water at core 1.

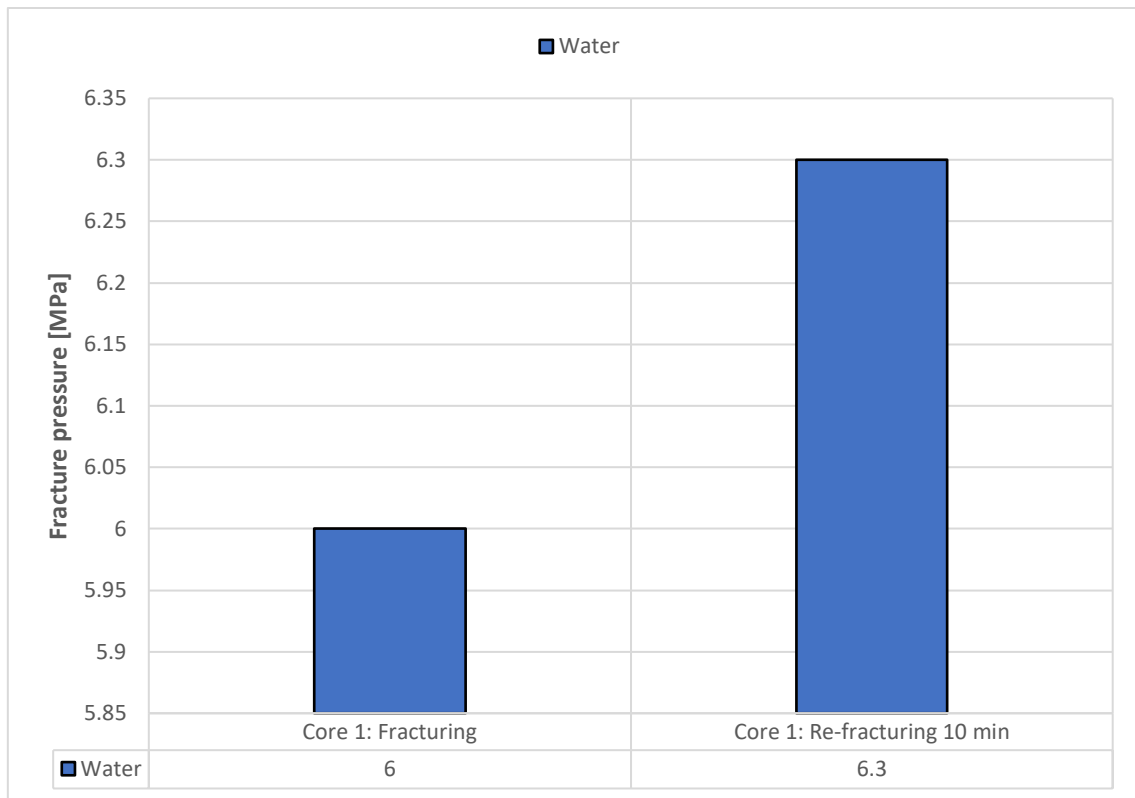


Figure C.8: Fracturing and 10 min re-fracturing pressure for water at core 1.